TECHNISCHE UNIVERSITÄT MÜNCHEN

Walter Schottky Institut

Zentralinstitut für physikalische Grundlagen der Halbleiterelektronik

Silicon Nanocrystal Films for Electronic Applications

Robert W. Lechner

Vollständiger Abdruck der von der Fakultät für Physik
der Technischen Universität München
zur Erlangung des akademischen Grades eines

Doktors der Naturwissenschaften

(Dr. rer. nat.)

genehmigten Dissertation.

Vorsitzender:	Univ.-Prof. Dr. P. Vogl
Prüfer der Dissertation:	1. Univ. Prof. Dr. M. Stutzmann
	2. Univ.-Prof. Dr. F. Simmel

Die Dissertation wurde am 30.10.2008 bei der Technischen Universität München eingereicht und durch die Fakultät für Physik am 06.02.2009 angenommen.

Contents

Zusammenfassung **7**

1 Introduction: Printable Semiconductors **11**
1.1 Organic semiconductors 16
1.2 Semiconductor nanoparticles 17
1.2.1 Size and surface 17
1.2.2 Materials 18
1.2.3 Growing silicon nanocrystals 19
1.3 Chapter Overview 21

2 Experimental Methods **23**
2.1 Material Processing 23
2.1.1 Gas phase production of silicon nanoparticles 23
2.1.2 Substrates 27
2.1.3 Dispersing silicon nanoparticles 28
2.1.4 Digital doping 29
2.1.5 Spin-coating 30
2.1.6 Oxide etching 31
2.1.7 Laser crystallization 32
2.1.8 Metal evaporation 33
2.1.9 Amorphous silicon deposition 34
2.1.10 Thermal annealing 34
2.1.11 Aluminum Etching 35
2.1.12 Hydrogen Passivation 35
2.2 Analytical Methods 36
2.2.1 Chemical Analysis 36
2.2.2 Structural analysis 37
2.2.3 Optical Spectroscopy 40
2.2.4 Electrical Characterization Tools 43

3 Physics of Silicon Nanocrystals **47**
3.1 Electron confinement 47
3.2 Metastability of nanocrystals 48
3.2.1 Sintering of nanoparticles 49
3.2.2 Size dependent melting of nanocrystals 50
3.3 Vibrational Properties 52
3.3.1 Raman spectroscopy 53
3.3.2 Phonon confinement model 55
3.4 Optical Properties 57
3.4.1 Band structure and dielectric constant 57
3.4.2 Free carrier absorption 59

3.4.3 Effective medium approaches . . . 60
3.5 Doping of Silicon Nanocrystals . . . 60
3.5.1 Bulk silicon dopant species and solubilities . . . 61
3.5.2 Formation energy and self-purification . . . 62
3.5.3 Binding energy or activation energy . . . 63
3.6 Electrical Transport in Nanocrystal Layers . . . 64
3.6.1 Percolation transport . . . 64
3.6.2 Discreteness of dopants and defects . . . 65
3.6.3 Coulomb blockade . . . 66
3.6.4 Space charge limited current, tunneling and hopping transport . . . 67
3.6.5 Grain Boundaries and Defects . . . 68
3.6.6 Potential fluctuations . . . 71

4 Properties of Silicon Nanoparticle Layers 73
4.1 Structural Properties . . . 73
4.1.1 Morphology . . . 73
4.1.2 Crystallinity . . . 78
4.1.3 Raman Analysis . . . 78
4.1.4 EPR analysis . . . 84
4.2 Chemical Analysis . . . 88
4.2.1 Contamination levels . . . 88
4.2.2 Surface oxidation . . . 89
4.2.3 Dopant concentration . . . 91
4.3 Optical Properties of Silicon Particle Films . . . 95
4.3.1 Reflectivity spectra . . . 95
4.3.2 Index of refraction . . . 96
4.3.3 Effective medium interpretation . . . 98
4.3.4 Optical absorption . . . 99
4.4 Electrical Properties of Silicon Particle Films . . . 104
4.4.1 Electrical conductivity . . . 105
4.4.2 Carrier compensation . . . 108
4.4.3 Temperature dependent conductivity . . . 109
4.4.4 Photoconductivity . . . 111
4.4.5 Thermal annealing . . . 113

5 Aluminum-Induced Recrystallization of Nanocrystalline Silicon Layers 117
5.1 Aluminum-Induced Layer Exchange with Amorphous Silicon . . . 117
5.1.1 Layer Structure . . . 117
5.1.2 Layer exchange . . . 118
5.1.3 Driving Force . . . 119
5.1.4 Al-Si Phase Diagram . . . 120
5.1.5 Thermal Activation . . . 122
5.1.6 Interface Reactions . . . 122
5.1.7 Diffusion Processes . . . 124
5.1.8 Oxide barrier-free structures . . . 124
5.1.9 Structure of the Silicon Precursor . . . 124
5.2 ALILE with Silicon Nanocrystals . . . 125
5.2.1 Structural Properties . . . 125

5.2.2 Process Dynamics . . . 131
5.2.3 Phenomenological model for ALILE with silicon particle layers . . . 138
5.2.4 Optical Properties . . . 139
5.2.5 Electrical Properties . . . 141
5.3 Acceptor Passivation of ALILE crystallized Silicon nanocrystals . . . 143
5.3.1 Effusion experiments . . . 143
5.3.2 Electrical properties of passivated layers . . . 146
5.3.3 Grain boundary barriers in ALILE recrystallized films . . . 146

6 Laser Annealing of Silicon Nanocrystal Layers 149
6.1 Laser Crystallization of Silicon . . . 149
6.1.1 Laser systems . . . 149
6.1.2 Pulsed laser crystallization of amorphous silicon . . . 150
6.1.3 Stepwise laser crystallization . . . 151
6.1.4 Laser crystallization of silicon nanocrystals . . . 151
6.2 Structural Properties . . . 152
6.2.1 Morphology . . . 152
6.2.2 Raman analysis of laser-crystallized films . . . 158
6.2.3 Defect density . . . 160
6.2.4 Dopant Segregation . . . 161
6.3 Optical Properties . . . 162
6.3.1 Absorption coefficient . . . 162
6.3.2 Fano effect . . . 163
6.4 Electrical Properties of Laser-Annealed Silicon Particle Layers . . . 168
6.4.1 Electrical conductivity after laser annealing . . . 168
6.4.2 Influence of the doping on the electrical conductivity . . . 170
6.4.3 Conductivity of digitally doped layers . . . 174
6.4.4 Impedance spectroscopy . . . 175
6.4.5 Carrier compensation in laser-annealed silicon nanocrystals . . . 177
6.4.6 Temperature dependent conductivity . . . 179
6.4.7 Carrier mobility . . . 181
6.4.8 Anisotropy of the electrical conductivity . . . 183
6.5 Thermoelectric Properties of Laser-Annealed Printed Silicon Layers . . . 183
6.5.1 Seebeck coefficient . . . 184
6.5.2 Q-function . . . 187
6.5.3 Thermal conductivity . . . 191
6.5.4 Figure of merit . . . 194

7 Summary and Outlook 197
7.1 Summary . . . 197
7.2 Outlook . . . 200
7.2.1 *pn*-Junctions . . . 200
7.2.2 Field Effect in Recrystallized Nanoparticle Layers . . . 202
7.2.3 Thermoelectric Devices . . . 203

Acknowledgements 207

List of publications 209

Bibliography **211**

Zusammenfassung

Als der wesentliche Vorteil der konventionellen Mikroelektronik hat sich die Möglichkeit bewährt, die Integrationsdichte der Halbleiterbauelemente durch wachsenden technologischen Aufwand stetig weiter in die Höhe zu treiben, um so stetig steigende Rechenleistungen auf immer kleinerer Fläche zu erzielen. Im Gegensatz dazu konnte sich aber über die letzten Jahrzehnte auch die sogenannte Makroelektronik behaupten. Zu dieser lassen sich großflächige elektronische Anwendungen zählen, in denen auch die Halbleiterbauelemente eine dementsprechend große Fläche einnehmen, so etwa die Bildschirmtechnologie, die Photovoltaik, großflächige Lichtquellen, aber auch z.B. großflächige Röntgendetektoren. Fernerhin Anwendungen, die zwar heute noch keine große wirtschaftliche Rolle spielen, denen aber enormes Potential zugetraut wird, wie passive Funketiketten (RFIDs) oder thermoelektrische Energiewandler zur Nutzung von Abwärme.

In diesen Bereichen besteht keine Notwendigkeit oder nicht einmal die Möglichkeit, die Halbleiterelemente weiter zu verkleinern. Stattdessen ist hier oft die Senkung der Produktkosten pro Fläche das Ziel. Einsparmöglichkeiten bieten sich hier vor allem durch den Einsatz alternativer kostengünstigerer Materialsysteme und durch großflächige Abscheidemethoden. "Druckbare Elektronik" ist in diesem Zusammenhang zu einem Schlagwort geworden, das den Traum ausdrückt, eine gut beherrschte und leicht skalierbare Technologie wie das Drucken auf Anwendungen zu übertragen, die bisher der Halbleiterhochtechnologie vorbehalten blieben. Um aber Halbleiter zu verdrucken, müssen entweder die Halbleitermaterialien selber in Flüssigkeiten löslich sein, wie es für organische Halbleiter der Fall ist, oder sie müssen in Form von Nanopartikeln vorliegen, um Dispergierbarkeit in Lösungsmitteln zu erfüllen. Hier wurde der zweite Ansatz verfolgt und überdies mit Silizium ein Material gewählt, das ungiftig ist, unter Raumbedingungen stabil ist und als Rohstoff schier unerschöpflich zur Verfügung steht. Ob sich aber Nanopartikel aus Silizium tatsächlich für solche Anwendungen eignen, ob daraus hergestellte Schichten halbleitende Eigenschaften aufweisen, ob sie sich dotieren lassen und ob zum Beispiel über die Dotierung die Leitfähigkeit eingestellt werden kann, sollte in der vorliegenden Arbeit untersucht werden.

Ausgangsmaterial hierfür waren zum einen sphärische Siliziumnanokristalle mit einer scharfen Größenverteilung und mittleren Durchmessern im Bereich von $4-50\,\mathrm{nm}$, die in Mikrowellenreaktoren direkt aus den Eduktgasen hergestellt wurden. Außerdem standen Heißwandreaktor-Siliziumpartikel zur Verfügung, die mit $50-500\,\mathrm{nm}$ deutlich größer sind, eine breite Verteilung der mittleren Größe und eine polykristalline Feinstruktur mit stark verzweigter äußerer Morphologie aufweisen. Beide Arten von Partikeln lassen sich jeweils mithilfe eines Kugelmühlverfahrens in niedrigviskose ethanolische Dispersion bringen, und durch Aufschleudern, bzw. Spin-coating, auf gängige Substrate erhält man so relativ glatte Schichten. Aus der Analyse des Brechungsindex lässt sich ermitteln, dass hierin die Partikel recht locker angeordnet sind, denn Porositäten von ungefähr 60% sind die Regel. Berücksichtigt man diesen Wert, entspricht der optische Absorptionskoeffizient von Schichten aus Mikrowellenreaktor-Nanokristallen im wesentlichen der von mikrokristallinen Siliziumschichten, wie man sie üblicherweise mittels chemischer Gasphasenabscheidung herstellt. Als Folge der deutlich unterschiedlichen Mikro-

struktur im Falle von Schichten aus Heißwandmaterial lässt sich hier eine deutlich erhöhte optische Absorption feststellen. Da die Siliziumpartikel nach ihrer aufwendigen Prozessierung stets von Hüllen aus natürlichem Oxid umgeben sind, wurden diese durch nasschemisches Ätzen entfernt. Erstaunlicherweise ist dieser Ätzschritt selbst auf bereits auf Substrate aufgebrachte Siliziumpartikelschichten anwendbar, und befreit die Oberflächen des porösen Partikelnetzwerkes hocheffizient vom Oxid, wie aus Infrarotspektren deutlich hervorgeht.

Es konnte gezeigt werden, dass die bereits im Mikrowellenreaktor während der Wachstumsphase zugemischten Bor- und Phosphor-haltigen Dotiergase auch tatsächlich zu einer entsprechenden Dotierung der Nanokristalle führen. Allerdings segregiert dabei der Großteil des Phosphors, nämlich bis zu 95%, an der Oberfläche der entstandenen Nanokristalle, wie sich durch massenspektroskopische Elementanalyse in Kombination mit Ätzexperimenten nachweisen lässt. Die Boratome sind, im Gegensatz dazu, gleichmäßig über das Volumen der Nanokristalle verteilt, dafür ist aber nur ein Bruchteil von ihnen elektrisch aktiv infolge einer bevorzugten Besetzung interstitieller Gitterplätze.

Durch Entfernen der Oxidhüllen um die Silizium-Nanokristalle lässt sich die elektrische Leitfähigkeit der Siliziumschichten zwar um zwei Größenordnungen verbessern, dennoch werden so noch keine Werte nennenswert über $10^{-10}\Omega^{-1}\,\mathrm{cm}^{-1}$ für undotierte Schichten erreicht. Auch bei Verwendung von schwach oder mittelmäßig hoch dotierten Nanokristallen bleibt die Leitfähigkeit bei vergleichbar geringen Werten. Erst für Konzentrationen im Bereich von $10^{19}\,\mathrm{cm}^{-3}$ Dotieratomen zeigt sich ein sprunghafter Anstieg der Leitfähigkeit um bis zu drei Größenordnungen. Da sich dieser Wert der kritischen Dotierkonzentration gut mit der Konzentration an nicht abgesättigten Siliziumbindungen, bzw. dangling bonds, in den Schichten deckt, kann Defektkompensation der freien Ladungsträger für diese Beobachtung verantwortlich gemacht werden. Diese Interpretation wird darüberhinaus bestärkt durch den abrupten Rückgang der Aktivierungsenergie der Leitfähigkeit im Bereich der kritischen Dotierkonzentration. Der relativ hohe Wert für die Defektkonzentration in den Schichten resultiert hierbei vornehmlich aus dem oben erwähnten Dispersionsverfahren.

Die geringen Leitfähigkeiten und die niedrigen Beweglichkeitswerte der Ladungsträger in den aufgeschleuderten Schichten aus Silizium-Nanokristallen legen es nahe, geeignete thermische Nachbehandlungsverfahren einzusetzen. So wurde gefunden, dass sich der Aluminium-induzierte Schichtaustausch (ALILE), eine Methode, die üblicherweise zur Rekristallisierung von amorphen Siliziumschichten Verwendung findet, auch auf die porösen Schichten aus Nanokristallen übertragen lässt. Dazu wird auf einen ca. 200 nm dicken Film eine Schicht von Siliziumpartikeln aufgebracht. Bei Temperaturen um $500-550\,^{\circ}\mathrm{C}$ unter Schutzatmosphäre bilden sich kristalline Keime aus Silizium in der Aluminiumschicht, wachsen dort heran und bilden schließlich eine polykristalline Siliziumschicht auf dem Substrat. Im Vergleich mit dem konventionellen ALILE-Prozess mit amorphem Silizium zeigen sich deutliche Unterschiede durch die Verwendung der partikulären Ausgangsschichten, wohingegen die Wahl zwischen Heißwand- oder Mikrowellenreaktormaterial das Ergebnis kaum beeinflusst. Die polykristallinen Siliziumfilme nach dem Prozess weisen eine große Zahl von Löchern und Einschlüssen auf, dafür ist die Oberfläche nach Entfernen der Aluminium- und Siliziumreste weitgehend frei von großen aufgelagerten kristallinen Siliziumkörnern, den sogenannten "hillocks" und "Insel"-Strukturen. In der erhaltenen Siliziumschicht sind große Kristallite von ungefähr $50\,\mu$m Durchmesser und einer Höhe, die der ursprünglichen Aluminiumschicht entspricht, durch dünnere kristalline Silizumregionen verbunden, sodass sich eine zusammenhängende Halbleiterschicht auf dem Substrat ergibt. Als größter Nachteil bei der Verwendung von Siliziumpartikeln erweist sich die starke Verlängerung

der Prozessdauer um zwei Größenordnungen. Ferner bedingt es die erhöhte Aktivierungsenergie, dass der Spielraum der Prozesstemperaturen maximal ausgeschöpft werden muss, um extrem lange Prozessdauern zu vermeiden. Ein phänomenologisches Modell wurde entworfen, das in der Lage ist, die spezifischen experimentellen Besonderheiten bei ALILE mit Nanopartikeln qualitativ zu erfassen.

Andererseits zeigen die ALILE-rekristallisierten Partikelfilme sehr ähnliche optische und elektrische Eigenschaften wie solche aus amorphen Ausgangsschichten. Als Folge des direkten Kontakts während des Schichtaustauschs sind die Siliziumschichten hoch Aluminium-dotiert, und Löcherkonzentrationen von $2 \times 10^{18}\,\mathrm{cm}^{-3}$ lassen sich nachweisen. Die Hallbeweglichkeiten der Ladungsträger sind im Bereich von $20 - 40\,\mathrm{cm}^2\,\mathrm{V}^{-1}\,\mathrm{s}^{-1}$, was angesichts des partikulären Ausgangsmaterials respektable Werte darstellt. Allerdings führt die bessere Schichtmorphologie bei konventionellen ALILE-Schichten noch zu deutlich höheren Beweglichkeitswerten.

Mit der Deuterium-Passivierung stand eine Methode zur Verfügung, die Ladungsträgerkonzentration in den polykristallinen Schichten zu verändern. Aus dem beobachteten Zusammenhang zwischen Ladungsträgerkonzentration und -beweglichkeit konnte geschlossen werden, dass der Transport in den Schichten durch den Einfang freier Ladungsträger an Grenzflächendefekten dominiert wird. Das Minimum der Beweglichkeit bei einer Löcherkonzentration von $5 \times 10^{17}\,\mathrm{cm}^{-3}$ stimmt im Rahmen eines Transportmodells für Korngrenzenbarrieren quantitativ mit einer Defektflächendichte von $3 \times 10^{12}\,\mathrm{cm}^{-2}$ an den Oberflächen und Korngrenzen überein. Die Ladungsträgerverarmung in den dünnen kristallinen Bereichen zwischen den großen Siliziumkristalliten dominiert hierbei das elektrische Verhalten der gesamten Schicht.

Zusätzlich zu ALILE wurde noch Laserkristallisieren als alternatives Nachbearbeitungsverfahren der Nanokristallschichten untersucht. Dazu wurde ein frequenzverdoppelter Nd:YAG Laser im Pulsbetrieb bei einer Wellenlänge von 532 nm verwendet, wobei Pulsserien mit ansteigender Laserenergiedichte zum Einsatz kamen, um die Siliziumschichten zu schonen. Wie sich an den erzielten strukturellen und elektrischen Eigenschaften zeigte, ist es unerlässlich, das die Partikel umhüllende natürliche Oxid vor der Laserbehandlung nasschemisch zu entfernen. Mit beiden Prozessschritten, Ätzen und Laserkristallisieren, haben sich flexible Kaptonfoliensubstrate als völlig kompatibel erwiesen. Die gepulste Laserbehandlung führt zur Bildung eines Netzwerks aus miteinander versinterten und verschmolzenen Nanokristallen, wenn die Laserenergiedichte einen Schwellenwert überschreitet. Dieser liegt bei $50\,\mathrm{mJ\,cm}^{-2}$, was sich mit Abschätzungen anhand von Literaturdaten aus Schmelzexperimenten mit Nanokristallen deckt. Für Nanokristallschichten mit einer Dicke von 700 nm wurden die besten Leitfähigkeitseigenschaften mit Laserenergiedichten von $100 - 120\,\mathrm{mJ\,cm}^{-2}$ erreicht, was zur Bildung von polykristallinen Siliziumfilmen mit $200 - 400$ nm großen sphärischen Oberflächenstrukturen führt. Diese bilden ein perkolierendes poröses Netzwerk, das stabil mit dem Polymersubstrat verbunden ist, wenn die Laserenergiedichte und die Schichtdicke günstig gewählt wurden.

Die effektive laterale elektrische Leitfähigkeit der laserbehandelten Filme zeigt hier in etwa dieselbe Schwellenenergiedichte wie sie anhand der strukturellen Veränderungen in den Nanokristallschichten ermittelt wurde. Für undotierte Nanokristallschichten erhöht sich nach der Laserbehandlung die Leitfähigkeit um drei Größenordnungen, während sogar eine Zunahme um bis zu neun Größenordnungen im Falle hoch dotierter Nanokristalle auftritt. Neben der erhöhten Leitfähigkeit macht auch die Zunahme der internen Kapazitäten in Impedanzmessungen das starke Anwachsen der Strukturgröße mit einhergehender Verringerung der Anzahl an inneren Grenzflächen deutlich. Für Dotierkonzentrationen bis zu $10^{18}\,\mathrm{cm}^{-3}$ ändert sich die Leitfähigkeit nicht mit der Dotierung und beträgt $10^{-8} - 10^{-7}\Omega^{-1}\,\mathrm{cm}^{-1}$ sowohl für Bor- wie

auch für Phosphordotierung. Hingegen nimmt die elektrische Leitfähigkeit bei einer kritischen Dotierung von $5 \times 10^{18} - 10^{19}\,\mathrm{cm}^{-3}$ sprunghaft um sechs Größenordnungen zu und steigt dann kontinuierlich weiter mit der Dotierung an. In hoch Bor- und Phosphor-dotierten Schichten lässt sich in optischen, elektrischen und massenspektroskopischen Messungen eine beinahe vollständige elektrische Aktivität der Dotieratome feststellen. Hochinteressant für die Anwendung als druckbares Halbleitermaterial ist außerdem die Tatsache, dass sich die effektive Dotierung in den laserkristallisierten Schichten durch Mischen zweier Dispersionen unterschiedlich dotierter Nanokristalle über einen sehr weiten Bereich gezielt einstellen lässt.

Auch in den laserbehandelten Schichten lässt sich die Kompensation freier Ladungsträger durch tiefe Defektzustände als Ursache der abrupten Leitfähigkeitszunahme bei der kritischen Dotierkonzentration identifizieren. Quantitative Elektronspinresonanzmessungen zeigen einen Rückgang des Defektsignals sobald die Dotierkonzentration den kritischen Wert übersteigt, wie man es erwarten würde, wenn ein Teil der Defekte infolge der Dotierung in einen geladenen Zustand übergeht. An der kritischen Dotierkonzentration nimmt auch die Aktivierungsenergie der Leitfähigkeit sprunghaft ab, was man im Rahmen des Korngrenzenmodells als eine Folge des Verschwindens von Korngrenzenbarrieren und als Rückgang der großräumigen Ladungsträgerverarmung interpretieren kann. Um auch den Einfluss eventueller Potentialfluktuationen auf den elektrischen Transport in laserkristallisierten Siliziumnanokristallschichten abzuschätzen, wurden temperaturabhängige Thermokraftmessungen durchgeführt, aus deren Auswertungen schwache Aktivierungsenergien für die Q-Funktion hervorgehen. Letztere Größe ist geeignet, Potentialfluktuationen in einem Material zu quantifizieren, wie sie zum Beispiel durch geladene Dotieratome oder durch in tiefen Störstellen lokal gebundene Ladungsträger verursacht werden. Im Bereich der kritischen Dotierkonzentration treten tatsächlich Fluktuationen einer Höhe bis zu 280 meV auf, was zeigt, dass dieser Interpretationsansatz vor allem im kritischen Dotierbereich mit berücksichtigt werden sollte.

Die Ladungsträgerbeweglichkeiten in laserkristallisierten Siliziumnanokristallschichten lassen sich vorsichtig abschätzen zu $0.1 - 0.5\,\mathrm{cm}^2\,\mathrm{V}^{-1}\,\mathrm{s}^{-1}$ für Elektronen und $0.02 - 0.1\,\mathrm{cm}^2\,\mathrm{V}^{-1}\,\mathrm{s}^{-1}$ für Löcher Im Zusammenhang mit den hohen Ladungsträgerkonzentrationen, die für vernünftige Leitfähigkeit nötig sind, scheinen diese Werte auf den ersten Blick das Anwendungsspektrum dieses Materials stark einzuschränken. Auf der anderen Seite konnten aber auch recht hohe Werte für den Seebeck-Koeffizienten bestimmt werden. In ähnlichem Maße wie die elektrische Leitfähigkeit im Vergleich mit einkristallinem Silizium reduziert ist, ist auch die thermische Leitfähigkeit der laserbehandelten Nanokristalle um Größenordnungen kleiner als im Volumenmaterial. In der thermoelektrischen Güteziffer, die die Effizienz von Materialien für thermoelektrische Elemente quantifiziert, heben sich diese beiden Effekte jedoch gegenseitig auf. Hochdotierte Schichten aus laserkristallisierten Siliziumnanokristallen könnten sich demzufolge als potentielles Material für thermoelektrische Anwendungen anbieten, da eine erste Abschätzung bereits eine Effizienz erwarten lässt, die mit der von kristallinem Silizium vergleichbar ist. Die inhärenten Vorteile der Nanopartikel, wie z.B. ihre einfache Legierbarkeit durch Mischen, können dabei noch zu zusätzlichen Steigerungen führen.

1 Introduction: Printable Semiconductors

To date, the unrivaled advantage that has allowed the triumphant advance of microelectronics industry consists in the compatibility of the successful bulk silicon wafer technology with the ever increasing areal structure density of electronic integrated circuits. However, in the shade of this success, another rapidly growing market has developed during the past decades, that may soon start to outrun the former in volume. Quite in contrast to Moore´s law, which connects the progress of performance with the need to steadily reduce the size of the individual electronic components, here the device or substrate area is the relevant scaling metric justifying the often used term of "macroelectronics" in this case [Sun07]. Examples for existing devices comprise switching transistors in active matrix displays, photovoltaic cells, and medical X-ray imaging devices. At present, amorphous silicon has become the most important semiconductor material for large area thin-film transistors, is widely used in thin-film solar cells, and already ranks second in economic importance of semiconductor materials behind crystalline silicon.

Thinking of new cost-efficient technologies that can be utilized for such applications, alternative thin-film processes on cheap substrates such as metal sheets, glass, polymer foils, or paper, appear most favorable. Here, printable semiconductors comprising the combination of printing techniques with semiconducting materials are expected to enable even the profitable realization of flexible displays, fabric integrated logics, active antennas, and "sensory skin" devices [Rog01]. Also, solar cells would highly benefit from substantial cost reduction by the application of cost-efficient printing techniques. Considering the almost unlimited solar energy supply, such technological advantages would be unequivocal in the face of the inherent scarcity of fossil energy sources and the human-induced global climate warming.

An additional alternative form of sustainable energy that can be utilized by the help of semiconducting materials is thermoelectric power generation. Based on the Seebeck effect, thermoelectric devices allow the direct transformation of a heat flow into electrical power. Thermoelectric materials have re-entered scientific research interest since energy prices started to increase dramatically and they are believed to play a significant role in future energy supply by taking advantage of otherwise lost excess heat [Dre07]. Similar to photovoltaic solar cells, thermoelectric energy conversion is emission-free once the energy payback time of the electronic device has passed. To power small mobile devices, which consume only very small amounts of energy, even the minute temperature difference between the human body and the surroundings can be sufficient. In this context, a scenario of consumer electronics integrated into the clothing is conceivable, where either small solar cells are used or the temperature gradient is exploited for power generation, and all components from the logic to the generator unit are realized by printed semiconductor materials.

Regarding the implementation of these ideas, several important stages have already been demonstrated by different material routes. In this introductory part, the possible material classes and promising material candidates will be highlighted, and their potential in the field will be discussed. However, first of all, we want to shortly focus on the necessary requirements, which are imposed by three exemplary potential applications.

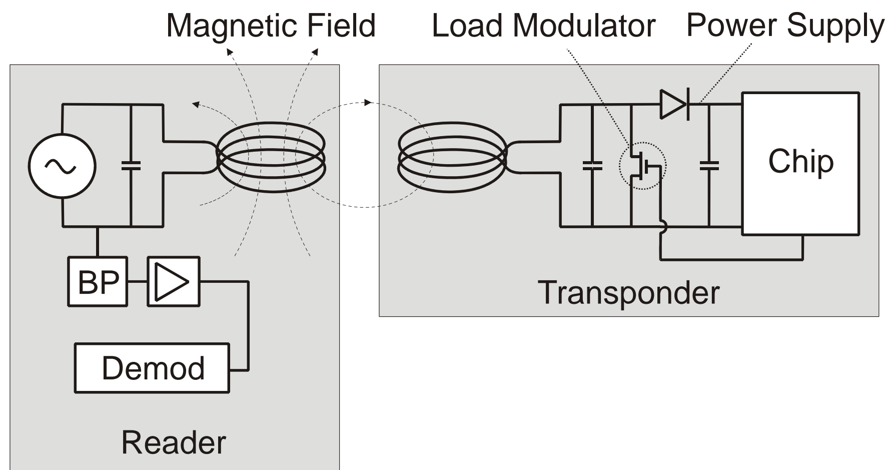

Figure 1.1: Circuit scheme of an RFID transponder (right) and the appropriate reader device (left) which communicate by inductive coupling at a resonant frequency (after [Fin06]).

Radio frequency identification tags

A highly auspicious type of device in all recent discussions regarding future applications of printable semiconductors, are radio frequency identification tags (RFID tags). These are passive communicating devices (transponders) that can be used as completely isolated tags on palettes, boxes or individual products that can be tracked throughout the logistics cycle by identifying information. RFID tags use an external radio frequency excitation both as the carrier wave as well as their power source. As the receiver circuit is coupled resonantly to this frequency, modulating the load by the transponder can be detected by the sender/reader as a slight change in the absorbed amplitude (10^{-6} to 10^{-8}, or 60 dB to 80 dB). Obviously, this technique is limited in its operating distance, because the intensity I of the sender wave drops off inversely proportional to the square product of the distance, $d : I \propto d^{-2}$. To be able to detect the transponder´s modulations, the distance between reader and transponder unit needs to be limited, depending on the reader´s sensitivity and the wavelength. Figure 1.1 displays a scheme of a reader/transponder system and their respective circuit diagrams.

As yet, no single standard for RFID communication has been established, but several details seem to emerge. As the carrier frequency, the high frequency (HF) 13.56 MHz band appears to be a reasonable standard, while alternatives exist also in the low frequency (LF) 128 kHz band and the ultra high frequency (UHF) band $850 - 950$ MHz. With decreasing wavelength also the coupling range changes from the very close (1 cm) near field coupling for the LF communication towards remote operation ($1 - 6$ m) for UHF where in the far field of the electromagnetic wave a reflected fraction is modulated. In this case, the shape of the antenna differs from an inductively coupled coil (as for LF/HF) and resembles more a dipole-like open antenna [Fin06].

While already many RFID systems are used in everyday life, *e.g.*, for registering books in libraries, as contactless tickets in ski lifts, or for individualized payment card systems, a real breakthrough is expected once the price per chip reaches the sub-cent price level so that every product can be equipped with RFID tags. It is estimated that such reduction of cost can not be realized by standard bulk semiconductor industry following Moore´s law, but will be one of the major application fields of printable semiconductors. As visible from the circuit diagram in Figure 1.1, the main components of RFID tags comprise the antenna, conductive leads, capacitors,

and diodes to rectify the AC current supply, a modulating transistor, and a logic chip, which itself contains numerous of the aforementioned electronic devices. So to produce RFID tags from printed materials, different types of inks need to be available to realize as well metallic features for highly conductive structures (antennae, leads), insulating properties (dielectrics in capacitors and gates), as semiconductors for the rectifying diodes and switching components (transistors).

Owing to the fact that RFID passive elements can be regarded as comparatively simple electronic devices, the pertinent requirements on the performance of the printable semiconducting material are low. However, the device should be able to communicate with reasonable bit rates, which are mainly limited by the cut-off frequency of the modulating transistors. This quantity is a function of the electronic mobility, μ, the temperature, T, and the transistor gate length, L_G. As for printed semiconductors, where the feature size depends mainly on the printing technique, a carrier mobility of $1\,\mathrm{cm^2/V\,s}$ would limit the cut-off frequency, f_T, according to:

$$f_\mathrm{T} \approx \frac{\mu \frac{k_\mathrm{B} T}{e}}{2(L_\mathrm{G})^2} = 12.5\,\mathrm{kHz}, \tag{1.1}$$

where k_B is the Boltzmann constant, and a gate length of $L_\mathrm{G} = 10\,\mu\mathrm{m}$ has been assumed at room temperature [Sze07]. The value resulting from this estimation will be sufficient for the communication of small amounts of information.

Thin film solar cells

The principle of photovoltaic energy conversion is the interior photoelectric effect occurring in semiconductors. Upon absorption of a photon, an electron-hole pair is generated inside the semiconductor if the photonic energy exceeds the band gap energy of the semiconductor. To avoid eventual recombination of these charge carriers, a space charge region has to be present inside the material, which is most commonly realized by a pn-junction or pin-stacked structure. In this space charge region, the electrons and holes experience an electric field and drift towards opposite directions. While the electrons accumulate in the n-type doped region, holes drift towards the p-type doped area. Between the contacts applied to the doped regions of either type, a photovoltage is formed during illumination, which can be used to drive a current through an external load circuit. Figure 1.2 illustrates the basic requirements for a solar cell schematically.

The exemplary cell shown here consists of a bulk p-doped semiconductor with a metallic contact electrode on the back. Adjacent to this hole conductor, an n-type region is realized, *e.g.*, by the in-diffusion of dopants, and a space charge region will form in between these areas of opposite polarity. On top of the electron conductor, a front contact grid is situated enabling the efficient extraction of electrons from the upper layer.

The photogeneration of carrier pairs takes place in a large volume, but only those carriers that can diffuse towards the space charge region within their lifetime can be separated and can contribute to the photocurrent. Due to this reason, a solar cell should be designed in a way that the minority carriers have the possibility to reach the space charge region. The thickness of the p- and n-type layers should consequently not exceed the respective minority carrier diffusion lengths. Additional important requirements comprise the lack of tunneling channels through one of the active layers or short circuits between the contacts. Already from these simple considerations it becomes clear that in solar cell design a trade-off between efficient absorption and good electrical properties has to be achieved.

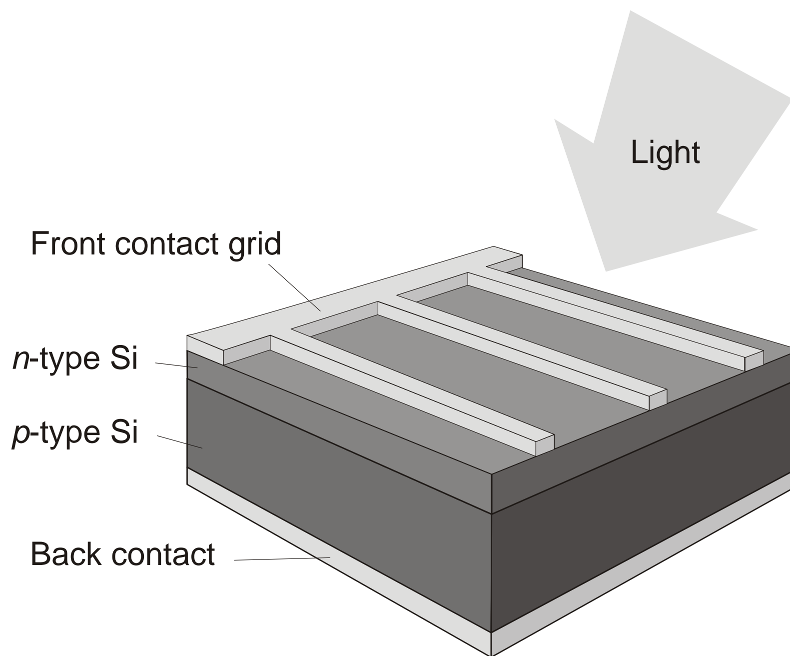

Figure 1.2: Schematic drawing of a crystalline silicon (*c*-Si) solar cell. In the most common geometry, a low-level *p*-type doped *c*-Si absorber layer adjoins to an in-diffused *n*-type surface emitter layer. Photogenerated charge carriers become separated in the space charge region around the intermediate junction. A planar metallic back electrode and a front contact grid are applied to extract the photogenerated carriers.

To combine the photovoltaic energy conversion concept with printable semiconductors, the cell design has to be adapted appropriately. For example, in nanoparticulate systems the concept of a space charge region is difficult to define, and particles of either doping should be positioned very close to each other to efficiently enable charge separation. Regarding organic semiconductors, concepts of mixed-phase aggregates have been proposed to achieve large effective interfaces, which is known as the "bulk hetero-junction" approach [Coa04].

Thermoelectric devices

The discovery of the thermoelectric effect by Seebeck in 1821 showed up the possibility to gain electric power from a temperature difference, as a solid state analog to the Carnot cycle, but without any moving parts. While the Seebeck coefficient, which determines the thermopower per Kelvin temperature difference, is very small in metals ($5\,\mu\mathrm{V\,K^{-1}}$), it can adopt significant values in semiconductors ($1\,\mathrm{mV\,K^{-1}}$), where the carrier statistics are strongly influenced by the temperature. Since the sign of the Seebeck coefficient is determined by the respective majority carrier type, the absolute value of the thermopower can be approximately doubled by oppositely connecting two *p*- and *n*-type semiconductor elements of comparable doping level in series. Real thermoelectric generators consist of numerous of such thermocouples in serial operation to achieve reasonably high output voltages, as illustrated in Figure 1.3.

Generating electrical power from a thermoelectric element is inevitably connected with loss processes such as the direct heat transfer from the hot to the cold side by thermal conduction and the ohmic losses due to the internal resistance of the device itself. If one balances these effects, a thermoelectric figure of merit ZT can be defined, which accounts for these contributions and

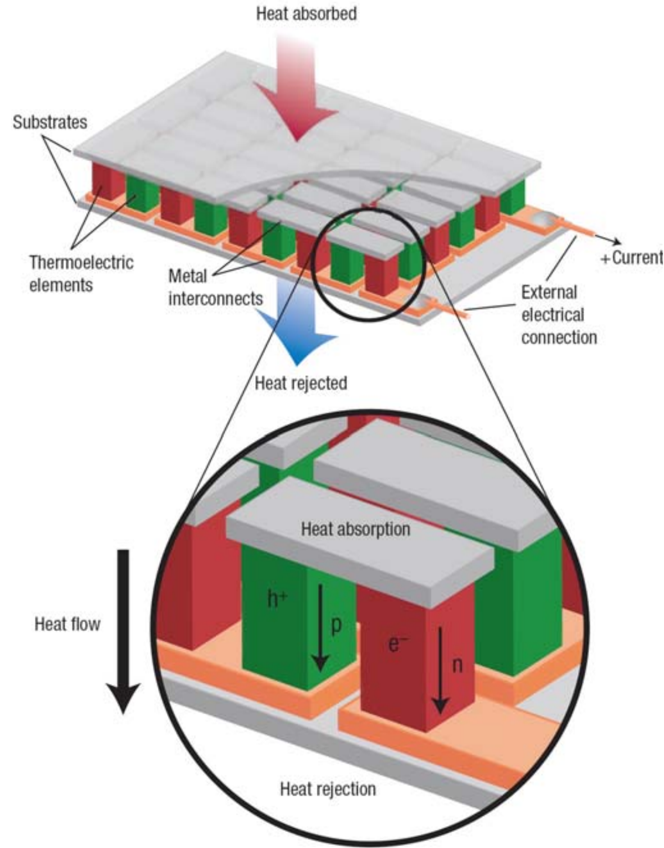

Figure 1.3: Schematic drawing of a thermoelectric generator consisting of cascaded thermocouples of *p*- and *n*-type doped semiconductor elements in series operation. From [Sny08].

gives a dimensionless number that helps to assess the material quality for thermoelectric applications. It can be deduced from specific material functions according to the formula:

$$ZT = \frac{S^2\sigma}{\kappa} T \; , \tag{1.2}$$

where S is the Seebeck coefficient, T is the temperature, σ is the electrical conductivity, and κ is the thermal conductivity of the material [Iof57]. Obviously, high values of S and σ compete with desirably low values of κ to achieve high efficiencies. While in bulk metals, σ and κ are connected via the Wiedemann-Franz-law, low-dimensional materials enable possibilities to decouple these quantities by introducing, $e.g.$, selective scattering mechanisms. In this respect, especially nanocrystals or nanowires embedded in a matrix or forming a network appear promising to reduce thermal transport along the temperature gradient. The challenge is to enable very efficient current transport at the same time manifesting itself in a large electrical conductivity.

The Carnot limit of efficiency holds also for this type of thermodynamic process. In fact, the efficiencies achieved with the best thermoelectric elements remain below about one third of the respective Carnot value, and consequently, thermoelectric generators will never be a competitor in large-scale power generation. Still, they can gain significant importance in areas where grid- and maintenance-free full-time operation is required.

Having in mind the potential applications of printable semiconductors, now we want to focus on the possible material routes towards these devices. Starting from organic semiconductors, small-

sized inorganic semiconductor particles will be introduced, such as they have been used in the course of this work.

1.1 Organic semiconductors

The discovery of organic semiconductors can be dated to the year 1963, when D. E. Weiss *et al.* first reported the semiconducting behavior of polypyrroles by transfer doping with iodine [Wei63]. However, the time was not ripe for this discovery then, and it was not before 1976, that semiconducting polymers were (re-)discovered by Alan J. Heeger, Alan G. MacDiarmid, and Hideki Shirakawa who were awarded the Nobel Prize in Chemistry in 2000 for their work on the chemically similar polyacetylene. The intensive research activities in the field have led to the development of all-organic field effect transistors with ever increasing values of the reported field effect mobility. Nowadays, the values have already approached the order of $0.1\,\mathrm{cm^2/V\,s}$ for polymers such as poly(3-hexyl-thiophene) (P3HT, [Sir99]) or PBTTT [McC06]. Even higher mobility values exceeding $6\,\mathrm{cm^2/V\,s}$ are observed in single crystals of small organic molecules (oligomers) such as pentacene or rubrene [Kel03, Wan07, Pod04].

In all organic semiconductors, electronic transport is possible through a system of conjugated π-orbitals. In oligomer crystals, these conjugated π-orbitals of neighboring molecules overlap and enable efficient charge transport. An example of such an organic crystal is given in Figure 1.4, which displays as well a single pentacene molecule and the unit cell of a crystalline monolayer of pentacene formed on an amorphous substrate [Fri04]. However, to obtain a high degree of crystallinity, it is necessary to evaporate oligomers by sublimation onto a substrate. In contrast, polymers can be solution-processed from a solvent, making this class of materials compatible with printable electronics. However, due to the largely increased disorder in polymers, the π-orbital overlap is severely reduced, which explains the by orders of magnitude smaller mobility in organic polymers.

Additionally, organic semiconductors are found to degrade with time, a process which is strongly enhanced under atmospheric conditions in the presence of oxygen and humidity [Bao97, DeL96, Dim02]. This effect is directly related to the conduction mechanism in these materials. Since any π-orbital represents an energetically unfavorable conformation, oxidants can easily distract electrons to form covalent bonds, which destroys the conjugation. Even if a large part of this effect can be prevented by sealing, this is a severe drawback for applications, since any complicated electronic circuit cannot tolerate the drift or degradation of its components with time.

A special case of large molecules that can be used for semiconducting applications are carbon nanotubes. They can be considered as consisting of a graphene sheet rolled up to a tube with a typical diameter of about one nanometer and a typical length of one micrometer. Semiconducting properties arise when the tubes are single-walled and special conditions for the chirality are fulfilled. While already complete integrated circuits have been realized onto a single carbon nanotube [Che06], the large-scale application of the material is difficult, since always a mixture of metallic and semiconducting nanotubes is obtained during growth. Consequently, solution processed thin film transistors from carbon nanotubes exhibit only small on-off ratios of 100 at low carrier mobilities [Bee07].

Instead, for large area applications, a material system would be preferable, which shows the properties of known bulk inorganic semiconductors: high carrier mobility, reliable performance and

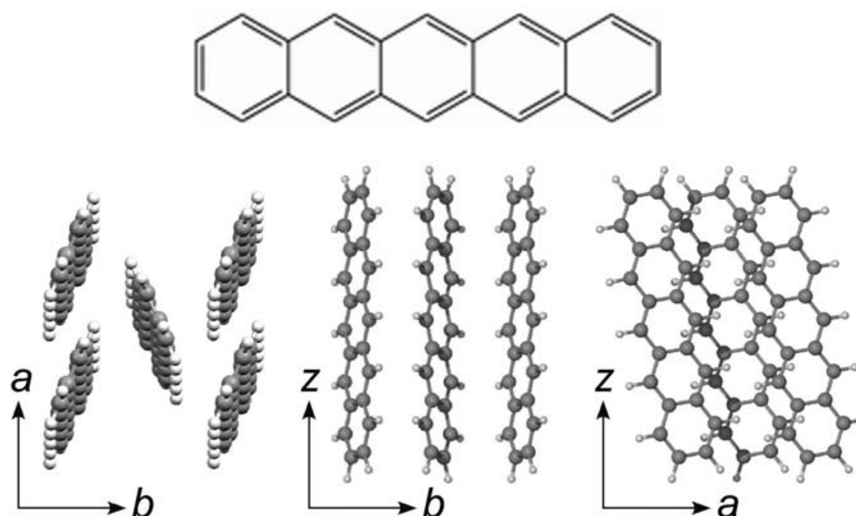

Figure 1.4: Structure formula of a pentacene molecule and three different projections of the crystalline unit cell of an evaporated pentacene monolayer (top image and bottom row, respectively [Fri04]). The ordered stacking of molecules in the crystal leads to overlap of the extended conjugated π-orbital systems and enables electronic transport .

stable operation under atmospheric conditions. To transform such an inorganic semiconductor into a printable material, the first approach would be to reduce the size towards small particles, which can form an ink after applying an appropriate dispersion technique. The size of the particles therein should be significantly smaller than the film thickness required for a functional semiconducting film, which is usually in the range of 50 nm to 5 μm. Using the conventional size nomenclature, we thus are dealing here with semiconductor nanoparticles of a diameter smaller than 100 nm.

1.2 Semiconductor nanoparticles

1.2.1 Size and surface

Due to their strongly reduced size, nanoscale semiconductor particles can easily be converted into printable dispersions and be subjected to, *e.g.*, ink-jet or offset printing, spin- or spray-coating or other methods to obtain thin films of functional material. In the best case, such printed layers should also exhibit the properties of the respective bulk crystals, which implies that the particles resemble nanocrystals of the respective host material. If the intra-particle properties compare with the situation in a bulk crystal, then the inter-particle properties will dominate the quality of a printed layer. Thus, special care has to be taken to realize surface and interface conditions that enable the desired layer properties. This point is especially of interest for the case of nanocrystals, since with reducing the size of any three-dimensional object, the ratio of the surface to its volume inherently increases, until surface effects can dominate the overall behavior.

An additional effect, which severely changes the properties of nanocrystals compared to the bulk, is quantum confinement. If the lateral dimensions of a particle become so small that the quantum

mechanical confinement energy of electrons and holes exceeds $k_B T$, the thermal energy at room temperature, then the observed behavior changes from bulk-type towards zero-dimensional. For particle sizes smaller than typically 5 nm (depending on specific material parameters like the effective carrier mass and degeneracy) this effect leads to an effective increase of the bandgap [Del93, Led00], or to a vast enhancement in the photoluminescence efficiency in indirect semiconductor nanoparticles [Can90], where the enhanced overlap between the electron and hole wave function strongly enhances radiative recombination processes.

For the applications in printable electronics highlighted above, quantum confinement is not a prerequisite. It can even be an obstacle, because, *e.g.*, a variation of the bandgap within one printed device consisting of different particles will lead to undesirable band alignment problems. In general, whenever the quantum confinement applies to a nanocrystal or particle, its zero-dimensional properties start to dominate. Then, problems arise for classical semiconductor applications due to the individual discrete energy levels and vanishing overlap in the density of states with the surroundings. On the other hand, *e.g.*, a stacked solar cell design can be imagined, which consists of several cells out of well-sorted nanoparticles each, with their bandgap decreasing from top to bottom. In this case, an even better exploitation of the solar spectrum is possible in principle.

Thus, to be printable, semiconductor particles need to be smaller than about 100 nm, while they should at the same time exceed a diameter of about 5 nm to avoid strong confinement of the electrons and holes. Also, they need to exhibit a crystalline structure and appropriate surface properties. So, the endeavour lies in finding a suitable semiconductor material and the respective optimal processing conditions during the crystal growth to this well defined size to achieve superior structural and electronic quality as well inside the particles as on their surface.

1.2.2 Materials

Due to the high level of material and growth technology achieved today, there is almost no semiconductor material, which has not yet been reported to enable nanoparticle or nanocrystal growth. Especially, from group II-VI semiconductors such as PbSe [Tal05], PbS, PbTe, CdS, CdSe [Rid99], ZnS, ZnSe, and ZnO [Meu98], size-controlled nanocrystals have been fabricated very efficiently. A large part of the success of these materials is the wet-chemical production method that allows growth from solution by the help of colloidal chemistry. Already, transistors with carrier mobilities of the order of $1\,\mathrm{cm^2/V\,s}$ have been achieved using printed CdSe nanocrystals with subsequent annealing [Rid99] or from PbSe nanocrystals without thermal treatment [Tal05]. Highly efficient photodetectors have been reported for the case of PbS [Kon06]. Erwin and Norris have demonstrated that the doping of II-VI nanocrystals can strongly depend on the surface facets and thus on the lattice structure of the nanocrystals [Erw05].

While these results seem highly promising at first sight, it turns out that most of the constituent elements are extremely problematic. Especially, for a large industry aiming at large area applications and printable systems, the large-scale consumption of heavy metals such as Pb and the even more toxic Cd is a severe danger for the environment. Beyond all question, these elements cannot be considered for the targeted sub-cent tags that are designed as more or less disposable devices. Additionally, although *e.g.* ZnO itself can be regarded non-toxic, ZnO nanoparticles are water soluble and have antimicrobial properties [Bra06], and thus the material is listed as "very toxic to aquatic organisms, may cause long-term adverse effects in the aquatic environment" by the European Chemicals Bureau of the European Commission (risk phrases R50/53 [ECB08]).

In contrast to these binary compound materials, silicon would be a preferred choice to produce nanoparticles and nanocrystals. The dominant role that silicon plays in today´s electronic and photovoltaic industry is a good prerequisite to conquer new application markets. Silicon is a non-toxic material, which is naturally abundant and stable under ambient conditions. It represents one of the best investigated material systems available and several methods to grow silicon nanoparticles or nanowires have been reported. The most relevant of the latter will be introduced in the following subsection.

1.2.3 Growing silicon nanocrystals

To synthesize silicon nanocrystals, quite different production routes can be followed starting from either the solid phase, a liquid precursor, or from gaseous compounds. Out of these, the most important approaches will be highlighted here.

Embedded clusters

Upon thermal annealing of silicon suboxide (SiO_x, $x \approx 1$) layers, silicon clusters form within a silicon dioxide (SiO_2) matrix by a phase segregation process, which is mainly driven by the incomplete oxygen coordination [YuL07]. Depending on the sample composition and the annealing conditions, the size of these clusters is in the range of several nanometers. So, this method can be used to generate silicon nanocrystals in an oxide matrix. The suboxide precursor is usually deposited by sputtering [Fuj96], chemical vapor deposition or by implantation [Shi04]. Recently, also a solution processable route has been demonstrated using a silsesquioxane precursor [Hes07]. By the use of regular stacks of SiO_2 and SiO heterolayers, at least the vertical position of the nanocrystals in the oxide after annealing can be predefined [Pav00, Ish96]. By co-sputtering silicon with phosphosilicate or borosilicate glass, boron and phosphorus-doped nanocrystals as well as co-doping and compensation have been achieved [Hay96, Fuj04].

While for all these methods the size dispersion of the individual crystals is relatively narrow, still, the resulting particles are electrically isolated within the SiO_2 matrix. However, the embedding gives rise to a good thermal contact and to a good surface passivation, which enables the occurrence of strong photoluminescence [Mim00, Fuj04]. By wet chemical etching, the silicon nanocrystals can be made accessible to electrical contacts. Naturally, the yield of this method is quite small, because only a very thin layer containing a few percent of nanocrystals can be achieved during each deposition step.

Nanoporous silicon

By etching bulk silicon wafers in a mixture of hydrofluoric acid (HF) and nitric acid, or by electrochemical etching in an electrolyte containing HF, a porous network of nanometer sized silicon structures results that is commonly referred to as porous silicon [Can90]. While the main research interest has focussed on the luminescence properties of this material, a few groups used this approach also to gain small amounts of isolated silicon particles or solvent suspended solutions [Bel02]. To this end, the porous layer needs to be scraped off from the host silicon wafer and is suspended in a solvent, which is typically aided by sonication to break up interparticle connections. In principle, this method can be applied to generate macroscopic amounts

of silicon nanoparticles, but it is extremely time and material consuming. Since the porosity in nanoporous silicon typically amounts to $60 - 80\%$ [The97], the largest fraction of the relatively expensive crystalline silicon material is lost by this technique during the wet-chemical etching.

Colloidal chemistry

The first report on the preparation of sub-micrometer sized silicon single crystals used the reduction of, *e.g.*, $SiCl_4$ by sodium metal at high temperatures and under high pressure [Hea92]. Later on, also low temperature and ambient pressure approaches have been demonstrated [Yan99]. For example, the Zintl salt Mg_2Si reacts with $SiCl_4$ in ethylene glycol dimethyl ether. An advantage of this method is the possibility to immediately terminate or functionalize the surface with hydrogen, hydrocarbon groups, or oxidic groups. First signs of phosphorus incorporation by the addition of PCl_3 to the reaction suggest that also doping can be realized by this approach if a suitable precursor can be prepared [Bal06].

Laser ablation

In this technique a pulsed laser is focussed onto a rotating silicon target. The local heating leads to the ablation of silicon atoms and to the formation of a silicon plasma around the heated surface region. Sample deposition takes place in vacuum, while a protective carrier gas stream (*e.g.* He) can be used to cool the plasma and enable the nucleation and growth of nanocrystals, which can then condensate on a substrate [Wer94]. The resulting silicon nanoparticles exhibit bare unpassivated surfaces, but by controlled oxidation and hydrogen passivation, visible luminescence can be achieved [Bur97, Wer94].

Gas phase growth

While it is possible to synthesize silicon nanocrystals already by simple thermal evaporation in a high pressure protective atmosphere [Hay90], much better process control can be obtained if gaseous silane is used as the precursor. This is usually implemented in chemical vapor deposition methods at high reaction pressures [She04]. This approach starting directly from the gas phase, represents one of the most efficient ways to produce silicon nanoparticles, and even quite narrow size dispersions can be achieved [Nis02]. While most of the methods use a high frequency electromagnetic excitation or microwaves to heat the silane precursor to a plasma, also laser-assisted decomposition has been reported [Can82, Ehb97]. More recently, high efficiency plasma processes have been established that lead to a higher throughput of gases and thus represent an interesting approach for the industrial realization [Kni04, Man05]. Section 2.1.1 will focus further on the details of this production process.

From all of the above mentioned alternatives, especially the colloidal chemistry and the gas phase production of silicon nanocrystals represent methods, which are scalable to an industrial production level. Thus, in this work the properties and the applicability of silicon nanocrystals for printable devices have been studied exemplarily with silicon nanocrystals grown from the gas phase.

1.3 Chapter Overview

The aim of this work is to study the properties of silicon nanocrystals as a starting material for semiconductor applications. The experimental details and methods applied during the course of this study will be presented in **Chapter 2**. Here, the preparation of the silicon particles, the formation of printable dispersions and stable silicon layers will be highlighted together with the different thermal post-processing methods and the analytical techniques applied to characterize the physical properties.

Chapter 3 introduces the most relevant of the specific properties of nanosized silicon nanoparticles as they are expected from theory and from the literature. Established models for the physical properties will be adapted and extended for the specific situation with the silicon particles used here.

In **Chapter 4** the structural, optical, and electrical characteristics of silicon nanocrystals and nanoparticles are presented. It will be shown that well-defined layers can be realized by spin-coating silicon particle dispersions, and the structural, optical, and electrical quality of such films will be assessed.

As a low-temperature method to recrystallize spin-coated films of silicon nanoparticles, the aluminum-induced layer exchange will be introduced in **Chapter 5**. Differences and similarities to the known process using amorphous silicon precursor material will be discussed. With the aid of deuterium passivation, the carrier concentration in the polycrystalline films will effectively be changed. A microscopic model will be applied to explain the observed correlation between the mobility and the carrier concentration.

In **Chapter 6**, laser annealing, as an alternative method, is shown to be a powerful tool to achieve conductive silicon films on flexible polymer substrates. Significant structural changes and a conductivity increase of several orders of magnitude occur after short pulse irradiation on low-temperature substrates. The critical onset of the electrical conductivity at a characteristic doping concentration will be explained in a quantitative compensation model. The thermoelectric properties of the laser-annealed silicon nanocrystal layers substantiate this finding further while also thermoelectric applications seem to make sense for this material.

In the final **Chapter 7**, the obtained results and the insights won in the previous chapters are summarized. The quality of the obtained layers will be discussed and will be assessed with respect to possible applications. First proofs of principle are demonstrated and the potential of the material for further research and optimization will be highlighted.

2 Experimental Methods

In this chapter, the experimental prerequisites for the experiments and observations performed during the course of this thesis are explained in detail. Special emphasis is given to the processing steps and techniques applied during sample preparation and on the analytical methods used for the subsequent characterization.

2.1 Material Processing

2.1.1 Gas phase production of silicon nanoparticles

In addition to the previously given advantages, a plasma or gas phase reactor can be designed in a way that almost only those elements come into contact with the emerging nanoparticles that are intended to form its constituents, except protective gases. This enables the production of extremely pure nanoparticles, a fact which is an important prerequisite especially for semiconductor applications. The required components of typical reactor systems for the growth of nanoparticles are exemplarily listed below for the example of the reactors that were available during the course of this thesis, with our cooperation partners Hartmut Wiggers at the Universität Duisburg-Essen, and Evonik Degussa GmbH Creavis in Marl.

Educt gases and doping To produce silicon nanoparticles or nanocrystals, a large variety of gaseous silane precursors can be applied, while mainly monosilane (SiH_4) and disilane (Si_2H_6) are used for this purpose in practice. To have control over the reactor conditions such as temperature, pressure, and residence time, usually also additional gases are admixed to the reactor. These can moreover be used to add further functionality to the plasma processes. While noble gases (Ar, He) dilute the radical concentration in the gas phase, hydrogen (H_2) can be used to passivate the surfaces of reactants and radicals and to reduce the reaction kinetics. As it is known from bulk silicon, hydrogen can passivate defects or dopants in the crystalline lattice and can thus also determine the product particle properties. Finally, dopant gases such as diborane (B_2H_6) and phosphine (PH_3) or related gases can be added directly to the system.

The doping concentration can to first order be expected to equal the ratio of dopant atoms to silicon atoms. In the case of phosphorus doping, the nominal phosphorus doping concentration [P] can be calculated from the silane and phosphine concentrations, $[SiH_4]$ and $[PH_3]$, respectively, in the precursor mixture according to $[P] = \rho_{at} \cdot [PH_3]/([SiH_4] + [PH_3])$, where ρ_{at} is the atomic density of silicon ($5 \times 10^{22}\,cm^{-3}$).

A slight difference has to be accounted for in the case of boron-doped samples. Due to the use of diborane as the dopant precursor, each dopant gas molecule contains two boron atoms instead of only one as in the case of phosphine. Thus, the nominal doping concentration is given by: $[B] = 2\rho_{at} \cdot [B_2H_6]/([SiH_4] + [B_2H_6])$.

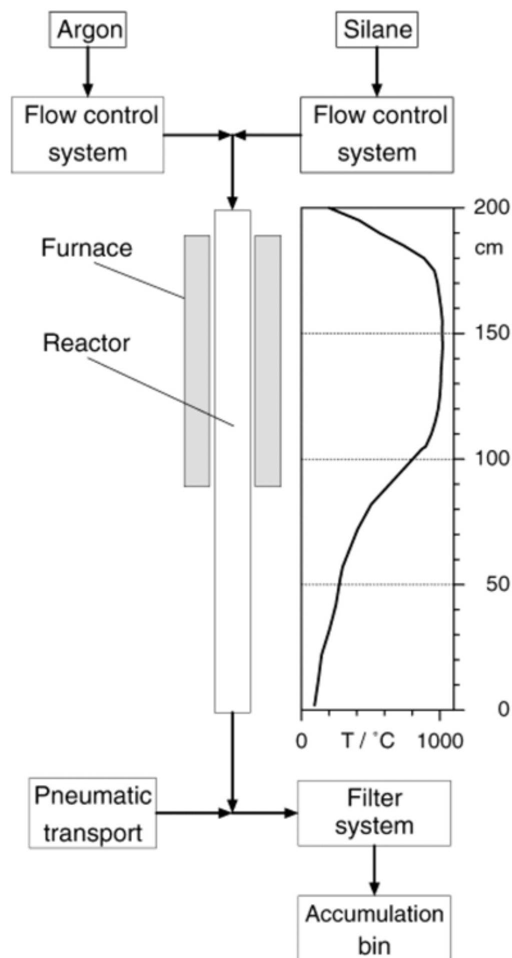

Figure 2.1: Schematic illustration of a hot wall reactor (HWR) system used for the growth of silicon nanoparticles. The temperature profile inside the reactor tube is also indicated [Wig01].

However, the concentration of dopants in the particles does not necessarily agree with the nominal doping concentration. Several physical processes such as segregation can prevent the incorporation of dopants or induce a loss of dopants during the growth period such as out-diffusion. In this case, the effective doping concentration can depend on the growth parameters and can vary for differently sized silicon nanocrystals. Therefore, it has to be calibrated by analytical methods.

Heating Sources To enable the reaction of the gases inside the reactor, they first have to be transferred into a reactive metastable state, in the form of radicals. This can either be achieved by the reaction of the gases at hot surfaces, by external laser irradiation (cp. 1.2.3) or by plasma heating via inductive or capacitive coupling. The first was realized in the form of a **hot wall reactor** (HWR), which is schematically depicted in Figure 2.1. Here a stream of SiH_4 diluted in Ar (in a concentration of $10 - 40\%$) is fed through a fused silica tube, which is heated by a toroidal furnace to temperatures of approximately $1000\,^\circ$C. The elevated temperature is sufficient to enable the formation of silane radicals and leads to the nucleation and growth of nanoparticles. Due to the relatively long residence time ($2 - 3$ s) of the individual particles in the high temperature region (which extends over ~ 80 cm), the resulting size dispersion is very broad and the primary

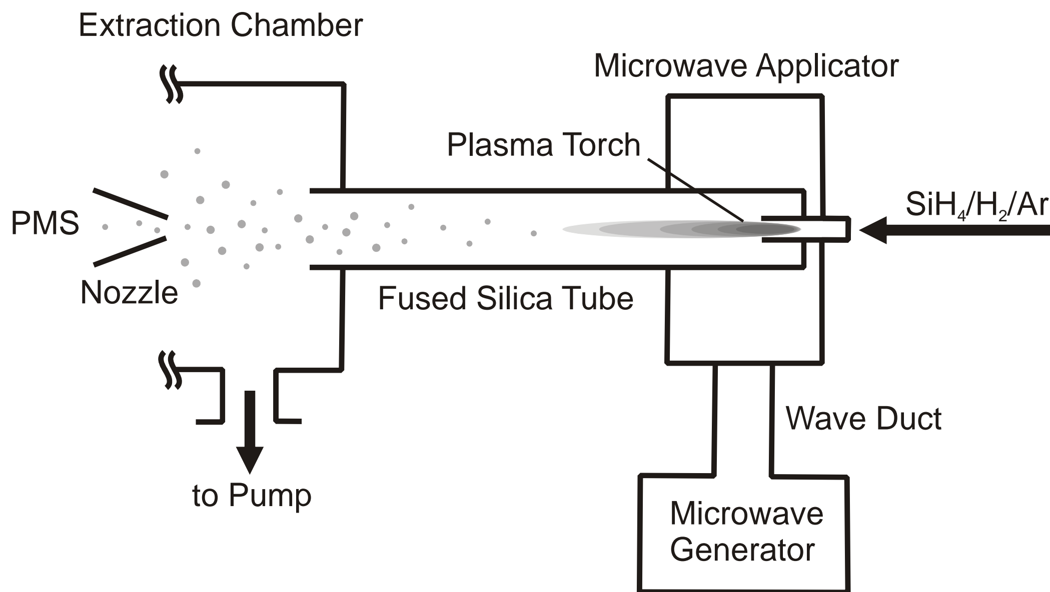

Figure 2.2: Schematic view of a microwave plasma reactor (MWR) for the gas phase production of silicon nanocrystals. Here, the hot reaction zone is limited to a very small microwave-heated reactor volume close to the precursor entrance nozzle. To monitor the particle size distribution *in-situ*, a particle mass spectrometer (PMS) can be applied (after [Kni04]).

particles can react with neighboring particles to form strongly agglomerated compounds. So, the silicon nanoparticles produced in a hot wall reactor exhibit multiply branched structures and do not resemble spherically shaped nanocrystals [Wig01].

Alternatively, silicon nanocrystals from two **microwave reactor** systems (MWR) were available in the course of this work. Here, as the name implies, the dissociation energy is coupled via the microwave heating into the reactor gas system, which leads to the ignition of a plasma. A schematic sketch of this reactor type is given in Figure 2.2.

As the figure illustrates, the precursor gases enter the reactor through a nozzle, positioned where the microwave forms a standing wave inside a tuned cavity. The high electromagnetic field amplitude heats the precursor mixture and transforms it into a plasma, containing radical silane compounds such as SiH_3, SiH_2, SiH, and ions thereof. The radical distribution is mainly determined by the pressure inside the reactor, which is usually in the range of several tens of millibars. Downstream of the nozzle a filter is situated before the vacuum pumping system. The main advantage of the microwave reactor in comparison with the hot wall reactor is the better process control, eminently due to the much shorter residence time within the hot plasma regions, which extend only over a very small spatial region.

Consequently, the nanoparticles grown in the microwave reactor exhibit a regular spherical shape, and the size distribution can be adjusted to relatively narrow values. While most of the silicon nanocrystals studied in this work had an average size of typically 20 nm, also many different sample charges with mean sizes ranging from 3.5 nm to 50 nm were available. Intrinsic as well as boron- and phosphorus-doped silicon nanocrystals could be realized by this method. Boron doping was realized at a microwave reactor at Creavis GmbH (MWR1) and the phosphorus doping was implemented at the reactor of the Universität Duisburg-Essen (MWR2).

Sample	P (W)	p (mbar)	SiH_4 (sccm)	Ar (sccm)	H_2 (sccm)	PH_3 (sccm)	[P] (cm^{-3})	[SiH_4] (10^{-3})	d (nm)
011206	1200	10	10	7000	3350	0.1	5×10^{20}	0.48	3.5
201106	1200	10	5	7045	3350	–	–	0.97	4.3
160806	1200	15	15	7000	3400	0.15	5×10^{20}	1.44	4.4
230205	1500	40	260	15240	1000	–	–	16	12
111004	1000	50	600	14000	500	–	–	39	14
191006	1800	40	601	6000	1400	0.015	1.2×10^{18}	75	46
250806	1800	100	15	7000	2350	0.15	5×10^{20}	1.6	11
130406	1800	100	60	16540	4000	–	–	2.9	16
100406	1800	100	180	9062	4000	–	–	9.0	21
190506	1800	100	115	8900	2000	0.15	6.5×10^{19}	10	–
250906	1800	100	155	8350	2350	0.05	1.6×10^{19}	14	29
100506	1800	100	180	9620	1800	–	–	16	33
280906	1800	100	205	9000	1800	0.05	1.2×10^{19}	19	44
140906	1800	200	250	12750	2750	–	–	16	47

Table 2.1: Process parameters for intrinsic and phosphorus-doped silicon nanoparticles produced in a microwave plasma reactor. Here, the microwave power, P, the reactor pressure, p, and the SiH_4, Ar, H_2, and SiH_4 gas fluxes are given. [SiH_4] denotes the silane gas concentration in the precursor, while [P] is the nominal phosphorus concentration in the particles with average diameter d.

Process parameters To demonstrate that the silicon nanocrystal growth can be controlled rather accurately in the microwave reactor, an exemplary sample overview for intrinsic and phosphorus-doped samples is given in Table 2.1. Here, the resulting average nanocrystal size, d, has been determined by an independent method (Brunauer-Emmett-Teller gas adsorption), which will be highlighted in the analytical methods section below. The table gives a selection from the variety of samples grown in MWR2 covering the full size spectrum available in this work.

The correlation of the particle size with the plasma process conditions is illustrated by Figure 2.3, where the resulting average crystallite size is displayed versus the silane concentration in the total gas flux, [SiH_4]. Different symbols represent different values of the reactor pressure, p, ranging from 10 mbar to 200 mbar.

As is evident from the graph, the mean particle size can be mainly controlled by adjusting the silane concentration in the precursor mixture, while an overall higher reactor pressure also leads to larger particle sizes. By this procedure, mean particle sizes in the range of $10 - 50$ nm can be continuously prepared at a reactor pressure of 100 mbar, and even smaller particles of 4 nm and less can be attained by reducing the reactor pressure down to $10 - 15$ mbar.

Extraction of the particles After a certain growth cycle time, the downstream filter of the reactor is purged to gain the grown silicon nanoparticles. While this process is undertaken under a protective argon atmosphere in the microwave reactor MWR1, this process is performed under ambient conditions in the reactor systems MWR2 and HWR, which of course may lead to a different degree of surface oxidation. To prevent the silicon nanocrystals from oxidizing under

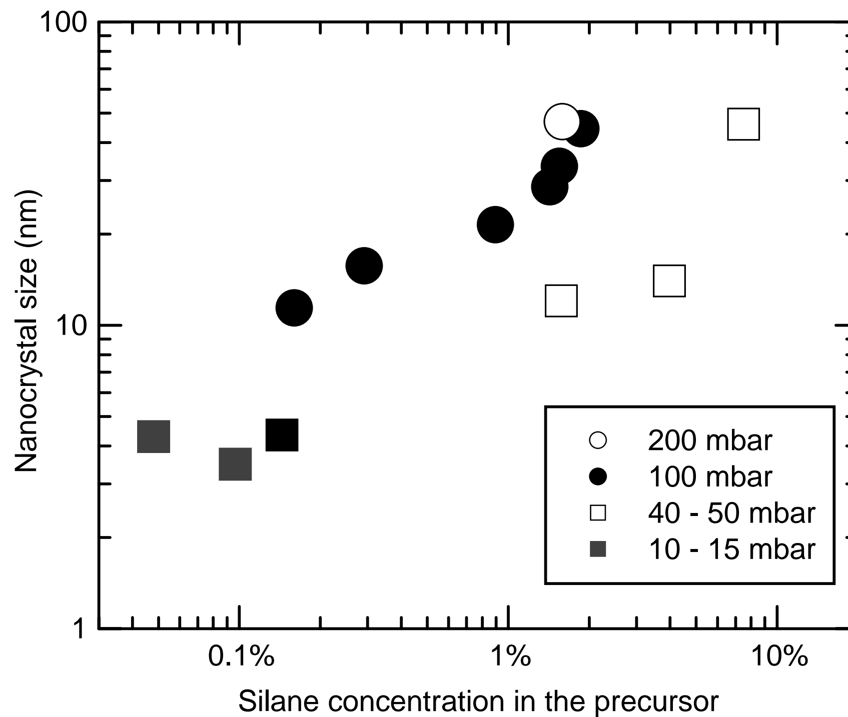

Figure 2.3: Silicon nanocrystal size as a function of the silane gas concentration in the total reactor gas flux for different values of the pressure in the microwave reactor.

room conditions, respective precautions have been implemented with MWR1, such as packaging and storing of the nanocrystals in a dry inert argon atmosphere.

2.1.2 Substrates

To form layers of silicon nanocrystals, different types of substrate materials were used, depending on the experimental and analytical methods which were intended to be applied. These were crystalline silicon (*c*-Si) wafers, glass and fused silica substrates (Heraeus HOQ 310), and polymer foils. The *c*-Si and fused silica substrates were used when a high temperature process step was necessary, or when spectroscopic measurements required substrates with a wide spectral transmittance. Also for measuring the thermal conductivity by Raman scattering, *c*-Si substrates were applied. Glass and fused silica substrates were used for metal induced crystallization experiments (see Chapter 5), where temperatures well below the softening point of the respective glass were chosen. To be compatible with the oxide etching step described in Section 2.1.6 two substrate materials were available: *c*-Si wafers and polymer foils. We chose Kapton® polyimide foil (Dupont™) due to its high thermal and chemical stability (including many organic solvents such as acetone). Other polymer materials have also been tested but showed inferior performance and reproducibility during the laser treatment described in Section 2.1.7. Important physical material parameters relevant for this work are summarized in Table 2.2.

The substrate dimensions for full samples were typically about $2 \times 2.5\,\mathrm{cm}^2$ while individual experiments were conducted with appropriately cut samples. Before their initial use, a thorough cleaning procedure was performed which comprised washing in acetone and isopropanol and subsequent drying with nitrogen. For electrical characterization of, *e.g.*, as-deposited silicon

Material	Melting point	Opt. transparency	Thermal expansion	HF resistive
c-Si	1410 °C	$0 - 1.1$ eV	$4.2 \times 10^{-6}\,\mathrm{K}^{-1}$	yes
Fused silica	1200 °C	$0.25 - 5.5$ eV	$0.54 \times 10^{-6}\,\mathrm{K}^{-1}$	no
Glass	550 °C	$0.6 - 5$ eV	$2 - 3 \times 10^{-6}\,\mathrm{K}^{-1}$	no
Kapton	(400 °C)	$0.3 - 2$ eV	$20 \times 10^{-6}\,\mathrm{K}^{-1}$	yes

Table 2.2: Material properties of substrate materials used for silicon nanocrystal samples.

nanocrystals films, interdigit metal contact structures with typical inter-contact distances of 5, 10, 20, and 50 μm were directly structured onto the substrates by optical lithography and thermal evaporation. Typical metal contacts consisted of a thin chromium adhesion layer and a gold contact film on top with a thickness of 10 and 100 nm, respectively. Such substrates were also used for spin-dependent transport measurements through silicon nanocrystal layers.

2.1.3 Dispersing silicon nanoparticles

To produce stable dispersions of silicon nanocrystals, a defined quantity was mixed with ethanol in the desired concentration (typically 6 wt.%), and yttrium stabilized zirconia beads (ZrO_2:Yt) were added in a comparable amount. Then, the mixture was placed on a shaker (Eppendorf Thermomixer Compact) and stirred for typically four hours at room temperature. Figure 2.4 a) shows the result of this procedure, which can be considered as a ball milling method, on the agglomerate size (D50) as determined from dynamic light scattering (Horiba LB 550) versus the dispersion time. Especially in microwave reactor material (open circles), this method reduces the viscosity of the liquid and decreases the fraction of large-scaled "soft" agglomerates in the dispersion. In hot wall reactor material (full squares), this effect is much weaker due to the presence of a large fraction of "hard" agglomerates.

Though dispersions can also be formed by ultrasonic excitation of the silicon nanocrystals in ethanol, only this ball-milling method led to smooth layers after subsequent spin-coating, without large inclusions or agglomerates in the resulting films. It is conceivable that this dispersion method will also be necessary for alternative printing methods such as ink-jet printing or offset printing, where the condition of a low concentration of agglomerates needs to be met. However, no optimization of the dispersion technique towards such alternatives was performed yet.

As to the choice of the solvent, the polarizability of the liquid is responsible for the outcome of the dispersion properties. Korgel and Fitzmaurice, *e.g.*, found that small concentrations of ethanol in chloroform can lead to multilayer self-assembly of alkyl-capped gold nanocrystals due to the high polarity of the ethanol (with a dielectric constant of $\varepsilon_{\mathrm{EtOH}} = 24.3$), whereas a similar dispersion in pure chloroform ($\varepsilon_{\mathrm{CHCl_3}} = 4.8$) led to a monolayer arrangement of the nanocrystals on a carbon substrate [Kor98]. With the silicon nanocrystals, also dispersing in chloroform, acetone ($\varepsilon_{\mathrm{CH_3COCH_3}} = 20.7$), toluene ($\varepsilon_{\mathrm{C_7H_8}} = 2.4$), and tetrahydrofurane ($\varepsilon_{\mathrm{C_4H_8O}} = 7.6$) has been found possible, but only acetone has been found to produce comparably good results in spin-coating as ethanol.

The long-term stability of silicon nanocrystal dispersions can be tested by probing the agglomerate size by dynamic light scattering as a function of time elapsed after a dispersion has been produced. As is evident from Figure 2.4 b), silicon nanoparticles grown from a microwave re-

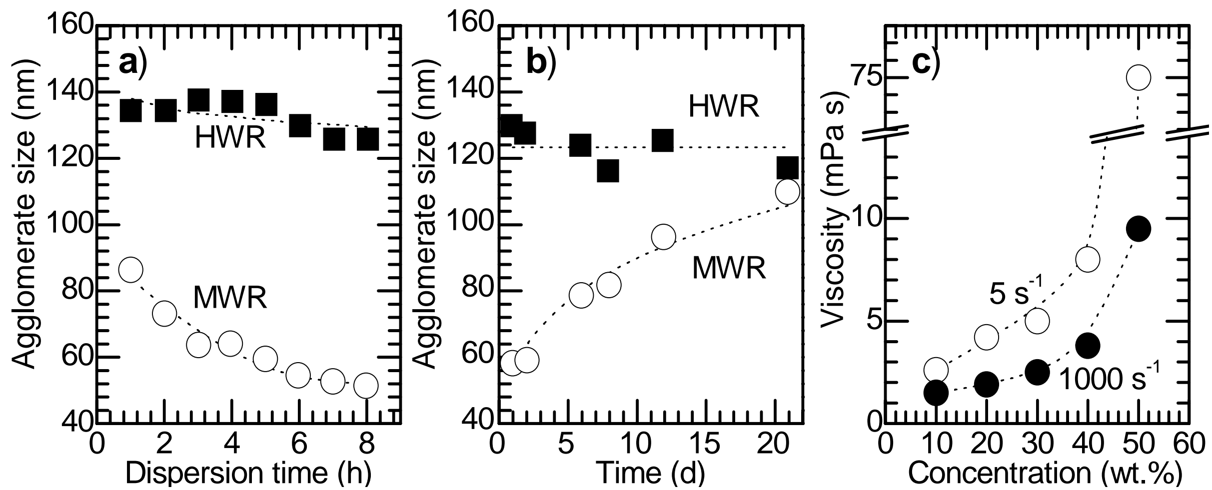

Figure 2.4: a) Agglomerate size in silicon nanocrystal dispersions as a function of the dispersion time for hot wall (HWR) and microwave reactor (MWR) particles. b) Reagglomeration of silicon nanoparticles in ethanolic dispersion with time. c) Dynamic viscosity of MWR silicon nanocrystal dispersions as a function of the solid silicon concentration [Lec05].

actor reagglomerate on a time scale of several weeks after dispersing, whereas no such effect can be observed via this method for hot wall material on this time scale. The appearance of dispersions which have been subject to reagglomeration is distinctly different from non-degraded dispersions. Reagglomerated samples form a pudding-like slurry of high viscosity which cannot be used for reasonable film formation. Also by a repeated ball milling procedure comparably favorable dispersion properties as obtained after the first dispersing cycle could not be restored.

Fresh silicon nanocrystal dispersions show also indications of non-Newtonian fluid behavior such as a shear thinning viscosity, which is a result of the dynamic liquid-solid interactions within the two-phase system. For example, ethanol dispersions containing 10 wt.% silicon nanocrystals (MWR1) with an average size of 20 nm show a dynamic viscosity of typically 2.6 mPa s and of 1.5 mPa s at shear rates of $5\,\mathrm{s}^{-1}$ and $1000\,\mathrm{s}^{-1}$, respectively[1] [Lec05]. The dependence of the viscosity on the solid silicon concentration is shown in Figure 2.4 c) for two different shear rates applied to microwave silicon nanocrystals with an average size of 20 nm. According to the graph, a large concentration range can be covered, with dynamic viscosities below 10 mPa s.

2.1.4 Digital doping

Several benefits arise from the usage of nanocrystals for applications in printable electronics. While the small size of the particles enables their dispersibility in a solvent and the formation of a printing ink as such, also the overall properties can be adjusted by mixing different inks together, if a subsequent thermal process is applied to melt the nanocrystals. Then, if a specific doping level is desired, it is not necessary to produce exactly the right doping concentration in the primary nanocrystals. Instead, the doping level can be adjusted by mixing two available doped inks in the right proportion. In the case of perfect intermixing of the components, the effective

[1] Determined with a Haake Rheometer RS 75 at a temperature of 23 °C. Note that the dynamic viscosity of ethanol at room temperature is 1.2 mPa s (water, for comparison, exhibits 1.0 mPa s).

doping concentration, N_{eff}, is then expected to follow from

$$N_{\text{eff}} = \frac{a_1 c_1 N_1}{a_1 c_1 + a_2 c_2} + \frac{a_2 c_2 N_2}{a_1 c_1 + a_2 c_2}, \tag{2.1}$$

where a_i and c_i are the relative volume fraction and the solid silicon content in dispersion i exhibiting a doping concentration of N_i, respectively. Even if n- and p-type dispersions are intermixed, this equation can be applied to calculate the resulting N_{eff} by simply choosing opposite signs for N_1 and N_2. This technique will be referred to as "digital doping" in the following, in contrast to the conventional doping by the dopant gas concentration during particle growth.

During the gas phase production of samples with extremely high boron concentrations of $5 \times 10^{20}\,\text{cm}^{-3}$ and $10^{21}\,\text{cm}^{-3}$, it was not possible to maintain the dopant gas flux throughout the growth run. However, the mean boron concentration found in mass spectrometry was rather constant for different macroscopic fractions of the same material. These specific ensembles of silicon nanocrystals can thus be considered to consist of a mixture of doped and undoped particles. These samples were later used for the digital doping experiments in combination with laser annealing. Due to the limited number of highly boron-doped silicon nanocrystals available, all boron doping levels exceeding $10^{19}\,\text{cm}^{-3}$ boron atoms were realized this way. In Subsection 6.4.3, it will be shown that the electrical properties of laser-annealed mixed nanocrystal layers indeed interpolate between those of the initial ensembles.

2.1.5 Spin-coating

Silicon particle dispersions were typically spread onto the substrates by spin-coating. Usually, the liquid was applied before the spin-coater was allowed to rotate and no intentional ramping was performed. Reasonable values for the rotational frequency during the spin-coating procedure were in the range of $1000 - 4000$ rpm and depend on the silicon nanoparticle solid concentration in the dispersion and on the desired layer thickness. Figure 2.5 illustrates how the resulting layer thickness is connected with the chosen solid concentration in ethanol and the rotational frequency during spin-coating.

Here, the layer thickness increases rather linearly with the concentration over a large concentration range for a fixed rotational frequency and particle size [Figure 2.5 a)], while only for solid concentrations larger than 15 wt.%, a slightly superlinear behavior becomes apparent. In contrast, a power-law dependence of the thickness on the solid concentration, c, with the thickness varying as c^n, is typically observed for spin-coating of viscous fluids, with the exponent n ranging from $1.4 - 2$ [Mey78]. Despite this deviation from other dispersed systems, smooth films of silicon nanocrystals in the range of 100 nm to more than 2 μm can be realized by spin-coating.

As Figure 2.5 b) suggests, films of adjustable thickness can be produced from one dispersion of fixed solid concentration by spin-coating at different rotational frequencies, ω. The inset in the figure displays the same data in a double logarithmic plot, demonstrating that the resulting film thickness varies as $\omega^{-0.41\pm0.05}$. This behavior comes quite close to the $\omega^{-0.5}$-dependence, which determines the spin-coating thickness if the evaporation of a solvent is involved, and if the liquid has a Newtonian viscosity [Mey78]. It is clearly seen from the figure that the resulting thickness can be modified by up to a factor of 2.5, simply by advancing the rotational frequency from $750 - 4000$ rpm.

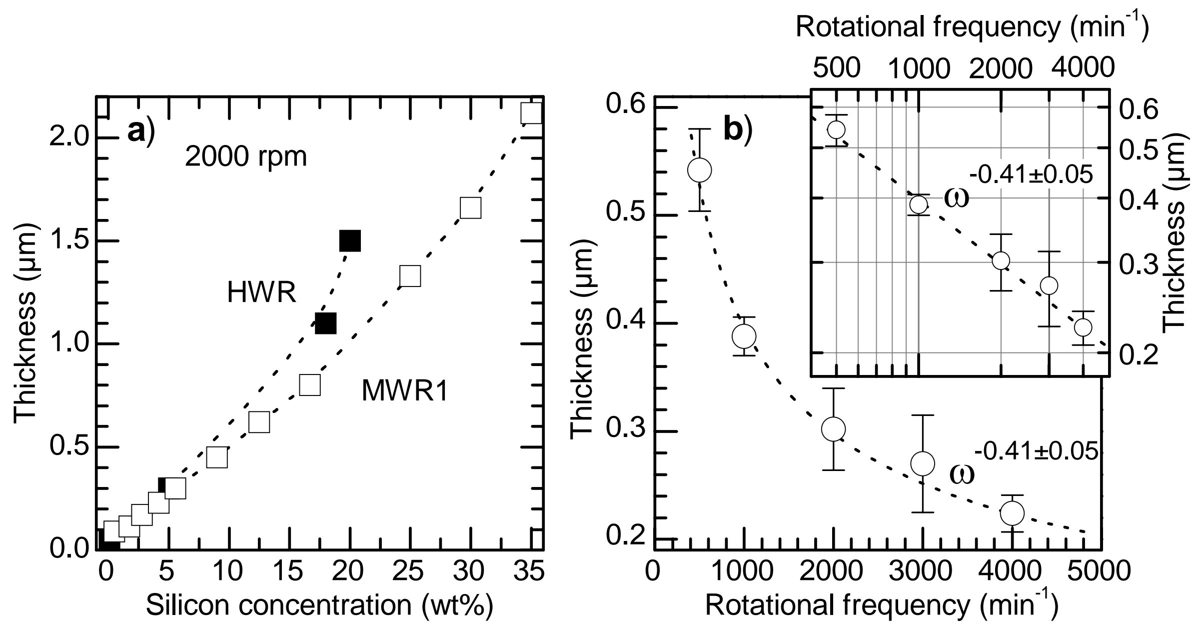

Figure 2.5: a) Dependence of the thickness of different silicon nanocrystal films spin-coated at 2000 rpm on the solid concentration in the liquid dispersion in ethanol. The crystallite sizes were 20 nm (open symbols, MWR1) and 80 nm (full symbols, HWR), respectively. b) Thickness of spin-coated nanocrystalline silicon films as a function of the spin-coating rotational frequency. The solid concentration was 5 wt% and the crystallite size was 20 nm (MWR1).

Additionally, also the particle size is expected to have an influence on the resulting layer thickness. However, this influence is very small as long as the particle size is significantly smaller than the film thickness and provided that the solid content is not too large so that the liquid dispersion behaves as a low-viscosity solution. So, for the film thicknesses, solid concentrations and particle sizes examined during the course of this work, no strong correlation between the particle size and the film thickness could be established within the measurement accuracy. Still, in Figure 2.5 a) an effect of the particle size becomes visible: here, the about four times larger hot wall nanoparticles show a stronger superlinear thickness dependence on the solid concentration. Part of this effect can be ascribed to the manifestly differing microstructure (cp. 4.1.1) of hot wall silicon nanoparticles, leading to higher viscosity at the same solid concentration. Consequently, the aforementioned non-Newtonian behavior of these dispersions becomes more dominant.

It was found that spin-coated layers of silicon nanoparticles showed reasonable mechanical stability and resistance against washing off by solvents if the layers were allowed to dry after spin-coating in an oven at 90 °C for 10 min. Such samples could then be used for further processing.

2.1.6 Oxide etching

To remove the oxide layer covering the surface of the silicon nanoparticles, a wet-chemical etching step was performed. Layers were immersed into a dilute solution of hydrofluoric acid (5 – 10% HF) in deionized water for typically 20 s at room temperature. Afterwards, the samples were washed in deionized water and blown dry with nitrogen. This etching step was found to be an essential prerequisite for achieving high electrical conductivity after laser annealing. A reduction of the film thickness by 25% was present for spin-coated layers of 20 nm particles.

This procedure could not be substituted by mere etching in hydrofluoric acid vapor. Only long-term etching in a highly HF-enriched atmosphere was observed to reduce the oxide shell of both silicon nanoparticle layers and powders. However, silicon nanocrystal layers deposited on gold films were found to be completely removed by vapor-phase etching in moist atmosphere for one week, most probably due to a combined reaction of oxidation and oxide etching in contact with the gold catalyst.

2.1.7 Laser crystallization

To crystallize thin films of silicon nanoparticles by optical heating, a frequency doubled neodymium-doped yttrium aluminum garnet laser (Nd:YAG) is used in pulsed operation at a frequency of 10 Hz. The laser-active Nd ions in the YAG crystal are optically pumped by krypton flash lamps. By an ultrafast switching of the laser cavity quality factor (Q-switch), the stored energy (typically 1 J) can be released by the emission of one single laser pulse within a period of time as short as 8 ns. Thus, the laser power of Nd:YAG systems can easily be as large as several 100 MW.

For our experiments, the emission wavelength of 1064 nm is fed into a birefringent potassium dihydrogen phosphate (KD*P) crystal, which generates a significant fraction of the second harmonic of the incoming wavelength (532 nm). By wavelength selective mirrors, this second harmonic wavelength is extracted and led to the optical table. A schematic sketch of the setup is shown in Figure 2.6. To attenuate the laser pulse energy, the polarization direction can be altered with a rotatable $\lambda/2$ plate, and a Glan-Taylor prism transmits only the vertically polarized fraction of the laser light to the optical table, while the horizontally polarized fraction is reflected into a beam dump.

The laser power is monitored by an off-angle polished fused silica plate as a beam splitter, which reflects 5% of the laser spot onto a bolometer. An electronic shutter regulates the number of laser pulses reflected onto the samples and can be used to effectively decrease the repetition rate of the laser pulses to 1 Hz. An z-y-translation stage enables multiple experiments on a sample with a typical size of $2.5 \times 2.5\,\mathrm{cm}^2$ by the help of an appropriate aperture ($5 \times 5\,\mathrm{mm}^2$). If not mentioned otherwise, the experiments were performed under normal ambient conditions.

For laser annealing of silicon nanocrystal layers, it turned out best to use a series of pulses with increasing energy density rather than firing single shots of different energy density. Otherwise, the silicon nanocrystal layers were heated immediately to too high temperatures, which led to the ablation of the larger part of the material. This effect is ascribed to an explosive desorption of condensed water and adsorbed gases on the silicon nanocrystal surfaces. The damage threshold energy density for this single pulse annealing is observed at a relatively low energy density of about $25\,\mathrm{mJ\,cm^{-2}}$.

The pulse sequence of typical pulsed laser annealing processes applied to the spin-coated silicon nanocrystal layers are depicted in Figure 2.7. To achieve a compromise between stepwise application of the laser energy and minimum thermal budget of the annealed layers, a number of ten pulses at a repetition rate of 1 Hz was chosen. The energy density was increased continuously during a pulse series, starting with an energy density of around $10\,\mathrm{mJ\,cm^{-2}}$ and ending with a final energy density in the range of $20 - 200\,\mathrm{mJ\,cm^{-2}}$. In these experiments, it was found that only the maximum pulse energy density value was decisive for the sample properties. So, if the energy density was decreased again during an annealing series, still the sample properties

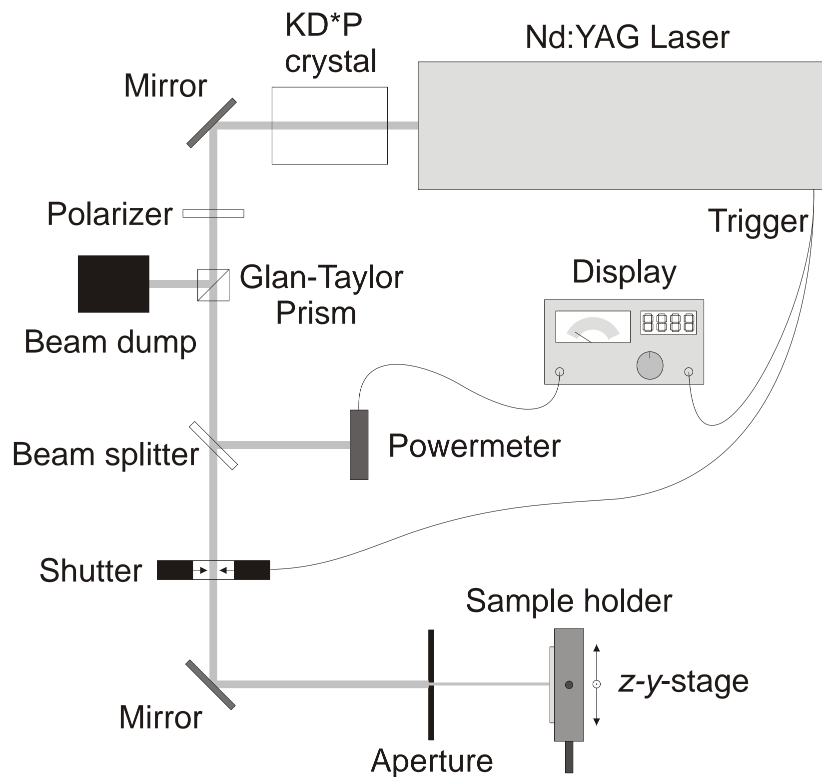

Figure 2.6: Schematic drawing of the setup used for the Nd:YAG laser annealing experiments. For details of the optical components see text.

were determined by the maximum value of the applied energy density. Thus, in the following, the maximum laser energy density value will be used to identify the individual laser treatment conditions.

The detailed number of laser pulses was not found to be a critical parameter, and no systematic differences could be observed for annealing experiments using series of up to 20 laser pulses. However, laser annealing with a series of 100 laser pulses led to deteriorated sample properties in some cases. On the other hand, sometimes a pre-annealing of several pulses below the single pulse damage threshold energy density was found advantageous for samples that were to be exposed to very high energy densities.

2.1.8 Metal evaporation

For use as electric contacts or as the metal precursor, *e.g.*, for aluminum induced crystallization (see Chapter 5), metal layers have been deposited. This was accomplished mainly by thermal evaporation from tungsten boats or tungsten filaments in high vacuum (typically 10^{-7} mbar). Two different materials could be deposited sequentially from independent boats that were filled with high purity feedstock of Al, Cr, Au, Ti, and Ag, respectively. To deposit high melting point metals such as Pt, also a four-pocket electron-beam evaporation unit was available integrated in the same vacuum system.

Alternatively, also an Ar plasma sputtering system was used for the deposition of thin Au layers to prevent charging during SEM imaging or as a fast metal layer. In this case, the pressure during

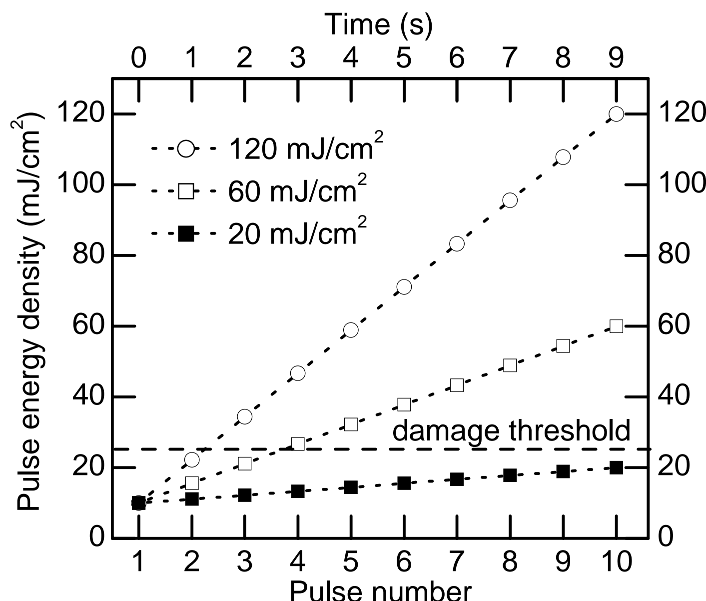

Figure 2.7: Schematic illustration of typical pulse sequences employed for the laser annealing of spin-coated silicon layers. Stepwise increasing of the energy density in a 1 Hz series of ten pulses up to final energy densities of 20 mJ cm^{-2}, 60 mJ cm^{-2}, and 120 mJ cm^{-2} can avoid layer damage.

the deposition was typically 0.2 mbar. If required, deposition masks were realized before the metallization by optical lithography using UV-sensitive photoresist (Shipley Microposit S1818). After the metal deposition, a lift-off-process was applied to remove unwanted metal structures. Alternatively, also shadow masks were used for simple contact structures.

2.1.9 Amorphous silicon deposition

To produce reference samples for the aluminum-induced crystallization, amorphous silicon layers were deposited. This was achieved in a high vacuum deposition chamber by means of electron beam evaporation. The used silicon feedstock had a 6N purity, which corresponds to a total impurity concentration of below 1 ppm. The background pressure in the evaporation chamber amounted to approximately 10^{-8} mbar. The typical deposition rates, which were controlled via a quartz microbalance, amounted to about 0.1 nm s^{-1}.

2.1.10 Thermal annealing

A setup specifically designed for annealing samples at medium temperatures (100−800 °C) could be operated both in vacuum (10^{-6} mbar) or in a protective nitrogen atmosphere (100 mbar − 1 bar). Here, the sample could be observed during the annealing procedure through a window, enabling the *in situ* monitoring of crystallite growth during the ALILE process (see Chapter 5). An optical microscope equipped with a CCD camera enabled the digital recording and analysis of the obtained micrographs. Digital image analysis software permitted the evaluation of the coverage fraction as a function of the annealing time.

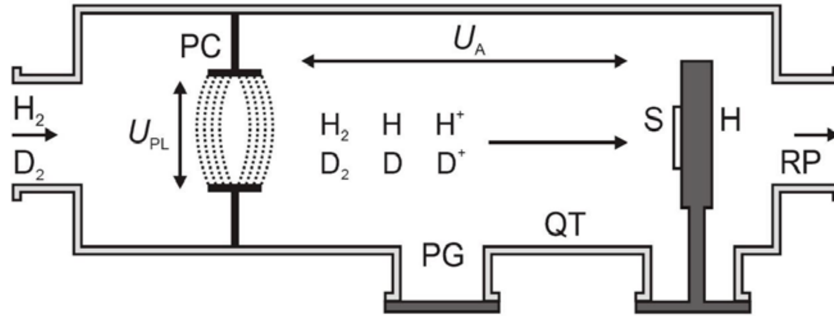

Figure 2.8: Remote plasma hydrogen/deuterium passivation system. H_2 or D_2 molecules are dissociated in the DC plasma of a plate capacitor (PC) in a quartz tube (QT). Molecules and ions drift towards the sample (S) mounted on a heating stage (H) which is at an accelerating potential U_A. A rotary pump (RP) is used for pumping and a Pirani gauge (PG) monitors the pressure in the system (from [Gju07]).

To study the influence of a high temperature annealing step on the properties of silicon nanoparticle layers, vacuum annealing experiments have been performed in a high vacuum setup. Samples deposited on fused silica substrates were positioned inside a fused silica tube which was evacuated to 10^{-8} mbar. Then the tube was heated by an external oven to temperatures in the range of $200 - 1000\,°C$. Both the temperature ramp as the total process time could be varied over a wide range. By allowing the oven to reach very high temperatures first before positioning it around the evacuated sample tube, even a form of rapid thermal annealing can be implemented.

2.1.11 Aluminum Etching

To remove remnants of aluminum from samples crystallized with the help of the aluminum-induced layer exchange (ALILE), a wet chemical etching step was applied. This consisted of a standard aluminum etch mixture of phosphoric acid, nitric acid, acetic acid, and water (H_3PO_4:CH_3COOH:HNO_3:H_20 in the volume ratio 16:1:1:2) at a temperature of 70 °C. Alternatively, the etching was performed in hot hydrochloric acid (HCl, 37%).

Also, remnants of spin-coated silicon layers after completion of the ALILE process with silicon nanoparticles were found to be effectively removed by immersing the samples into boiling mixtures of the standard aluminum etching solution. After the etching, samples were immersed and washed in deionized water and blown dry with nitrogen.

2.1.12 Hydrogen Passivation

To passivate defects or dopants in silicon, deuterium passivation was utilized. The system used is shown schematically in Figure 2.8 and consists mainly of a quartz tube (QT) evacuated by a rotary pump (RP) to a pressure of 10^{-3} mbar controlled by a Pirani gauge (PG). Either hydrogen (H_2) or deuterium (D_2) gas is then fed into the tube and a pressure of 0.8 mbar is adjusted. By applying a high dc voltage ($U_{PL} = 1300\,V$) between the electrodes of a plate capacitor (PC), a plasma is ignited which enables the dissociation of the H_2 (D_2) into H_2^+, H, H^+ (D_2^+, D, D^+) and electrons (e^-). The sample (S) is mounted on a heated sample stage (H), which is kept at a negative potential ($U_A = -260\,V$) to enable the drift of protons or deuterons towards the

sample. This accelerating voltage is not able to induce damage by ion bombardment because of the remote sample position downstream of the plasma (15 cm) and because of the relatively high pressure in the system leading to rapid thermalization of the ion kinetic energy.

2.2 Analytical Methods

Several analytical methods and measurement techniques have been applied to determine the chemical composition, structural and optical properties, and the electric transport characteristics of the samples. The most important of these methods will be introduced in the following subsections.

2.2.1 Chemical Analysis

Mass spectroscopy

The chemical composition of the silicon nanocrystals has been analyzed with the help of several mass spectroscopy methods, namely glow discharge mass spectroscopy (GDMS), inductively coupled plasma mass spectroscopy (ICPMS), and secondary ion mas spectroscopy (SIMS). Here, the GDMS and ICPMS has been performed by Evonik Degussa (Aqura Analytic Solutions, Marl), while a commercial provider conducted SIMS measurements with our samples (RTG Mikroanalyse GmbH, Berlin).

For the GDMS measurements, silicon nanocrystals were pressed into a pellet to form the cathode of a low pressure ($\sim$ 1 mbar) Ar gas discharge. After igniting the plasma, erosion of the cathode sets in and the sputtered neutral species of the exposed sample surface can escape from the surface and diffuse into the plasma where they are ionized. Positively charged ions are then extracted from the plasma and accelerated into a high resolution mass spectrometer where they can be separated and identified by their mass-to-charge ratio.

The main difference between ICPMS measurements and the GDMS method is that, in ICPMS, an inductively heated Ar plasma is used, requiring no direct electrical contact to the sample, which is directly introduced into the hot plasma core. This allows also the analysis of liquid sample solutions and dispersions on a suitable sample holder. The ionization in the plasma and the detection of constituent elements is then analogous to GDMS.

A set of samples was also analyzed by SIMS. To this end, layers of silicon nanocrystals were spin-coated on Kapton substrates. During the measurement, the samples are sputtered by a beam of primary ions (*e.g.*, O_2^+, Cs^+, Ar^+, Xe^+, Ga^+) and the charged fraction of the sputtered components (secondary ions) of the silicon nanocrystal layers are consequently analyzed in a mass spectroscopy chamber. To avoid sample charging effects typical for high resistive materials, a 100 nm thick gold layer was evaporated onto the Kapton for as-deposited samples. To analyze laser-annealed nanocrystal layers, also a thin sputtered top layer of gold served well, however.

All these mass spectroscopic methods exhibit excellent relative accuracies. Even in the case of particulate systems such as the silicon nanocrystals examined here, the sensitivity is fairly high to a wide range of elements, whereas the intrinsically high depth resolution (down to $2-5$ nm for SIMS) is not available in the case of highly porous layers. Thus, also no information on the

position of the elemental components in the silicon nanocrystals can be won from mere SIMS or GDMS measurements.

Thermal desorption spectroscopy

To determine the quantity and species of elemental components that can be desorbed from samples by thermal annealing in vacuum, thermal desorption (or effusion) experiments were performed. While the applied system was designed to detect the concentration of passivating species such as hydrogen or deuterium inside solid state semiconductor samples, it can also be used to detect fragments of organic molecules bound to the sample surface. By this means, physisorbed molecules can be discerned from chemisorbed covalently bound compounds simply by the characteristic desorption temperature.

During the measurement, the sample is placed in an evacuated fused silica tube, which is pumped to a residual pressure of 10^{-8} mbar by a turbo-molecular pump. The sample temperature is set by a software-controlled external oven, while the partial pressures of up to ten different gases in the system are detected by a high resolution quadrupole mass spectrometer (Hiden Analytics) and are recorded by a computer software program at the same time. Usually, measurements are performed by ramping the sample temperature slowly with a constant rate ($5 - 20\,\mathrm{K\,min^{-1}}$) from room temperature to a temperature slightly above the highest temperature of interest up to a limit of $1000\,^{\circ}\mathrm{C}$. Thus, the measurement method is sometimes also referred to as temperature programmed desorption (TPD).

From the characteristic peak temperatures of different effusing species, conclusions can be drawn on the surface binding state of the respective molecule or molecule fraction.

2.2.2 Structural analysis

Adsorption spectroscopy

A widespread method to determine the surface area of porous or colloidal media is via measuring the adsorption of gases on the surface as a function of the temperature. Extending Langmuir´s monolayer adsorption theory, Brunauer, Emmett, and Teller (BET) deduced the adsorption isotherm (Equation 2.2) for the adsorption of gas molecule multilayers on a surface [Bru38]. By fitting this equation to the experimentally determined quantity of adsorbed gas ν_{Ads} as a function of the gas equilibrium pressure p, the amount of gas adsorbed in a monolayer ν_{mono}, and the BET-constant C, can be derived:

$$\nu_{\mathrm{Ads}} = \frac{\nu_{\mathrm{mono}} \cdot C \cdot p}{(p - p_0)\left[1 + \frac{p}{p_0}(C-1)\right]} \tag{2.2}$$

where p_0 is the saturation pressure of the gas, marking the limit at which no further gas is adsorbed on the surface upon increasing the pressure. The validity of the BET isotherm is given in a range between $0.05 < \frac{p}{p_0} < 0.3$ [Bru38], and in this regime the BET constant is given by the adsorption energy of the first monolayer E_1 and by that of all further adsorbed layers, E_{L}: $C = \mathrm{e}^{-(E_1 - E_{\mathrm{L}})/RT}$. Additionally, the BET-surface, S_{BET}, can be evaluated by calculating $S_{\mathrm{BET}} = N_{\mathrm{A}} \nu_{\mathrm{mono}} \phi$, where N_{A} is the Avogadro constant and ϕ is the adsorption cross section ($\phi = 16.2 \times 10^{-16}\,\mathrm{cm^2}$ in the case of nitrogen molecules).

For the silicon nanocrystals examined in the course of this work, BET measurements have been performed at the Universität Duisburg-Essen using N_2 gas at a temperature of 77.4 K. From the specific BET surface, σ_{BET}, which was obtained by normalizing to the sample mass, the silicon nanocrystal diameter d_{BET} can be readily calculated if a spherical nanocrystal shape is assumed:

$$d_{BET} = \frac{6}{\rho \cdot \sigma_{BET}}, \tag{2.3}$$

where ρ is the bulk mass density of the nanocrystal material. In the case of silicon nanocrystals ($\rho = 2.33\,\mathrm{g\,cm^{-1}}$), this relation transforms into

$$d_{BET} = \frac{2575}{\sigma_{BET}/\,\mathrm{m^2\,g^{-1}}}\,\mathrm{nm}. \tag{2.4}$$

Since microwave reactor grown silicon nanocrystals resemble spherical particles, the results of this calculation show good agreement with complemental TEM and in-flight mass spectroscopy measurements for this material [Kni04]. In the case of hot wall reactor grown particles, this assumption is not valid, but the obtained size can still be regarded as a reasonable measure to assess the particle dimensions and pore sizes.

Optical microscopy

For structural and topological analysis, optical micrographs were taken using a Zeiss optical microscope. A digital CCD camera connected to the microscope could be used to directly record digital images with available magnifications ranging from 50× to 1000×. Both transmission and reflection mode micrographs were possible to record by the help of two halogen lamps for illumination in dark and bright field mode.

The magnifications obtained in the digital micrographs depend on the chosen objective and the resulting scales have to be calculated accordingly. The dimension of a single pixel is given for different magnifications for a total image resolution of 768 × 570 pixels in the table below.

Magnification	50×	100×	200×	500×	1000×
Pixel dimension	3 μm	1.3 μm	0.65 μm	260 nm	130 nm

Scanning electron microscopy

Electron micrograph images were recorded using a Hitachi S-4000 scanning electron microscope (SEM). The accelerating voltage of the involved field emission electron source was typically 10 kV, enabling resolutions down to 5 nm. If not explicitly mentioned otherwise, the micrographs were recorded under normal angle in top view. For cross-sectional micrographs, silicon wafer substrates were preferred to polyimide foils because of their favorable cleavage properties. Alternatively, SEM characterization was also performed at Evonik Degussa (Aqura Analytical Solutions, Marl). Also in this case, the lateral resolution amounted to 5 nm or less.

To avoid charging effects with low-conductivity samples, their preparation included the sputtering deposition of a 10 nm Au film prior to the SEM analysis. At very large magnifications, the coagulation of this thin metallic surface layer can be seen as a wavy surface pattern on the micrographs with typical lateral dimensions of $5 - 10$ nm.

Profiler measurements

To determine the layer thickness of samples, a Sloan Dektak Profiler was utilized. This setup uses a sample translation stage and a microtip, which is kept in touch with the sample at a constant force while the sample is scanned. The tip radius is about 0.3 μm and the stylus force was kept at 5 mN. To determine the film thickness, the sample was locally scratched and the resulting step profile was analyzed using a typical scan length of 500 μm. The resulting profile was evaluated keeping in mind a typical height accuracy of the system of $\pm$50 nm.

Atomic force microscopy

Surface morphology was additionally imaged by the help of atomic force microscopy (AFM) in tapping mode operation (Digital Instruments MMAFM-2). In this measurement method, a micromachined silicon cantilever is mechanically excited at its resonant frequency (typically 300 kHz), while the sample is being scanned across the tip with a piezo actuator. A silicon faceted tip at the end of the cantilever interacts with the surface experiencing different surface interactions, which lead to a damping of the oscillation. This damping is detected by a laser reflected from the cantilever end to a segmented photodiode, and the signal is used to regulate the sample-tip distance via a control circuit.

While the lateral resolution of this method is limited by the scanning tip radius (typically 20 nm), the vertical resolution depends only on the piezo and can reach sub-nanometer resolution, enabling, *e.g.*, the imaging of monatomic steps in epitaxial layers.

For layers of silicon nanocrystals, this microscopic technique has proven to be applicable if a certain care was taken during the measurements. For instance, rapid scanning of porous layers of silicon nanocrystals leads to a fast degradation of the tip curvature, resulting in washed out lateral and vertical resolution. Since the resulting micrographs represent a convolution of the actual morphology and the tip microstructure, this point was particularly important during recording the morphology change upon laser annealing. Check scans were performed on as-deposited silicon nanocrystal layers to ensure that the morphology is real and not a product of a worn-out AFM tip.

Raman measurements

During the course of this work, Raman spectroscopy was applied to analyze the structural quality of the samples and to measure the thermal conductivity of laser-annealed silicon nanocrystal layers. The measurements were performed with a Dilor XY 231 triple stage spectrometer. A liquid nitrogen cooled CCD camera enabled the multichannel detection on 1024 diodes covering a spectral region of $300 - 650\,\mathrm{cm}^{-1}$ width, depending on the spectrometer position with respect to the laser line. This Raman setup was equipped with an optical microscope, enabling micro-Raman measurements with a resolution of about 1 μm. To this end, a 50$\times$ objective was applied, producing a laser spot of approximately 2 μm in diameter. The beam of an Ar^+ laser was used to probe the sample at a wavelength of 514.5 nm (2.41 eV). Alternatively, where a shorter penetration depth of the probing light was desired, the 488.0 nm (2.54 eV) line was employed.

Spectral calibration of the Raman setup was performed by positioning the spectrometer well on the wavenumber position corresponding to the energy of the probing laser line. A crystalline silicon reference sample was used to calibrate the correlation of the Raman energy shift with the individual diodes of the CCD camera.

Mapping of the samples was possible by a sample translation stage to test the spatial homogeneity of the samples and the probing position could be monitored by the optical microscope. The slit apertures chosen for the measurements were 100 μm for the entrance and output slits (S1 and S3) and 3000 μm for the intermediate slit (S2´). Typical settings were a laser power of about 100 mW and an optical neutral density filter with a transmittance of 1% before the sample to avoid heating, while integration times of 1000 s and longer were applied. The laser power at the sample under these conditions was smaller than 50 μW, resulting in a power density of about 16 W mm^{-2}.

To determine the local temperature of the samples during the Raman measurements, as well the Stokes as the Anti-Stokes Raman signals were recorded under identical conditions. The relative intensities of both contributions were used to estimate the steady-state temperature of the sample as a function of the applied heating laser power. The same effect was exploited to measure the thermal conductivity of laser-annealed silicon nanocrystal layers. These samples were deposited and laser-annealed on crystalline silicon substrates, which intrinsically exhibit a high thermal conductivity. By direct comparison of the laser heating effect of the nanocrystal layer and of the crystalline silicon alone, the thermal conductivity of the nanocrystals could be assessed (see Section 6.5.3).

2.2.3 Optical Spectroscopy

UV/Vis/NIR

To characterize the strong optical absorption of samples and the reflectivity, a Perkin Elmer Lambda 900 optical spectrometer was employed. This system is equipped both with a halogen lamp and a deuterium lamp and is able to cover a spectral region of 186−3280 nm (0.38−6.7 eV) corresponding to the near infrared (NIR), visible (Vis), and ultra violet (UV) parts of the electromagnetic spectrum. A PbS photodetector unit and a photomultiplier served to detect the spectral intensity in the NIR and in the shorter wavelength regions, respectively. Both, transmission and reflection measurements could be performed with the help of special sample holders, and an Ulbricht sphere for the detection of diffuse reflectance and transmittance was available.

All spectra have been normalized to the lamp intensity, the transmittances of the optical components, and the spectral sensitivity of the detectors by recording the transmission of an empty sample holder, and the reflectivity of an aluminum coated mirror, respectively. For measurements with the Ulbricht sphere, a diffuse white reflector ($BaSO_4$) was utilized for normalization.

To determine the absorption coefficient α from the transmission and reflection measurements, the following relation was evaluated [Pan75]:

$$\alpha(\hbar\omega) = -\ln\left[\frac{T(\hbar\omega)}{(1-R(\hbar\omega))^2}\right]\cdot d^{-1} \tag{2.5}$$

where $T(\hbar\omega)$ and $R(\hbar\omega)$ are the spectral transmittance and reflectance of the sample and d is the sample thickness, respectively. This equation takes into account multiple internal reflections,

but not phase interference effects. It is thus valid only for films which are not too thin and do not show interference fringes.

In contrast, under the presence of thin film interference oscillations, a more complex set of equations has to be adapted to the data, and to obtain the absorption coefficient is less straightforward [Swa84, Aqi02]). A convenient method to derive the index of refraction from the spectral position of the interference extrema will be described in Subsection 4.3.2.

Photothermal deflection spectroscopy

To detect only small absolute values of the optical absorption of thin films, the above described method based on transmission and reflection measurements is not sensitive enough. Then, the direct detection of the absorption by photothermal deflection spectroscopy (PDS) is the method of choice that can still give reasonable signals. In this method, the local heating of the sample by absorption of the pumping light with energy $\hbar\omega$ is directly measured via a laser beam striding almost parallel to the sample surface. The thermal gradient evolving in the surrounding medium induces a gradient of its index of refraction, and this gradient deflects the probing beam. The position of the deflected beam is detected via a segmented diode, and, if the pumping light is chopped, the PDS signal can be recorded using lock-in detection.

As the detection medium, a variety of substances, gaseous or liquid can be applied [Boc80]. In our experiments, the organic solvent perfluorohexane (C_6H_{14}) has been chosen due to its advantageous relative change in the index of refraction with temperature, due to the absence of absorption in a wide spectral range, and due to being non-toxic. All recorded spectra were normalized to a baseline scan performed with a graphite sample as an almost perfect absorber under identical measuring conditions.

The absorption coefficient can then be evaluated from the normalized PDS signal $I_{\mathrm{PDS}}(\hbar\omega)$ via the relation:

$$\alpha(\hbar\omega) = -\ln\left(1 - 0.95 \cdot I_{\mathrm{PDS}}(\hbar\omega)\right) \cdot d^{-1}, \qquad (2.6)$$

where, again, d is the thickness of the measured sample.

Fourier-transform infrared spectroscopy

Further optical characterization in the middle and far infrared (MIR/FIR) has been performed. The method which is favored for this spectral region, where optical gratings have a small efficiency, is the Fourier-transformed infrared spectroscopy (FTIR). Here, an interferometer with a moving mirror is used in combination with a detector which records the full intensity as a function of the mirror position. Fourier back-transformation yields the signal intensity as a function of the photon energy.

Both, transmission and reflection measurements were performed by the use of specific sample holders. Unpolarized room temperature IR transmission spectra were obtained in the spectral range of $500 - 5000\,\mathrm{cm}^{-1}$ with a resolution of $1\,\mathrm{cm}^{-1}$ using a Bruker IFS 113v FTIR spectrometer. As the light source, a glowbar was applied, while Ge-KBr beam splitters in combination with a deuterated triglycine sulfate (DTGS) detector served best to record high intensity spectra. During the measurements, the sample chamber was pumped to reduce the influence of water vapor and CO_2 on the transmission spectra. Appropriate background correction was performed

with an empty sample holder and a gold coated glass slide for transmission and reflection mode, respectively.

In some cases, the silicon nanoparticles were also mixed with dried potassium bromide (KBr) powder and pressed into pellets with a diameter of 12 mm and a thickness of approximately 0.3 mm. Here, the particle concentrations were kept low at about 0.2 wt.% to avoid saturation. In this case, two consecutive spectra were analyzed: one for a pure KBr sample and a second for silicon particles embedded in a tablet of KBr with the same thickness. The ratio between the intensities of both spectra determined the relative transmission of the silicon particle sample.

Electron paramagnetic resonance measurements

Electron paramagnetic resonance (EPR) can be used to identify and to quantify paramagnetic states in a sample. To this end, an external magnetic field, B_0, is applied leading to a Zeeman splitting of different spin states. Upon absorption of irradiated photons with a fixed energy $\hbar\omega$, spin flips can be induced in the material. While from the intensity of the absorption the concentration of paramagnetic states can be determined, the magnetic field at which the absorption takes place is characteristic for the spin state involved:

$$\hbar\omega = g\mu_{\mathrm{B}}B_0. \tag{2.7}$$

Here, g is the characteristic g-factor for the electronic state and μ_{B} is the Bohr magneton. If a magnetic field of up to 1 T is available, the corresponding energy required for a spin-flip for a free electron with $g \approx 2$ is in the microwave spectral region (0.1 m wavelength). For our measurements, we used a Bruker X-band spectrometer (around 9 GHz) and magnetic fields in the range of $0.3 - 0.4$ T.

A schematic of the measurement setup is shown in Figure 2.9 a). The microwave from the microwave bridge is coupled via a tubular waveconductor to a 3 dB splitter, which splits half of the signal to the reference arm and the other half to the sample arm where the microwave is then coupled into the cavity resonator by the circulator. The reflected fraction is completely led to the second 3 dB splitter, where the signal merges with the fraction from the reference arm, which consists of a phase matching element (Φ) and an attenuator (A). The microwave intensity at this joint position is then measured via the current through a rectifying diode. The sample is placed in a He-flow cryostat inside the microwave cavity.

Before the measurement, the microwave frequency is tuned exactly to the cavity mode so that only a minimum amount of microwave power is reflected from the sample arm. Whenever the external magnetic field is in resonance with a spin transition in the probe material, part of the irradiated microwave power is absorbed in the sample according to Equation 2.7 and the magnetic susceptibility of the sample changes slightly. Due to the high Q-factor of the cavity, this is sufficient to detune the cavity and increase the reflected microwave power, inducing a current change in the diode. The phase difference between the reference and the sample arm is chosen in such a way that the imaginary part of the sample susceptibility is detected (absorptive mode). The corresponding resonance is illustrated in the Breit-Rabi diagram in Figure 2.9 b). High sensitivity is obtained by modulating the external magnetic field with frequencies of $1 - 100$ kHz with a modulation amplitude of $2 - 10$ G and using a lock-in amplifier, which filters the signal for the modulation frequency components (as a consequence, the spectra exhibit the shape of the

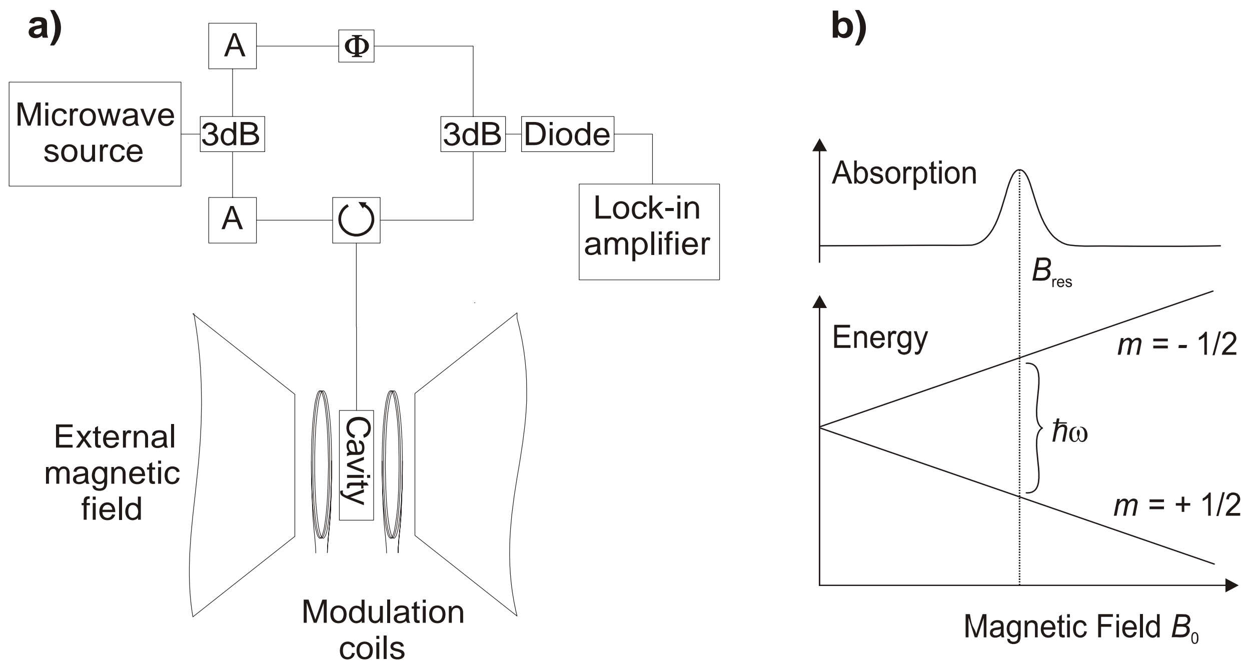

Figure 2.9: a) Schematic view of an electron paramagnetic resonance experiment. b) Breit-Rabi diagram showing the resonance condition for microwave absorption during EPR.

derivative of an absorption peak). By this means, a total of about $10^{10} - 10^{11}$ spins per Gauss linewidth can be detected by this EPR system.

2.2.4 Electrical Characterization Tools

Current/Voltage characterization

To characterize the electrical conductivity of the samples, electrical contacts have been deposited by thermal evaporation. As the favored contact geometry, the Van der Pauw geometry was chosen, consisting of four small contact pads in the corners of a square shaped sample [Van58]. Current/voltage characteristics have been recorded with the help of a Keithley K617 source-measurement electrometer unit, whereas for samples with high conductivity also a Keithley K2400 could be used.

The electrical conductivity, σ, can be derived from the individual resistances between neighboring contacts:

$$\sigma = \frac{\ln 2}{\pi d} \frac{I_{AB}}{U_{CD}}, \tag{2.8}$$

where d is the thickness of the sample and I_{AB} is the current flowing between neighboring contacts A and B if a voltage U_{CD} is applied across contacts C and D [Van58]. In this nomenclature, contacts A, B, C, and D are distributed clockwise in the sample corners. For a symmetric sample, the result is invariant under cyclic permutation of A − D, whereas in the case of real samples, the values differ slightly, and averaging is necessary. For fast conductivity checks, also two-point measurements were performed.

Current/Temperature measurements

To determine the temperature dependence of the conductivity, the samples were mounted onto the cold finger of a He cryostat. The cryostat was pumped for thermal isolation and the sample was immersed in He contact gas and the setup was cooled by liquid He. A constant voltage was applied across the sample contacts by a Keithley K6517 source-measure electrometer unit and the current through the sample was recorded as a function of the temperature of the cryostat determined via a thermocouple.

Alternatively, measurements were performed in the thermopower setup explained in more detail below, with the sample sticking completely to one of the copper plates and a thermocouple placed on top of the sample surface. Here, the sample was kept under vacuum. During heating/cooling cycles, both setups showed no hysteresis of the conductivity due to the good thermal contact with the thermal reservoir.

Hall effect characterization

The electrical characterization was supplemented by Hall effect experiments. An electromagnet was used to apply a magnetic field, $B = 1.8\,\mathrm{T}$, perpendicular to the sample surface. An electrical current, I, was fed through diagonal contacts in van-der-Pauw geometry with a constant current source, and the Hall voltage, U_H, was recorded across the opposite contacts with a voltmeter. The two possible configurations were permutated and the values for U_H were averaged. Assuming the Hall scattering factor to be unity, the charge carrier concentration, N, was derived from $N = IB/U_\mathrm{H}d$, where d is the sample thickness.

Knowing the carrier concentration, the mobility of the carriers could be calculated from the conductivity: $\mu = \sigma/eN$. The sign of the Hall signal in these measurements and thus the carrier type was calibrated with the help of reference silicon samples of known polarity. The present carrier type could additionally be corroborated by thermopower measurements.

Spectrally resolved photoconductivity measurements

The spectral photoconductivity was measured by illuminating samples with monochromatic light that was focussed onto the sample. The change in the conductivity was detected by applying a fixed voltage across parallel contacts and measuring the current through the sample by the potential drop at a variable measuring resistor. To achieve high accuracy, the light was chopped at a frequency of typically 8 Hz and the photosignal was recorded using a lock-in amplifier. The obtained values were corrected for the spectral intensities of the used halogen ($400 - 3000\,\mathrm{nm}$) and xenon ($200 - 800\,\mathrm{nm}$) lamps and for the spectral response of the used optical filters and the grating by dividing through a spectrum recorded with a pyrometer at the sample position.

Thermopower measurements

Thermopower measurements were performed in two different experimental setups. A fast method comprised a voltmeter and two measurement tips, one of which could be heated to temperatures in the range of $200 - 450\,^\circ\mathrm{C}$ whereas the other was kept at room temperature. The sample was

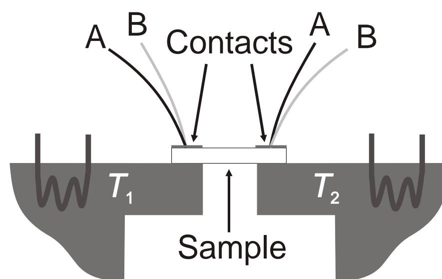

Figure 2.10: Schematic drawing of the experimental setup to determine the thermopower and the Seebeck coefficient. A and B represent the Chromel and Alumel wires, respectively.

kept at ambient atmosphere and the measurement consisted of placing both tips onto the sample in a distance of typically 2 mm for approximately 5 s until a stable voltage had established between the hot and the cold end of the sample. The electrical potential difference between the cold spot and the hot spot then defined the thermopower of the material.

On the one hand, this method has the clear advantage that it is very fast and especially well-suited for screening of sample series and for testing the lateral homogeneity of individual samples. On the other hand, it can well be argued that the thermal gradient across the sample is not very well-defined since the thermocouple for controlling the temperature is situated inside the hot tip and the heat resistance of the interface between the tip and the sample is not known. Also, the influence of an electrical barrier on the thermopower cannot be corrected for. Thus, this method is only applicable if large thermal gradients are applied. In addition, also atmospheric influences on the measurement cannot be excluded by this approach. However, by direct comparison with the second setup described below, no strong deviations were found.

An alternative setup allowed for the application of much smaller thermal gradients in vacuum at different mean temperatures. A schematic drawing of this system is depicted in Figure 2.10. The setup consists of two half-cylindrically shaped copper plates inside a small stainless steel vacuum chamber. These plates act as the hot and cold sides and are separated from each other by a small gap. Both can either be cooled with liquid nitrogen or be heated by a resistive heater element. The temperature of each plate could be adjusted by a Eurotherm (Type 902/903) heater-control unit, enabling the independent control of both half-cylinders. Well above room temperature, the system is able to stably regulate temperatures in the range of $100 - 500\,^{\circ}$C fully automatically, whereas the lack of active cooling requires manual temperature adjustment around and below room temperature. At low temperatures, static measurements are not possible with this setup, because no cryostat is available for the implemented design. Still, controlled temperature ramps can be performed by first cooling down manually, placing the heater in the system and then running a programmed temperature ramp.

The samples were placed on the gap between both plates in a way that the sample contacts were flush with the gap. To enhance the thermal contact with the copper plates, heat conductive paste was applied. The electrical leads were formed by two Ni/NiCr Thermocouples (Type K, 50 μm thick soldered Chromel and Alumel wires, schematically depicted by "A" and "B" in the figure) glued onto the sample contacts with silver paste. These thermocouples were each connected to the heater-control units of the respective plate. The thermopower was detected by measuring the voltage drop between the Alumel wires with a high impedance electrometer (Keithley K6517).

The temperatures at the contact positions were recorded together with the resulting thermopower values by a designated software program.

To rule out the parasitic influence of barrier voltages at the contacts, robust thermopower measurements consist of measuring not only the thermopower as a function of temperature, but also as a function of the thermal gradient at a fixed mean temperature [Bra98]. To obtain continuous data of the Seebeck coefficient, also temperature ramps with different ramp rates for the hot and the cold plates have emerged to be a convenient method.

3 Physics of Silicon Nanocrystals

Semiconductor nanocrystals have emerged as a rapidly growing area of scientific research over the recent decade. Especially the beneficial electro-optical properties of nanocrystals, which mainly arise from their small size approaching the quantum confinement regime have been attracting great interest for new fields of semiconductor applications. In the context of this thesis, the confinement effects of the electronic wavefunction plays only a minor role due to the still relatively large size of the nanocrystals applied for printable semiconductors. Instead, the thermodynamic questions of the stability of the particles and on the efficient incorporation of dopants will be in the focus of the present and of the following chapters. After a short overview on the effects of electron confinement, thus the metastability of nanocrystals and the phononic properties will be highlighted in the following. In the final subsection, the electrical behavior of nanocrystal networks will be discussed.

3.1 Electron confinement

From textbook solid state physics, it is known that electrons form energy bands in a semiconductor crystal with valence and conduction bands separated from each other by the forbidden energy gap. If the crystal does not extend over a large spatial region but is limited to a thin film, a narrow wire, or to a small sphere, electron confinement can occur in one, two, or three dimensions, respectively. Accordingly, allowing for their two-, one-, and quasi-zero-dimensional physical situation, these systems are commonly referred to as "quantum wells", "quantum wires", and "quantum dots", respectively. Then, the strong localization of the electron wave function induces a contribution to the energy of the electrons, which is known as the confinement energy.

The pure three-dimensional ground state energy, E_{conf}, of a particle in a confining spherical potential well follows from simple quantum mechanics as:

$$E_{\mathrm{conf}} = \frac{h^2}{2mL^2}, \tag{3.1}$$

if the potential walls are considered infinitely high. Here h is Planck´s constant, while m and L are the particle mass and the well diameter, respectively. If this simple example is adapted to the solid state situation of semiconductor nanocrystals, the free electron mass transforms into the effective mass, m^*, and L is identified with the diameter of the nanocrystals. In a more accurate consideration, also the Coulomb interaction of the charge carriers has to be respected for [Del93]. In any case, if L is reduced, E_{conf} increases inversely proportional to the square of the diameter. Hence, if the electron wave function is strongly confined, this contribution to the total energy can soon amount to significant values.

In a semiconductor nanocrystal this effect leads to an effective increase of the band gap. Due to the confinement of the electrons and the holes, the corresponding confinement terms have to be added to the bulk bandgap energy. Optical transitions well above the bulk bandgap can thus occur

and the dependence on the crystallite size has been shown experimentally, *e.g.* by luminescence experiments [Fur88, Led00].

As a rule of thumb, such quantum confinement starts to play a role if the particle size falls below the free-exciton Bohr radius, which amounts to about 4.3 nm in crystalline silicon [Del93]. There, the following relation can describe the fundamental bandgap as a function of the crystallite size [Del93]:

$$E_g(d) = E_0 + \frac{3.73}{(d/\,\mathrm{nm})^{1.39}}\,\mathrm{eV}, \tag{3.2}$$

where E_0 is the bulk bandgap value of crystalline silicon.

An often discussed topic is whether also a transition from indirect to direct optical transitions can be achieved upon reducing the size of silicon nanocrystals. As a consequence of smearing out of the electron and phonon momentum, the momentum conservation rule for optical transitions might be lifted. However, from characteristic phonon signatures in optical transitions it becomes evident that also in silicon nanocrystals with diameters as small as 4 nm the indirect nature of the fundamental emission prevails in silicon [Ior07, Mei07].

Regarding the silicon nanocrystals examined during this thesis, confinement effects could be shown to play a role for the hyperfine interaction of electrons bound in the Coulomb potential of phosphorus dopants in electron spin resonance at low temperatures. With a reduction of the crystallite size, the hyperfine splitting increases, which allows conclusive statements about the localization of the electrons at the position of the phosphorus nucleus [Ste08a]. These results show that the electron confinement effects are visible already for much larger crystal sizes than reported by Fujii *et al.* [Fuj02], which can be explained in a model taking into account the effective dielectric constant of the single silicon nanocrystals [Per08].

3.2 Metastability of nanocrystals

Apart from the above introduced quantum confinement, also more classical thermodynamic effects play a role with ensembles of small scale nanocrystals. Here, the relative influence of the surface atoms on the overall stability of a nanocrystal becomes relevant when the surface atoms constitute a large fraction of the total amount of atoms. Since the number of bonds is reduced at the surface, these surface atoms are more mobile in thermally activated diffusion processes. The multitude of structural and morphological changes provoked by diffusion, material flow, and sublimation is usually referred to as sintering, which can dominate structural changes in granular materials in an intermediate temperature range.

If the thermal energy available is further increased, or the size of the nanocrystal further reduced, the stability of the whole nanocrystal will decrease, enabling the transition into the liquid state. This is found to occur at temperatures well below the bulk melting point, due to the relative significance of the fraction of weakly bound surface atoms. In the following subsections, both of these two mechanisms will be highlighted on the basis of the thermodynamic stability.

3.2.1 Sintering of nanoparticles

At elevated temperatures, small-sized particles can undergo structural relaxation processes to reduce the amount of free surface, without the need for a transition to the liquid phase. This consequence of the high surface energy contribution to the free energy of nano-scaled material can lead to drastic changes of the morphology. Such sintering processes are mainly diffusive in nature and exhibit thermal activation as a consequence of the binding situation of the surface atoms. However the necessary thermal activation energy is reduced with respect to values typical for diffusion processes in the bulk material indicating the metastability of the nano-scaled phases.

The physical processes that induce the sintering of neighboring particles can be one or several from four different basic material transport steps: viscous or plastic material flow, evaporation and condensation, volume diffusion, and surface migration. Herring was the first to formulate scaling laws to describe the difference in time resulting from a difference in particle size for each of these processes [Her50]. For particles B exceeding particles A in size by a factor of λ ($L_\mathrm{B} = \lambda L_\mathrm{A}$), he deduced a retardation factor of λ^n for the time required for the same sintering process: $\Delta t_B = \lambda^n \cdot \Delta t_A$. Here, the exponent, n, amounts to 1, 2, 2, and 4 for the respective sintering processes listed above. From evaluating differences in the characteristic sintering time for different particle sizes, thus a possibility is given to identify the underlying sintering mechanism.

Johnson proposed a sintering model by which all of the significant material transport mechanisms can be identified, even though more than one may be operating simultaneously [Joh69]. As in many other sintering models, the junction site of two attaching spherically shaped particles is the starting point in the geometrical considerations. During thermal annealing, atoms in this grain boundary region diffuse towards the edges of this junction to form a sintering neck, while the convergence of the particles leads to a shrinkage of the effective volume. From measurements of the neck size, of the shrinkage and of the shrinkage rate, the volume and grain-boundary diffusion coefficients were calculated and the surface diffusion coefficient was fitted numerically. All derived values were found to be in good agreement with literature data [Joh69]. The overall one-dimensional shrinkage, y, at the time t, can be described by this relation:

$$y(t) \approx \sqrt{\tau^{-1} t} \quad \text{with} \quad \tau^{-1} = \frac{8 D \sigma}{k_\mathrm{B} T \cdot \rho_\mathrm{at} r^3}. \tag{3.3}$$

Here, the characteristic rate constant, τ^{-1}, is composed of the atomic diffusion constant in the particles, D, the surface tension, σ, and the atomic density, ρ_at, while k_B and T are Boltzmann´s constant and the temperature, respectively. The cubic dependence on the particle radius, r, shows that the particle mass limits the material densification.

For the evolution of the geometry change with time, Friedlander and Wu found a linear decay law giving a characteristic frequency for the deviation from the spherical shape [Fri94]. According to their calculations, the decrease rate of the area, a, of a sintering particle is proportional to the areal difference to a spherical shape, varying as:

$$\frac{\mathrm{d}a}{\mathrm{d}t} = -2\tau^{-1}(a - a_\mathrm{sph}), \tag{3.4}$$

where $a_\mathrm{sph} = 4\pi r^2$ is the surface area of a spherical particle with radius r. The characteristic rate constant, τ^{-1}, is identical with that obtained by Johnson in Equation 3.3.

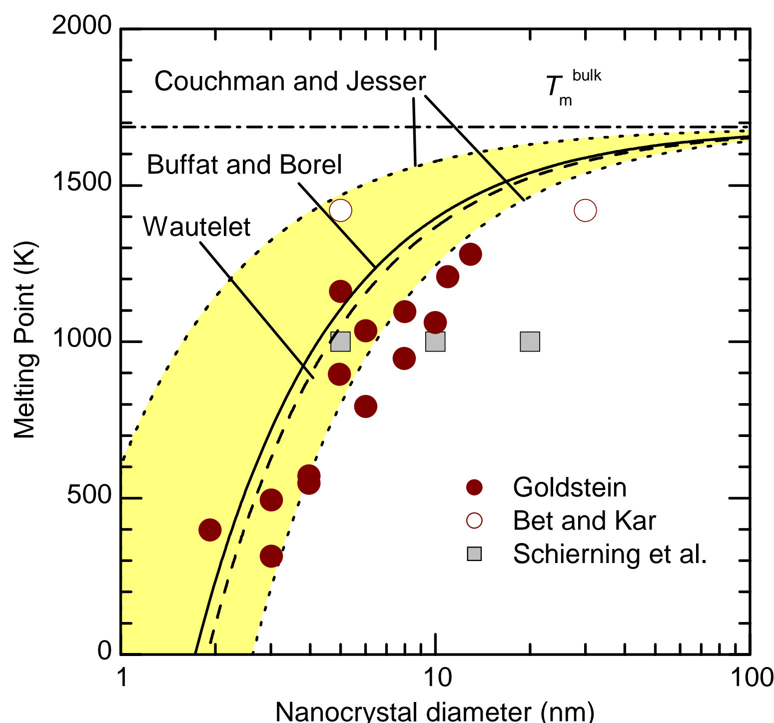

Figure 3.1: Reduction of the melting point of silicon nanocrystals as a function of the diameter. Experimental data are taken from [Gol96], [Bet04], and [Sch08]. The shaded region denotes the upper and lower limits derived in [Cou77]. The dashed line displays the surface phonon instability model [Wau91] while the result of a three phase equilibrium model is given by the solid line [Buf76]. The dashed-dotted line marks the melting point of bulk crystalline silicon at 1687 K [Mad84].

3.2.2 Size dependent melting of nanocrystals

While the sintering processes introduced above are described by the movements of several individual atoms, a collective solid-liquid phase transition occurs if the thermal energy is sufficiently high. In the case of nanocrystals, the reduced thermodynamic stability expresses itself in an effective decrease of the melting point with respect to the bulk material. For silicon nanoparticles, the reported experimental data are subject to a high degree of scatter. For example, a depression by 17% of the melting point temperature has been reported by Bet and Kar from scanning differential calorimetry. In this measurement, however, the melting transition stretched over a large temperature range and the result should be taken with care. Moreover, the melting "point" was found unaffected by the silicon nanoparticle size being 5 nm or 30 nm [Bet04]. A more substantiated study has been performed by Goldstein [Gol96]. During *in-situ* transmission electron microscopy measurements, he observed a strong size dependence of the melting point of silicon nanocrystals. In a recent study, Schierning *et al*. combined both in-situ transmission electron microscopy and scanning differential calorimetry with silicon nanocrystals from the same microwave reactor as used in this work (MWR1) [Sch08]. In both methods, they observed the melting of the nanocrystals already at a temperature of 1000 K, again independent of the nanocrystal size. Figure 3.1 illustrates the results of Goldstein, Bet and Kar, and Schierning *et al*. (full circles, open circles, and grey squares, respectively) together with different theoretical predictions as a function of the nanocrystal size.

Among the theoretical models included in the graph, the surface phonon instability model by Wautelet is plotted in the graph by the dashed line [Wau91]. In this approach, the free energy of the nanocrystals is composed of an atomic and of a phononic contribution. By the assumption of a linear softening function, which reduces the phonon frequency in the material with increasing the volume concentration of structural defects, an expression for the melting point depression is deduced:

$$\frac{T_{\mathrm{m}}}{T_{\mathrm{m}}^{\mathrm{bulk}}} \simeq 1 - \frac{\Delta}{L}, \tag{3.5}$$

where $T_{\mathrm{m}}^{\mathrm{bulk}}$ and T_{m} are the melting temperatures of the bulk and that of a nanocrystal with diameter L, respectively, while Δ is a characteristic atomic distance that is calculated from the value of $T_{\mathrm{m}}^{\mathrm{bulk}}$ and from the formation energy of vacancy defects in the material. For silicon, Wautelet gives a value of $\Delta = 1.88\,\mathrm{nm}$, which leads to the dashed line shown in Figure 3.1.

As the figure shows, the melting temperature from the proposed model approaches $T_{\mathrm{m}}^{\mathrm{bulk}}$ for crystal sizes above 100 nm, whereas significant reduction is present for crystal sizes below 10 nm. Nanocrystals with a diameter smaller than 2.3 nm are predicted to be liquid at room temperature. In comparison with the experimental data, only qualitative agreement can be found. The results of Goldstein show the melting transition at nanocrystal sizes that are systematically larger by almost a factor of 1.5. However, apart from the crystal softening function, Wautelet´s model contains no free parameters and is thus a quite elegant way to treat the problem. Alternatively, Couchman and Jesser formulated the thermodynamic limits for the melting transition considering the coexistence of a liquid and a solid phase during the melting [Cou77]. From balancing the Helmholtz free energy of the nanocrystals, they give expressions for the upper and lower limits for the size dependent melting point, $T_{\mathrm{m,u}}$ and $T_{\mathrm{m,l}}$:

$$T_{\mathrm{m,u}} = T_{\mathrm{m}}^{\mathrm{bulk}}\left[1 - \frac{4}{l_0 L}\frac{\sigma_{\mathrm{sl}}}{\rho_{\mathrm{s}}}\right], \qquad \text{and} \qquad T_{\mathrm{m,l}} = T_{\mathrm{m}}^{\mathrm{bulk}}\left[1 - \frac{6}{l_0 L}\left(\frac{\sigma_{\mathrm{s}}}{\rho_{\mathrm{s}}} - \frac{\sigma_{\mathrm{l}}}{\rho_{\mathrm{l}}}\right)\right]. \tag{3.6}$$

Here, l_0 is the latent heat of fusion and L is the nanocrystal diameter, while σ and ρ are the surface energy and the mass density each of the solid and the liquid phase and of the solid-liquid interface as denoted by the subscripts s, l and sl, respectively. Obviously, this formalism requires much more information on material parameters, which are difficult to determine, than does the model by Wautelet.

Using literature values for these parameters in the case of silicon, $\rho_{\mathrm{s}} = 2.329\,\mathrm{g\,cm^{-3}}$, $\rho_{\mathrm{l}} = 2.533\,\mathrm{g\,cm^{-3}}$, $l_0 = 1105.3\,\mathrm{J\,g^{-1}}$, $\sigma_{\mathrm{sl}} = 4.13\,\mathrm{mN\,cm^{-1}}$ and $\sigma_{\mathrm{l}} = 7.33\,\mathrm{mN\,cm^{-1}}$ [Iof08, Tan06, Fuj06], the expected range for the size dependence of the melting temperature is given by the shaded region in Figure 3.1. Here, $\sigma_{\mathrm{s}} = 18\,\mathrm{mN\,cm^{-1}}$ has been used, which is the result of averaging the values reported for different crystallographic planes in silicon [Jac63]. As the figure shows, about half of the experimental data points by Goldstein are situated within the - admittedly rather broad - predicted region.

By similar surface and interface energy considerations, under the condition of a three-phase equilibrium between the spherical solid particle, a liquid particle of the same mass, and the vapor phase, Buffat and Borel derived a relation that directly predicts $T_{\mathrm{m}}(L)$ [Buf76]:

$$T_{\mathrm{m}} = T_{\mathrm{m}}^{\mathrm{bulk}}\left\{1 - \frac{4}{\rho_{\mathrm{s}} l_0 L}\left[\sigma_{\mathrm{s}} - \sigma_{\mathrm{l}}\left(\frac{\rho_{\mathrm{s}}}{\rho_{\mathrm{l}}}\right)^{2/3}\right]\right\} \tag{3.7}$$

As figure 3.1 illustrates, the result of this consideration leads to a very similar curve as predicted by Wautelet´s phonon instability model if the above introduced material parameters from the

literature are used. However, all the theoretical considerations shown here slightly underestimate the extent of the melting point depression for the silicon nanocrystals. And especially the size-independent melting observations cannot be reproduced by theory. In this case, more complicated interactions between the neighboring particles might become dominant [Sch08].

It has to be added that the thermodynamic stability of the nanocrystals can be restored by a proper surface termination. For instance, theoretical first principles calculations can reproduce stable nanoclusters of a small number ($5-400$) of silicon atoms, which would be expected to be liquid at room temperature according to the above considerations. In such studies, the surface bonds are typically saturated with hydrogen atoms [Bel02, Ram05, Mel04a]. By this means, the surface energy of the nanocrystals is decreased so that a stable crystalline structure is obtained. Also in reality, unsaturated silicon surface bonds will tend to bind to available oxygen and hydrogen atoms. Experimentally, the hydrogen termination of silicon nanocrystals has been proven to be much more stable than that of a bulk crystalline silicon surface [Bau05].

A difficult experimental task is to observe single nanocrystals that are not influenced by their surface properties or their surroundings. If a dense layer of nanocrystals is analyzed, the liquid phase will be present for only a very short period of time until the size has considerably increased. This makes the accurate determination of size-dependent melting difficult. If the surface is additionally oxidized, the melting behavior can be significantly altered. For 4 nm silicon nanocrystals that were deliberately surface-functionalized with alkyl groups, Yang *et al*. observed agglomeration and sintering of the particles already after a one-hour anneal in an inert solvent at 162 °C [Yan00]. As to the experimental data shown in Figure 3.1, Goldstein used silicon nanocrystals with native oxide capping,whereas Schierning and coworkers removed the surface oxide layer by etching.

If nanocrystals are surrounded by a solid state environment, the latter can dominate their thermodynamic behavior. For the situation of germanium nanocrystals embedded in a silicon oxide matrix, significant superheating and supercooling effects, which even exceed the effect of the small size (5 nm) have been observed by Xu and coworkers [XuS07]. Extending the kinetic model by Couchman and Jesser [Cou77] and taking into account the respective interface energies, the observed melting hysteresis of 470 K can be sufficiently described by a nucleation barrier present during the formation of liquid and solid phases, respectively [XuS07].

3.3 Vibrational Properties

In solid state samples, the vibrational properties are strongly influenced by the crystalline structure of the material. Apart from neutron scattering, which can yield the phonon dispersion in the material, a very versatile tool to analyze the vibrational properties is given by Raman spectroscopy. This spectroscopic method allows the characterization of a broad range of physical properties such as the chemical composition, the physical microstructure, the sample temperature, the material strain, the carrier concentration, and other important properties of solid state samples, liquids and gases.

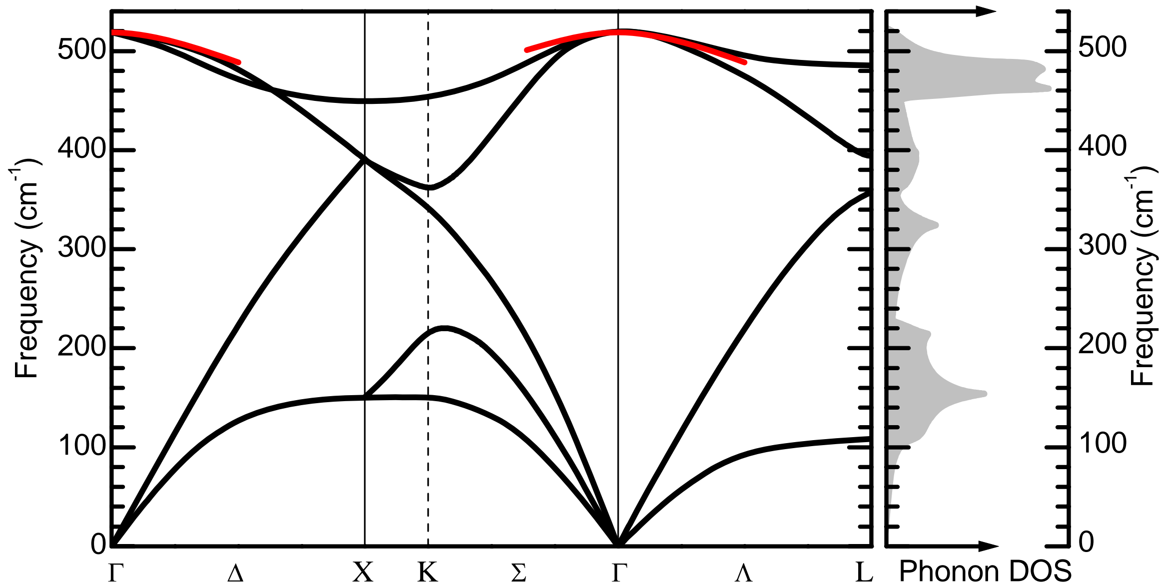

Figure 3.2: Phonon dispersion of crystalline silicon and phonon density of states (DOS) as calculated via the adiabatic bond charge model by Weber [Web77]. The red lines demark the isotropic approximation to the phonon dispersion around the zone center implemented in the phonon confinement model.

3.3.1 Raman spectroscopy

During Raman measurements, the monochromatic light of a laser is inelastically scattered by vibrational modes in the probed molecule or crystal. In solid state crystals, the main application of this method is to probe phonons, but also other collective excitations such as magnons or plasmons can interact with the exciting light. To fulfill the momentum conservation for the phonon-photon interaction, the wavevector $\vec{q}$ of the contributing phonon needs to be close to zero (in the vicinity of the Γ-point), which can be either met by zone center optical phonons with an energy of $521\,\mathrm{cm}^{-1}$, or by second order processes involving acoustic phonons or combinations of acoustic and optical phonons. In the case of highly disordered materials such as amorphous silicon, the translational symmetry is lost and $\vec{q}$ is not defined any longer. Then, the Raman cross section rather mirrors the phonon density of states in the material. From Figure 3.2, which displays this quantity together with the silicon phonon dispersion along directions of high symmetry in the first Brillouin zone, it is evident that in this case a broad Raman peak around $480\,\mathrm{cm}^{-1}$ will be observed [Web77].

Since Raman spectroscopy is sensitive to so many internal and external influences, special care is required to interpret Raman spectra correctly. Especially free-standing low-dimensional materials, such as nanowires or nanocrystals inherently are situated in almost thermal isolation, and the sample heating during the measurement can lead both to laser annealing and to temperature-distorted measurement results. Various examples can be found in the scientific literature, which ascribe the peak shift and broadening characteristic for laser-induced sample heating to either the phonon-confinement in low-dimensional samples [Li99] or to the wurtzite-type hexagonal silicon polymorph (Si IV) [Gog99, Fon07]. On the other hand, the possibility to heat small-scaled structures easily by a laser can also be of advantage. For example, it can be exploited to determine the thermal conductivity of a porous thin film [Per99], as it has been applied also in this work (see Section 6.5.3).

Influence of the temperature

Upon heating, the one-phonon Raman signal is observed to shift to lower frequencies, while the peak width increases simultaneously. This is a consequence of an effective softening of the crystal lattice, reducing the characteristic vibrational frequencies. Here, the concomitant increase in peak width is the result of a change in the lifetime of the Raman transition [Bal83].

The redshift of the Raman peak is a hyperbolic function of the temperature, but it can be approximated by a linear relation above room temperature. For crystalline silicon, the relative shift of the peak position with the temperature has been interpolated by $\Delta\omega/\omega_0 = -5 \times 10^{-5}\,\mathrm{K}^{-1} \cdot T$, which holds for a temperature range of $300 - 1200\,^\circ\mathrm{C}$ [Tsu82, Per99], and is in agreement with the data of Balkanski *et al*. [Bal83].

Apart from the linewidth and peak position, the temperature also influences the relative Raman scattering cross sections for the emission and absorption of phonons. Here, scattering processes involving the excitation of a phonon are commonly referred to as Stokes scattering and lead to a red-shift of the scattered light energy, while the absorption of a phonon is denominated Anti-Stokes scattering, resulting in a re-emitted photon of higher energy. At low temperatures, only few phonons are available for Anti-Stokes processes, and thus Raman scattering can be used to probe the temperature of the sample. The relative intensities of both scattering contributions depend strongly on the temperature according to the relation:

$$\frac{I_{\text{Anti-Stokes}}}{I_{\text{Stokes}}} = \left[\frac{\omega_{\mathrm{AS}}}{\omega_{\mathrm{S}}}\right]^3 \mathrm{e}^{-\hbar\omega_0/k_{\mathrm{B}}T} \tag{3.8}$$

which holds if the slight change of the absorption coefficient and of the Raman cross sections between the Stokes and Anti-Stokes photon energies, ω_{S} and ω_{AS}, can be neglected [Bal83]. In the equation, $I_{\text{Anti-Stokes}}$ and I_{Stokes} represent the intensities of the Anti-Stokes and the Stokes line, respectively, and $\hbar\omega_0$ is the phonon energy. Thus, in practice, the Stokes line is used for Raman characterization due to its much higher intensity (by a factor of ten for silicon at room temperature).

Raman scattering was exploited to determine the thermal conductivity of laser-annealed silicon nanocrystal layers in the course of this work. Out of the two possibilities to determine the temperature from Raman measurements, the Stokes-to-Anti-Stokes ratio was preferred because it gives absolute results and requires no calibration. In contrast, the evaluation of the peak position (and width) leads to distinctly different values than known crystalline silicon references. Typically both the peak shift as well as the increase of the peak width is found to be much stronger for the nanocrystalline material. If this variant is used for temperature measurements, calibration measurements on a heating stage are inevitable.

Influence of the crystallite size

Soon after microcrystalline silicon deposition techniques had been developed, it was noticed that the Raman spectra of polycrystalline silicon samples with small crystallite sizes below 20 nm showed crystalline silicon peaks in Raman spectroscopy, but with a red-shifted and asymmetrically broadened peak [Iqb79]. With decreasing the crystallite size, the red-shift and the broadening became more pronounced [Iqb82]. These observations motivated Richter and coworkers to examine the consequences of the confinement due to the finite crystal size on the one-phonon

Raman spectra, which can be explained in a phonon confinement model [Ric81]. Campbell and Fauchet later extended this model also to confinement in only two or even one spatial dimension as applicable in thin films or in quantum wires, where the same effect is found to be much weaker [Cam86].

Basically, a reduction of the crystallite size induces an uncertainty of the phonon wavevector, q. While in general the translational symmetry necessary to define q as a good quantum number is not exactly valid for any crystal of finite size, this does not affect the physical properties unless its dimensions become comparable with the lattice constant, a. Then, the discrete values of q, which are spaced by $\frac{2\pi}{L}$ are of the same order of magnitude as the Brillouin-zone edge at $\frac{\pi}{a}$, and the concept of a dispersion relation becomes obsolete. In the extreme situation of a "crystalline" cluster formed by only two atoms, only one molecular vibrational mode with fixed energy is left, equivalent to a standing wave at the "Brillouin-zone edge". The following subsection will focus on the phonon confinement model, which can describe the change in the phonon spectra for small crystals quantitatively.

3.3.2 Phonon confinement model

One consequence of the limited size of a nanocrystal is that phonons cannot be described as plane waves, but instead need to be approximated by wave packages containing a continuous set of q-components that can be calculated by a Fourier-transformation of the spatial confinement function. As a Gaussian function has been found to best describe the spatial confinement of the phonons in the crystal [Cam86], these Fourier components $C(q)$ can be written as:

$$|C(q)|^2 \cong \mathrm{e}^{-\alpha q^2 L^2}. \tag{3.9}$$

Here, L is the crystal size, and α is a scaling factor determining the phonon amplitude at the crystal boundary. Then the Raman cross-section $I(\omega)$ at the frequency ω becomes

$$I(\omega) \cong \int \frac{|C(q)|^2}{(\omega - \omega(q))^2 + (\Gamma_0/2)^2} \mathrm{d}^3 q, \tag{3.10}$$

where Γ_0 is the natural linewidth of the silicon Raman mode and $\omega(q)$ is the phonon dispersion relation of silicon showing negative dispersion of the optical phonons in the zone center as visible in Figure 3.2. The integral runs over the Brillouin-zone and the contribution of non-zero q values increases for smaller crystallite sizes L. In the case of a very large crystal, this formalism changes to a single Lorentzian line at $\omega(q = 0)$.

To calculate the Raman intensity from Equation 3.10, many authors use an analytic fit to the optical phonon dispersion around the Γ-point adapted from [Tub73]:

$$\omega(q) = \left[1.714 \times 10^5 + 10^5 \times \cos \frac{q\pi}{2}\right]^{0.5} \mathrm{cm}^{-1}. \tag{3.11}$$

However, this approximation is only valid for phonons along the [100] directions and it is not clear *a priori* why this direction should be preferred in scattering processes in silicon nanocrystals. Paillard *et al*. point out that the influence of the dispersion relation on the phonon confinement effects is even more critical than the choice of a phonon confinement function [Pai99]. They showed that by using the sum rule of Brout [Bro59], the optical phonon dispersion relation

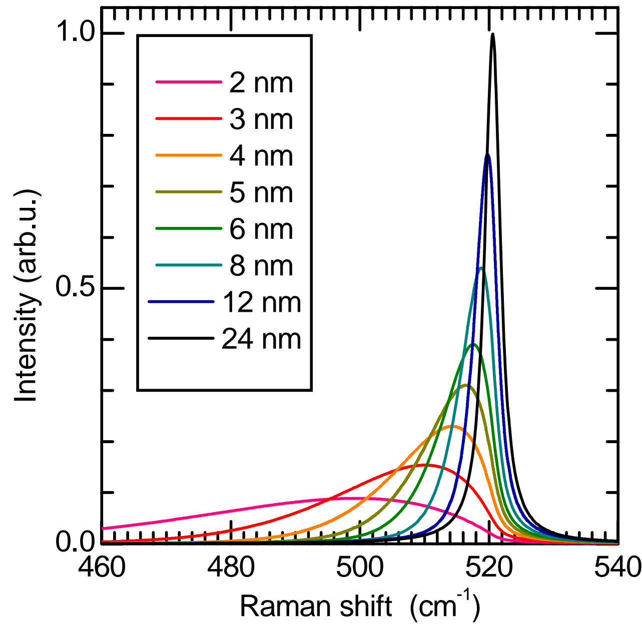

Figure 3.3: Calculated Raman spectra of silicon nanocrystals with different crystallite sizes using the phonon confinement model of Richter, Campbell, and coworkers and an isotropic phonon dispersion relation after Paillard and coworkers.

can be averaged along the Δ, Σ, and Λ symmetry directions where the degeneracy of the phonon modes and the respective symmetry are taken into account:

$$\varpi(q_\mathrm{r}) = \left[(522)^2 - \frac{1.261 \times 10^5 q_\mathrm{r}^2}{|q_\mathrm{r}| + 0.53}\right]^{0.5} \mathrm{cm}^{-1} \qquad |q_\mathrm{r}| < 0.5. \tag{3.12}$$

In the above equation, q_r is the reduced wavevector. This isotropic formulation of the silicon optical phonon dispersion is also shown in the silicon phonon dispersion diagram in Figure 3.2 by the red lines to show the effect of the averaging and the differences compared to the anisotropic real phonon dispersion. Due to the double degeneracy of the transverse modes and the symmetry, the obtained relation follows mostly the transverse optical phonons along the Δ- and Λ-lines, as can be seen in the graph.

To fit experimental curves with Equations 3.10 and 3.12, the vertical offset $\varpi(q_\mathrm{r} = 0)$ is calibrated using the spectral position of a reference silicon wafer under comparable measurement conditions. The integral in Equation 3.10 is then taken over the spherical Brillouin zone replacing $\mathrm{d}^3 q_\mathrm{r} = 4\pi q_\mathrm{r}^2 \mathrm{d}q_\mathrm{r}$, with q_r running from 0 to 1. Doing so, the condition of Equation 3.12 is fulfilled for crystal sizes $L > 2\,\mathrm{nm}$. Figure 3.3 shows the results of the calculations of the Raman spectra of spherical silicon crystals with different sizes using a scaling factor of $\alpha = \frac{1}{8a^2}$, where a is the lattice constant of crystalline silicon ($a = 0.543\,\mathrm{nm}$). In the graph, the spectra have been normalized to the integral intensity $I(L) = \int I(\omega)\mathrm{d}\omega$ corresponding to a constant total Raman cross section. The phonon confinement model gives very good agreement with the experimental data of Iqbal *et al.* and Richter *et al.*, [Iqb82, Ric81], for the correlation [Iqb79] between the peak shift and the peak width as a function of the crystallite size.

Real samples of nanocrystals always exhibit a distribution of particle sizes instead of exactly identical particle sizes. Due to the finite width of the probing laser focus, even in Micro-Raman

measurements always an ensemble consisting of various different crystal sizes is probed. Consequently, the statistical distribution function of particle sizes has to be accounted for during calculations of the Raman spectra. This will be performed in Section 4.1.3 for the size distribution present for the silicon nanocrystals under study here.

3.4 Optical Properties

The optical properties of a material contain valuable information on its microscopic structure. This is because the propagation of electromagnetic waves within a medium is determined by the polarizability of the material and by its absorption behavior. The dynamic response of the material to the oscillatory electromagnetic excitation depends on the frequency, and thus on the energy of the light. If the Maxwell equations are solved by a set of plane waves, the dielectric function, ε, expresses the dispersion relation of the medium, which is the interconnection between c, the vacuum speed of light, the wavevector, k, and the angular frequency, ω, in the material:

$$\varepsilon = \frac{c^2 k^2}{\omega^2}. \tag{3.13}$$

At zero energy, ε is given by the sum of all contributions to the polarizability, including optical phonons and valence and core electrons. At higher energies, whenever there is an energy overlap of internal excitations with the energy of the light, resonant interactions become possible. Apart from inter- and intraband transitions, *e.g.*, excitons, phonons, polarons, and polaritons belong to the variety of collective excitations inside the solid state material, which can resonantly couple to the electromagnetic wave. All these effects leave their characteristic "fingerprints" at specific energies in the complex dielectric function, $\varepsilon = \varepsilon_1 + i\varepsilon_2$.

Apart from the real and imaginary part of the dielectric function, ε_1 and ε_2, for practical reasons the equivalent formulations of the index of refraction, n, and the absorption coefficient, α, are more commonly used. While the refractive index determines the effective wavelength within the material, the absorption coefficient is a measure of the wave extinction along the light path. This set of optical functions determines the amount and the direction of transmitted and reflected light via Lambert-Beer´s-law, Snell´s law, and the Fresnel equations. The correlation of n and α with ε is as follows:

$$n = \sqrt{\tfrac{1}{2}}\left(\sqrt{\varepsilon_1^2 + \varepsilon_2^2} + \varepsilon_1\right)^{1/2} \quad \text{and} \quad \alpha = \frac{2\omega}{\sqrt{2}c}\left(\sqrt{\varepsilon_1^2 + \varepsilon_2^2} - \varepsilon_1\right)^{1/2}, \tag{3.14}$$

3.4.1 Band structure and dielectric constant

Optical interband transitions influence the dielectric function in a characteristic way. Since according to the Pauli-principle and Fermi´s golden rule optical transitions require suitable initial and final states, the combination of both in the form of the joint density of states, D_j, is a measure of the transition probability. This quantity gives the combined probability for a given energy E_{cv} to find available occupied electronic initial states at an arbitrary energy E in the valence band and vacant final states situated at an energy $E + E_{\mathrm{cv}}$ in the conduction band. It can be written as an integral on a sphere of constant energy, $S_{\vec{k}}$, in reciprocal $\vec{k}$-space, which sums up all contributions

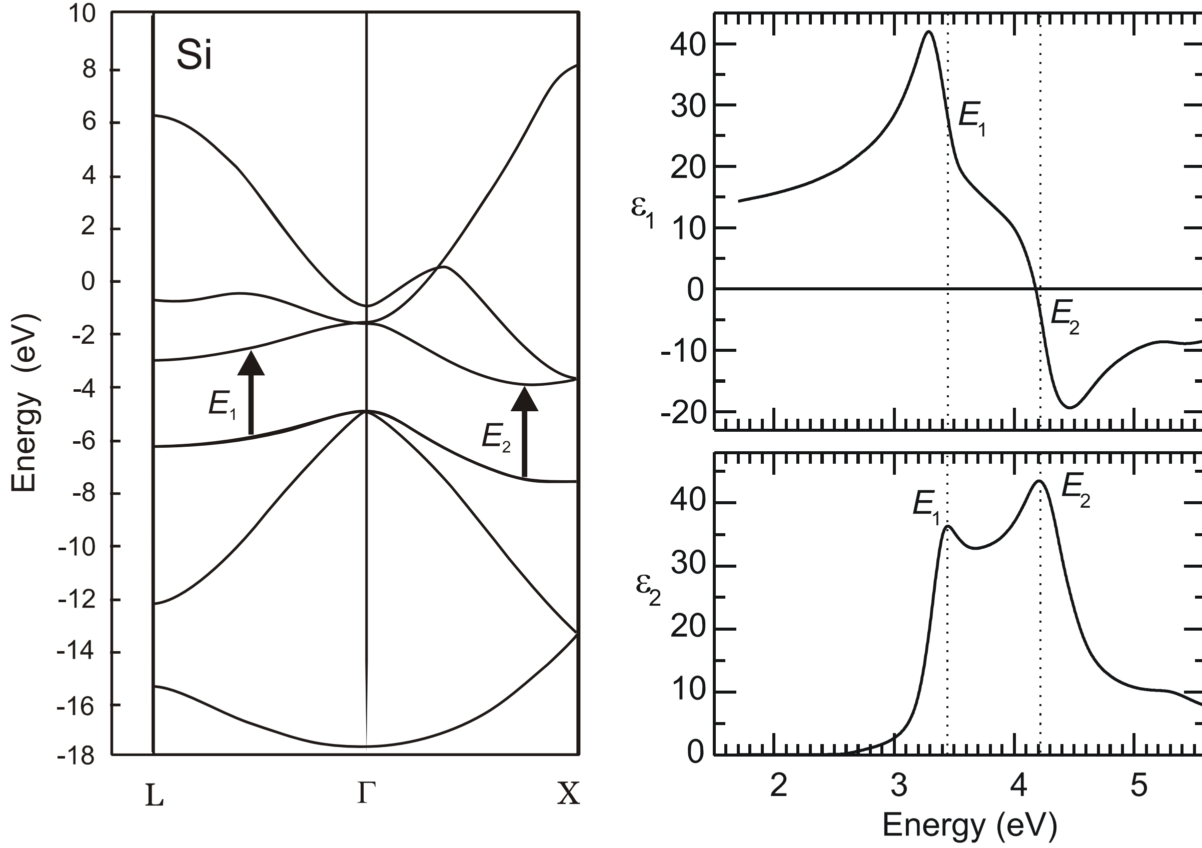

Figure 3.4: Electronic band structure and dielectric function of crystalline silicon (left and right hand side, respectively). The parallel valence and conduction bands lead to characteristic peaks in ε_2 at the van-Hove energies E_1 and E_2. Data are from [Kri86] and [Asp83].

with suitable $\vec{k}$-vectors [YuC99]:

$$D_j(E_{\text{cv}}) = \frac{1}{4\pi^3} \oint_{E_{\text{cv}}=const} \frac{\mathrm{d}S_{\vec{k}}}{\nabla_{\vec{k}}\left(E_{\text{c}}(\vec{k}) - E_{\text{v}}(\vec{k})\right)}. \tag{3.15}$$

Here, $E_{\text{v}}(\vec{k})$ and $E_{\text{c}}(\vec{k})$ are the valence and conduction band energies at a given $\vec{k}$, respectively.

Whenever $\nabla_{\vec{k}} E_{\text{c}}(\vec{k}) = \nabla_{\vec{k}} E_{\text{v}}(\vec{k})$, *i.e.* the conduction and the valence band run parallel over a significant area in $\vec{k}$-space, the denominator of Equation 3.15 vanishes and the joint density of states becomes singular. The so-called Van-Hove-singularities thus occur for parallel regions of the electronic bands as indicated by the arrows in the electronic band structure of silicon displayed in Figure 3.4.

Also the dielectric function can be expressed via the joint density of states by [YuC99]:

$$\varepsilon_2(\omega) = \frac{2\pi e^2}{m^*\omega} \int_0^{\hbar\omega} |P_{\text{cv}}|^2 \, D_j(E_{\text{cv}}) \mathrm{d}E_{\text{cv}}, \tag{3.16}$$

and the real part of the dielectric function is closely connected with ϵ_2 via the Kramers-Kronig-relation:

$$\varepsilon_1(\omega) = 1 + \frac{2}{\pi} \mathcal{P} \int_0^{\infty} \frac{\omega' \varepsilon_2(\omega')}{\omega'^2 - \omega^2} \mathrm{d}\omega'. \tag{3.17}$$

Here e and m^* are the electric charge constant and the effective mass, while $|P_{cv}|^2$ is the matrix element for the optical dipole transition.

Consequently, the Van-Hove-singularities lead to the occurrence of characteristic peaks in the imaginary part of the dielectric function of the material, whereas the real part shows inflection points at these energies. The peaks in ε_2 at the van Hove critical energies E_1 and E_2 are visible in the right hand side diagram in Figure 3.4. By their energy positions they can help to identify the chemical composition of a material and can act as a proof of the crystalline structure [Phi67, Asp83, Gju05]. In contrast, disordered solids lack sharp peak features in their optical spectra because of the absence of well-defined electronic bands [Asp84].

As to silicon as an indirect semiconductor the weak indirect transitions can be easily distinguished from the strong direct optical transitions at the Van-Hove-peaks. While the fundamental bandgap of silicon has been found to be effectively increased by quantum confinement of the electron wave function, *e.g.*, in luminescence measurements, no energy shift of the strong Van-Hove-transitions has been reported as yet. In *ab initio* calculations, Ramos and coworkers could show that the strong Van-Hove-transitions in the visible and UV part of the optical spectrum are not influenced by reduction of the size of silicon and germanium nanocrystals except for very small aggregates. In the case of germanium nanocrystals formed by 147 atoms ($L = 2\,\mathrm{nm}$), a significant shift of the characteristic E_1 transition from 2.3 eV to 3 eV was calculated [Ram05]. At these small sizes, the clusters exhibit already a zero-dimensional optical absorption spectrum consisting of discrete molecule-like transitions.

3.4.2 Free carrier absorption

In the case of a high doping concentration, the free carrier concentration in the material, N, provokes a shielding of external electromagnetic fields known as the plasma resonance. This phenomenon can be theoretically described as a dilute metal in the Drude theory. In doing so, the dielectric function changes to

$$\varepsilon(\omega, N) = \varepsilon_{\mathrm{intr}}(\omega) - \frac{\omega_{\mathrm{p}}^2(N)}{\omega(\omega + i\Gamma)}. \tag{3.18}$$

Here, $\varepsilon_{\mathrm{intr}}(\omega)$ is the dielectric function of the undoped material, while ω_{p}^2 and Γ are the plasma frequency and the carrier scattering rate defined by

$$\omega_{\mathrm{p}}^2(N) = \frac{Ne^2}{\varepsilon_0 m^*} \quad \text{and} \quad \Gamma = \frac{e}{\mu m^*}, \tag{3.19}$$

with the carrier mobility, μ, and the effective mass, m^*.

At low frequencies, the free carrier concentration leads to a characteristic increase of the absorption, which is not present in the undoped material. The quantitative amount of this absorption can be used as a non-contact measure to probe the carrier concentration and the carrier mobility in the material, and is thus a favorable method for the characterization of nanocrystals. In the low energy region the imaginary part of the dielectric function follows the relation

$$\varepsilon_2(\omega) = \frac{Ne^2}{\varepsilon_0 m^* \omega} \frac{\Gamma}{\omega^2 + \Gamma^2}. \tag{3.20}$$

This is the response of a Lorentzian harmonic oscillator around a resonant frequency of $\omega = 0$. The oscillator strength is given by the carrier concentration, whereas the damping is determined by the inverse of the carrier mobility and the effective mass.

3.4.3 Effective medium approaches

In the optical spectroscopy performed in the course of this work, the examined semiconductor nanocrystals are much smaller than the wavelength of the probing light. Moreover, layers of nanocrystals typically exhibit a large overall porosity. Therefore, effective medium theories need to be applied to model the effective dielectric function, ε_{eff}, of the system consisting of particles with their bulk dielectric function, ε, and that of the surrounding medium, ε_{M} (*e.g.* for air $\varepsilon_{\text{M}} \approx 1$). In this context, the effective porosity, p, is equivalent to the relative air volume fraction.

A very well-known formalism is given by the Clausius-Mossotti equation (also known as the Maxwell-Garnett or Lorentz-Lorenz approximation), which takes into account one sphere of dielectric material surrounded by air. This simple approach is not valid exactly and fails for small values of the overall porosity because it does not at all respect the microtopological situation in the medium.

A much better formalism which is quite often used to describe dispersed media is the Bruggemann effective medium approach [Bru35] given by

$$p\frac{\varepsilon_{\text{M}} - \varepsilon_{\text{eff}}}{\varepsilon_{\text{M}} + (d-1)\varepsilon_{\text{eff}}} + (1-p)\frac{\varepsilon - \varepsilon_{\text{eff}}}{\varepsilon + (d-1)\varepsilon_{\text{eff}}} = 0, \tag{3.21}$$

where d is the dimensionality of the problem. In a more general formulation, Bergmann separated the influence of the geometry from the dielectric functions of the constituents by the introduction of a geometrical spectral density function g. This function is a normalized distribution function taking into account the electrical interactions within the system and thus is strongly dependent on the porosity and the microstructure [Ber78]. The resulting Bergmann representation of the effective dielectric constant of a composite medium has the form:

$$\varepsilon_{\text{eff}} = \varepsilon_{\text{M}}\left(1 - (1-p)\int_0^1 \frac{g(n,p)}{\frac{\varepsilon_{\text{M}}}{\varepsilon_{\text{M}}-\varepsilon} - n}\text{d}n\right). \tag{3.22}$$

Here, n is the spectral coordinate for the integration. It can be shown that the here used geometrical density function, g, is also implicitly included in the Bruggemann Equation 3.21 where it is equivalent to a porosity threshold for the "percolation strength" $g_0 = g(0, p)$, which is the relevant parameter describing the electrical or thermal conductivity of the porous system [The97]. In the Bruggemann approximation, g_0 vanishes for a porosity larger than $\frac{2}{3}$, which is a reasonable value for solid or liquid mixture systems but may lead to errors in case of a different underlying percolation behavior (which, of course, is a direct consequence of the real microstructure). A more simple expression for ε_{eff} can be achieved by a suitable parametrization of Equation 3.22, which still enables good reproduction of the present microtopology [The97].

3.5 Doping of Silicon Nanocrystals

Doping, the controlled incorporation of impurity atoms onto substitutional lattice sites, is one of the most important techniques to control the conductivity of semiconductors. In crystalline

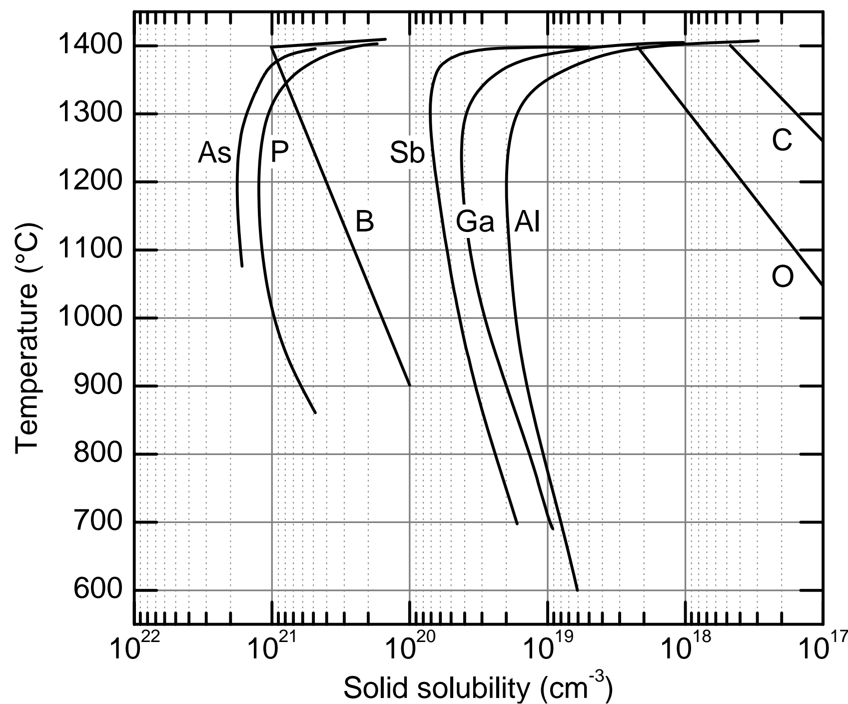

Figure 3.5: Solid solubilities of various impurity elements in crystalline silicon as a function of the temperature. A retrograde solubility is found for most impurity elements in silicon with a maximum solubility around 1200 °C. The data are taken from [Mad84].

silicon, the doping efficiency of shallow dopant atoms such as boron or phosphorus is fairly high and can be varied in a controlled way from one dopant atom in 10^8 silicon atoms up to the solid solubility of about 1 dopant atom in 100 silicon atoms. Nevertheless, the doping efficiency is found to strongly depend on the structural quality of the material and other effects. In nanocrystals, a large relative number of surface states is present and confinement effects can play a role, which imposes severe changes to basic dopant properties such as the dopant formation energy or the binding energy.

3.5.1 Bulk silicon dopant species and solubilities

In crystalline silicon, substitutionally incorporated boron and aluminum atoms act as shallow acceptors and contribute to free holes at room temperature with ionization energies of 45 meV and 72 meV, respectively. On the other hand, phosphorus, antimony, and arsenic are the most important shallow donors contributing to electron conduction at room temperature with ionization energies of 45 meV, 43 meV, and 54 meV, respectively [Sze07, Iof08]. For the dopant species examined in this study, boron and phosphorus, the solid solubility in crystalline silicon can amount to very high concentrations of up to 10^{21} cm^{-3} depending on the relevant process temperature, as is illustrated in Figure 3.5. During the growth of the silicon nanocrystals from the gas phase, temperatures exceeding 1000 °C are present, which makes successful doping up to degenerate doping concentrations appear feasible.

While at first sight the high doping concentrations seem to be irrelevant for semiconducting applications, in the case of semiconductor nanocrystals, the situation is quite different. A quite

simple geometrical constraint holds for semiconductor nanocrystals if they are very small. The diameter of a spherical nanocrystal formed by a number of m atoms is $L = (3m/4\pi)^{1/3}a$, with the lattice constant of crystalline silicon, $a = 0.543$ nm. Thus, the effective doping concentration by single dopant atoms in each individual nanocrystal is $N = 3/4\pi\,(a/L)^3\rho_{\mathrm{at}}$ if the crystallite size is $L = 4$ nm. Here, $\rho_{\mathrm{at}} = 8a^{-3}$ is the atomic density of silicon. The result of this estimation is a value of $3 \times 10^{19}\,\mathrm{cm}^{-3}$, which corresponds to an already fairly large bulk doping concentration.

As a comparison with Figure 3.5 shows, this doping concentration already exceeds the maximum aluminum solubility attainable in bulk silicon. If the bulk solubility limit holds also for silicon nanocrystals, doping with single aluminum acceptors becomes impossible for diameters below 4.6 nm. Similar critical sizes can be defined for gallium and antimony by 3.6 nm and 3.0 nm, respectively. Boron and phosphorus, however, due their high solid solubility can in principle be used to realize silicon nanocrystal ensembles doped with single impurity atoms down to a crystal size of about 1.2 nm. In more accurate considerations, the microscopic situation needs to be taken into account influencing not only the incorporation probability of dopant atoms but also their electrical activity.

3.5.2 Formation energy and self-purification

With decreasing crystalline quality, *i.e.* increasing disorder of the lattice or reduced crystal dimensions, the dopant solubility may vary significantly. For example, the proximity of the surface or internal grain boundary interfaces may enable the segregation of incorporated dopants by out-diffusion to these regions. In very small crystallites, even the formation of dopants during growth can be suppressed for energy reasons. This finite-size effect of the nanocrystals has been entitled "self-purification" and has been calculated, *e.g.*, for the situation of Mn dopants in CdSe nanocrystals [Dal06]. Here, the formation energy for substitutional impurities is found to increase with decreasing crystal diameter, which is claimed to be an intrinsic property of semiconductor nanocrystals. Experimentally, Erwin and coworkers found that the incorporation efficiency in II-VI group nanocrystals to be a strong function of the surface facets accessible during solution-phase growth. Only by the deliberate control of the growing facets manganese doping of CdSe quantum dots was achieved [Erw05]. However, this doping concept cannot be transferred to silicon, which as a non-polar covalent semiconductor will show much less energy anisotropy for impurity surface adsorption during growth.

Cantele and coworkers calculated the neutral impurity formation energies for substitutional boron and phosphorus in silicon nanocrystals in *ab initio* plane wave density functional theory using pseudopotentials. An increase of the formation energy by about 0.5 eV with respect to the bulk values was found for both boron- and phosphorus-doped 2 nm diameter silicon nanocrystals, and the formation energy is observed to increase linearly with the inverse nanocrystal diameter [Can05]. With decreasing crystal size thus the stability of the impurity inside the nanocrystal is strongly reduced. The possibility of structural relaxation was observed to effectively decrease the formation energy for boron impurities positioned in the vicinity of the nanocrystal surface. This is an indication that the dopants energetically prefer to occupy such sub-surface layer positions. Consequently, they most likely will not contribute to shallow dopant levels, but their electrical activity on these lattice states was not analyzed in this study, however.

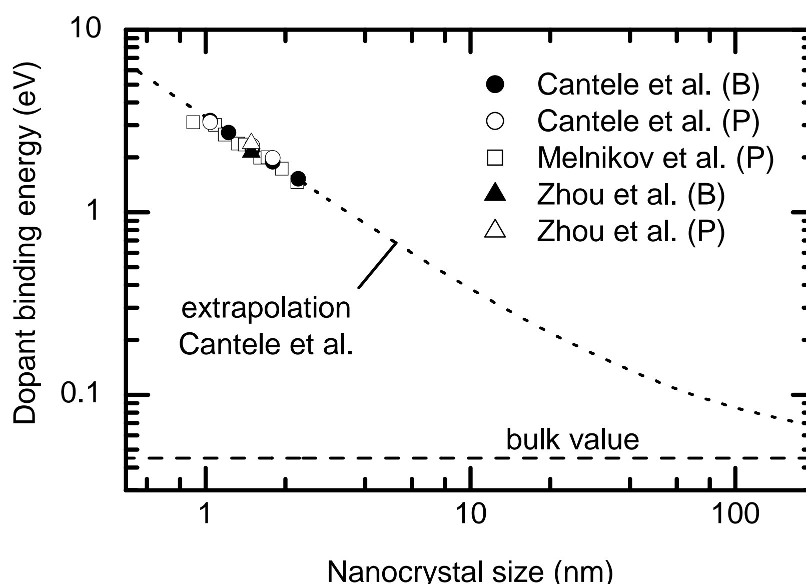

Figure 3.6: Donor and acceptor binding energies for boron- and phosphorus-doped silicon nanocrystals calculated from density functional theory by various groups as a function of the nanocrystal diameter [Can05, Mel04a, Zho07]. The dotted line is an extrapolation to the bulk value from [Can05].

If the incorporation of dopant impurities into the lattice is energetically unfavorable, especially at high growth or processing temperatures the segregation of the dopants will be observed. For the case of silicon nanowires, *i.e.* prolate silicon nanostructures with confinement in two spatial dimensions, Fernandez-Serra calculated the segregational behavior of boron and phosphorus dopants by density functional theory [Fer06a]. For silicon nanowires with diameters of 1.1 nm, 1.6 nm, and 3.0 nm and for different surface terminations, they found that both impurity species are likely to segregate to electrically inactive sites at the nanowire surface, with a higher segregation energy for phosphorus (-1 eV, compared to -0.1 eV for the case of boron). If a surface dangling bond was additionally included in the model the tendency to segregate was further promoted, changing the segregation energies to -1.6 eV and -1 eV for phosphorus and boron, respectively. These results lead to the assumption that also in silicon nanocrystals a large concentration of the dopants will be incorporated at electrically inactive surface sites.

3.5.3 Binding energy or activation energy

The binding or activation energy, E_{A}, necessary to ionize boron and phosphorus dopants in silicon nanocrystals was calculated by Cantele *et al.* [Can05]. A linear correlation with the inverse nanocluster diameter in a range of 0.5 nm to 2.3 nm was obtained, which extrapolates to the bulk values for both impurity species: $E_{\mathrm{A}} = 51\,\mathrm{meV} + 3260\,\mathrm{meV} \cdot (L/\,\mathrm{nm})^{-1}$. In the opinion of the authors, the high values of the activation energy of about 1.5 eV for 2.3 nm nanocrystals can explain the low electrical activity of even high dopant concentrations in etched porous silicon samples [Can05]. For silicon nanocrystals of this particular size, also the fundamental bandgap has increased significantly and amounts already to 4.3 eV according to Equation 3.2.

In a similar first-principles approach based on hybrid density functional theory with complete geometrical optimization, Zhou and coworkers determined the energy levels of several dopants comprising boron, aluminum, gallium, and indium acceptors and nitrogen, phosphorus, arsenic,

and antimony donor impurity atoms situated at the central site in the nanocluster $Si_{86}H_{76}$ (1.49 nm). They also obtain acceptor and donor binding energies, which exceed the bulk silicon values by far (2.13 eV and 2.38 eV for boron and phosphorus, respectively), in good agreement with the results of Cantele *et al*. [Zho07]. The chemical trends observed for different impurity species are found to be in agreement with their electronegativity as a further consistency check of the results. The values reported by both groups are visualized in Figure 3.6 together with those obtained by Melnikov and Chelikovsky in real-space *ab initio* pseudopotential calculations within the local-density approximation. In the figure, the symbol shape identifies the respective research group (see legend), whereas open and full symbols denote phosphorus and boron data, respectively. The binding energies of both impurity species align quite well, which also is the case in bulk silicon (45 meV).

Unfortunately, due to the vast computational effort connected with large numbers of atoms involved, no theoretical data are available for nanocrystal sizes exceeding 2.5 nm as yet. Especially in the experimentally accessible size range of $2-20$ nm, the extrapolation by Cantele *et al*. from the calculated results to the bulk value (dotted and dashed lines in Figure 3.6, respectively) does not appear to be a reliable assumption. In any case, the high activation energies necessary for carrier generation will lead to severe problems for nanocrystals in electronic applications and also for conventional semiconductor technology approaching the 16 nm production node by the year 2018.

3.6 Electrical Transport in Nanocrystal Layers

The electrical properties of layers consisting of semiconductor nanocrystals will be influenced by a combination of various physical effects. Percolation and discrete size effects will dominate the macroscopic transport while quantum size effects can be present within the individual nanocrystals. Defects in the particle layers can provoke a space-charge limited current behavior, can compensate dopants, and impose barriers on the macroscopic transport. All these potential contributions will be shortly highlighted in the following subsections.

3.6.1 Percolation transport

The macroscopic transport properties of systems consisting of a large number of semiconductor nanocrystals depend on the degree of material filling. Especially if the nanocrystals are suspended in a matrix material that itself does not contribute to electronic transport, a nanocrystal density exceeding the percolation threshold density is required to obtain macroscopic conductivity. From percolation theory, the probability that macroscopic clusters of interconnected nanocrystals exist within the matrix can be derived [Sch00].

Balberg and coworkers studied the conductivity of silicon nanocrystals embedded in a silicon oxide matrix as a function of the silicon nanocrystal concentration [Bal07]. They observed a significant increase in the conductivity of the samples at silicon contents of $25-40\%$, which can be identified with the percolation threshold in the dilute nanocrystal system. In fact, in three dimensions, a percolation threshold is expected at a critical volume fraction around 16% (corresponding to site occupation probabilities of $20-31\%$) considering the results for the partial

occupation of free space modeled on a three dimensional hexagonal close packed lattice, a face- and a bond-centered cubic, and a simple cubic lattice [Lor98, Sch70].

In such a system, the conductivity will exhibit a sudden increase and, above the percolation threshold, will follow a critical exponent behavior $\sigma_{\text{eff}} \propto (\rho - \rho_c)^t$, where σ_{eff}, ρ, and ρ_c denote the effective conductivity, the volume fraction, and the threshold volume fraction, respectively. The critical exponent, t, was observed by Balberg *et al.* to exhibit a value of 2.0 in the silicon particle network, quite close to the theoretically expected value of 1.89 for the three-dimensional situation [Sar85, Sch00].

Interestingly, the percolation is connected with the optical properties via the Bergmann representation $\sigma_{\text{eff}} = g_0(1-p)\sigma$, where $p = 1 - \rho$ and σ are the porosity and the bulk conductivity, respectively. In this formalism, the critical power law is implicitly included in the spectral function $g_0(p) = g(0, p)$ of Equation 3.22 [The97].

If the nanocrystals are deposited onto a substrate directly from the gas phase or from a solid dispersion, a self-supporting structure with percolation will be obtained, naturally. However, the individual properties at the interfaces of attaching crystals may differ strongly, *e.g.*, the thickness of the native oxide, or the doping situation. In such cases, additional percolation mechanisms can be applied to model the effective lateral conductivity.

3.6.2 Discreteness of dopants and defects

Given the situation that the incorporation of dopants into nanocrystals was achieved and also the thermal activation of a certain fraction is obtained, still the discrete nature of the individual nanocrystals imposes limits on the overall conductivity. If only those particles contribute to the conductivity, which are effectively doped, within the structurally percolating nanocrystal layer an additional electrical percolation process is superimposed.

With N being the overall doping concentration, each individual atom out of the m atoms in a nanocrystal with size L is a dopant atom with the probability $\zeta = N/\rho_{\text{at}}$. Consequently, the probability that a nanocrystal contains at least one dopant atom is given by $\vartheta = 1 - (1 - \zeta)^m$. As a criterion that a percolation path of conductive nanocrystals has formed throughout the nanocrystal layer, ϑ has to amount to about 0.3 for three-dimensional percolation. However, due to the already perforated structure of the structural percolation paths, the problem can as well exhibit a lower fractional dimensionality with the critical value of ϑ thus increasing up to the typical two-dimensional percolation threshold around 0.4 [Sch00].

It is easy to see that under these assumptions the macroscopic conductivity of a layer of nanocrystals will exhibit a strong size dependence. As ζ is typically smaller than 10^{-2}, the approximation $\vartheta \simeq m\zeta$ is valid. Thus

$$\vartheta \simeq \frac{\pi}{6} L^3 N. \tag{3.23}$$

Figure 3.7 shows the result of calculations showing the doping concentration necessary to achieve a fixed value of ϑ as a function of the nanocrystal size for $\vartheta = 0.1 - 1.0$. As a consequence of the third power dependency, it makes a large difference, whether the nanocrystal size is 2, 6, or 10 nm.

If, moreover, the electrical inactivity of dopant atoms situated at the surface of the nanocrystals is considered, the curves in the figure will effectively shift to larger nanocrystal sizes, and for

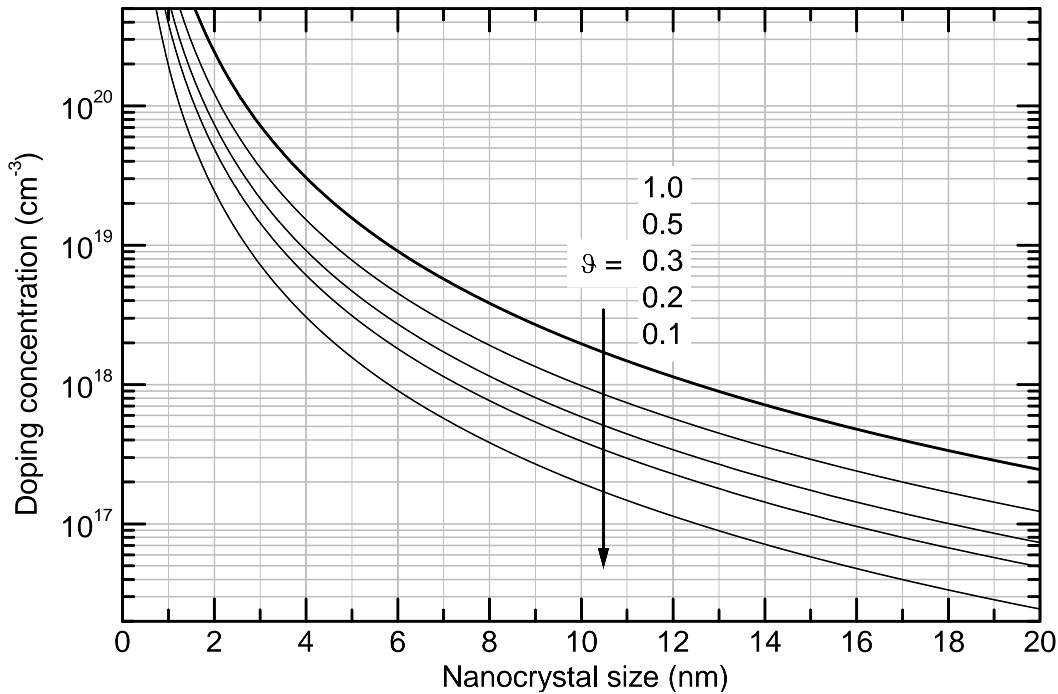

Figure 3.7: Correlation between nanocrystal size and doping concentration for fixed values of the probability that a given particle contains one dopant atom, $\vartheta = 0.1, 0.2, 0.3, 0.5$, and 1.0.

a given crystal size, a higher total doping concentration is required to obtain a sufficient value for ϑ. Also, the additional compensation of a fraction of the dopants by deep defects in the nanocrystals will provoke the same effect.

3.6.3 Coulomb blockade

Due to the small capacitance of silicon nanocrystals, the charging energy of single electrons or holes can become a decisive quantity for the lateral transport. This so-called Coulomb blockade is usually observable only in elaborate geometries at cryogenic temperatures. However, in all dielectrically confined systems, the Coulomb energy can contribute significantly to the discrete energy states of nanocrystals.

The coupling of resonant energy states in neighboring quantum dots can be made visible in Coulomb oscillations. By controlled charging via external gates, the current transmission of electrons through few nanocrystals in close proximity can be characteristically influenced [Kha04]. The so-called "Coulomb diamond" pattern emerging if the differential conductivity is contour-plotted versus the two gate voltages shows discrete regions of occupation by a constant number of carriers in the system of two or more coupled nanocrystals.

Balberg and coworkers detected single electron effects in room temperature conductivity measurements in macroscopic ensembles of oxide embedded silicon nanocrystals in the vicinity of the percolation threshold. Under these conditions, single nanocrystals can dominate the effective conductivity through macroscopic samples enabling the observation of single electron effects as characteristic steps in the total current [Bal07]. The high energy barriers between the silicon nanocrystals and the oxide matrix allow this effect to persist even at room temperature [Kha04].

3.6.4 Space charge limited current, tunneling and hopping transport

In systems with low bulk conductivity values, such as oxides or amorphous semiconductors, the phenomenon of space charge limited current transport is commonly observed. For the example of hole transport, it can be deduced from the existence of a distribution of trap states, which extends into the forbidden bandgap from the valence band edge decreasing exponentially as

$$dn_\mathrm{t}/dE = N_\mathrm{t}/E_\mathrm{t} \exp(-E/E_\mathrm{t}). \tag{3.24}$$

Here, dn_t/dE, E, N_t, and E_t are the trap density of states, the energy, the total trap density and a characteristic trap energy, respectively. This situation can be identified with band tail states as known for many disordered semiconductors. It can be shown [Bur97, Raf05] that the current density, j, in this case follows the applied voltage, V, in a non-linear way described by

$$j = aV + bV^l. \tag{3.25}$$

Obviously, the first term which is linear in V will produce an Ohmic behavior at low electric fields, whereas the second term leads to the characteristic power law dominant at high electric fields. The exponent l is larger than 2 owing to the shape of the energy distribution of trap states. If a narrow distribution is present in the material, even higher values of l are obtained [Raf05]. A similar field dependence of the current density can also be explained by Fowler-Nordheim-tunneling ($j \propto V^2 \exp(-b/V)$, [Sze07]). However, this concept assumes the field ionization of trapped carriers in a classical approach and does not yield useful information on the properties of the nanocrystal ensemble.

In 300 nm thick layers consisting of gas phase grown silicon nanocrystals with a diameter of 8 nm, Rafiq *et al.* found space charge limited current flow to be the dominant hole conduction mechanism in the temperature range from 200 K−300 K [Raf05]. The corresponding exponential distribution of trapping states exhibited a characteristic trap energy of 140 meV below the valence band edge. The total deep trap concentration was $2.3 \times 10^{17}\,\mathrm{cm}^{-3}$, which is of the same order of magnitude as the volume density of nanocrystals.

Burr and coworkers measured the electrical characteristics of silicon nanocrystal films deposited by laser ablation. The reported current-voltage characteristics can both be explained by space charge limited current transport as well as by tunneling processes on percolation paths through the network [Bur97]. At low temperatures, Rafiq *et al.* found a change in the conduction behavior towards nearest neighbor hopping processes in the electrical transport with the same set of samples that exhibited space charge limited current around room temperature [Raf06]. In this temperature regime, the temperature dependence of the conductivity follows

$$\sigma \propto \exp\left[-\left(\frac{T_0}{T}\right)^{0.5}\right] \tag{3.26}$$

which is characteristic for both so-called Efros-Shklovskii variable range hopping as also for a combined percolation and hopping transport via nearest neighbor tunneling as demonstrated by Šimánek [Sim81]. Since nearest neighbor tunneling processes of thermally activated carriers are closer to the real situation in the nanocrystal ensemble, the latter explanation has been favored [Raf06].

Following from the literature, the transport behavior of silicon nanocrystal ensembles seems to vary strongly with the concerned research groups, as if it was strongly dependent on the actual

processing conditions [Raf05, Bur97, Bal07, Kha04, Raf06]. Furthermore, the temperature dependence of the conductivity for itself is ambiguous, as already pointed out above, and it can have different origins, which leaves the correct microscopic situation unclear. Balberg and coworkers criticize that many authors in their studies do not define, *e.g.*, the hopping sites, the energy levels, and the origin of the carriers involved in the hopping. By supplementing their conductivity data with additional photoconductivity measurements showing the same percolation characteristics, they can prove that the carriers originate from the nanocrystals [Bal07]. They argue that by a combination of the basic physical transport processes, *i.e.*, inter-particle tunneling and Coulomb blockade, the physical situation can be sufficiently described in a qualitative manner. To better describe the experimental findings, a lot more effort needs to be invested than is possible at the moment to theoretically simulate the combined electrical properties of silicon nanocrystals.

3.6.5 Grain Boundaries and Defects

If the silicon valence and conduction bands are envisioned to originate from the overlapping molecular bonding and anti-bonding combinations of sp^3-orbitals, it is no wonder that unsaturated silicon bonds give rise to energy states in the middle of the bandgap. These "dangling bonds" are singly occupied sp^3-orbitals when they are electrically neutral (db^0), but their charge state can be altered by the capture of an additional electron or hole (db^-, db^+). Thus, they represent amphoteric deep defect states, which represent efficient recombination centers and, *e.g.*, reduce the lifetime of minority carriers vastly.

While the majority of dangling bonds at silicon surfaces can be efficiently passivated, *e.g.*, by thermal oxidation, still a defect concentration of typically $10^{12}\,\text{cm}^{-2}$ remains at the internal silicon-SiO_2 interface [Joh83]. Also silicon nanowires and silicon nanocrystals covered with a native oxide surface layer exhibit a comparable value [Bau05]. Moreover, grain boundaries in polycrystalline silicon are characterized by internal defect concentrations of the same order of magnitude [Set75].

Due to their tendency to trap free carriers, the presence of these defects significantly influences the electrical properties of silicon in the vicinity of internal interfaces and of the surface. Especially in the case of silicon nanocrystals, the pertinent effects completely alter the material properties. Starting from the conditions at single grain boundaries we will thus examine the impact of dangling bond defects on silicon nanocrystal layers in the following.

Among the many studies in the literature considering the effects of grain boundary effects in silicon and germanium, two main groups may be discerned. While the first group of publications both theoretically as well as experimentally examined single grain boundary effects [Tay52, Pik79, Sea79], the second focuses on the consequences for electronic transport in polycrystalline material with crystal sizes as small as 20 nm [Kam71, Set75, Bac78].

The basic assumptions of both groups are very similar. These are illustrated in Figure 3.8 a) as a one-dimensional cross section through a polycrystalline semiconductor film. The typical length of the crystalline grains is assumed to be the constant L. At the boundaries between neighboring grains, a constant areal defect density, Q_t, is supposed, which is capable of trapping of up to the same amount of majority carriers per unit area at the interfaces [Tay52, Kam71]. And for simplicity, all defects are assumed to reside at an energy level, E_t, corresponding to a delta-like density of states [Set75].

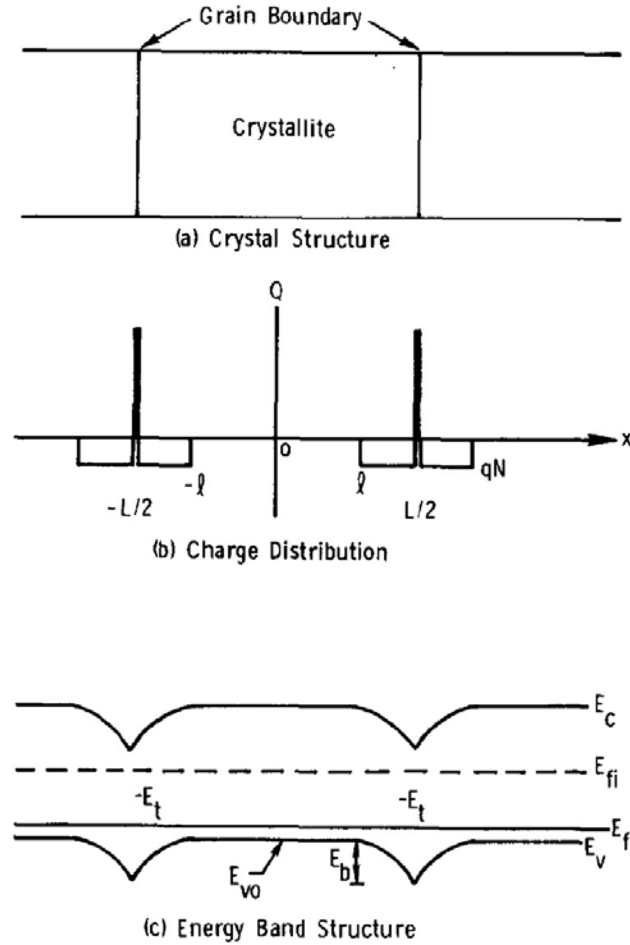

Figure 3.8: Schematic drawing of the spatial arrangement of a polycrystalline film in a cross-sectional view in (a), (b) one-dimensional charge distribution in the film after trapping of majority carriers, and (c) resulting band structure with energetic barriers around the grain boundary regions (from [Set75]).

From this situation, Seto derived the resulting carrier concentration within the grains, the height of the potential barriers at the grain boundaries, and the mobility of the carriers, μ, as a function of the doping concentration, N, assuming full ionization of the dopant atoms. In the following, two cases can be distinguished: (i) if the number of dopants inside the grains, LN, is smaller than the available number of trap states, Q_t, the crystals will be fully depleted, whereas (ii) only partial depletion will result if $LN > Q_t$, as is illustrated by Figure 3.8 b) and c). While the space charge region, W, will span over the full crystal in the first case, in the latter, charge neutrality leads to the condition that $W = Q_t/N$.

From the Poisson equation, the height of the energy barrier (with respect to the valence band in the case of acceptor doping) can be readily given as

$$\text{(i)} \quad E_B = \frac{e^2 L^2 N}{8\varepsilon_0 \varepsilon_r}, \qquad \text{(ii)} \quad E_B = \frac{e^2 Q_t^2}{8\varepsilon_0 \varepsilon_r N}, \tag{3.27}$$

where e, ε_0, and ε_r are the elementary charge, the vacuum permittivity and the dielectric constant of the material, respectively. As these equations show, the energy barrier grows linearly with the doping concentration in case (i), whereas a decay with $1/N$ is present for (ii). A maximum value

of $E_\mathrm{B} = e^2 L Q_\mathrm{t}/8\varepsilon_0\varepsilon_\mathrm{r}$ occurs at the critical doping concentration, $N = Q_\mathrm{t}/L$, when all traps are charged and the crystalline grains are fully depleted of carriers.

The electrical transport through the polycrystalline films is dominated by thermionic emission over these potential barriers. Potential contributions to the current by tunneling can be neglected in the above outlined situation, because the space charge regions are small enough only if the energy barriers are shallow, anyway. Consequently, the thermionic emission current over the grain boundary barriers will be the dominant current contribution, and the effective mobility in the films in small electric fields can be derived [Set75]:

$$\mu_\mathrm{eff} = \frac{eL}{\sqrt{2\pi m^* k_\mathrm{B} T}} \exp\left(-\frac{E_\mathrm{B}}{k_\mathrm{B} T}\right). \tag{3.28}$$

Accordingly, the mobility in the region of the critical doping concentration, where E_B is large, will exhibit a pronounced minimum, whereas at very small or at very large doping concentrations, where E_B is small, the intrinsic mobility of the bulk material can become apparent.

The electrical conductivity can be obtained by deriving appropriate expressions for the effective hole concentrations and can be written (i) for the sub-critical and (ii) for the over-critical doping conditions as:

$$\text{(i)}\quad \sigma \propto \exp\left[-(E_\mathrm{t} - E_\mathrm{v}^0)/k_\mathrm{B} T\right], \qquad \text{(ii)}\quad \sigma \propto T^{-1/2} \exp\left[-E_\mathrm{B}/k_\mathrm{B} T\right], \tag{3.29}$$

with E_v^0 being the energy of the valence band edge in the center of the crystal grains [Bac78, Ort80].

As the Equations 3.29 (i) and (ii) illustrate, temperature dependent conductivity measurements can help to identify the respective doping situation. While a rather large constant activation energy closely connected to the energy level of the trap states, E_t, characterizes $\sigma(T)$ in the region of $LN < Q_\mathrm{t}$, the barrier energy, E_B, can be extracted from the data in the highly doped region. However, E_B can only be evaluated as long as it is larger than the thermal energy of the carriers ($E_\mathrm{B} > k_\mathrm{B} T$). At very high doping concentrations, $E_\mathrm{B} \approx k_\mathrm{B} T$, and the Equations 3.28 and 3.29 are not valid any longer [Set75].

By applying this model to polycrystalline silicon, broad qualitative and quantitative agreement was found with experimental results, not only regarding the correlation of the carrier concentration and the mobility with the doping concentration, but also the position of the critical doping concentration [Set75, Kam71, Bac78]. Combining typical values of the interface defect concentration of $3 - 4 \times 10^{12}\,\mathrm{cm}^{-2}$ with the grain sizes determined from crystallographic methods, the mobility minimum at $N = Q_\mathrm{t}/L$ could be perfectly reproduced. Apart from silicon, a large variety of polycrystalline material systems was found to behave comparably, comprising Ge, CdS, CdSe, InSb, InP, $CuInS_2$, and PbS with crystallite sizes ranging from 20 nm to 8 μm [Ort80].

As a modification of the above described model, Baccarani and coworkers examined the consequences of different trap density distributions [Bac78]. In their study, they found that a delta-function describes the density of trap states in polycrystalline silicon best, and that a continuous energy distribution of defects all over the bandgap in contrast does not lead to satisfactory agreement with the measurements.

The grain boundary barrier theory has the problem that it is just a one-dimensional consideration of the physical situation. However, in large-grained material where the grain size exceeds the film thickness, the surface and the substrate interface states are mainly responsible for the depletion

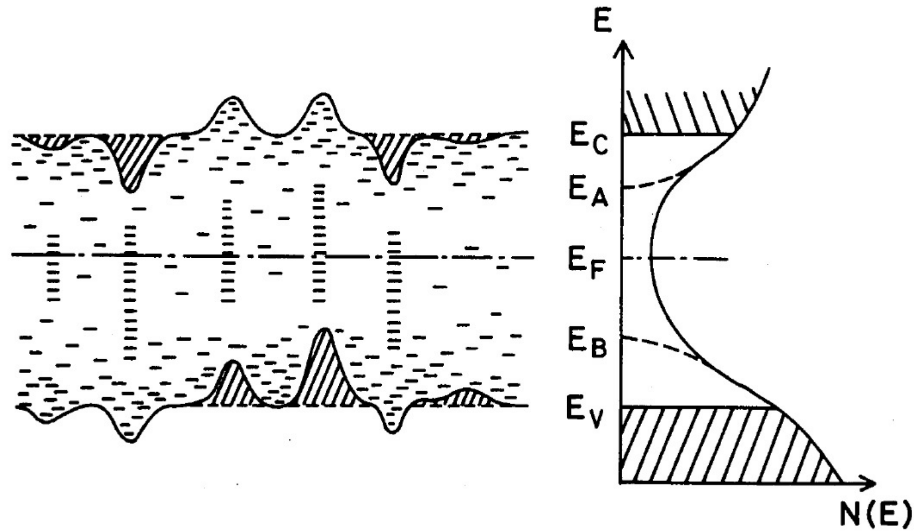

Figure 3.9: Illustration of the potential fluctuations present in defect-rich polycrystalline silicon. The correspondent density of states is illustrated at the right hand side (from [Tan80]).

of the film, leading to an effective reduction of the active layer thickness [Gju07]. On the other hand, in very small-grained material, the one-dimensional treatment is not valid and a three-dimensional approach is necessary. Moreover, in this case few defects are distributed over the spherical surfaces of crystallites and the illustrative picture of band bending is not applicable any longer.

3.6.6 Potential fluctuations

An alternative picture of the physics of polycrystalline silicon has been discussed, *e.g.*, by Taniguchi and coworkers [Tan80]. Instead of well-defined potential barriers at localized boundaries in the material, charged regions distributed throughout the material can lead to an effective fluctuation potential. Especially in small-grained material an almost homogeneous distribution of trapping centers evokes an effective potential landscape with long-range fluctuations that influences the carrier mobility and the conductivity. Figure 3.9 illustrates these spatial variations of the potential energy. In the corresponding density of states, which is displayed in the right hand side of the figure, a mobility edge separates the effectively localized electronic states from the extended transport states visualized by the shaded region).

At temperatures below 200 K, a more weakly activated conduction mechanism becomes dominant that can be identified with tunneling transport of states below the mobility edge. A similar model is also known for the situation in amorphous semiconductors, which has emerged successful to describe the electrical properties of hydrogenated amorphous silicon [Fri71].

To quantify the amount of the potential fluctuations, the so-called Q-function can be defined, which follows from the conductivity, σ, and the Seebeck coefficient, S, of the material. For a non-degenerately p-doped semiconductor the latter two can be written as

$$\sigma(T) = \sigma_0 \exp\left[-\frac{E_\mathrm{F} - E_\mathrm{v}}{k_\mathrm{B}T}\right] \qquad \text{and} \qquad \frac{e}{k_\mathrm{B}} S(T) = \frac{E_\mathrm{F} - E_\mathrm{v}}{k_\mathrm{B}T} + A(T), \tag{3.30}$$

where E_v is the energy position of the valence band maximum, while $A(T)$ is a scattering factor, sometimes also referred to as the heat of transport coefficient [Bey79]. A is obtained from extrapolating $S(T)$ in the limit $1/T \to 0$. By combining σ and S as follows:

$$Q = \ln\left[\frac{\sigma}{\Omega^{-1}\,\mathrm{cm}^{-1}}\right] + \frac{e}{k_\mathrm{B}}\,|S|\,, \tag{3.31}$$

a quantity is obtained that is independent of the Fermi level position and can be used to characterize the transport paths through the material [Bey79]. This becomes evident by inserting Equations 3.30 in Equation 3.31:

$$Q = \ln\left[\frac{\sigma_0}{\Omega^{-1}\,\mathrm{cm}^{-1}}\right] + A(T). \tag{3.32}$$

From the thermal activation energy of Q, the potential fluctuations can be estimated [Ove81, Bra98, Ruf99].

Indeed, the interpretation by potential fluctuations can reproduce well, *e.g.*, the electrical data of hydrogenated microcrystalline silicon from plasma-enhanced chemical vapor deposition [Ruf99]. In this nanocrystalline semiconductor material with typical crystallite sizes of 10 nm, the electrical and thermoelectric properties could not adequately be described by the sole grain boundary barrier interpretation.

4 Properties of Silicon Nanoparticle Layers

Before the silicon nanocrystals and nanoparticles, which have been produced in the hot wall and microwave plasma reactor systems can be used in electronic applications, the material properties need to be characterized. We thus want to examine the structural, chemical, optical, and electrical properties of the silicon nanoparticles and layers thereof. The material properties will be discussed regarding potential applications and will be compared with other state-of-the-art material classes.

4.1 Structural Properties

4.1.1 Morphology

In this subsection, the morphological properties of material from different reactor systems will be classified. It will become clear, why material grown in microwave reactors can be perfectly described by the term nanocrystals whereas for the hot wall reactor grown silicon the term "silicon nanoparticles" will be used in the following due to its high degree of non-uniformity and completely different morphological properties.

Hot wall reactor silicon nanoparticles

The microscopic morphology of silicon nanoparticles grown in the hot wall reactor system is highly characteristic. These particles exhibit an elongated and branched structure and often consist of several randomly oriented arms or side-chains. The transmission electron micrograph in Figure 4.1 illuminates that the primary structure of a typical particle extending over 800 nm is made up of a substructure consisting of rather spherical components with typical dimensions of about $50 - 100$ nm. It seems that during the growth process in the hot wall reactor, primary particles of this size have formed in the reactor and have sintered together at the elevated temperatures giving rise to the large branched structures visible in the figure. Moreover, the electron diffraction pattern in the inset demonstrates that also the side arm regions represent polycrystalline material consisting of several crystalline domains with different orientations. It can thus be concluded that the primary silicon nuclei within the individual subgrains have a typical size of $20 - 50$ nm.

As the figure shows, the sintering necks in between neighboring primary structures have almost reached the width of the primary particles. It can thus be concluded that the reordering processes during the in-flight sintering have produced very stable structural configurations. This assumption will be confirmed by the observations during the dispersion method via ball-milling, which preserves the structure of these "hard agglomerates".

The large structure sizes which can be present for hot wall silicon nanoparticles will also have an impact on the properties of silicon nanoparticle layers fabricated from liquid dispersions of the

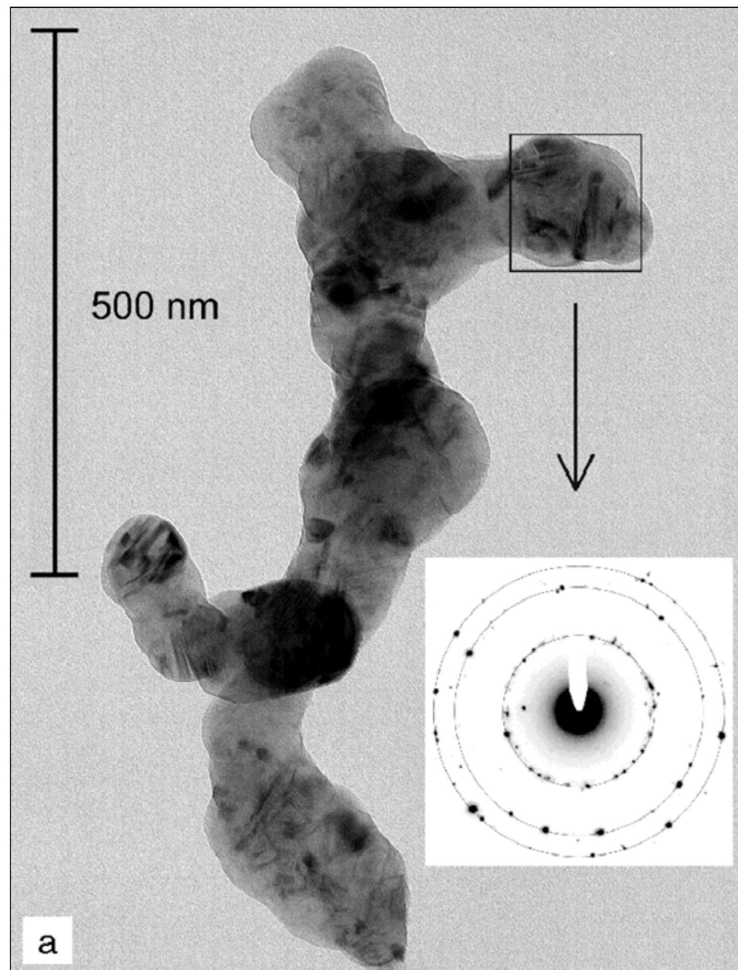

Figure 4.1: Transmission electron micrograph of a HWR silicon nanoparticle. The inset shows the electron diffraction pattern of the indicated region [Wig01].

material, which will be outlined below. The large amount of internal interfaces in between sintered silicon nuclei will have consequences on the defect properties of hot wall silicon nanoparticles as will be discussed in Section 4.1.4.

Microwave reactor silicon nanocrystals

In contrast, a completely different sample morphology is present for silicon nanocrystals grown in the microwave reactor systems. As Figure 4.2 demonstrates, these exhibit a clearly spherical shape and consist of only one crystalline domain, thus being real single nanocrystals. The TEM micrograph shows the crystalline interference fringes from the lattice planes in the nanocrystalline volume, but also an outer shell showing no signs of crystalline order is evident. This shell is considered as the surface oxide (consisting of silicon suboxide, SiO_x, with $1 < x \leq 2$), which is usually present on samples that have been subject to oxidation at ambient atmosphere, such as the shown samples, which were prepared for the TEM measurements under room conditions. The natural oxide shell is typically 1 nm in thickness and serves as a passivation layer for further oxidation of the silicon nanocrystals similar to the case of bulk crystalline silicon surfaces. When oxidized at high temperatures, the oxide thickness can increase to significantly thicker

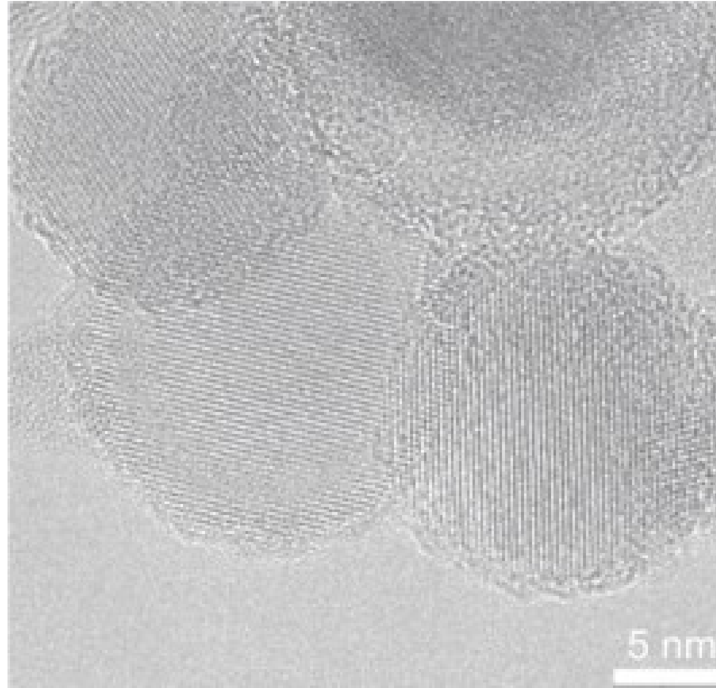

Figure 4.2: High resolution transmission electron micrograph of MWR silicon nanocrystals. Except for a thin surface oxide layer around the crystals, no disordered phases are visible, and large single crystalline domains are evident from the interference fringes (Taken from [Kni04]).

sizes while also in this case a self-limiting saturation occurs due to strain caused by the outer oxide layer [Cof05].

The size distribution of the microwave reactor silicon nanocrystals follows a log-normal distribution function, which represents a scale-independent Gaussian normal distribution. This type of size dispersion is typical for continuous growth processes where the nucleation and the growth of the nanoparticles are independent processes and where the mean particle size is determined by the average persistence time in the reactor only [Gra76]. However, also for segregational growth of silicon nanocrystals in a suboxide matrix, this size distribution is commonly observed.

The log-normal distribution function, f_{LN}, is obtained by exchanging the linear size axis, x, of a standard normal distribution by its natural logarithm, $\ln x$:

$$f_{\mathrm{LN}}(x,\sigma) = \frac{1}{(2\pi)^{\frac{1}{2}} \ln\sigma} \exp\left(-\frac{(\ln x - \overline{\ln x})^2}{2\ln^2\sigma}\right). \tag{4.1}$$

Here, $\overline{\ln x}$ and σ are the statistical median or mean value of the distribution and the geometric standard deviation, respectively, which are defined by

$$\overline{\ln x} = \frac{\sum_i n_i \ln x_i}{\sum_i n_i}, \quad \text{and} \quad \ln\sigma = \left(\frac{\sum_i n_i (\ln x_i - \overline{\ln x})}{\sum_i n_i}\right)^{\frac{1}{2}}. \tag{4.2}$$

Where n_i denotes the relative frequency of the value x_i. Since a product of different log-normal distributions again gives a log-normal distribution, accordingly also the volume and the surface distributions of nanocrystals can be described by Equation 4.1, if the distribution of the diameters of the nanocrystals follows f_{LN}.

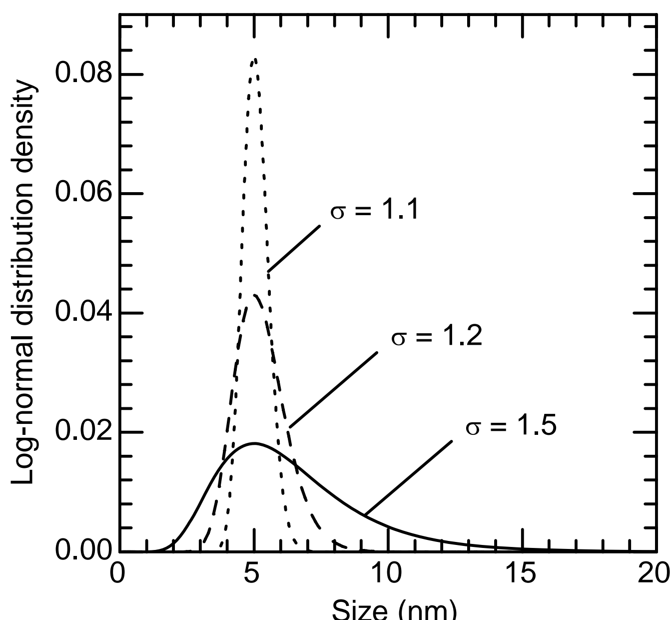

Figure 4.3: Log-normal size distribution density functions for an average size of 5 nm and standard deviations of $\sigma = 1.1$, $\sigma = 1.2$, and $\sigma = 1.5$. The curves have been normalized to their integrated area.

Examples of differently broad size dispersions are shown in Figure 4.3. Here, the effect of changing the standard deviation σ from 1.1 to 1.2 and 1.5 is shown for a mean size of 5 nm. The spectra have been normalized to the integrated area of the distribution function giving the log-normal distribution densities $f_{LN}(x, \sigma)/(\int_0^\infty f_{LN}(x, \sigma)\mathrm{d}x)$. Especially for larger values of σ, the asymmetric shape of the log-normal distribution function is visible. A steep onset just below the median is accompanied by a broad tail towards large values of x. For example, the figure illustrates that a significant amount (10%) of particles with sizes larger than 10 nm can be found in a $\sigma = 1.5$ size dispersion. In contrast, $\sigma = 1.1$ corresponds to the almost monodisperse situation where only a negligible quantity of particles smaller than 4 nm or larger than 6.5 nm is present in the ensemble.

While the mean size of the silicon nanocrystals can be adjusted via the microwave plasma conditions as outlined in Section 2.1.1, the concomitant width of the size dispersion cannot be adjusted alone but is closely connected with the average size. For the size distribution of silicon nanocrystals grown in microwave reactor systems, typical values of $\sigma = 1.15 \ldots 1.3$ are observed for small silicon nanocrystals in the range of $4 - 20$ nm, whereas larger values of about $\sigma = 1.5$ are present if the average size of the silicon nanocrystal ensemble is in the range of $30 - 50$ nm.

Spin-coated layers

After dispersing silicon nanoparticles and nanocrystals in ethanol, films thereof have been fabricated by spin-coating on substrates as introduced in the previous sections 2.1.3 and 2.1.5. Here, the differences between the hot wall and microwave reactor grown initial material transfer into the morphology of the resulting layers after spin-coating. However, both materials can be used to realize reasonably smooth and well-defined material layers as Figure 4.4 demonstrates.

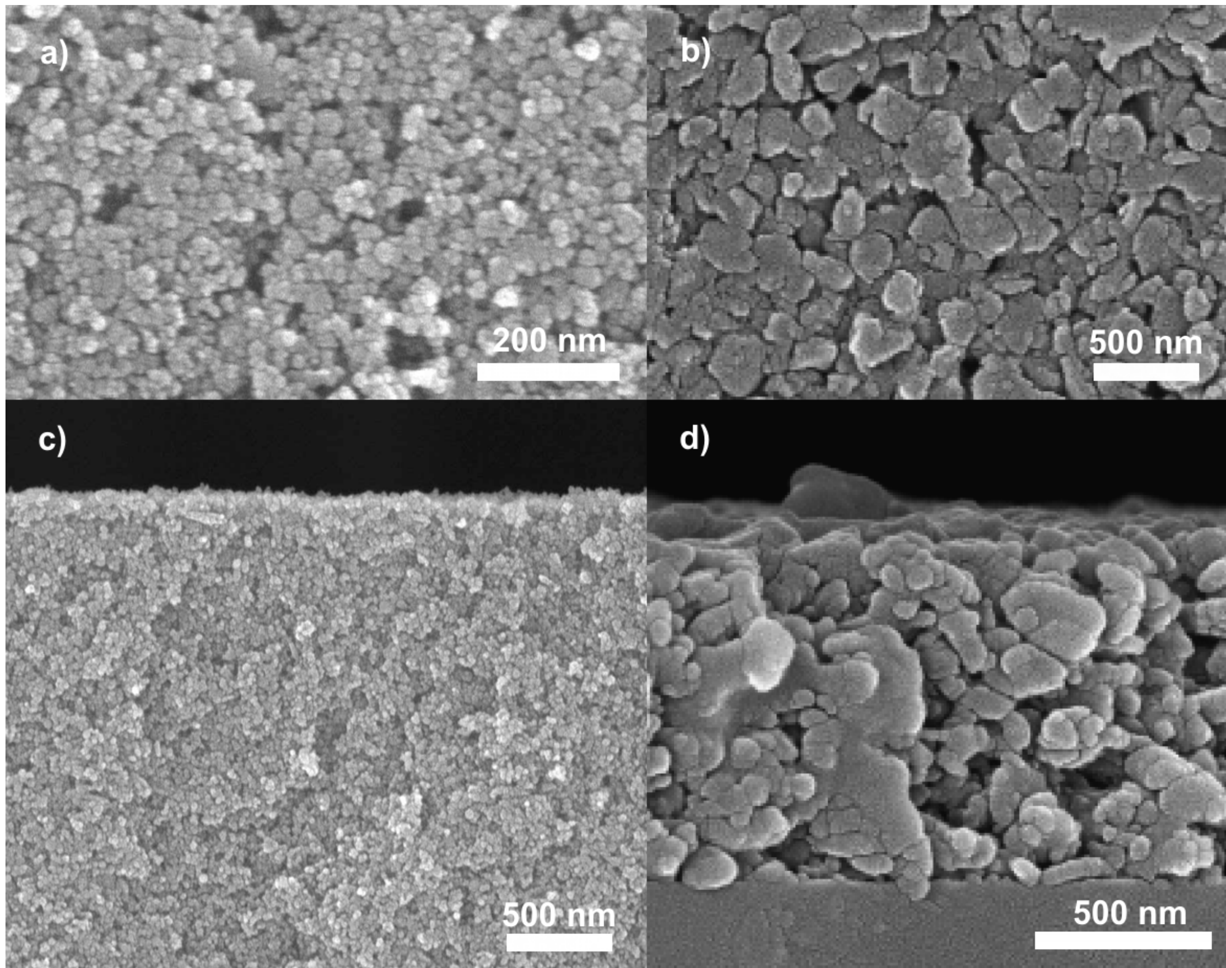

Figure 4.4: Scanning electron micrographs of spin-coated silicon layers. (a) and (c) show top and cross-sectional views of microwave reactor silicon nanocrystal films, whereas (b) and (d) denote top and cross-sectional views of hot wall silicon nanocrystal layers, respectively.

Figures 4.4 a) and c) show the result of 20 nm microwave reactor silicon nanocrystals spin-coated to form a 3 μm thick film on a fused silica substrate in top and cross-sectional view. As evident from the figure, the layer is quite homogenous and consists of "soft agglomerates" of densely packed silicon nanocrystals surrounded by pores. Due to the fact that rather large pores are present, a low volume filling factor can be assumed. However, the estimation of the overall porosity from such micrographs is subject to large inaccuracy, because the depth information is lost in the images.

A contiguous thin film is also achieved with the hot wall silicon nanoparticles as illustrated by Figure 4.4 b) and d). The main difference is the much larger structure size of the particles in this case ranging from 50 nm spheres to almost 1 μm large agglomerates. In spite of the extremely heterogeneous nature of the nanoparticles, still a rather well-defined layer results after spin-coating, but the pores seem to cover a larger volume fraction in this case.

4.1.2 Crystallinity

As a complementary method to high resolution transmission electron microscopy, where the crystalline structure becomes clear due to lattice plane interference fringes, also, X-ray diffractometry has been performed with hot wall reactor silicon nanoparticles and microwave reactor silicon nanocrystals [Wig01, Kni04]. Strong contributions of the (111), (220), and (311) Bragg reflexes and weaker signals of the (400), (331), (422), and (333) peaks were observed. These combinations of Miller indices clearly identify a diamond silicon lattice structure via the underlying selection rules: in the possible reflexes (ijk), the indices i, j, and k are either all odd or all even numbers, and in the latter case, the sum is a multiple of four ($i + j + k = 4n$, with an integer $n > 0$).

For microwave reactor material, the derived lattice constant of $a = 5.429$ Å is only slightly smaller than that of bulk crystalline silicon ($a = 5.431$ Å). In the case of hot wall reactor particles, additionally a size dependent shift of the lattice constant has been observed. Using the Scherrer formula, the average size of the microwave reactor silicon nanocrystals was estimated from the peak width resulting in a value of $d = 6$ nm, in good agreement with the corresponding BET measurements giving a crystal size of 5 nm [Kni04]. The sizes determined for hot wall reactor nanoparticles are significantly larger and range from $20 - 30$ nm [Wig01]. This is smaller than the diameter of the side-chains observed in Figure 4.1, indicating that these regions are polycrystalline, which agrees with the observation of superimposed sets of diffraction spots in the inset.

The amount of potential amorphous contributions is more difficult to quantify. In X-ray diffractometry, amorphous fractions lead to a broad background which is hard to evaluate. Raman measurements usually also give a peak contribution typical for amorphous material. However, this can also be ascribed to surface effects of purely crystalline material. While microwave reactor silicon nanocrystals show no signs of an amorphous silicon phase in high resolution transmission electron micrographs, it is conceivable that highly disordered amorphous phases exist within the heterogeneous hot wall silicon nanoparticles. However, also purely amorphous silicon nanoparticles have been available during the course of this work by choosing the microwave reactor growth conditions appropriately, so that no crystalline signatures were obtained in the subsequent analysis.

4.1.3 Raman Analysis

Size dispersion

In Subsection 3.3.2, the basic consequences of the size reduction on the Raman spectra have been introduced. Since the ensembles of nanocrystals under study here exhibit a log-normal size dispersion, the Raman cross sections follows from an integration over the size-dependent expression from Equation 3.10 weighted by the underlying log-normal distribution function $f_{\mathrm{LN}}(L)$:

$$I_{\mathrm{LN}}(\omega) \cong \int f_{\mathrm{LN}}(L) \frac{1}{I(L)} \int \frac{|C(q)|^2}{(\omega - \omega(q))^2 + (\Gamma_0/2)^2} \mathrm{d}^3 q \, \mathrm{d}L. \tag{4.3}$$

Here, the contributions of individual sizes have been normalized to their integral spectral intensity $I(L)$ to make sure that all size components contribute with equal total Raman cross sections.

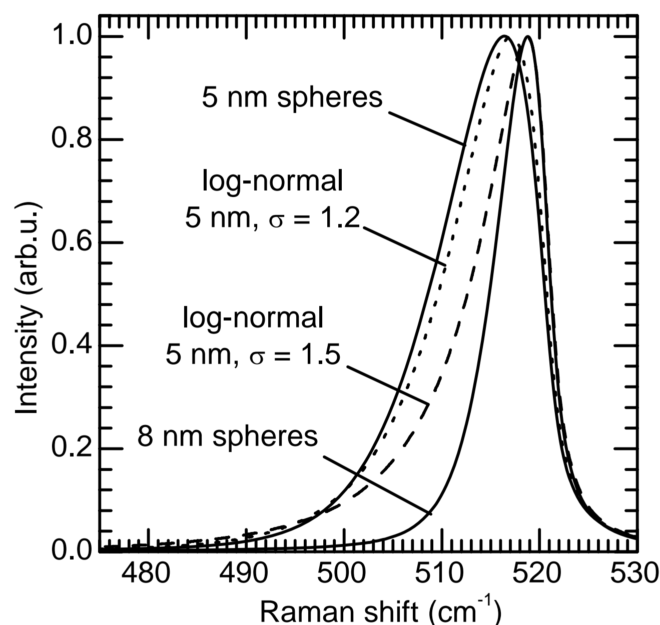

Figure 4.5: Calculated Raman spectra of ensembles of spherical silicon nanocrystals with a log-normal distribution function for an average diameter of $x = 5$ nm and standard deviations of $\sigma = 1.2$ and $\sigma = 1.5$. The spectra of monodisperse spherical nanocrystals with sizes of 5 nm and 8 nm are shown for comparison.

The result of such a calculation can be seen in Figure 4.5 for the case of an average size of 5 nm and standard deviations of $\sigma = 1.2$ and $\sigma = 1.5$, together with Raman spectra of monodisperse spherical crystallites with average sizes of 5 nm and 8 nm. As is evident from the figure, a size dispersion with a standard deviation of $\sigma = 1.2$ (dotted line) leads to only minor changes in the peak position towards apparently larger crystals while the peak width remains rather constant. However, in the case of $\sigma = 1.5$ (dashed line), the peak shape changes drastically compared to monodisperse 5 nm crystals. In fact, the peak position has shifted by 3 cm^{-1} towards the bulk value and effectively resembles that of monodisperse 8 nm crystals due to the contributions of the larger nanocrystals in the size dispersion. However, the overall width of the curve has increased by 2 cm^{-1}, which helps to distinguish a broad size dispersion from a monodisperse 8 nm nanocrystal ensemble.

In Figure 4.6, the resulting consequences on the peak shift and the peak full width at half maximum (FWHM) for Raman scattering is demonstrated. The peak position is shifted considerably towards larger crystal sizes, owing to the asymmetry of the size distribution in this direction. The characteristic correlation of the Raman peak shift with the peak width might even help to identify the present size distribution by Raman measurements. However, as we have seen in Figure 4.5, in the case of narrow size dispersions with $\sigma < 1.2$, the differences to the monodisperse situation will become too small to unambiguously distinguish between the two cases. And above mean sizes of 15 nm, the differences to monodisperse Raman spectra of larger particles become minute even for a $\sigma = 1.5$ log-normal distribution. In contrast, if the mean particle size is known and is smaller than 15 nm, substantiated conclusions on the size dispersion can be drawn from Raman data.

Being in the lucky situation that we know the average size and standard deviation of the size distribution of the silicon nanocrystals, we can fit calculated Raman spectra to the experimen-

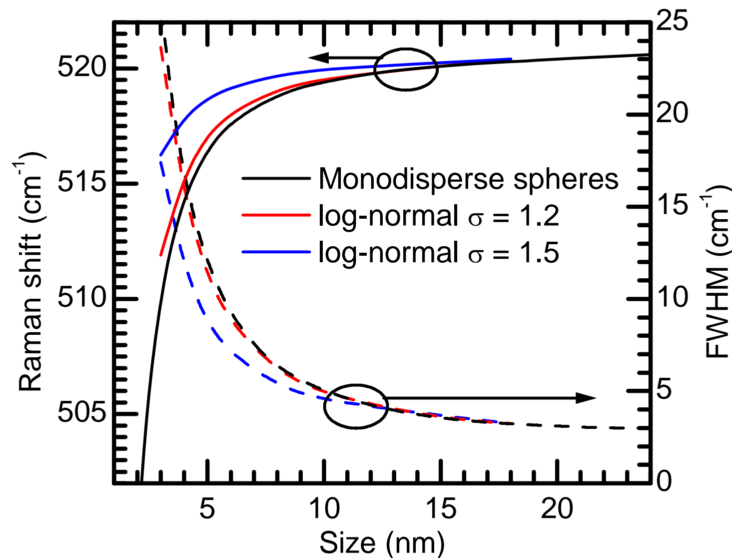

Figure 4.6: Calculated results for the correlation between the Raman peak position, the peak width, and the nanocrystal size (FWHM), for monodisperse spherical silicon nanocrystals and for log-normal ensembles with $\sigma = 1.2$ and $\sigma = 1.5$.

tal data. By subtracting this fit, additional contributions to the Raman spectra due to different physical mechanisms can be studied.

Raman spectra of silicon nanocrystals and nanoparticles

Figure 4.7 shows examples of Raman spectra of an undoped microwave reactor silicon nanocrystal layer (a) and of a layer of hot wall reactor silicon nanoparticles (b). The peak position of the crystalline silicon reference sample is marked by the dotted line at $522\,\text{cm}^{-1}$. Both spectra were fitted with an additive superposition of two contributions (dashed lines): a finite-size particle ensemble spectrum calculated via the phonon confinement model for log-normal size distribution and a broad Lorentzian background centered around $\omega_c = 490 - 500\,\text{cm}^{-1}$ with a width of $\Delta = 70 - 90\,\text{cm}^{-1}$. Alternatively, also a multiple peak fit is possible for the background, *e.g.*, by a peak of an disordered phonon contribution at $480\,\text{cm}^{-1}$ and a contribution of stacking faults around $495\,\text{cm}^{-1}$ as performed for instance by [Iqb82, Xia95]. However, due to the spectral overlap and the large width of these signatures, such a deconvolution is not unambiguous. Here, such possibilities will be discussed during the interpretation of the background peak width and position.

The spectrum in Figure 4.7 a) was measured with an ensemble of undoped silicon nanocrystals with an average size of 4.3 nm. A distinct asymmetric peak protrudes from a broad background shoulder at lower wavenumbers. The thick line represents a numerical simulation of the experimental data. This curve is the superposition of two peaks (dashed lines). The size-confined contribution around $517\,\text{cm}^{-1}$ was calculated for a silicon nanocrystal ensemble with an average crystal size of 5 nm and a standard deviation of $\sigma = 1.2$, which comes very close to the real situation. A broad Lorentzian line forms the background of the spectrum at $\omega_c = 490\,\text{cm}^{-1}$ with a peak width of $\Delta = 50\,\text{cm}^{-1}$.

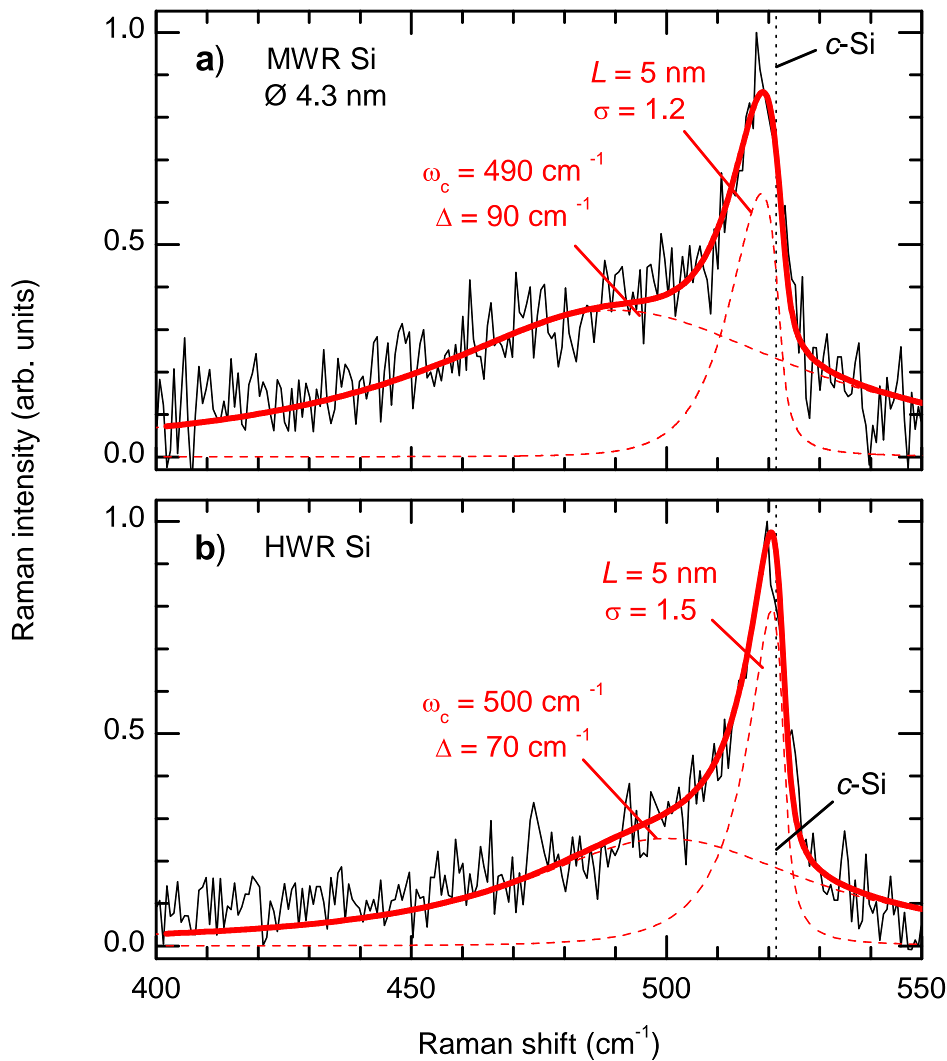

Figure 4.7: Raman spectra of (a) 4.3 nm microwave reactor silicon nanocrystals and (b) hot wall reactor silicon nanoparticles (thin solid lines). Simulated Raman spectra of silicon nanocrystal ensembles with log-normal size distributions and broad Lorentzian lines contribute to fits to the data (dashed lines and thick solid line).

Both the peak position and width of this background come close to the characteristic values of an amorphous silicon phase ($\omega_c = 480\,\text{cm}^{-1}$, $\Delta = 70\,\text{cm}^{-1}$ [Iqb79]), which is typically present in nano- and microcrystalline silicon deposited from the gas phase [Iqb82, Len03]. While for this deposition method the presence of an amorphous phase is an accepted fact, this Raman band is also present for size-selected silicon nanoparticle ensembles [Pai99, Isl05]. Only in the case of very small-grained nanocrystalline silicon with $L < 3\,\text{nm}$ [Xia95] or with electrochemically etched nanoporous silicon samples [Kan93], the Raman spectra can be sufficiently well reproduced from the mere phonon confinement model.

Consequently, the broad Raman band does not necessarily stem from an amorphous silicon volume fraction, *e.g.*, in the form of an amorphous silicon shell around a nanocrystalline core region. Neither the TEM data, nor the good size agreement of the phonon confined peak substantiate such an assumption. In contrast, this effect might be a consequence of the inherent disorder in the surface regions of the nanocrystallites or be an indication of Raman surface modes in the

small crystals [Xia95, Pai99]. The alternative interpretation proposed by Islam and coworkers that the background stems from a bimodal size distribution with an additional population of 2 nm nanocrystals [Isl05] can produce good fits to our data as well, but no signs of such a size distribution have been found in particle mass spectroscopy or TEM analysis [Kni04].

The Raman spectrum of a typical hot wall silicon nanoparticle layer is depicted in Figure 4.7 b). Again a similar fitting procedure as in (a) was performed here, but in this case, the peak around $520\,\mathrm{cm}^{-1}$ is narrower and is described best by a $\sigma = 1.5$ log-normal size dispersion with a mean crystal size $L = 5$ nm. This rather small crystallite size is contrary to the results from evaluating the XRD peak width for this material ($20 - 30$ nm). However, from the TEM micrographs, the existence of a large volume fraction of fine-grained nanocrystals within the sintered nanoparticle dendrites appears possible. Due to the significantly higher optical absorption of such defect-rich regions, their relative contribution to the Raman cross-section may easily exceed their volume fraction (compare sections 4.3.4 and 4.1.4).

A distinctly different background signature is found in the case of the hot wall reactor silicon nanoparticles. Not only is the relative intensity of the broad Lorentzian contribution reduced compared to the situation with the microwave nanocrystals, but also the peak position is shifted to higher wavenumbers around $500\,\mathrm{cm}^{-1}$ and the width has decreased to $\Delta = 35\,\mathrm{cm}^{-1}$. Apart from the above discussed possible origins, here, the additional contribution of stacking faults appears plausible. Due to the sintering processes at the multiple internal grain boundaries, a relatively large number of stacking faults might be incorporated. These lead to well-known Raman signatures around $495\,\mathrm{cm}^{-1}$, whereas typical widths of $15\,\mathrm{cm}^{-1}$ are observed [Kob73, Ban93]. Superimposed to the disorder effects around $480\,\mathrm{cm}^{-1}$, the effective peak shift and narrowing of the background signal can be explained.

Other influences on the Raman spectra

Apart from the crystal size (and the temperature, which was ruled out during these measurements) also other factors have strong impact on the shape of the Raman spectra. As in Raman scattering the vibrational properties of the crystalline lattice and thus the elastic properties of the material are probed, the presence of biaxial strain will be directly mirrored in the Raman spectra. In the case of a thick oxide shell surrounding nanosized particles, stress can develop similar to the situation of nanocrystals grown in an oxide matrix [Sha05]. Then, the different thermal expansion coefficients of silicon and SiO_2 or the fact that the oxide expands during growth can lead to a significant stress present in free-standing nanocrystals. However, this leads to an isotropic stress inside the spherical nanocrystals, and consequently, the Raman peak position will not be affected [Ana91, Len02].

The presence of a large concentration of covalently bonded impurity or alloy atoms leads to characteristic local vibrational modes in the crystalline lattice. In a first approximation, the energy of the vibrational mode scales as $\sqrt{m_X/m_{Si}}$, where m_X and m_{Si} are the atomic masses of the impurity and the silicon atoms, respectively. If the mass of the impurity is close to the mass of silicon, it is conceivable that this method will not be able to resolve the latter, as is the case for phosphorus in silicon ($^{28-30}$Si versus ^{31}P natural isotopes). In contrast, the light boron isotopes ^{11}B and ^{10}B can be identified in the silicon lattice by Raman measurements, leading to lines at $620\,\mathrm{cm}^{-1}$ and $644\,\mathrm{cm}^{-1}$, respectively [Cer74, Cha80]. However, since the Raman intensity is a function of the concentration of the relevant impurity and because second-order Raman scattering

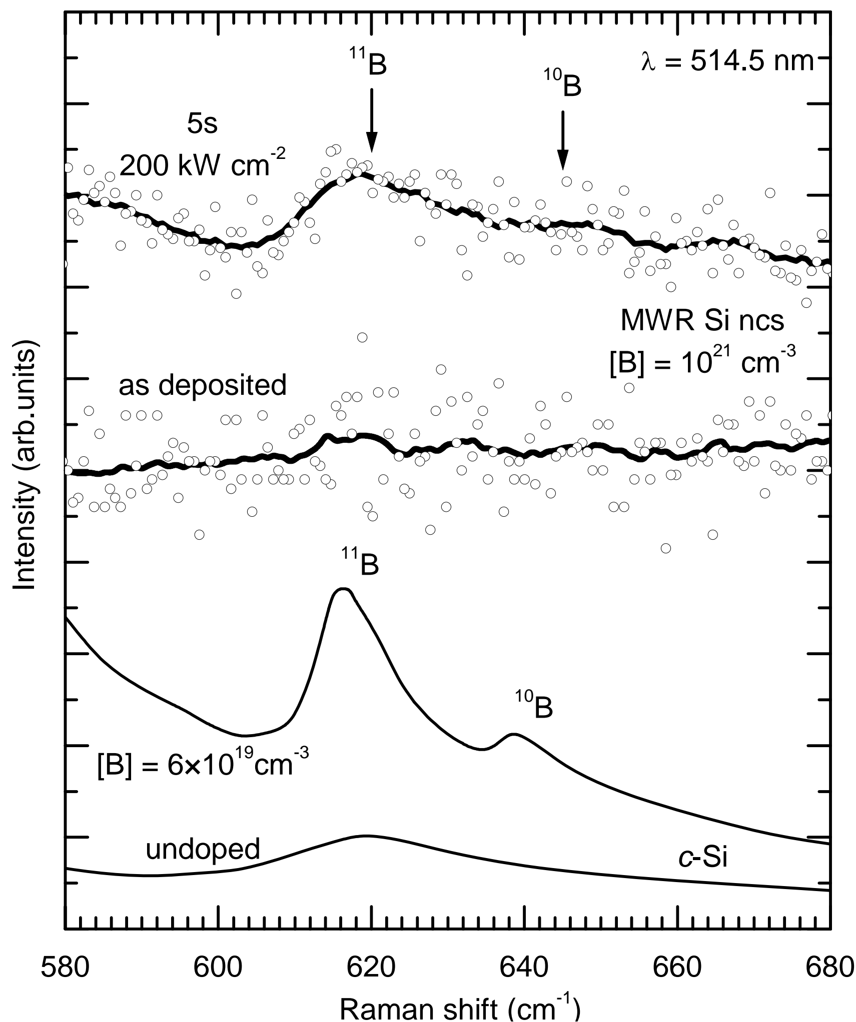

Figure 4.8: Raman spectra of highly boron-doped silicon nanocrystals before and after a short term irradiation at high power density with the probing laser. Reference spectra of undoped and boron-doped crystalline silicon are shown for comparison [Stu87a].

by longitudinal acoustic phonons occurs at 620 cm^{-1} also in undoped samples (compare Figure 4.8), only impurity concentrations exceeding 10^{19} cm^{-3} can be clearly identified [Stu87a].

In highly doped silicon, also the presence of free carriers can influence the Raman spectra if the carrier concentration is sufficiently high. Then, a continuum of free hole or electron states can interact with the zone-center optical phonons involved in Raman scattering, giving rise to the so-called Fano effect or Fano resonance, which allows the determination of the carrier concentration from contact-free optical measurements [Cer73, Cer74].

Indeed, local boron modes could be observed in the Raman spectra of extremely boron-doped silicon nanocrystal layers as illustrated in Figure 4.8. However, this was possible only if the sample spot analyzed in micro-Raman measurements was exposed to a high laser power before the measurement. Without this "annealing" at typical power densities around 200 kW cm^{-2}, neither free carrier effects nor local modes were detected in Raman measurements of highly boron-doped silicon nanocrystal layers. This is an indication that not all boron atoms are incorporated substitutionally in the nanocrystals and require an annealing step to become fully electrically active.

Also if the highly boron-doped samples are processed with pulsed laser annealing, they show both the local boron modes as well as the free-hole interactions in the Raman spectra. In Section 6.3.2 this effect will be exploited to determine the free carrier concentration of laser-crystallized silicon nanocrystal films.

4.1.4 EPR analysis

Paramagnetic defects (spins) present in semiconductor samples can have a strong impact on the overall properties of the material. Unsaturated silicon bonds (dangling bonds) situated at surfaces or grain boundaries in crystalline silicon represent one example of a paramagnetic defect species, which give rise to deep states in the middle of the bandgap. Due to the large relative contribution of the surface, control over these states is especially important for the silicon nanoparticles and nanocrystals under study here.

Primary particles

A typical room temperature EPR spectrum of microwave silicon nanocrystals is shown by the open circles in Figure 4.9. A mean size of $L = 29\,\mathrm{nm}$ and a doping concentration of $8 \times 10^{17}\,\mathrm{cm}^{-3}$ phosphorus atoms was present in this case. Concerning the impact of the phosphorus doping, the below subsection will discuss the specific influence of the phosphorus doping. The detected signal can be attributed to unsaturated bonds of trivalent silicon atoms in two different coordinations. One component arises from so-called P_b-centers, which are axially symmetric defects of silicon atoms at the silicon interface to the surface oxide. From the multitude of orientations of these defects with respect to the applied magnetic field, a characteristic powder pattern arises, which is characterized by the delimiting g-factors for perpendicular and parallel relative orientation [Wei94]. The dotted line displays this powder pattern in the figure extending between $g_\perp = 2.0089$ and $g_\parallel = 2.0022$.

The second fraction of paramagnetic defects found in the nanocrystals is identified with silicon dangling bonds in a disordered environment with a characteristic g-factor of 2.0055. Such defects are also found in dislocation-rich crystalline silicon, at grain boundaries in poly- or microcrystalline silicon, and are the dominant structural defect in amorphous silicon [Stu87b]. Their contribution to the total EPR signal is illustrated in the figure by the dashed line. A sum of both dangling bond components gives a good fit to the experimentally found EPR curve (solid line).

From integrating twice over the curve, the typical concentration of dangling bonds in 29 nm microwave reactor silicon nanocrystals can be quantified to $10^{18}\,\mathrm{cm}^{-3}$, corresponding to an estimated surface defect concentration of about $3 \times 10^{11}\,\mathrm{cm}^{-2}$ for the nanocrystal size shown here. This comes close to the value of $10^{12}\,\mathrm{cm}^{-2}$ structural defects, which are typically observed at the native oxide interface of crystalline silicon wafers [Joh83].

In contrast, hot wall reactor silicon nanoparticles do not show a strong P_b-signature in EPR measurements and instead, the contribution of the isotropic dangling bonds in disordered surroundings around $g_\mathrm{db} = 2.0055$ dominates the corresponding spectra. Also, a significantly higher overall defect concentration is detected in these samples. Here, the typical defect concentration amounts to around $10^{19}\,\mathrm{cm}^{-3}$. To understand this difference, it is helpful to quantify the internal surface area of the hot wall silicon nanoparticles.

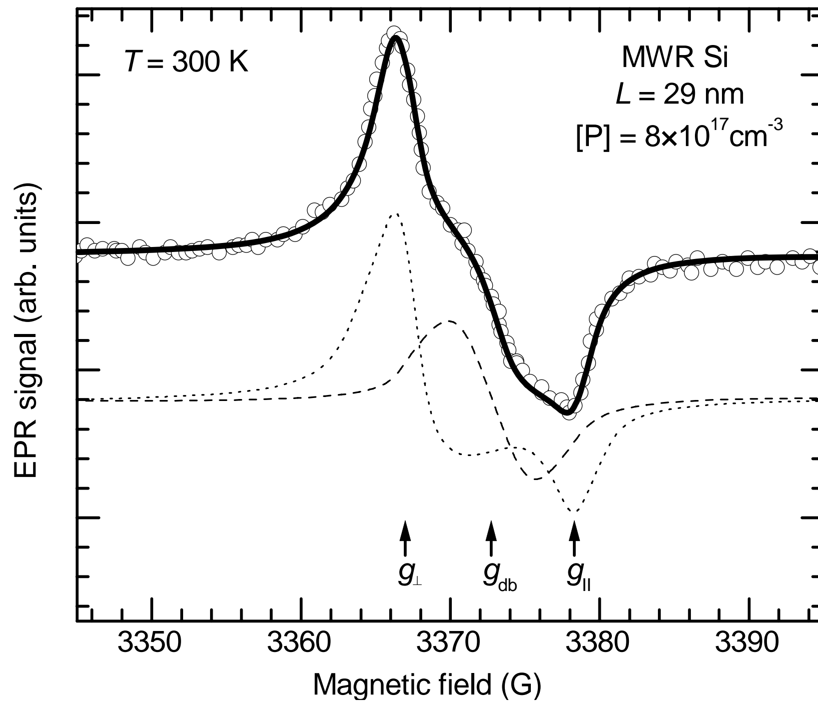

Figure 4.9: Room temperature EPR spectrum of phosphorus-doped microwave reactor silicon nanocrystals with an average size of 29 nm (open circles). A numerical fit to the spectrum is obtained by a superposition of an isotropic dangling bond signal at $g_{\mathrm{db}} = 2.0055$ and a P_{b} powder pattern contribution with $g_{\perp} = 2.0089$ and $g_{\parallel} = 2.0022$ (full, dashed, and dotted lines, respectively).

If the crystal grain size as derived from the XRD diffraction peaks via the Scherrer formula (20 nm) is supposed, a rough estimation of the internal interface area yields a result comparable to the surface area of an ensemble of 20 nm microwave reactor silicon nanocrystals. In this case, it has to be concluded that a significantly higher defect concentration of about $3 - 5 \times 10^{12}\,\mathrm{cm}^{-2}$ is present at intergrain interfaces in the sintered hot wall reactor nanoparticles.

If, alternatively, the additional presence of smaller crystallites with a size on the order of 5 nm is presumed, the observed defect density is consistent with the typical silicon interface defect concentration of $10^{12}\,\mathrm{cm}^{-2}$. Possibly, apart from the larger grains in the range of $20 - 50$ nm visible in the TEM micrographs, also highly disordered and defect-rich material of effectively smaller grain size is present in the sintered regions of the hot wall reactor silicon nanoparticles. The presence of diffraction rings in the TEM diffraction pattern in the inset of Figure 4.1 can further justify this assumption. In XRD, the larger crystallites dominate the spectra, while small crystallites and disordered volume fractions lead to relatively small background signals, which are hard to evaluate quantitatively [Wig01, Kni04].

However, the results of the Raman analysis in Section 4.1.3 substantiate both the presence of small-grained material of this dimension and of a significant fraction of stacking faults. Together with these indications, the change of the EPR spectra towards the characteristics of isotropic dangling bonds in disordered surroundings lends evidence to the second possibility.

Spin-coated layers

A further important observation is the fact that spin-coated layers of silicon nanocrystals exhibit a significantly higher defect concentration than was present in the initial material. After dispersing the nanocrystals, the defect concentration has risen by one order of magnitude to typically $2 - 3 \times 10^{19}\,\text{cm}^{-3}$. Additionally, the characteristic signature of the paramagnetic defects has changed significantly. The inset in Figure 4.10 demonstrates that the anisotropic fraction of P_b-like defects has disappeared and now the isotropic $g \approx 2.006$ signal with a line width of $7 - 8\,\text{G}$ is the dominant contribution to the EPR spectra.

The reason for the increase of the spin density of the nanocrystal layers with respect to the initial material can be found in the dispersing process. The considerable mechanical strain involved during the ball-milling in ethanol leads to an increase of the dangling bond density similar to the situation of mechanical damage to crystalline silicon surfaces. The defects observed in silicon clusters created during cleavage of crystalline silicon also exhibit a g-factor of 2.0055 [Stu87b]. In this light, also the shape of the EPR curve, which is more similar to hot wall reactor grown material can be understood.

An increase of the dangling bond density in spin-coated layers occurs especially for microwave reactor silicon nanocrystals, while hot wall reactor silicon nanoparticles show no strong increase of the spin density within usual dispersion times. However, if an extended long-term dispersing is done, also here an increase of the defect density was observed by Reindl and coworkers. An accompanying overall amorphization of the material during prolonged ball milling is evident from disappearing Bragg peaks in X-ray analysis and from a growing fraction of amorphous phases detected by Raman analysis and high resolution transmission electron microscopy [Rei07]. These long-term experiments directly prove that the mechanical impact during ball-milling is sufficient to completely alter the structural properties of nanoparticles.

The high concentration of defects present after dispersing and spin coating can be slightly reduced by wet-chemical etching of the oxide during immersion of the samples in dilute and concentrated hydrofluoric acid for 30 s. A decrease by 10% can be obtained by this procedure as is depicted in Figure 4.10. The alternative exposure to the vapor of concentrated hydrofluoric acid for 2 min has a similar effect. The fact that only a minor reduction of the spin density can be achieved indicates that only a small fraction of the defects created by the ball milling is situated at the oxide interface, which is also suggested by the absence of major P_b signatures in the EPR spectra. Seemingly, the detectable defects are present in the silicon matrix within regions that are not etched away when the oxide itself is removed.

Substitutional phosphorus

One of the advantages of electron paramagnetic resonance spectroscopy is that substitutionally incorporated phosphorus dopants can be detected at low temperatures via characteristic resonance lines. Well below room temperature, the surplus electron of the pentavalent phosphorus impurities is bound in the Coulomb potential of the dopant atom. Because of the s-like character of the wave function of the electron, its non-zero probability at the position of the phosphorus nucleus leads to a Fermi contact hyperfine interaction between the electron spin and the nuclear spin of the stable isotope ^{31}P ($I = 1/2$). As a consequence, a pair of symmetric lines is observed around a central g-factor of $g = 1.998$ with a splitting of 42 G. If the dopant concentration ap-

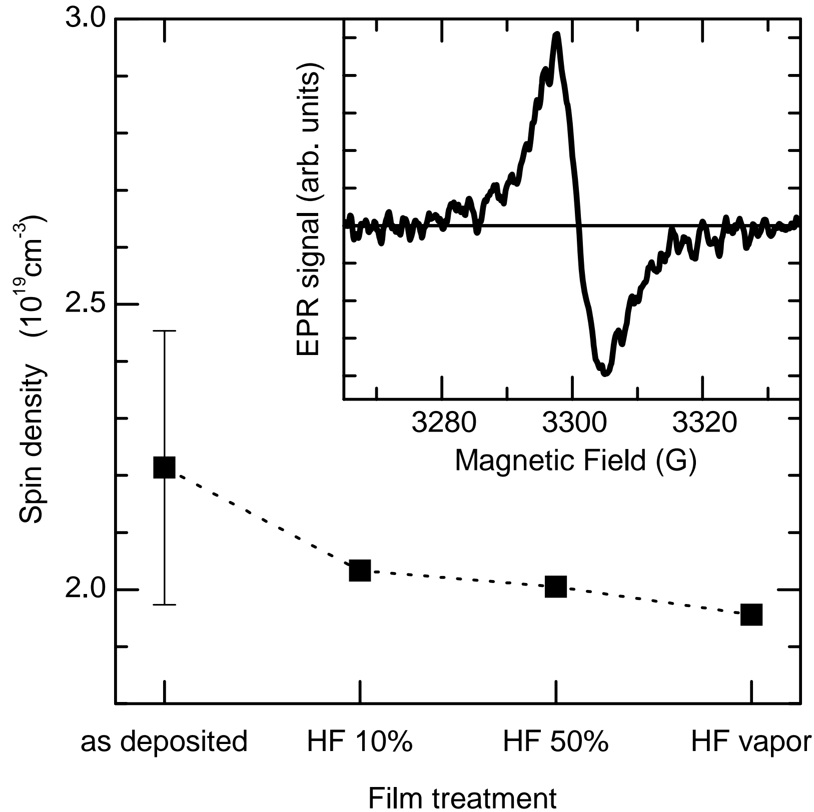

Figure 4.10: Volume spin density of silicon nanocrystal films for different sample treatments. The inset shows a typical EPR spectrum of a silicon nanocrystal layer after dispersing in ethanol and spin coating.

proaches $10^{17}\,\mathrm{cm}^{-3}$, however, an additional contribution at the center position emerges, which is attributed to exchange-coupled electrons at nearby dopant positions. Above a concentration of $10^{18}\,\mathrm{cm}^{-3}$ phosphorus atoms in the silicon lattice, the hyperfine split lines are not observed any longer and only the center line persists in the spectra [Cul75].

In the case of phosphorus-doped silicon nanocrystals, the same behavior can be observed. Figure 4.11 shows the EPR spectra of silicon nanocrystals with different size and doping concentration measured at 20 K. While in the case of nanocrystals with a phosphorus concentration of $7 \times 10^{16}\,\mathrm{cm}^{-3}$ and a mean size of 46 nm both, the hyperfine line pair and the central signal are visible, for the sample doped with $3 \times 10^{19}\,\mathrm{cm}^{-3}$ and an average size of 11 nm, only the $g = 1.998$ contribution is present additionally to the broad dangling bond signal, which dominates the overall spectra in both cases.

These results directly prove the substitutional incorporation of phosphorus dopants in the silicon nanocrystal lattice during gas-phase nanocrystal growth. Furthermore, the absolute amount of electrically active phosphorus dopants in the nanocrystal ensemble can be determined quantitatively from double integration of the spectra. In all samples, the obtained phosphorus concentrations are significantly below the nominal doping concentrations. However, since other physical properties of the phosphorus-doped nanocrystals hinted on a low incorporation efficiency as well, the phosphorus doping profile was analyzed in detail in mass spectrometry, see Section 4.2.3. For nanocrystal sizes exceeding 20 nm, the phosphorus concentration from EPR is found in good agreement with these results. Only for small particles ($L < 20\,\mathrm{nm}$) a systematic decrease

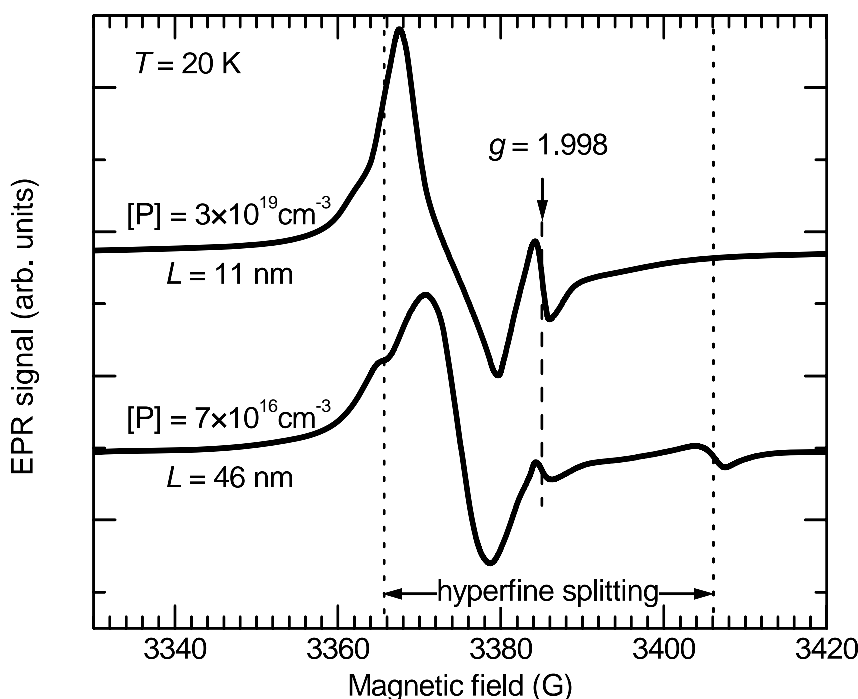

Figure 4.11: Signatures of substituational phosphorus dopants in the EPR spectra of microwave reactor silicon nanocrystals recorded at $T = 20\,\mathrm{K}$. A prominent feature at $g = 1.998$ is present for phosphorus-doped samples accompanied by a pair of hyperfine-split resonance lines for low doping concentrations.

of the phosphorus concentration visible in EPR with decreasing nanocrystal size is present. In a model including several size-dependent physical effects, this observation can be quantitatively explained [Ste08b].

4.2 Chemical Analysis

4.2.1 Contamination levels

The chemical purity of the silicon nanocrystals grown in MWR1 was analyzed after growth by glow discharge mass spectroscopy (GDMS) and, complementary, also by inductively coupled plasma mass spectroscopy (ICPMS). The contamination levels determined from both techniques were mostly in the range of few ppm down to the resolution limit of the methods at 0.004 ppm, but in several cases significant amounts of metal impurities could be detected. As Table 4.1 shows, especially iron and aluminum were found in relatively large concentrations (2.5 ppm and 1.0 ppm, respectively). While the stainless steel corpus of the microwave reactor is believed to be the source of the intrinsic iron contamination, the aluminum, apart from traces present also in stainless steel, might as well be incorporated in the samples during preparation for the GDMS analysis, where an aluminum plate comes into direct contact with the silicon nanocrystals.

Other typical contaminating species comprise, *e.g.*, sodium, zinc, calcium, and chromium in typical concentrations in the range of fractions of ppm, giving rise to a background impurity level of about $10^{17}\,\mathrm{cm}^{-3}$. Samples which have undergone the ball-milling and dispersing procedure in ethanol, additionally exhibit a high concentration of zirconium due to the attrition of

Fe	Al	Na	Zn	Ca	Cr	K	Mg	Ni	P	Ti	Cu	Mn	Mo	Sn
2.5	1.0	0.7	0.6	0.5	0.4	0.3	0.3	0.3	0.3	0.3	0.1	0.08	0.04	0.04

Table 4.1: Maximum concentrations of various impurity elements in three undoped charges of microwave reactor silicon nanocrystals as detected by GDMS. All values are in ppm.

the yttrium stabilized zirconia beads used during the ball-milling. Here, contamination levels of $10 - 1000$ ppm were found, however it could not be clarified how much of this zirconium is still present in the form of the chemically inert zirconium oxide.

For conventional bulk semiconductors, these effective values of impurity concentrations would be intolerable. However, they cannot be regarded as bulk concentrations. To some extent, these contaminations are also due to atmospheric substances and moisture adhering physically to the nanocrystal surface. The effect of such impurities then strongly depends on the subsequent sample processing. While part of the impurities can be washed off by solvents during the coating and sample cleaning, a heat treatment or annealing step allowing the in-diffusion, *e.g.*, of adhered metals, might lead to high concentrations also inside the nanocrystals. Still, the consequences of this situation cannot be predicted *a priori*, so the discussion of the impact of potential impurities will be continued after the physical properties of the silicon nanocrystals and layers thereof have been presented.

4.2.2 Surface oxidation

The surface of the microwave reactor silicon nanocrystals and of the hot wall reactor silicon nanoparticles after growth is almost free of oxide and is partially covered by a hydrogen surface termination. This can be concluded from the presence of the hydrogen-related vibrational modes in FTIR analysis characteristic for oxygen-free surroundings, and from the absence of oxygen-related infrared absorption bands. If the silicon nanocrystals and nanoparticles are kept in inert atmosphere after growth, the almost oxide-free surface conditions can be preserved over a period of several days [Ebb07].

However if the material has been processed under ambient atmosphere before the FTIR analysis, the coexistence of partly oxidized and hydrogen-terminated surface areas is evident [Kni04, Wig01]. The native oxide can be distinguished in the high resolution transmission electron micrographs as an oxide shell formed around the nanocrystals with a thickness of $1 - 2$ nm. Also after the dispersion and ball milling process in ethanol, the silicon nanocrystals exhibit a comparable native oxide shell due to the contact with the atmosphere and with the solvent. The oxide layer can be removed from the spin-coated silicon nanocrystal layers by simply immersing the samples in dilute hydrofluoric acid as described in Section 2.1.6.

Figure 4.12 a) shows the FTIR spectrum of a 500 nm thick layer of silicon nanocrystals, which had a size of 11 nm after spin-coating in comparison with the respective spectrum taken after wet chemical oxide removal (b). The absorbance spectrum of the as-deposited silicon nanocrystals exhibits prominent oxide-related features such as the dominant broad absorption band in the spectral region of $1050 - 1200\,\mathrm{cm}^{-1}$. The origin of this band has been attributed to oxygen stretching modes where two silicon and one oxygen atom are bonded in a Si-O-Si configuration [Kir88]. In our case, this configuration is most probable to occur at the surface oxide layer of the silicon nanocrystals [Kni04]. Also, hydrogen-related vibrational modes of silicon bonded

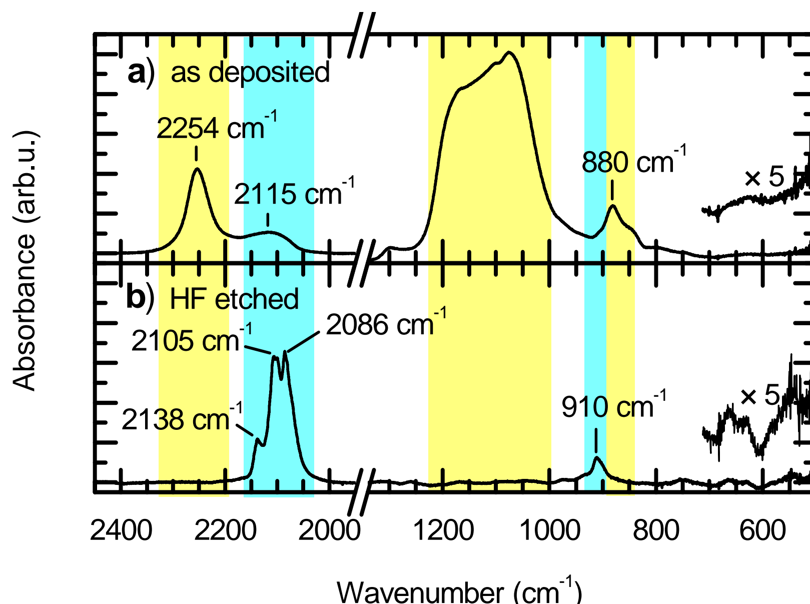

Figure 4.12: Infrared absorbance of microwave reactor silicon nanocrystal layers (a) directly after spin-coating and (b) after an additional etching step in dilute hydrofluoric acid. The silicon oxide-related absorption bands and the bands due to oxygen-free vibrations are highlighted by yellow and light blue background, respectively.

to three oxygen atoms (O_3-Si-H), such as the Si-H stretching mode at 2254 cm^{-1} and the Si-H wagging mode at 880 cm^{-1} are visible [Luc83, The97]. The small peak at 2115 cm^{-1}, finally, is the band of hydrogen stretching modes of one or more hydrogen atoms bound to a silicon atom in a silicon surrounding (Si_{4-x}-Si-H_x, [The97]). Consequently, even after the dispersion procedure and spin-coating, remnants of the as-grown hydrogen termination are present.

In this context, it is important to note that in the FTIR spectra of the spin-coated silicon layers, no characteristic ethanol bands are visible. This is due to the drying process usually performed after spin-coating and due to the volatility of the ethanol solvent. We thus can assume that no major concentrations of ethanol are left after film deposition, and that the properties of the layers once established are not influenced by the solvent.

After etching the spin-coated layers in dilute hydrofluoric acid, no vibrational modes related to oxygen containing species can be found in the spectrum in Figure 4.12 b). Instead, the intensity of the absorption band around 2115 cm^{-1} strongly increases and additional fine structure is resolved. Now, three different peaks can be discerned, with the central peak at 2105 cm^{-1} originating from the monohydride stretching mode in the Si_3-Si-H bonding situation (which is more plausible than a contribution of the trihydride stretching mode: Si-Si-H_3), whereas the anti-symmetric and the symmetric dihydride stretching modes (in the configuration Si_2-Si-H_2) become manifest in a pair of lines at 2086 cm^{-1} and 2138 cm^{-1} [The97]. At 910 cm^{-1}, also the silicon dihydride scissors mode is found contributing to a small peak (Si_2-Si-H_2, [The97]) and also weak signatures of hydrogen wagging or bending modes around 670 cm^{-1} are evident in the low-energy region of the absorption spectrum [Luc83, The97]. All of these modes (blue background in the figure) hint on a pure silicon surrounding. Consequently, the surface oxide phase (indicated by the bands with yellow background in the figure) has been effectively removed throughout the porous silicon network in the film by the post-deposition etching step.

Since silicon oxide is an isolator with a very large bandgap of $E_g \approx 9\,\text{eV}$, the presence of oxide interfaces is equivalent to high energy barriers for the electronic transport. At moderate temperatures, quantum mechanical tunneling is the only reasonable transport mechanism through such an oxide barrier, which becomes almost impossible if the oxide thickness exceeds 2 nm. Thus, the possibility to remove the oxide barriers by etching and to passivate the nanocrystal surface bonds with hydrogen opens the way for electrically conductive silicon particle layers. However, the stability of the silicon-hydrogen bond is limited and a reformation of the oxide layer is observed on a time scale of about 100 h under ambient conditions [Bau05].

4.2.3 Dopant concentration

To exploit the full potential of semiconducting nanoparticles, it is desirable to control their conductivity and the dominant carrier type at room temperature within the material by doping. Taking into consideration that the concentration of thermal carriers at room temperature is negligible ($10^{10}\,\text{cm}^{-3}$ in silicon), and that the effective degree of disorder in nanosized materials is high merely due to the reduced structure size, extrinsic doping is an essential requirement to achieve conductivity at all. For this study, doping of silicon nanocrystals grown in MWR1 and MWR2 was pursued by the addition of dopant gases to the gaseous precursors during growth. No doping has been implemented with the alternative hot wall reactor system so that only nominally undoped hot wall reactor silicon nanoparticles were available in the course of this study.

Dopants in the primary nanocrystals

As dopant impurities boron and phosphorus were chosen, which give rise to well-known shallow acceptors and donors in bulk crystalline silicon, respectively, with equal ionization energies of 45 meV. In the microwave plasma the precursor gases (Ar, H_2, SiH_4, B_2H_6, and PH_3) are to a large degree subject to dissociation, leading to the presence of all constituents in a radical form. In cooler regions of the plasma, where the dissociation gives way to nucleation processes, crystalline silicon nuclei can form and continue to grow.

During the growth period, also the dopant radicals will be incorporated into the growing crystals corresponding to the relative concentration present in the precursor mixture. However, there exist a number of physical effects, which can invoke a dopant concentration in the resulting nanocrystals differing strongly from the nominal value. In Chapter 3 the formation energy of dopants was shown to be a function of the silicon nanocrystal size [Can05], while also surface segregation needs to be considered as a possibility [Fer06a]. At the high temperatures present during plasma reactor growth, also the out-diffusion of already incorporated dopant impurities can play a role.

Table 4.2 displays the results of mass spectroscopy measurements of intrinsic and boron-doped silicon nanocrystals via GDMS, and of phosphorus-doped samples by SIMS analysis. The nominal doping concentrations given by the dopant gas fraction in the precursor mixture is included in the table. For the intrinsic sample, the resolution limit of the method sets a lower limit to the actual residual boron concentration.

The extremely high boron concentration in sample "Fl. 106" is the result of an uncontrolled doping procedure. Here, the complete doping gas bottle was consumed before one process run was

Sample	Reactor	Particle size (nm)	Dopant	Nominal concentration (cm^{-3})	GDMS / SIMS (cm^{-3})
Fl. 66	MWR1	20 nm	undoped	–	$< 5 \times 10^{14}$
Fl. 106	MWR1	20 nm	boron	$10^{18} - 10^{19}$	1.4×10^{21}
Fl. 107	MWR1	20 nm	boron	–	5×10^{20}
Fl. 111	MWR1	20 nm	boron	–	10^{19}
Fl. 297	MWR1	4.3 nm	boron	8×10^{17}	3×10^{18}
Fl. 295	MWR1	4.3 nm	boron	3×10^{17}	2×10^{18}
220807	MWR2	6.1 nm	phosphorus	5×10^{20}	8×10^{20}
250806	MWR2	11 nm	phosphorus	5×10^{20}	3×10^{20}
160807	MWR2	12 nm	phosphorus	1.7×10^{20}	1.6×10^{20}
270307	MWR2	17.5 nm	phosphorus	6.5×10^{19}	8×10^{19}
250906	MWR2	29 nm	phosphorus	1.6×10^{19}	1.4×10^{19}

Table 4.2: Nominal dopant concentrations in silicon nanocrystals in comparison with the values determined from mass spectroscopy methods. SIMS was applied to the phosphorus-doped samples while GDMS analysis was performed with intrinsic and boron-doped samples.

finished. As a consequence, an average boron concentration of 2.5% was present after growth. However, a rather inhomogeneous distribution of dopants in this material can be assumed, corresponding to a mixture of doped and undoped particles.

Although no further diborane was added during the subsequent growth runs in MWR1, also those samples exhibited high boron concentrations. The resulting doping concentrations of $5 \times 10^{20} - 10^{19}\,cm^{-3}$ may be a result of contamination inside the reactor or by intermixing with extremely boron-doped material in the filter unit. All of these samples have to be considered as mixed ensembles of doped and undoped nanocrystals, which is the reason why they were mainly used for digital doping experiments.

The GDMS measurements of nanocrystals produced from MWR1 show systematically higher boron concentrations than nominally intended during growth. At intermediate doping levels around $10^{18}\,cm^{-3}$ a discrepancy by a factor of $3 - 6$ is present, which can be a consequence of the specific reactor design. In contrast, the SIMS results of nanocrystals grown in MWR2 match well with the intended phosphorus concentrations.

Phosphorus segregation

To clarify inconsistencies in the phosphorus incorporation efficiency with respect to that of boron as apparent from electrical measurements and from EPR spectroscopy, mass spectroscopy measurements were performed also after removal of the silicon nanocrystal native oxide layer. The results of these measurements are displayed in Figure 4.13. Depth profiles of the phosphorus concentration of a spin-coated layer of silicon nanocrystals before and after a wet chemical etching step in dilute hydrofluoric acid are plotted in (a). The size of the primary particles was 12 nm, with a nominal doping concentration of $1.7 \times 10^{20}\,cm^{-3}$ phosphorus atoms, and the layer thickness was $0.5\,\mu m$. The doping concentration in the spin-coated silicon film resembles a flat

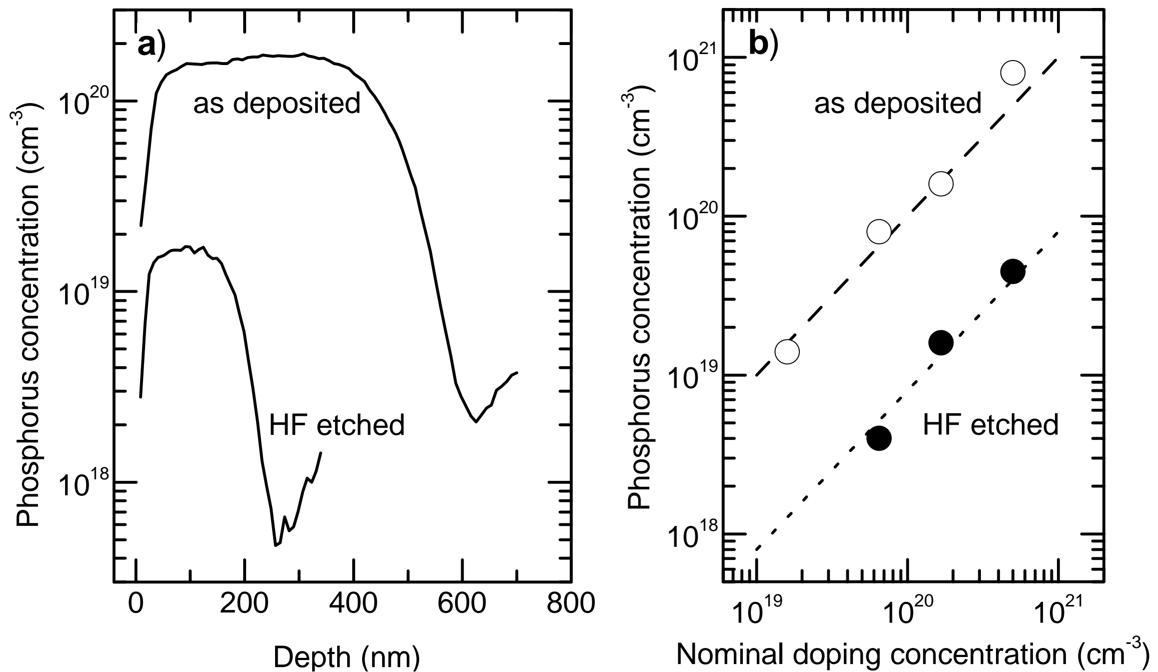

Figure 4.13: a) Depth profile of the phosphorus concentration as determined by SIMS measurements of a spin-coated phosphorus-doped silicon nanocrystal layer before and after HF etching. b) Mean phosphorus concentration in spin-coated silicon films before and after etching versus the nominal phosphorus concentration.

plateau at a value of about $1.6 \times 10^{20}\,\mathrm{cm}^{-3}$, which is in good agreement with the nominal value. After the oxide etching step, the phosphorus concentration in the silicon layer is found to be reduced by an order of magnitude to $1.5 \times 10^{19}\,\mathrm{cm}^{-3}$.

Also apparent from the data is a reduction of the layer thickness by the etching step. This effect is due to a large degree of surface oxidation for silicon samples from MWR2. After the etching of these samples, it is found that an upper part of the layer is lost due to undercutting and lift-off. Thus, the remaining layer thickness is only about half of the initial value, and in the case displayed in (a) the final film thickness amounts to about 200 nm. In contrast, for silicon nanocrystal layers from MWR1 the typical layer thickness reduction by the etching step amounts to only $10 - 30\%$ [compare, *e.g.* Figure 4.14 a)].

The average phosphorus concentration in layers of spin-coated silicon nanocrystals before and after the etching step in dilute hydrofluoric acid is shown in (b), plotted versus the nominal doping concentration. While the data points of the as-deposited samples lie close to the nominal values marked by the dashed line, the etching step results in an effective reduction of the phosphorus concentration by more than an order of magnitude. As the etching procedure removes the native oxide layer from the nanocrystal surface as was demonstrated in 4.2.2, the conclusion can be drawn that about $90 - 95\%$ of the phosphorus atoms are situated in this native oxide layer after dispersing and spin-coating of the nanocrystals. There, they are not electrically active and are lost as donors of the silicon nanocrystals.

Since the removal of the surface oxide from silicon nanocrystals is a crucial step for the preparation of conductive layers and a necessary precondition for laser annealing, a nominal phosphorus concentration exceeding the desired value by a factor of 20 needs to be targeted during mate-

rial growth. This finding is of high importance for possible applications of silicon nanocrystals. Since the phenomenon is observed regardless of the size of the silicon nanocrystals in the range of $5 - 50$ nm, the size dependence of the dopant formation energy cannot be the reason. To explain the observed segregation, a microscopic model taking the conditions of the nanocrystal growth in the microwave reactor into account will be proposed instead in the following paragraph.

After nucleation, the silicon nanocrystals grow in the reactor at high temperatures above 1000 °C. Due to the presence of phosphorus atoms in the gas phase, these will be incorporated in the forming silicon grains. By attaching to unsaturated silicon surface atoms and by subsequent overgrowth, phosphorus atoms are effectively incorporated both at substitutional lattice sites in the interior of the silicon nanocrystals as well as at surface sites of the nanocrystal. During further growth of the nanocrystals, their surface area increases. Phosphorus atoms from the gas phase will adhere to surface sites, while also already incorporated phosphorus can diffuse towards these surface states due to the high diffusional mobility of phosphorus in silicon at high temperatures [Sze07]. These diffusion processes continue as long as the crystallites remain at high temperatures, even after the nanocrystals have already left the reactive plasma regions and their growth has stopped.

As a consequence of the reduced melting point of small particles (compare Section 3.2.2), it is also very probable that the growing particles exist as liquid droplets in the hot zones of the reactor. In this case, the mobility of the phosphorus impurity atoms is even higher and enables efficient surface segregation. By either of these mechanisms, a thin surface layer will develop with the local phosphorus concentration exceeding the concentration inside the nanocrystals by far.

The tendency of phosphorus to segregate at silicon surfaces has already been observed in different situations. A "pile-up" of phosphorus atoms at the Si/SiO_2 interface has been identified by Johannessen *et al.* during the oxidation of highly phosphorus-doped silicon samples [Joh78]. Here, the phosphorus concentration at the interface exhibits a sharp peak exceeding the bulk doping level. Also, Margalit and Lau *et al.* report on the segregation behavior of phosphorus. Due to the high density of unsaturated silicon bonds at the interface, phosphorus can concentrate in a very thin region at the interface [Lau89, Mar72], where the phosphorus atoms are not electrically active and are lost for electronic transport [Joh78, Lau89]. Also during the epitaxial growth of crystalline silicon, the segregation of phosphorus is a known phenomenon. Thus, in molecular beam epitaxy the growth temperature has to be kept below 350 °C to enable efficient phosphorus incorporation and to avoid excessive phosphorus enrichment of the surface layer [Fri92, Nüt96, Qin05].

In the case of boron, no comparable segregation has been reported in the literature. While boron is also subject to diffusion, the extreme segregation to surfaces and interfaces as is the case for phosphorus is not observed [Nüt96, Lau89]. Consequently, efficient boron incorporation is easily achieved during molecular beam epitaxy. The corresponding SIMS measurements with spin-coated films of boron-doped silicon nanocrystals showed no decrease of the boron concentration after the removal of the oxide as can be seen from Figure 4.14. Later in this work, the almost complete incorporation of substitutional boron acceptors in laser-annealed films of silicon nanocrystal layers will be demonstrated. Only in the case of extremely boron-doped samples exceeding concentrations of $6.5 \times 10^{20}\,\mathrm{cm}^{-3}$ partial boron segregation has been reported in the literature, whereas concentrations of up to $1.3 \times 10^{20}\,\mathrm{cm}^{-3}$ led to no such effects [Pea49]. Thus, we cannot rule out the possibility of slight segregation for the samples with the highest doping concentrations in the range of $5 \times 10^{20} - 10^{21}\,\mathrm{cm}^{-3}$.

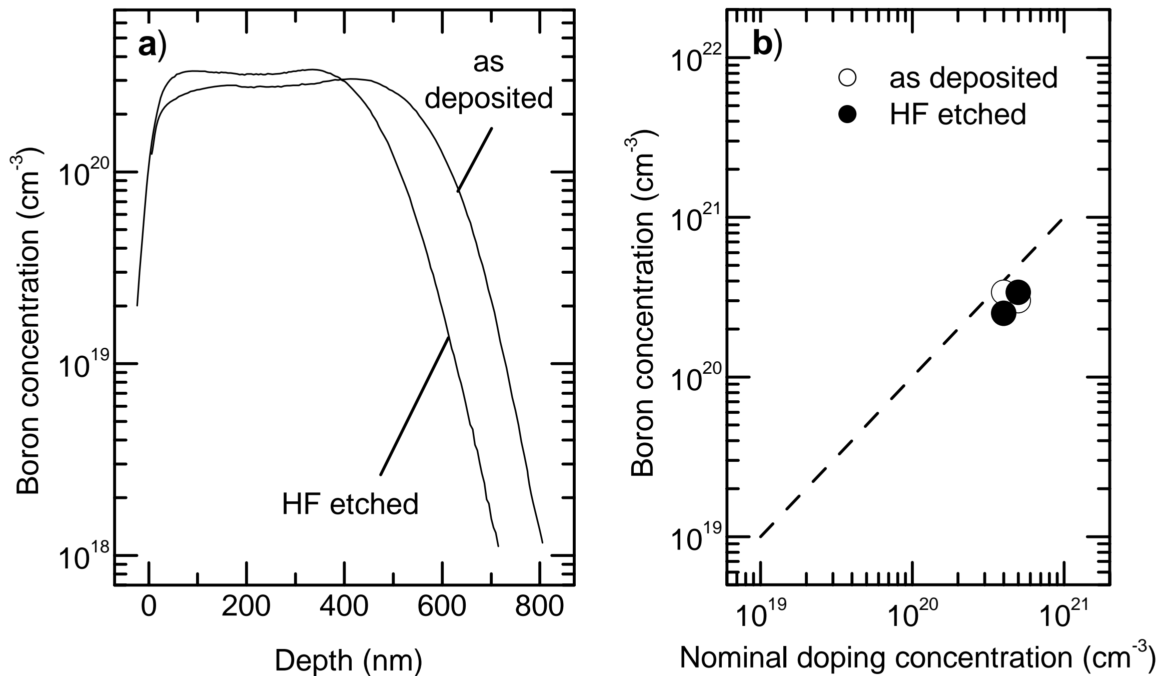

Figure 4.14: a) Depth profile of the boron concentration as determined by SIMS measurements of a spin-coated boron-doped silicon nanocrystal layer before and after HF etching. b) Mean boron concentration in spin-coated silicon films before and after etching versus the nominal boron concentration.

For reasons of clarity, if not explicitly mentioned otherwise, the doping concentrations stated in this work always refer to the actual doping concentrations as determined from mass spectrometry after oxide removal. In the case of samples for which this analysis was not available, the nominal doping concentration was divided by a factor of 20 for phosphorus-doped samples, which is in agreement with the EPR phosphorus concentrations, while no such correction was performed for boron-doped samples.

4.3 Optical Properties of Silicon Particle Films

4.3.1 Reflectivity spectra

In Section 3.4 the intimate connection of the dielectric function with the structural properties of a material has been pointed out, making this quantity a measure, *e.g.*, of the crystallinity or of an alloy composition. The dielectric function as a function of the light energy can be either determined from spectroscopic ellipsometry, or from complementary reflectance and transmittance measurements in the case of thin film samples. Via the Fresnel equations and the Lambert-Beer law of absorption, the optical reflectance and the transmittance are closely interlinked with the dispersive and the absorptive part of the dielectric function and form an equivalent representation of the optical properties.

Figure 4.15 depicts the results of reflectivity measurements of a 1 μm thick spin-coated film of hot wall silicon nanoparticles, of a 1.2 μm thick microwave silicon nanocrystal layer with a mean crystal diameter of 20 nm, and of a crystalline silicon reference (top to bottom). Two

main regions can be discerned in the spectra of the thin silicon particle films: in the low energy region of the spectra, regularly spaced thin film interference fringes are evident, whereas broader characteristic peaks appear in the UV spectral region. The position of the latter coincides with the Van-Hove-energies E_1 and E_2 of crystalline silicon at photon energies of 3.4 eV and 4.5 eV, respectively (see Section 3.4 and Figure 3.4).

Apart from the crystalline reference in Figure 4.15, the Van-Hove-peaks are distinctly visible for the microwave reactor silicon nanocrystal layer. This shows that a crystalline silicon electronic band structure is present in the silicon nanocrystals. The electron wavevector values at which the relevant transitions occur ($k \in [0, \frac{2\pi}{\sqrt{3}a}]$ and $k \approx 0.8\frac{2\pi}{a}$ for E_1 and E_2, respectively) show that the Brillouin-zone is well-defined for the silicon nanocrystal layer. The similarity with the crystalline reference sample in this spectral region is an argument that the microwave reactor silicon nanocrystals consist of single crystalline material, which is in agreement with the XRD analysis and the TEM observations.

In the case of the hot wall silicon nanoparticles, only a faint signature of the Van-Hove-peaks is present in the reflectivity spectrum. This is an indication that only a fraction of the material exhibits crystalline grain sizes of 20 nm that has been derived from analyzing the XRD diffraction peak width. The larger part shows crystalline grains on the order of 5 nm in diameter, leading to the onset of electron confinement effects. Similar to the situation discussed in Section 3.3.2 for the case of phonons, here the electron wavevector becomes undefined and the characteristic transition energies become diffuse. In this respect, the results of Raman scattering and EPR spectroscopy are confirmed, which both hinted at a much smaller average size in the ensembles of hot wall reactor silicon nanoparticles.

However, also other effects like the microscopically rough surface of the hot wall reactor nanoparticle film have to be kept in mind for the interpretation of the reflectivity spectrum. Unlike for the microwave nanocrystals, the probing wavelength is comparable with the surface structure dimensions for the hot wall material. Thus, a part of the reduced visibility of the Van-Hove-peaks can also be attributed to scattering effects.

4.3.2 Index of refraction

From the thin film interference fringes apparent in the IR and the visible spectral regions in Figure 4.15, the wavelength in the material and thus the index of refraction can be evaluated as a function of the photon energy. These oscillations are a consequence of constructive and destructive interference of multiple internal reflections of the reflected or transmitted light. From the spectral position of the interference extrema in reflectivity or transmission measurements, the index of refraction can be determined with great accuracy if the thickness of the thin film is known [Swa84, The97].

As can be seen in the figure, the amplitude of the interference fringes decreases for higher photon energies until at some point no interferences are discernible any longer. This is the case for strong absorption in the film at higher photon energy enabling *e.g.* interband transitions in the material. Part of the decreasing amplitude has to be ascribed to the surface roughness of the samples, leading to a loss of coherence for multiply reflected shorter wavelengths. From a detailed analysis of the interference fringes in transmission measurements, evaluating the energy positions of these extrema and the damping of the interference amplitude, it is possible not only to determine the refractive index and the absorption coefficient, but also the surface roughness of the thin film

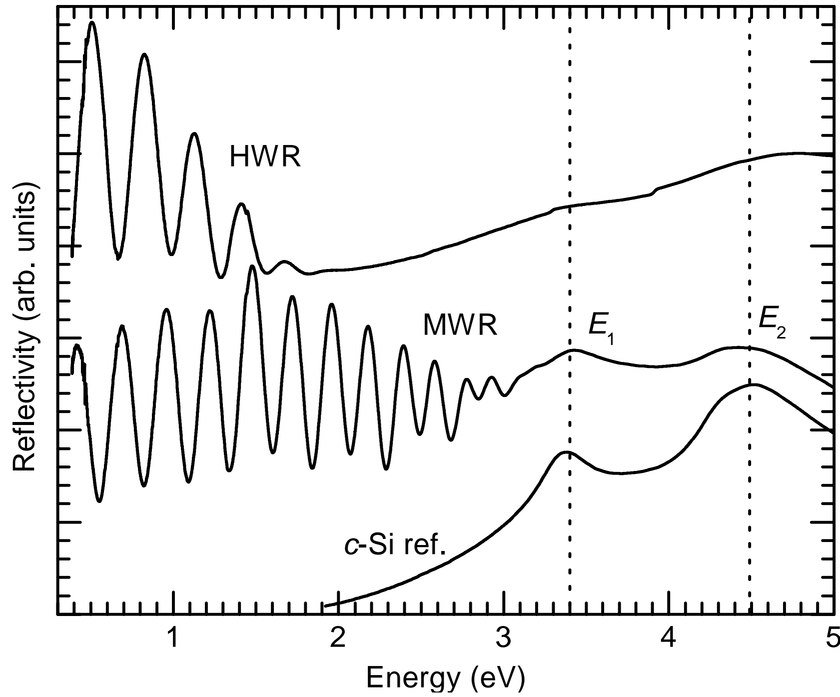

Figure 4.15: Reflectivity spectra of spin-coated layers of hot wall reactor silicon nanoparticles and of microwave reactor silicon nanocrystals in comparison with that of a *c*-Si reference. Thin film interference fringes and van-Hove-peaks dominate the low and the high energy spectral regions, respectively.

[Aqi02]. A simple equation holds for the index of refraction n at the position of an interference extremum:

$$n(\lambda) = \frac{m\lambda}{4d} \tag{4.4}$$

where m is the order of the extremum, λ is the wavelength at the extremum, and d is the thickness of the thin film. The extremum order, m, is an integer number that is even for maxima and odd for minima in the reflectivity and vice versa for transmission spectra, while an additional phase shift, *e.g.*, in the case of a highly reflecting substrate, leads to a reversal of this behavior. If m is not known, for instance because only a small spectral region is accessible, alternatively the following relation can be applied, which follows from Equation 4.4 evaluated for subsequent maxima or minima positions:

$$\frac{n(\lambda_{m+2})}{\lambda_{m+2}} - \frac{n(\lambda_m)}{\lambda_m} = \frac{1}{2d}. \tag{4.5}$$

From a combination of Equations 4.4 and 4.5, m and n are obtained. The determination of the index of refraction via this method is preferable to evaluating the Fresnel equation for normal reflection in the spectral regions of thin film interferences, whereas the latter lends itself in regions of strong absorbance.

Figure 4.16 shows the result of this analysis for several layers consisting of hot wall silicon nanoparticles and microwave reactor silicon nanocrystals (open and full circles, respectively). Although quite different materials and different film thicknesses were present, the index of refraction agree well, showing a global underlying material property. The absolute value of the index of refraction is significantly lower than in the case of crystalline silicon (solid line, [Asp83, Asp99]). In contrast, a comparison with the refractive index of an etched porous silicon sample

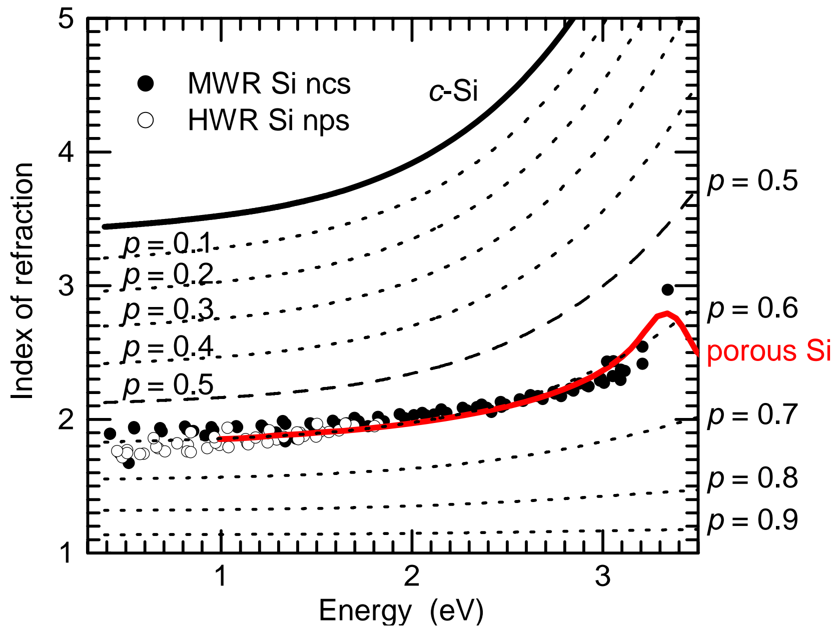

Figure 4.16: Index of refraction of hot wall silicon nanoparticles (HWR Si nps) and microwave reactor silicon nanocrystals (MWR Si ncs) as a function of the photon energy (open and full circles, respectively). The index of refraction of crystalline silicon and of an etched porous silicon sample are also shown [Iof08]. The dotted and dashed lines display the calculated optical dispersion for a Bruggemann effective medium of silicon with the indicated porosity values.

with 60% porosity (red line, [Iof08]) shows very good agreement. Consequently, the porosity of the network of spin-coated silicon nanoparticles and nanocrystals should amount to a similar value, which will be modeled by an effective medium theory in the following.

4.3.3 Effective medium interpretation

The optical properties of the porous spin-coated silicon layers can be described as an effective medium, which exhibits, *e.g.*, an intermediate refractive index between those of crystalline silicon and air. Several concepts of constructing such an interpolation have been highlighted in Section 3.4.3, and, both, the Maxwell-Garnett and the Bruggemann effective medium theory have been applied to the data for the spin-coated layers. It is found that the Maxwell-Garnett approximation is most probable not applicable to the present situation. The obtained porosities are too small, while the dispersion is constantly underestimated. If the data are interpreted in this approach, the porosity changes with the energy and amounts to 45% around 0.5 eV, while a porosity of 30% is obtained at 3.3 eV.

If instead, the Bruggemann effective medium approach is used (dotted lines in Figure 4.16), the refractive index of the spin-coated silicon layers is well described by a constant porosity value of 60%. Both, the hot wall reactor silicon nanoparticles and the microwave reactor silicon nanocrystals follow the spectral shape of the interpolated refractive index. The same holds for the porous silicon data from literature [Iof08]. Thus, the Bruggemann effective medium approximation is able to describe all three materials and the percolation threshold at $p = \frac{2}{3}$, which is implicitly included in the Bruggemann model seems to be compatible with the microtopological situation

present in the spin-coated silicon layers and the porous silicon. This enables us to apply Equation 3.21 to interpolate the optical functions of the layers, instead of having to use a parametrized version of the general Bergmann representation fit to the data for this purpose [The97].

The good agreement with the etched porous silicon is surprising considering the different microscopic structure. The wet-chemically etched porous silicon is a self-supporting network of interconnected silicon nanostructures, whereas the spin-coated hot wall reactor silicon nanoparticles and microwave reactor silicon nanocrystal layers are loosely connected aggregated films. In porous silicon, a percolating backbone structure is present as a consequence of the electrochemical etching process. In contrast, the mechanical stability of the spin-coated particle network stems only from interparticle contact regions mediated by capillary forces during the solvent evaporation. The different microstructure of both materials should influence the polarizability and the optical functions according to Subsection 3.4.3.

An interesting difference between hot wall reactor and microwave reactor material is that in the case of hot wall reactor silicon nanoparticles, the interference oscillations in Figure 4.15 disappear already at photon energies of about 1.8 eV, whereas in microwave reactor silicon nanocrystals, they are observed up to photon energies of 3.3 eV, just below the strong absorption edge of crystalline silicon (E_1). This can either be due to a stronger absorption in the hot wall nanoparticles or be a consequence of a larger surface roughness, leading to phase decoherence during multiple reflections and thus to a stronger damping of the interference fringes. Not only to clarify this question, we will turn to the absorption coefficient of the silicon layers in the next subsection.

4.3.4 Optical absorption

Absorption coefficient of silicon nanocrystals

The absorption coefficient, α, of as-deposited microwave reactor silicon nanocrystal layers has been determined by optical reflection and transmission measurements and by photothermal deflection spectroscopy. To cover the full dynamic range of the absorption coefficient, which in semiconductors typically spans over many orders of magnitude, these two measurement techniques were combined and were applied to samples with different thicknesses giving the solid curve in Figure 4.17. As can be seen in the figure, the absorption coefficient indeed increases by five orders of magnitude with the energy increasing from 0.5 to 5 eV. For better comparison, The data in the graph are corrected for the layer porosity following the Bruggeman effective medium theory. For a porosity of 60%, this correction comes close to multiplying the spectra by a constant factor of five (compare, *e.g.* [Kov96]). This procedure leads to a good overlap with the absorption coefficient of crystalline silicon (dashed curve, [Das55, Asp99]) in the UV spectral region of strong absorption.

The absorption in the as-deposited silicon nanocrystals for energies below 3 eV is significantly stronger than in single crystalline silicon material, as Figure 4.17 illustrates. This result is similar to the situation in microcrystalline silicon grown from chemical vapor deposition (dotted line, [Stu94]). The enhanced optical absorption can be a consequence of internal scattering in the heterogeneous microcrystalline phase and also be due to the higher disorder with respect to crystalline silicon, which also applies for our silicon nanocrystals. Defect states within the band gap allow absorption processes that are not possible in crystalline silicon. Hence, the absorption

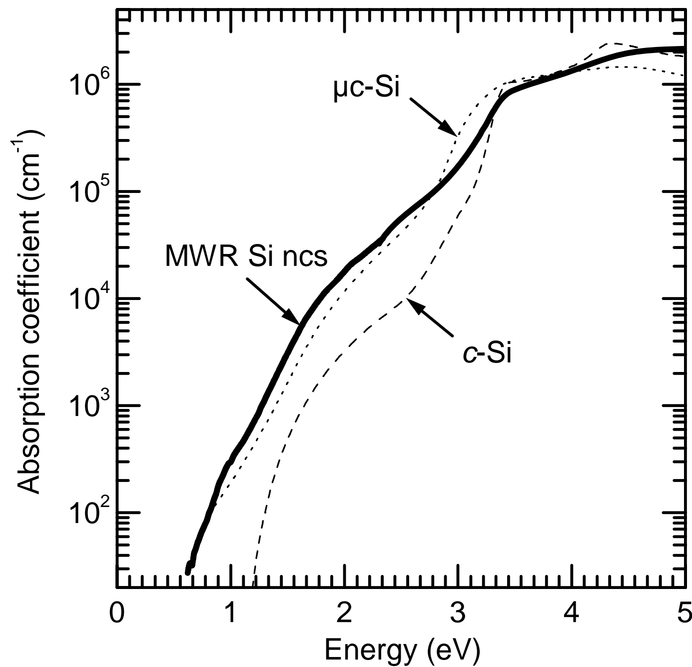

Figure 4.17: Absorption coefficient of spin coated layers of microwave reactor silicon nanocrystals (solid curve). Literature data for *c*-Si and microcrystalline silicon are also shown (dashed and dotted lines, respectively).

coefficient of microcrystalline silicon and of the silicon nanocrystal layers does not exhibit one sharp edge as can be observed for the crystalline silicon band gap at an energy of about 1.2 eV, but shows a continuous decrease towards lower photon energies.

Such behavior is typical for disordered systems such as amorphous silicon, where additional to the "optical band gap" energy the energy slope of the exponential decrease below the band gap, the so-called "Urbach energy", is used to characterize the tail state distribution of a material. In the case of the spin-coated silicon nanocrystals, only in the spectral region around $0.5 - 1.5$ eV, an exponential increase of the absorption coefficient can be assigned. A similar absorption coefficient increase is known for etched porous silicon samples, which can be regarded as a material with similar physical properties. However, in temperature dependent measurements, Kovalev *et al.* could show that the continuous increase of the absorption coefficient in porous silicon is is not a consequence of an Urbach tail [Kov96].

Absorption in hot wall reactor nanoparticles

In the case of hot wall reactor grown silicon nanoparticles, the absorption coefficient determined from optical reflectivity and transmission measurements is significantly larger than that of microwave reactor silicon nanocrystals. As Figure 4.18 displays, the absorption is by a factor of six stronger than in the microwave silicon nanocrystal layers. In fact, if the data are downshifted by this factor, both curves coincide.

The observation that the hot wall material is a significantly better absorber material than microwave reactor silicon nanocrystal layers explains also the strong damping of the interference fringes in Figure 4.15. On the other hand, the measured absorption coefficient appears even

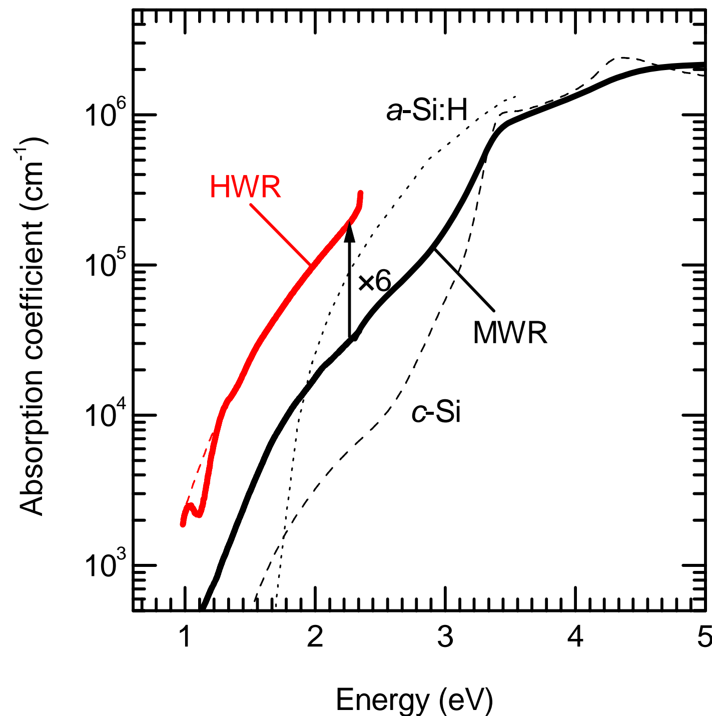

Figure 4.18: Absorption coefficients of hot wall reactor silicon nanoparticles and microwave reactor silicon nanocrystals. The literature values for crystalline silicon (*c*-Si) and hydrogenated amorphous silicon (*a*-Si:H) are also shown for comparison [Stu94, Buc98].

higher than in the case of the completely disordered amorphous silicon for which the absorption coefficient is also given in Figure 4.18 (dotted line [Buc98]). The structural investigation of this material, *e.g.*, in high resolution transmission electron microscopy, indeed revealed the presence of disordered or amorphous inclusions and a significantly larger dangling bond concentration has been found in hot wall nanoparticle samples by electron paramagnetic resonance.

Due to the specific microstructure of the porous hot wall reactor silicon nanoparticle network, light trapping effects can effectively improve the coupling of the incoming light into the thin film. The feature size of the structures visible in Figure 4.4 b) and d) is in the range of 100 − 500 nm, which is smaller than, but of the same order of magnitude as the wavelength of the light in the pertaining energy range (the absorption saturates at an energy of 2.3 eV, which corresponds to a wavelength of 540 nm). Thus, spin-coated hot wall silicon nanoparticle layers of about 1 μm thickness appear already rather dark brown. The internal scattering increases the effective thickness of the films and thus leads to the enhanced absorption coefficient with respect to amorphous silicon.

Absorption in doped silicon nanocrystals

The influence of the doping on the optical absorption in microwave reactor silicon nanocrystal layers is shown in Figure 4.19. Here, the optical absorption of an intrinsic silicon nanocrystal layer, of phosphorus-doped samples with doping concentrations of $3 \times 10^{18}\,\mathrm{cm}^{-3}$ and $3 \times 10^{19}\,\mathrm{cm}^{-3}$, and of a highly boron-doped sample with a boron concentration of $10^{21}\,\mathrm{cm}^{-3}$ are shown. At these high doping concentrations, the absorption of free carriers in the infrared spectral

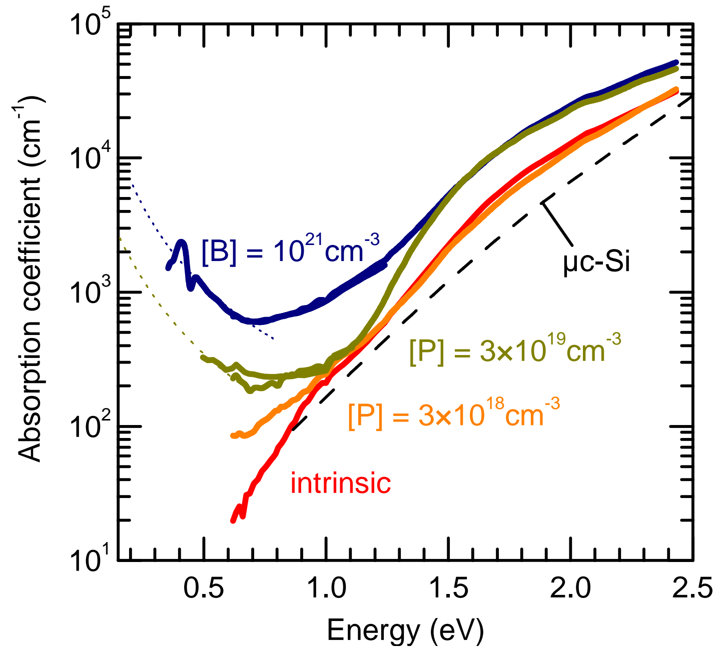

Figure 4.19: Absorption coefficient of intrinsic, boron- and phosphorus-doped microwave reactor silicon nanocrystal layers. Literature data of the absorption coefficient of microcrystalline silicon and simulations following the Drude model are also shown.

region increases with decreasing energy and dominates the absorption coefficient of crystalline silicon [Sch81]. Indeed, for the extremely boron-doped sample, an increase of the absorption at energies below 0.7 eV is clearly evident.

While the absolute absorption coefficient as a function of the photon energy corresponds well to experimental data for crystalline silicon samples doped around 10^{20} cm^{-3} boron atoms [Sch81], the shape of $\alpha(\hbar\omega)$ has also been fitted by the Drude model corresponding to Equation 3.20, which is depicted by the dotted lines in the figure. Indeed, an effective carrier concentration value of 1.0×10^{20} cm^{-3} is returned from the simulation, and as a second parameter, a carrier mobility of 14 cm^2 V^{-1} s^{-1} is obtained.

This value is found to fit the curvature of the experimental data best. Higher values of the mobility lead to smaller damping of the plasma oscillation and to a much steeper increase of the absorption coefficient with lower energy. Smaller mobilities, in contrast, lead to a different absorption behavior with an onset of strong absorption at higher energies. In this calculation, the effective density of states mass of the valence band, $m^*_{dv} = 0.81 m_0$, has been used to determine the damping constant, where m_0 is the free electron mass [Iof08].

In contrast, the intrinsic sample exhibits a continuously decreasing absorption coefficient with decreasing energy, in good agreement with the literature data for microcrystalline silicon also displayed in the figure. Notice that the shoulder in the absorption coefficient around $1.5 - 1.7$ eV can be found in many absorption spectra of silicon nanocrystals. It occurs exactly in the region where the absorption of crystalline silicon curves down to the indirect band gap energy and mirrors the shape of the absorption of crystalline silicon in this spectral region.

For the phosphorus-doped silicon nanocrystal layer doped with 3×10^{19} cm^{-3} phosphorus atoms, the absorption increase in the infrared spectral region is not as pronounced as in the case of the

highly boron-doped sample. Here, the absorption remains at a rather constant level in the photon energy range of $0.7 - 1.0\,\text{eV}$ and a weak increase of the absorption coefficient in the energy range of $0.5 - 0.7\,\text{eV}$. The dotted line shows the calculated free carrier absorption for an electron concentration of $1.5 \times 10^{19}\,\text{cm}^{-3}$ and a mobility of $30\,\text{cm}^2\,\text{V}^{-1}\,\text{s}^{-1}$. Due to the small overlap with the data, however, these values have to be regarded as a more qualitative result. The significantly higher carrier mobility is a consequence of the decreased effective mass in the conduction band of silicon $m^*_{dc} = 0.36 m_0$ [Iof08].

If the phosphorus concentration is reduced further, no free carrier absorption in the accessible spectral region can be distinguished any longer, as is shown for the sample doped with $3 \times 10^{18}\,\text{cm}^{-3}$ phosphorus atoms. In comparison to the intrinsic sample, only weak additional absorption processes around $0.6 - 1\,\text{eV}$ can be found. A quantitative evaluation of the carrier concentration and mobility is not possible in this case.

Summarizing the above results, we have direct evidence of free carriers in the silicon microwave reactor nanoparticles as a consequence of doping with boron and phosphorus. The apparent carrier mobilities are quite high and are of the order of $10\,\text{cm}^2\,\text{V}^{-1}\,\text{s}^{-1}$. In the case of the highly phosphorus-doped sample, an electron concentration amounting to about half of the actual phosphorus concentration in the nanocrystals can explain the absorption increase at low energies. In contrast, the hole concentration seen in the absorption spectrum of the extremely boron-doped sample is significantly smaller than the doping concentration by a factor of 10.

This supports the hypothesis that a significant fraction of the boron dopants are not incorporated substitutionally during the nanocrystal growth as can be concluded from the Raman measurements of the highly boron-doped layer in the as-deposited state (see Subsection 4.1.3). This interstitial boron incorporation will be further discussed in sections 6.3.1 and 6.3.2. There, a laser annealing procedure will be demonstrated to be necessary to see both the free carrier effects as well as the characteristic vibrational modes of substitutional boron atoms. To exclude that a systematically different absorption behavior is present for free carriers in the nanoparticles, it will be helpful to compare our results with literature data of similar systems in the next subsection.

Free carrier absorption of embedded nanocrystals

Mimura *et al.* have examined the free carrier absorption in 5 nm silicon nanocrystals produced by segregational growth in a cosputtered phosphosilicate glass matrix at temperatures of 1100 °C. For samples doped with nominal phosphorus concentrations of $4.5 \times 10^{20}\,\text{cm}^{-3}$ and $6 \times 10^{20}\,\text{cm}^{-3}$, they measured the characteristic increase of the free carrier absorption towards lower energies as depicted in Figure 4.20 [Mim00]. While this doping concentration range is comparable with the values of the extremely boron-doped microwave reactor silicon nanocrystals, the absorption coefficient they determine is even smaller by an order of magnitude than what we observe for the boron-doped silicon nanocrystals. However, this does not hold as a proof for systematically weaker free carrier signatures in doped nanoparticle systems, as will be discussed below.

First, Mimura *et al.* could not determine the actual phosphorus concentration within the silicon nanocrystals. As was demonstrated in Subsection 4.2.3, after growth at high temperatures this quantity can disagree from the nominal dopant concentration by more than a factor of ten due to phosphorus segregation at the oxide interface. Second, the normalization procedure the authors use to calibrate the absorption coefficient is not necessarily applicable to the weakly absorbing

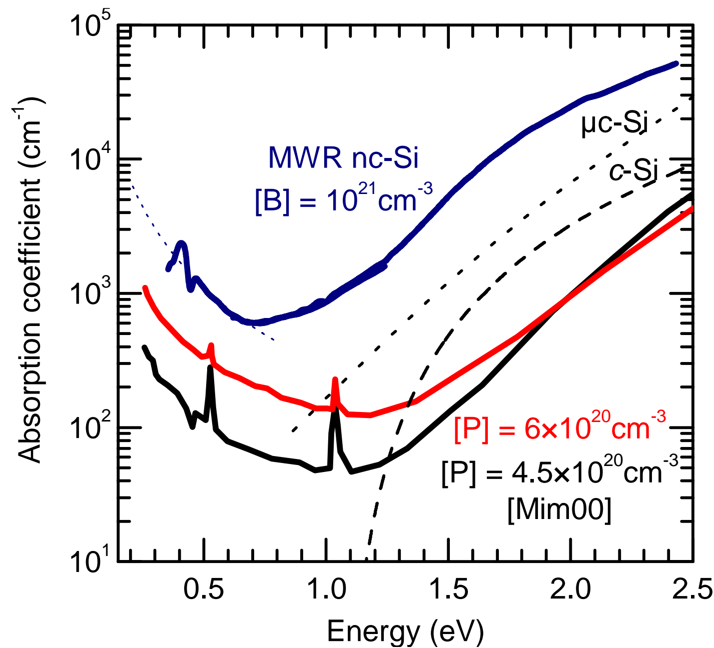

Figure 4.20: Absorption coefficient of highly phosphorus-doped silicon nanocrystals embedded in an oxide matrix [Mim00] in comparison with the absorption coefficients of micro- and single crystalline silicon and highly boron-doped microwave reactor silicon nanocrystals.

IR spectral region [Hay96]. Also, no light scattering effects within the optically thin system of oxide embedded nanocrystals were taken into consideration. Indeed, in the energy range above 1.3 eV their results fall even short of the absorption coefficient of crystalline silicon, as Figure 4.20 shows. Instead, an absorption coefficient in between that of microcrystalline and crystalline silicon is expected if structural defects are partly passivated by the surrounding oxide matrix. Thus it appears necessary to shift the absorption coefficient upwards by a correction factor of about five to adequately calibrate the absorption behavior of the pure nanocrystal material. On doing so, the free carrier absorption comes into good alignment with the calculated absorption coefficient for a free carrier concentration of about 10^{20} cm^{-3} [Sch81]. Also the values we measure for the extremely boron-doped microwave reactor silicon nanocrystals are of the same order of magnitude. If the correct concentrations of electrically active carriers were taken into account, and if the spectra were properly normalized, the both different types of doped nanocrystals might turn out to be quite similar.

4.4 Electrical Properties of Silicon Particle Films

The electrical properties of the spin-coated layers of silicon nanoparticles have been investigated next. From the point of view of potentially printable electronics, it would be interesting if a conductive system could be achieved by large-area coating of a substrate or by different printing techniques such as inkjet or screen printing. If not explicitly mentioned otherwise, the conductivity values given in the following have been measured on insulating polyimide substrates.

4.4.1 Electrical conductivity

Oxide barriers

The dark conductivity of as-deposited layers of microwave reactor silicon nanocrystals and hot wall reactor silicon nanoparticles is very low, making it difficult to specify reliable values. Anyway, typical results fall into the range below $10^{-12}\,\Omega^{-1}\,\text{cm}^{-1}$. The main reason for the high resistivity can be found in the numerous oxide interfaces between the loosely interconnected silicon nanocrystals in the spin-coated layers. After extraction from the plasma reactor and dispersing in ethanol, each single silicon nanocrystal is surrounded by a native oxide shell, which has a typical thickness on the order of $1-2\,\text{nm}$.

For the charge carriers in the nanocrystals, this silicon oxide (SiO_2) or suboxide phase (SiO_x, $1 < x < 2$) represents a high barrier confining them inside the nanocrystal and preventing drift or diffusion towards neighboring nanocrystals. Due to the large bandgap of SiO_2 ($E_g \approx 9\,\text{eV}$), it is almost impossible for the carriers to overcome this barrier by thermal activation (thermionic emission). However, due to the small thickness of the oxide layer, tunneling through the oxide layers is possible with a small but non-vanishing probability.

For the macroscopic conductivity, hundreds of thousands of such tunneling junctions have to be overcome, and upon applying an electric field a current can flow along a percolation path with the effectively smallest total oxide thickness (compare Section 3.6.1). The overall current will concentrate around relatively few spots exhibiting high current densities and making the overall conductivity unstable. This situation leads to the unreliable behavior mentioned above.

As already demonstrated in Figure 4.12, the oxide interfaces between the silicon nanocrystals can effectively be removed by a wet chemical etching step in dilute hydrofluoric acid. Astonishingly enough, this etching step does not lead to the complete destruction by dissolving the porous layer system, and only a reduction of the layer thickness by $10-50\%$ occurs, depending on the degree of surface oxidation of the silicon nanocrystals. However, the overall positive effects prevail, and the oxide removal leads to a great enhancement of the conductivity of the spin-coated layers. After the etching step, the conductivity of undoped silicon nanocrystal layers is typically on the order of $10^{-10}\,\Omega^{-1}\,\text{cm}^{-1}$.

Influence of doping

The dark conductivity of spin-coated boron- and phosphorus-doped silicon nanocrystal layers as determined after the oxide removal is shown as a function of the doping concentration in Figure 4.21.

As evident from the graph, the conductivity is around the intrinsic value of $10^{-10}\,\Omega^{-1}\,\text{cm}^{-1}$ for nominal doping concentrations ranging from $10^{15}\,\text{cm}^{-3}$ up to $10^{19}\,\text{cm}^{-3}$. Only if the doping concentration is increased further, a significant increase of the conductivity with the doping concentration is visible. Here, an abrupt rise of the conductivity is found for doping concentrations exceeding $1-2\times10^{19}\,\text{cm}^{-3}$ dopant atoms. In this high doping region, conductivity values on the order of $10^{-9}-2\times10^{-7}\,\Omega^{-1}\,\text{cm}^{-1}$ can be reached, which is several orders of magnitude higher than for the nominally undoped or the intermediately doped samples.

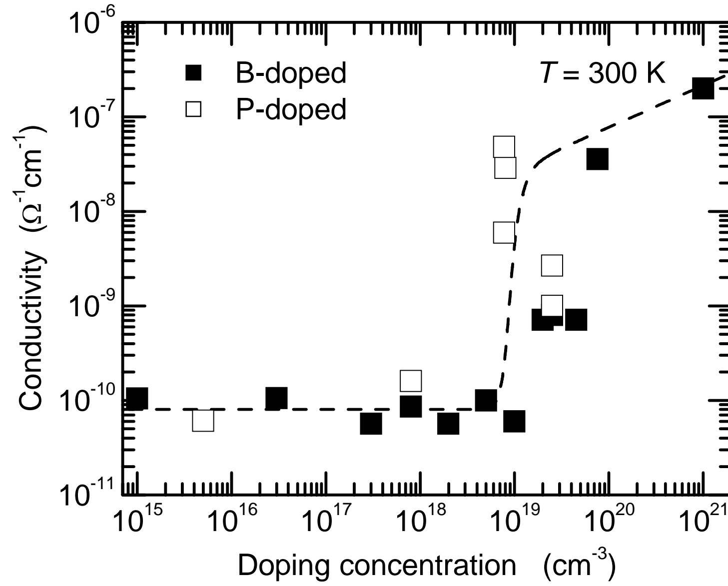

Figure 4.21: Electrical dark conductivity of as-deposited boron- and phosphorus-doped silicon nanocrystal layers versus the doping concentration. The native oxide shell has been removed by etching. The dashed line is a guide to the eye.

In the figure, the dashed line acts as a guide to the eye, marking roughly the highest obtained values for spin-coated silicon nanocrystals as a function of the doping concentration. It is composed of three components:

1. A constant conductivity value of $8 \times 10^{-11}\,\Omega^{-1}\,\mathrm{cm}^{-1}$ independent of the doping concentration at low and medium doping densities,
2. a sudden increase around a doping density of $10^{19}\,\mathrm{cm}^{-3}$, and
3. a sublinear increase of the conductivity, σ, with the doping concentration, N, for doping concentrations exceeding $2 \times 10^{19}\,\mathrm{cm}^{-3}$: $\sigma \propto N^{0.5}$

As Figure 4.21 shows, the curve constructed in this way (dashed line) qualitatively describes the electrical conductivity obtained with as-deposited boron- and phosphorus-doped silicon nanocrystal layers. It is clearly evident that the doping has an influence on the conductivity of the spin-coated silicon nanocrystal layers only if a sufficiently high doping density is chosen. Besides the free carrier absorption shown above as a microscopic characterization method, this is an additional direct proof that the dopants are at least partly active in the spin-coated nanocrystal network. For the boron-doped samples, the sudden onset of conductivity appears to be shifted to higher doping concentrations around $10^{20}\,\mathrm{cm}^{-3}$. If the same mechanism is responsible for this onset as for the phosphorus-doped samples, this might be a further sign of predominantly interstitial boron incorporation as was evident from the optical properties.

To clarify the sudden onset of the conductivity at a critical doping concentration, the mixed percolation and discrete-size effect model introduced in Section 4.4 can be applied. Under the assumption that only some of the particles are doped by single atoms, a percolation threshold for the transport through doped particles exists. However, according to Figure 3.7, the size of the

nanocrystals would have to amount to about 5 nm to explain the onset of conduction occurring at a critical doping concentration of $10^{19}\,\mathrm{cm}^{-3}$. In contrast, the silicon nanocrystals in Figure 4.21 had an average size of 20 nm, for which the model would lead to a steep onset of the conductivity around doping concentrations of $10^{17}\,\mathrm{cm}^{-3}$.

Consequently, mechanisms that contribute to an effective loss of carriers need to be included in the discussion. Here, as the most common structural deep defect, we want to focus on the intrinsic dangling bonds in the silicon nanocrystals. As amphoteric deep trap states they can trap both electrons and holes, which then are lost for transport as explained in Section 3.6.5.

Due to the energy position of the dangling bonds around midgap, the probability for free carriers in the nanocrystals to be trapped is almost 100%, and thus a compensation of up to the same amount of carriers as dangling bonds are present in the system is possible. As was shown in Section 4.1.4, the typical dangling bond concentrations in spin-coated layers of silicon nanocrystals are quite high and are around $2 \times 10^{19}\,\mathrm{cm}^{-3}$. Since this corresponds to the critical doping concentration observed in Figure 4.21, the critical onset is obviously dominated by a mere compensation mechanism rather than by the doping and percolation model. Temperature dependent conductivity data and EPR measurements will be able to corroborate this assumption.

Effective carrier mobility

To describe the macroscopic electric properties of these layers, above we have used the electrical conductivity of the films. The conductivity, σ, promoted by free carriers can be written as $\sigma = e\mu_\mathrm{e}n + e\mu_\mathrm{h}p$, where e is the elementary charge, n and p are the electron and hole concentrations, respectively, and $\mu_\mathrm{e,h}$ is the mobility of the respective carrier type. As we do not know the concentration of carriers in the layers, we cannot apply the above formula rigorously. Still, we can define an effective mobility μ_eff accounting for the unknown doping efficiency η, which gives the ratio of the carrier concentration within the films to the doping concentration N: $\eta = n, p/N$. The effective mobility then is

$$\mu_\mathrm{eff} = \eta\mu_\mathrm{e,h} = \frac{\sigma}{eN}. \tag{4.6}$$

In this view, the above results mean that the effective mobility in the doping range exceeding $4 \times 10^{19}\,\mathrm{cm}^{-3}$ is smaller than $3 \times 10^{-9}\,\mathrm{cm}^2\,\mathrm{V}^{-1}\,\mathrm{s}^{-1}$. As long as we cannot determine the real carrier concentration present in the doped silicon nanocrystal layers (or the doping efficiency η) we have no means to draw conclusions on the actual mobility of carriers through the silicon nanocrystal network. However, if we take into account the hole concentration of $5 \times 10^{19}\,\mathrm{cm}^{-3}$ visible in the free carrier absorption for a sample doped with $10^{21}\,\mathrm{cm}^{-3}$ boron atoms, a mobility value of $3 \times 10^{-8}\,\mathrm{cm}^2\,\mathrm{V}^{-1}\,\mathrm{s}^{-1}$ is obtained, which can be regarded as an upper limit for the overall mobility for the charge transport in the spin-coated silicon nanocrystal layers.

These low values of the carrier mobility seem to range well below what is necessary for any potential semiconductor application. Similarly small values have been reported for different production routes of silicon particle layers. In silicon nanocrystal films deposited by laser ablation, Burr *et al*. observed mobility values of $10^{-6}\,\mathrm{cm}^2\,\mathrm{V}^{-1}\,\mathrm{s}^{-1}$ [Bur97]. In etched nanoporous silicon films, Peng and coworkers determined a value of $10^{-4}\,\mathrm{cm}^2\,\mathrm{V}^{-1}\,\mathrm{s}^{-1}$, [Pen96]. Both types of materials are characterized by a more intimate interparticle contact. While the laser ablation is used for film formation in vacuum, free from any native oxide barriers, in the etching approach the silicon "nanoparticles" are not completely separated from each other, but are connected by

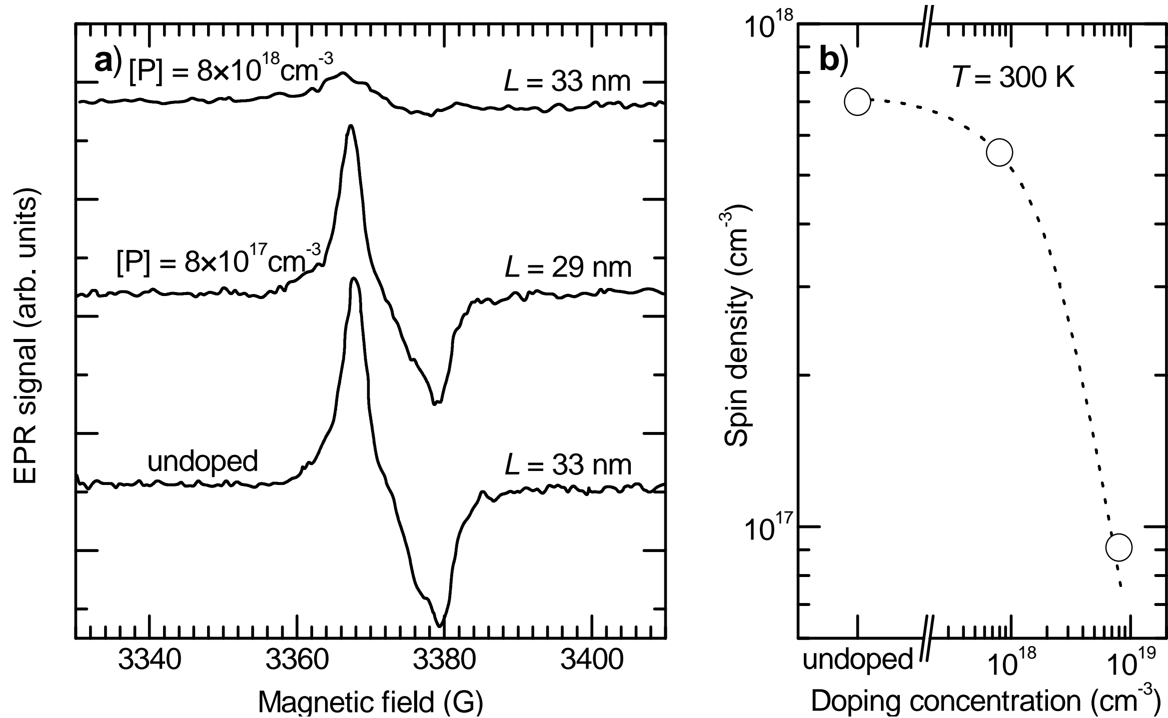

Figure 4.22: a) Room temperature EPR spectra of undoped and phosphorus-doped silicon nanocrystals. The decrease in the spin density is plotted in (b) as a function of the doping concentration.

silicon bridges. In contrast, the contact regions in between the spin-coated and etched silicon nanocrystals are rather small, which is responsible for the lower conductivity in this case.

The concept of an effective mobility fails in the intermediate doping concentration region where the conductivity is unaffected by the doping. Here, the electrical transport is carried by alternative transport paths such as space charge limited current or hopping transport through defect states.

4.4.2 Carrier compensation

Only the electrically neutral singly occupied dangling bonds (db^0) give rise to paramagnetic electronic states that are detectable in EPR measurements. Thus, if a fraction of the dangling bonds upon p- or n-type doping is transferred to a db^+ or db^- charge state, the total spin density of the sample should decrease accordingly. By measuring the spin density as a function of the doping concentration, the compensation of the carriers by dangling bonds in the nanocrystals can be directly evaluated.

The EPR spectra of undoped and phosphorus-doped silicon nanocrystal ensembles with average sizes around 30 nm are displayed in Figure 4.22. Upon increasing the phosphorus concentration, the intensity of the EPR signal is observed to decrease. The correlation with the doping concentration is shown in (b), where the total spin density derived from the spectra in (a) is displayed versus the phosphorus concentration. While a dangling bond concentration of $7 \times 10^{17}\,\mathrm{cm}^{-3}$ is observed in the undoped nanocrystals, $6 \times 10^{17}\,\mathrm{cm}^{-3}$ and $9 \times 10^{16}\,\mathrm{cm}^{-3}$ of such defects are present for phosphorus concentrations of $8 \times 10^{17}\,\mathrm{cm}^{-3}$ and $8 \times 10^{18}\,\mathrm{cm}^{-3}$, respectively.

Thus, the EPR data provide quantitative evidence for the interpretation by compensation through dangling bonds. If the dopant concentration exceeds the defect concentration in the layers, the majority of the defects become charged and the paramagnetic signal decreases. The other way round, almost all free carriers are trapped for doping concentrations below the defect concentration in the layers. Thus, the critical doping concentration in Figure 4.21 at which the sudden increase of the conductivity of spin-coated silicon films is observed corresponds to the defect concentration in the layers, in good agreement with the quantitative EPR results after dispersing and spin-coating ($2 \times 10^{19}\,\mathrm{cm}^{-3}$). In a more detailed analysis, also statistical effects have to be taken into account, because the discrete nature of the nanocrystals leads to a size-dependent degree of the carrier compensation [Ste07, Ste08b].

With boron-doped silicon nanocrystals, a comparable decrease of the defect density with increasing doping concentration could not be shown. This is mainly due to the fact that no homogeneously boron-doped nanocrystals with concentrations above $10^{19}\,\mathrm{cm}^{-3}$ were available. Instead, all samples in this doping range consisted of mixed ensembles of doped and undoped silicon nanocrystals. As a consequence of the mutual isolation of the silicon nanocrystals, only relatively small changes in the defect concentration can occur if the boron concentration is increased only in a fraction of the nanocrystals. The justified assumption that the majority of the boron atoms occupies interstitial lattice sites in the silicon nanocrystals adds further complexity to this situation.

4.4.3 Temperature dependent conductivity

Apart from the room temperature values of the dark electrical conductivity, the thermal activation of the conductivity gained from temperature dependent measurements allows conclusions on the transport processes involved. Figure 4.23 displays the results of such characterization in an Arrhenius plot. Here, the electrical conductivity is shown for an intrinsic sample and two samples with doping concentrations of $8 \times 10^{17}\,\mathrm{cm}^{-3}$ and $8 \times 10^{18}\,\mathrm{cm}^{-3}$ phosphorus atoms as a function of the inverse temperature. As can be seen from the figure, both, the absolute values of the conductivity and the slope of the conductivity depend strongly on the doping concentration. From the conductivity slope in the Arrhenius plot in the temperature range of $200 - 300\,\mathrm{K}$, thermal activation energies, E_A, have been derived according to the relation $\sigma(T) = \sigma_0 \exp(-E_\mathrm{A}/k_\mathrm{B}T)$.

While the room temperature conductivities of the intrinsic silicon nanocrystal layer and the sample doped with $8 \times 10^{17}\,\mathrm{cm}^{-3}$ phosphorus atoms differ only by a factor of two, their thermal activation energies differ largely (450 meV versus 290 meV), leading to a conductivity difference of more than one order of magnitude already at 200 K. The sample with a phosphorus concentration of $8 \times 10^{19}\,\mathrm{cm}^{-3}$, shows a significantly higher room temperature conductivity as was already shown in Figure 4.21. Additionally, the thermal activation energy of the conductivity is only 70 meV, which is much smaller than for the other two samples. Similar trends can also be observed for the spin-coated boron-doped silicon nanocrystal layers.

The behavior of the activation energy with the doping concentration can be understood within the compensation mechanism by the dangling bonds. At low doping concentrations, the Fermi level resides at the position of the dangling bond defects, E_t, which form a peak in the density of states at midgap at $\left|E_\mathrm{t} - E_\mathrm{c,v}\right| \approx 0.5\,\mathrm{eV}$,.where $E_\mathrm{c,v}$ is the energy of the respective electronic band. Thus, the conductivity is activated with $E_\mathrm{A} = \left|E_\mathrm{t} - E_\mathrm{c,v}\right| \approx 0.5\,\mathrm{eV}$.

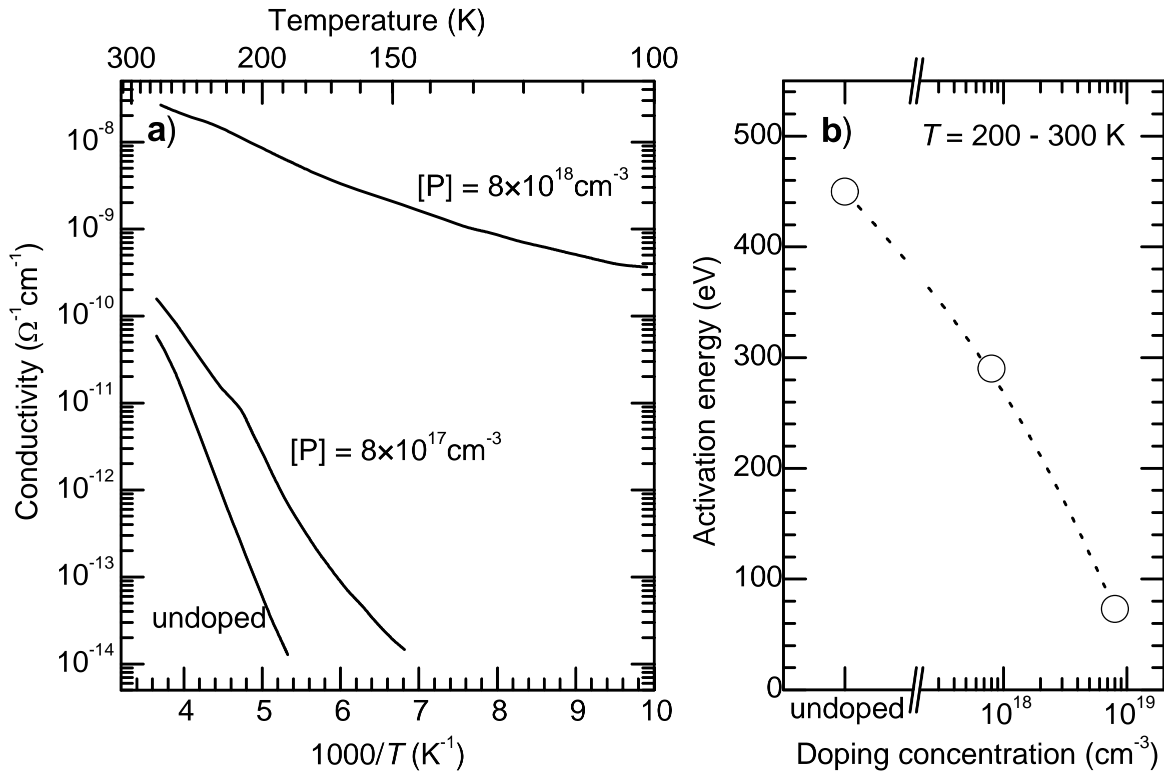

Figure 4.23: a) Temperature dependent conductivity of spin-coated intrinsic and phosphorus-doped silicon nanocrystal layers. (b) Thermal activation energies of the conductivity as derived from (a) versus the doping concentration.

If the doping concentration is increased, an increasing number of defects will be charged, and if the doping concentration has approached the defect density, the Fermi level will approximately be in between the both energy values. Indeed for the sample with a phosphorus concentration of $[P] = 8 \times 10^{18}\,\mathrm{cm}^{-3}$, which roughly equals the typical defect density in the spin-coated layers, $N_\mathrm{t} = 10^{19}\,\mathrm{cm}^{-3}$, the observed activation energy amounts to $290\,\mathrm{meV} \approx \left|E_\mathrm{t} - E_\mathrm{c,v}\right|/2$. Further increase of the doping density leads to a shift of the Fermi level towards the involved band and further decline of the activation energy is the consequence.

Alternative interpretations can be applied using the grain boundary barrier model introduced in Section 3.6.5, or the concept of potential fluctuations in Section 3.9. However, at this stage, the physical properties of the spin-coated silicon nanocrystal layers are sufficiently described by this compensation model. We will come back to the other two possible explanations in the context of polycrystalline silicon layers from metal-induced crystallization and laser annealing in the subsequent chapters.

While the electrical data cannot well be described by space-charge limited current in this temperature range, alternatively a hopping mechanism can be assumed for the electrical transport. Then, the characteristic temperature constant, T_0, can be evaluated from the data according to Equation 3.26. The obtained values of $T_0 = 5 \times 10^5\,\mathrm{K}$, $2 \times 10^5\,\mathrm{K}$, and $1.3 \times 10^4\,\mathrm{K}$ for the undoped sample and phosphorus concentrations of $8 \times 10^{17}\,\mathrm{cm}^{-3}$ and $8 \times 10^{18}\,\mathrm{cm}^{-3}$, respectively, indicate that in general such an interpretation is possible. For comparison, Rafiq *et al.* found $T_0 = 1.1 \times 10^4\,\mathrm{K}$ in conductivity measurements in vertical geometry with undoped 8 nm silicon nanocrystal ensembles [Raf06]. While Efros-Shklovskii variable range hopping could

explain the much larger values observed with our samples, the dependence of T_0 on the doping concentration is still unclear in this case. Due to the good agreement with the above discussed compensation model, the latter interpretation is favored.

4.4.4 Photoconductivity

Photo- versus dark conductivity

In the spin-coated layers, the conductivity strongly depends on the illumination level. Due to the inherently low concentration of carriers, especially undoped and weakly doped silicon nanocrystal layers are very sensitive to illumination. As Figure 4.24 illustrates, an increase of the absolute conductivity by two orders of magnitude can be observed upon illuminating the undoped silicon nanocrystal layer with a white light halogen lamp. Here, interdigital contact structures with a lateral contact distance of 25 μm have been deposited onto the substrate before the silicon nanocrystals were spin-coated on top. The samples were illuminated through the top nanocrystal layer and the full spectral irradiation intensity in this experiment was estimated to about $< 1\,\mathrm{W\,cm^{-2}}$.

As can be seen from the figure, the conductivity reacts relatively fast on the change in illumination. Both, the dark conductivity as well as the photoconductivity values recover their initial values after repeated switching. No significant persistent photoconductivity effects are found, except for the RC-relaxation time constant of the sample in the range of several seconds.

Due to the large effect on the conductivity upon illumination, it was possible to measure the photoconductivity as a function of the photon energy and so to test whether the absorption processes forming the spectra shown in Section 4.3.4 are an intrinsic property of the silicon nanocrystals and contribute to the generation of charge carriers in the layers, or whether they are partly due to extrinsic effects such as contaminations in the layers.

Spectrally resolved photoconductivity

In Figure 4.25 the result of a spectrally resolved photoconductivity measurement of a layer of undoped microwave reactor silicon nanocrystals is shown (symbols). To be able to assess and interpret the spectral shape of the conductivity, the absorption coefficient of a layer of the same undoped silicon nanocrystals from Section 4.3.4 is also shown for comparison (full red line) together with the literature values for crystalline and microcrystalline silicon (dashed and dotted red lines, respectively). The left and the right hand axes are scaled by a constant factor to align the photoconductivity signal with the absorption coefficient in the low energy region.

As is evident from the figure, in the low energy region of the spectrum, a good alignment of the photoconductivity with the absorption coefficient can be achieved, whereas for energies higher than 2 eV, the increase in the photoconductivity is weaker than the increase of the absorption coefficient. Still, the photoconductivity continues to increase up to photon energies of 5 eV, where the difference between the photocurrent and the scaled absorption coefficient amounts to more than one order of magnitude.

The shape of the spectrally resolved photoconductivity in the low energy region demonstrates again the presence of band-tail states and defects at energies below the fundamental bandgap of

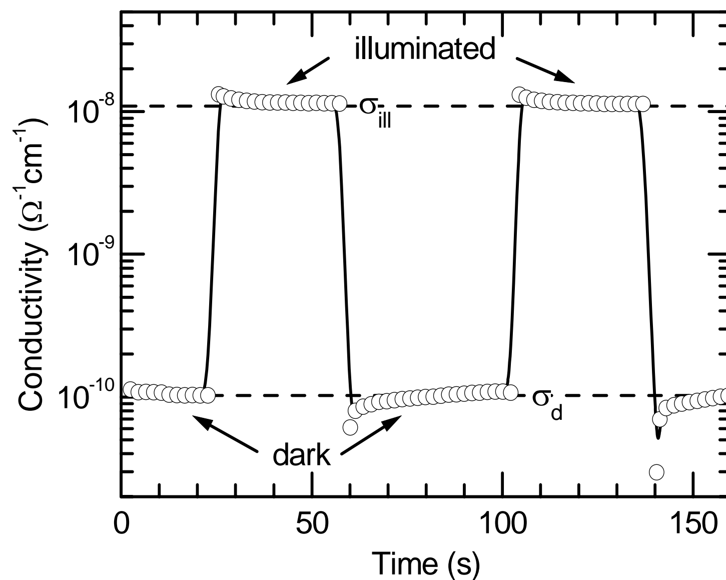

Figure 4.24: Room temperature photoconductivity response of an undoped silicon nanocrystal layer upon illuminating with a white light halogen source. The two switching cycles show the reversibility of the effect.

crystalline silicon. These states extend down to energies of 0.6 eV, almost approaching midgap energy values. Optical processes that contribute to the current at these low energies can, *e.g.*, comprise the excitation of carriers trapped at the dangling bond trap states around midgap.

The reason for the discrepancy between the absorption coefficient and the photoconductivity at high photon energies can be found in the combination of diminished absorption length at the respective energies and the microstructure of the silicon nanocrystal films. For low photon energies, the absorption cross-section of the incoming light is fairly small, and the photons are thus absorbed statistically distributed over the full porous silicon nanocrystal network. An increase of the photon energy in this spectral region leads to a more efficient light absorption, to a larger excess carrier concentration and thus to an increased photoconductivity.

At about 1.7 eV, the absorption coefficient of the silicon layer has approached the inverse thickness of the film (700 nm), leading already to a considerable decrease of the light intensity at the bottom of the illuminated film. For higher photon energies, the penetration depth of the light in the silicon nanocrystal layers continues to decrease, whereas the absorption probability for the light becomes higher for the individual nanocrystals close to the film surface. Due to the high degree of porosity, however, even at absorption coefficients corresponding to penetration depths of < 7 nm, the photoconductivity continues to increase, because a significant fraction of the light is still scattered through the pores of the network. It needs to be remembered, however, that the absorption coefficient given in Figure 4.25 is the result of a correction for the porosity, and that, *e.g.*, a thinner silicon nanocrystal film with a thickness of 140 nm still has a transmittance of 3% at 4.5 eV.

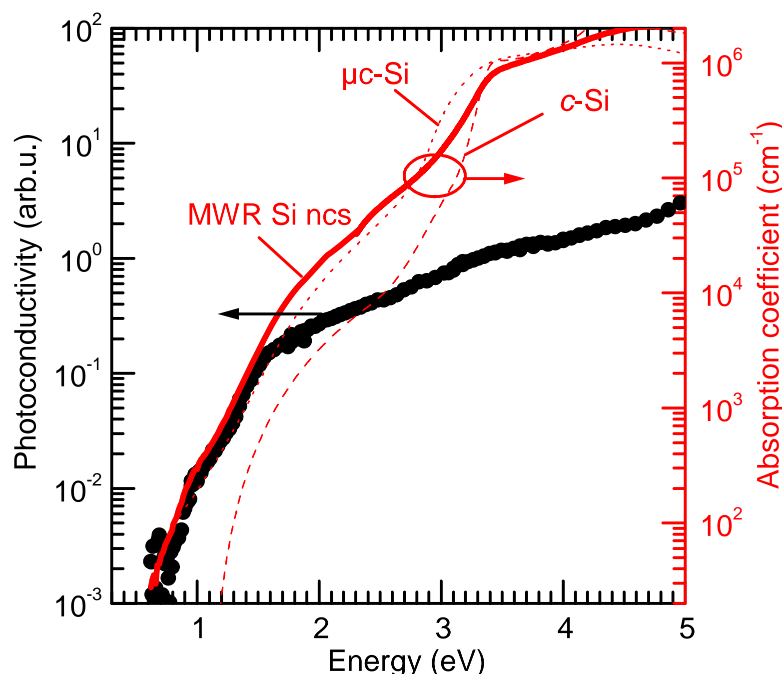

Figure 4.25: Spectrally resolved photoconductivity of an undoped 700 nm spin-coated silicon nanocrystal layer at room temperature. The absorption coefficients of the silicon nanocrystals, crystalline, and microcrystalline silicon are also given for comparison.

4.4.5 Thermal annealing

Recapitulating the electrical properties of the spin-coated silicon nanocrystal layers, it is necessary to state that the conductivity of these layers is extremely small, even after the removal of the native oxide surrounding the nanocrystals. For the applicability of this material, processes need to be developed that largely increase the overall mobility of the layers and enable the application of the material for semiconductor devices. In this context, annealing of the spin-coated layers seems to be one possibility. As pointed out in Section 3.2.2, due to their reduced size and the increased volume to surface ratio, nanocrystals exhibit a significantly reduced melting point, which can be exploited for this purpose [Gol96, Yan00, Bet04].

As an exploratory experiment, a one-hour isochronal annealing of spin-coated silicon nanocrystal layers was performed under vacuum ($< 10^{-7}$ mbar). Figure 4.26 shows the obtained dark conductivity of three exemplary samples in an Arrhenius plot versus the inverse annealing temperature. After the annealing the conductivity of the undoped hot wall reactor nanoparticle layers has increased significantly compared to the as-deposited samples once an annealing temperature of 800 K has been exceeded. Increasing the temperature further leads to a continued rise of the conductivity of up to almost four orders of magnitude for a one-hour anneal at 1073 K. In the temperature range of $673-1073$ K, a linear slope of 1.6 eV is observed for the conductivity from the Arrhenius plot in the figure.

This activation energy amounts to about one half of the value that is typical for the recrystallization of amorphous silicon, for instance [Spi98]. However, it is not straightforward to connect this value with the sintering and restructuring processes involved in the increase of the conductivity. Since the conductivity is the product of mobility and carrier concentration, both of these

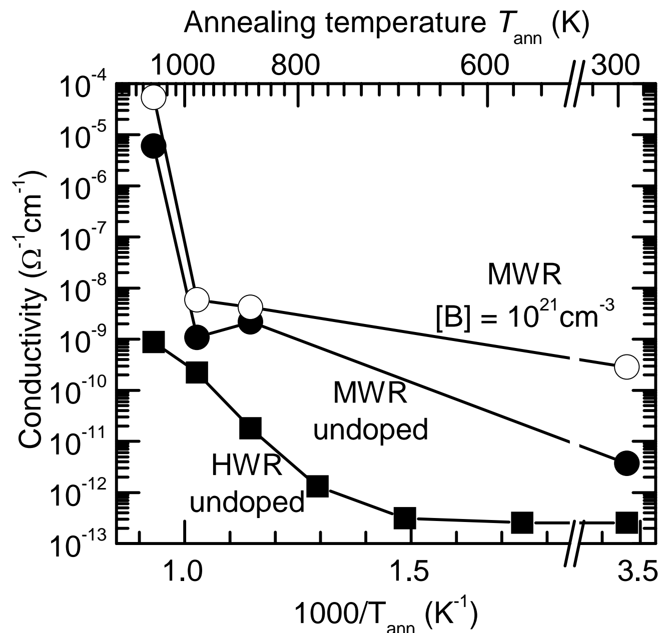

Figure 4.26: Dark conductivity at room temperature of vacuum-annealed layers of undoped hot wall reactor nanoparticles and undoped and boron-doped microwave reactor nanocrystals versus the inverse annealing temperature. The lines are guides to the eye.

properties might depend on the annealing in a complicated way. In addition, also the percolation through the particle network has to be taken into account.

For the microwave reactor silicon nanocrystals, the increase in the conductivity upon annealing is even more pronounced. Annealing at $873 - 973\,K$ provokes an improvement of the film conductivity by three orders of magnitude and an overall increase of six orders of magnitude is gained for a temperature of 1073 K. Strangely enough, doping the nanocrystals with the extreme concentration of $10^{21}\,cm^{-3}$ boron atoms does not lead to a large difference in the conductivity after the annealing. Instead, the initial difference of two orders of magnitude in the conductivity decreases to a factor of about ten after the anneal at 1073 K, indicating the possibility that the dopants present in the spin-coated films for example diffused out of the sample during the long-term anneal or were passivated by contaminants.

It needs to be mentioned that these samples were not etched with dilute hydrofluoric acid as usually performed to achieve conductive layers. Consequently, also the conductivity values cannot be directly compared to those in Figure 4.21. It appears that omitting the oxide etch of the spin-coated silicon layers leads to different physical behavior due to the presence of significant oxide inclusions. However, for this experiment, it was not possible to find a suitable substrate both compatible with the high temperature step and resistive against dilute hydrofluoric acid at the same time. So it can only be regarded as an illustrative experiment demonstrating the necessity of an annealing procedure in principle.

For an annealing process that could seriously be considered competitive with state-of-the-art thin film semiconductor production techniques, it will be required that first, the carrier mobility and thus the conductivity of the layers can be strongly increased, second, control over the doping level is achieved, and third, a largely increased processing speed can be realized at low substrate temperatures. In a large-scale industrial implementation, roll-to-roll processes without the need

for evacuation will certainly be preferred to this slow annealing process at high temperatures and under high vacuum conditions.

Thus, in the following chapters, alternative methods will be presented, which allow the transformation of the as-deposited silicon nanocrystal layers into electronically functional semiconductors with reasonably high mobility values. While the first method utilizes the metal assisted crystallization of silicon in contact with aluminum films, the second method is quite close to the thermal annealing described above. Only, the thermal energy is deposited in the films by a pulsed laser within very short periods of time in a non-equilibrium process. Both methods allow the thermal process to be performed on substrates, which do not need to resist temperatures above 600 °C, the first by the catalytic metal layer, and the second by the short period of time required for the overall heating procedure.

5 Aluminum-Induced Recrystallization of Nanocrystalline Silicon Layers

The ability of many metals to induce crystallization of amorphous silicon and germanium layers at relatively low temperatures has been known for more than three decades [Her72, Gju05]. Especially crystallization processes mediated by aluminum as a standard material in silicon device fabrication and as a shallow acceptor in silicon and germanium was extensively studied [Ott74, Maj79, Kon92, Haq94, Kim96, Nas98]. Recently, this aluminum-induced crystallization regained interest due to the observation that it can be used to form large-area polycrystalline silicon and silicon-germanium films on foreign low-temperature substrates such as glass [Nas98, Gal02, Gju04]. In this special modification the method is commonly referred to as aluminum-induced layer exchange (ALILE), because the amorphous silicon layer and the aluminum film exchange their relative positions during the transformation.

This method is a solid state recrystallization process of an amorphous silicon layer, which has to fulfill tight geometrical conditions. Thus, it is not expected a priori that it can also be applied to recrystallize the porous spin-coated silicon particle layers. While the morphological properties of the obtained polycrystalline films show some constraints in the transferability of the process to our material, the beneficial influence on the electrical properties of the resulting films, however, is unquestionable.

5.1 Aluminum-Induced Layer Exchange with Amorphous Silicon

While a more detailed description of the ALILE process can be found, *e.g.*, in [Nas00a], [Nas00c], or [Gju07], a short overview over the processes leading to the layer exchange will be given in this section. Starting from the typical layer structure required for the observation of the layer exchange, the main process steps will be highlighted and discussed in terms of the underlying physical context and by models from the literature.

5.1.1 Layer Structure

The basic layered sample structure consists of a substrate (usually glass), which is coated with a thin film of aluminum (typically $100 - 500$ nm). To establish a diffusion barrier, the aluminum surface is covered with a native oxide by exposure to ambient air. Alternatively, also an artificial oxide can be employed, *e.g.*, by deliberate coating with a layer of evaporated Al_2O_3 [Gju07], or by anodic oxidation of the aluminum. Then, amorphous silicon is deposited on top, which can be done by thermal or electron beam evaporation, by chemical vapor deposition, or by sputtering. The resulting layered structure, except for the very thin oxide interface, can be identified in the cross-sectional micrograph in Figure 5.1 a). The focussed ion beam micrographs in the figure were taken from [Nas00a].

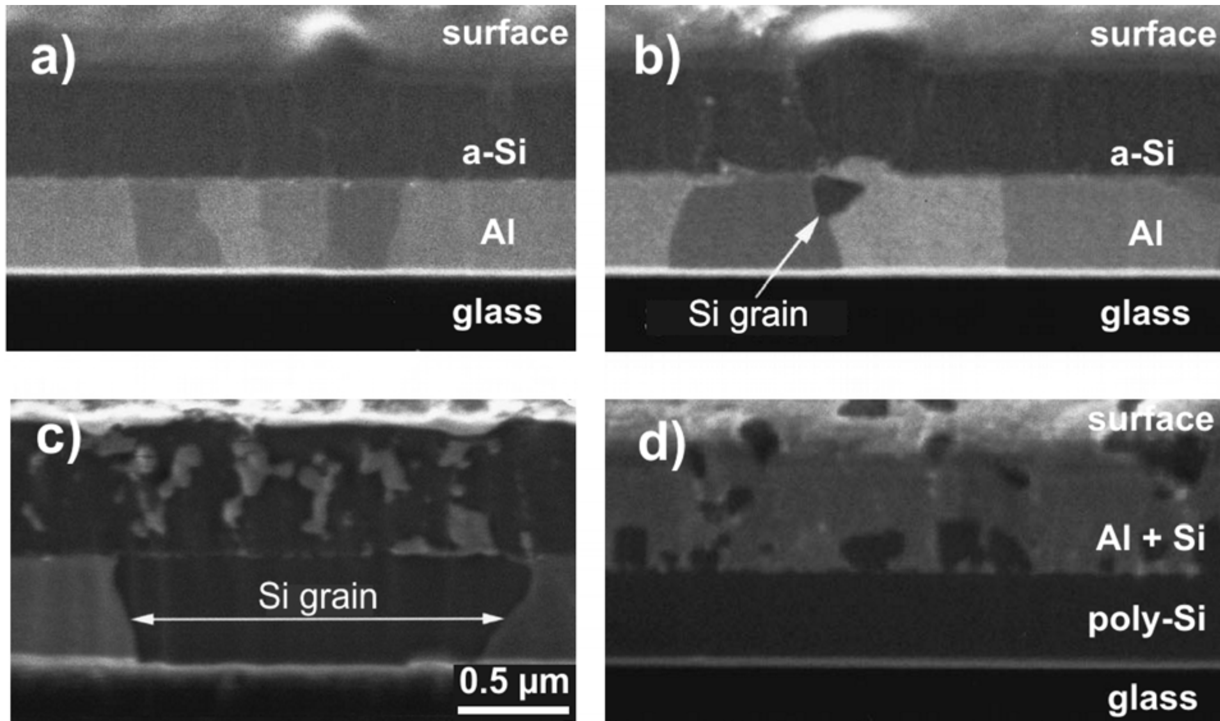

Figure 5.1: Cross-sectional micrographs of different stages of the aluminum-induced layer exchange (ALILE). The initial layered sample is shown in (a), whereas (b-d) show the situation after annealing at a temperature of 500 °C for (b) 5 min, (c) 10 min, and (d) 60 min [Nas00a].

The thickness ratio between the aluminum and the amorphous silicon layer is an important parameter for the subsequent layer exchange process. If the amorphous silicon layer is much thinner than the aluminum film, the ALILE process cannot be completed because the silicon supply will be exhausted at some stage during the process. If, on the other hand, the silicon film is much thicker than the aluminum film, the remaining silicon will form a large amount of crystallized silicon structures on top of the crystallized film leading to disadvantageous film morphology [Nas00a]. The optimum thickness ratio is usually found close to unity, while a slight surplus of silicon has been found to produce even more satisfying results [Wid02, Gju07].

5.1.2 Layer exchange

The layer exchange is initiated by annealing the sample in vacuum or under a protective atmosphere at temperatures ranging from $300 - 570\,^{\circ}\mathrm{C}$ to enable the thermally activated layer exchange process. As a first step, silicon atoms dissociate from the amorphous network and are solved in the aluminum film. The mechanism of surpassing the interjacent oxide barrier will be addressed in Subsection 5.1.6. When the silicon concentration in the film reaches supersaturation, silicon nuclei can precipitate within the aluminum matrix. Due to the higher thermodynamic stability of the crystalline phase, the forming grains do not exhibit the disordered structure of the amorphous precursor layer but show a crystalline order. In direct contact with these growing nuclei, the aluminum matrix acts as a diffusion bridge and the growth of the crystalline grains continues. A nucleus grown to about 150 nm can be distinguished in Figure 5.1 b) at the junction of an aluminum grain boundary with the oxide interface.

As long as sufficient material supply is provided by the in-diffusion of silicon atoms, the growth of silicon grains within the aluminum layer can continue. At the same time, the corresponding volume of aluminum is displaced towards the initial amorphous silicon layer position, while the oxide barrier is found to remain in between the layers throughout the entire layer exchange process [Kim96, Nas00b]. Once the silicon crystallites occupy the full thickness of the aluminum matrix, they proceed to grow laterally, confined between the substrate and the interfacial oxide. This lateral growth and the displacement of the aluminum onto the top layer is illustrated by Figure 5.1 c). For the experimental observation, this fact is of great benefit, because the high optical contrast between the silicon crystallites and the aluminum matrix allows the *in situ* observation of the overall layer exchange process through the glass substrate.

Eventually, the silicon grains can grow together, forming a closed polycrystalline silicon layer on the substrate if a sufficient amount of silicon is present throughout the diffusional grain growth process. Figure 5.1 d) illustrates how the aluminum and silicon films have exchanged positions, which motivated the nomenclature of ALILE in the beginning. The striking difference, which cannot be seen in the figure however, is that the silicon has adopted a polycrystalline structure in the process. If the aluminum remnants on top of the crystallized silicon film are selectively removed by wet-chemical etching, a polycrystalline silicon film remains on the substrate with a thickness corresponding to that of the initial aluminum film. So-called hillocks or island-like crystalline silicon structures cover the polycrystalline silicon film as a consequence of the contact of the repelled aluminum with the top amorphous silicon layer during intermediate stages of the ALILE process [Wid02]. The maximum height of these structures is the thickness of the initial amorphous silicon film.

Considering the fact that the ALILE process depicted in the Figures 5.1 a) – d) was performed at a temperature of 500 °C on a glass substrate and that it took no longer than 60 min in total, the high potential of this method for thin-film semiconductor applications on low-temperature substrates becomes evident. Ranging from thin film active matrix displays, thin-film electronics to thin-film photovoltaics, many areas are imaginable were such a crystallization method can give decisive advantages compared to conventional methods. Still, the vacuum deposition steps included in producing the initial sample configuration are a certain drawback for applications.

5.1.3 Driving Force

Since the ALILE process is connected with irreversible structural changes converting the silicon from the amorphous phase to the crystalline state and with an exchange of positions of almost all the involved atomic species, an overall driving thermodynamic potential behind the layer exchange is necessary. This driving force is the metastability of the amorphous with respect to the crystalline phase, which is quantified in the higher Gibbs free energy of the former.

The Gibbs free energy, G, is the relevant thermodynamic potential for processes occurring at constant temperature, T, and pressure, p. Under these conditions, the chemical potential of the i-th atomic species, μ_i, corresponds to the change in Gibbs energy by adding or removing one mole, $\mathrm{d}N_i = \pm 1$ mol to or from the system:

$$(\mathrm{d}G)_{T,p} = \sum_i \mu_i \mathrm{d}N_i, \qquad \text{or} \qquad \mu_i = \left(\frac{\mathrm{d}G}{\mathrm{d}N_i}\right)_{T,p} \tag{5.1}$$

Here, μ_i and N_i are the chemical potential and the number of moles for the i-th component, respectively. The difference in the chemical potential of silicon atoms in the amorphous phase to those in the crystalline phase can then be expressed in terms of the molar excess enthalpy ($h^{a\text{-Si}-c\text{-Si}} = 11.9\,\text{kJ}\,\text{mol}^{-1}$ [Don83]) and the molar excess entropy ($s^{a\text{-Si}-c\text{-Si}} = 1.66\,\text{J}\,\text{mol}^{-1}$ [Spa74]):

$$g^{a\text{-Si}-c\text{-Si}} = \mu^{a\text{-Si}} - \mu^{c\text{-Si}} = h^{a\text{-Si}-c\text{-Si}} - T s^{a\text{-Si}-c\text{-Si}}, \qquad (5.2)$$

where $g^{a\text{-Si}-c\text{-Si}}$ is the molar excess Gibbs energy.

If we now compare amorphous and crystalline silicon in contact with aluminum, we have to take into account that the concentration of silicon that establishes in the solid depends on the respective chemical potentials:

$$\mu^{a\text{-Si}} = \mu_0 - RT \ln c_\text{a}, \qquad \text{and} \qquad \mu^{c\text{-Si}} = \mu_0 - RT \ln c_\text{c}, \qquad (5.3)$$

with μ_0 being a reference chemical potential, c_a and c_c the concentrations of silicon in aluminum in contact with amorphous and crystalline silicon at temperature T, respectively, and R the universal gas constant. As the amorphous silicon has a higher chemical potential, a higher concentration of silicon is solute in the aluminum if it is in contact with the amorphous silicon phase: $c_\text{a} > c_\text{c}$. The factor of this increase is the thermodynamic activity, a, which is obtained by combining Equations 5.2 and 5.3 [Kon92]:

$$a = \frac{c_\text{a}}{c_\text{c}} = \exp\left(-\frac{g^{a\text{-Si}-c\text{-Si}}}{RT}\right) = \exp\left(\frac{s^{a\text{-Si}-c\text{-Si}}}{R} - \frac{h^{a\text{-Si}-c\text{-Si}}}{RT}\right). \qquad (5.4)$$

In the temperature range relevant for the ALILE process, the activity decreases from a value of 30 at 200 °C down to 4.4 at 577 °C. The maximum silicon concentration which can form in aluminum in contact with amorphous silicon can thus be increased by the same factor.

5.1.4 Al-Si Phase Diagram

Aluminum in combination with silicon forms a simple eutectic alloy system, because a miscibility gap exists between both components. As illustrated by the phase diagram in Figure 5.2, only very small concentrations of silicon are present in the solid α-phase of aluminum and the silicon β-phase is practically free of aluminum at temperatures below the eutectic temperature of 577 °C [Mur90]. While the former exhibits a face-centered cubic structure and may contain up to 1.5 at.% silicon, the latter has a diamond lattice with a solid solubility maximum of only 0.04% at the retrograde point at 1200 °C, as is visible in Figure 3.5. At the eutectic temperature, well below the melting points of the components, a liquid phase consisting of 12 at.% silicon and 88 at.% aluminum forms. With increasing the temperature further, the allowed compositional range of this liquid eutectic phase strongly broadens (represented by the shaded area in the phase diagram which is delimited by the so-called liquidus lines).

It has been pointed out in the previous subsection that the solubility of silicon in aluminum is effectively increased in contact with amorphous silicon. This fact is illustrated by the dashed lines in Figure 5.2, which take into account the thermodynamic activity of amorphous silicon as deduced above. As a result, the maximum silicon concentration in the aluminum can approach as much as 6.5%. However, if such a large silicon concentration is present within the aluminum, this is an unstable situation and the aluminum is then supersaturated with respect to the crystalline

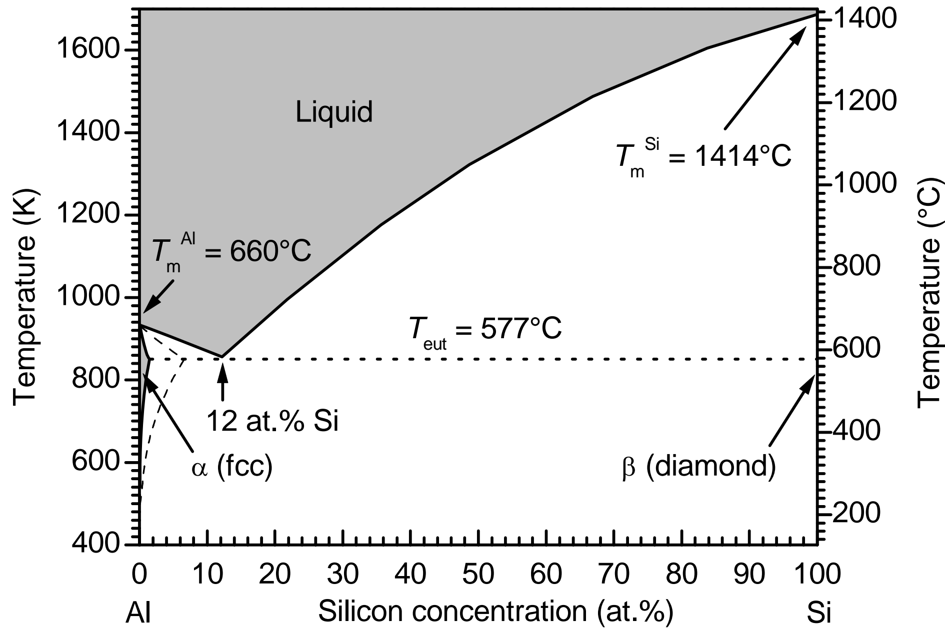

Figure 5.2: Binary phase diagram of the eutectic Al-Si alloy system. Above the eutectic temperature of 577 °C, well below the melting points of the constituents, a mixed liquid phase coexists with the solid aluminum-rich α-phase and solid silicon [Mur90]. The dashed line gives the maximum attainable silicon supersaturation in the α-phase if in contact with amorphous silicon.

silicon phase. Consequently, the precipitation of the crystalline β-phase is thermodynamically favored to relieve the silicon supersaturation and to restore a stable α-phase.

Of course, after the nucleation of crystalline β-phase grains and by relief of the supersaturation, the situation would be in an equilibrium state, having transformed an amorphous silicon/aluminum interface into a crystalline silicon/aluminum interface. The important fact which enables the macroscopic layer exchange is that the precipitation rate is rather small and the silicon atoms diffuse over long distances in the aluminum matrix to attach to farther away grown crystalline silicon grains.

The reason for this condition is the suppressed nucleation of silicon grains [Sch05]. The formation of small crystalline nuclei is energetically unfavorable due to the large interfacial term in the Gibbs energy. Only if a critical nucleus size is exceeded, further growth is possible and the total Gibbs energy is decreased. This fact is well known from classical nucleation theory, for instance during the nucleation of crystalline silicon grains in amorphous silicon for solid phase crystallization [Spi98]. Sarikov *et al.* successfully employed a similar kinetic model to simulate the nucleation behavior of the ALILE process [Sar06].

As long as the aluminum stays in direct contact with amorphous silicon, the material supply is provided and the dissolution of silicon atoms in the α-phase and the precipitation of β-phase silicon will continue. If we now consider a diffusional transport process of silicon atoms from the interface of the amorphous silicon with the α-phase towards the interface between the α- and the β-phase, we obtain the basic process steps in the phenomenological ALILE model.

It has to be added that temperatures above the eutectic point of the silicon-aluminum phase system cannot be applied for ALILE because then the full layer is transformed into a eutectic melt. While the crystallization of amorphous silicon can also occur in contact with a saturated liquid Al-Si eutectic melt, the obtained layer geometry is highly unfavorable due to the intermixing of the initial layers during melting and due to the destruction of the separating interface [Nas98]. Upon cooling the melt below the eutectic temperature again, homogeneous precipitation of crystalline silicon takes place throughout the mixed eutectic alloy. The resulting silicon crystallites exhibit a fractal dendritic structure and form a lamellar texture with the aluminum phase. The structure size hereby can only be weakly influenced via the cooling rate.

5.1.5 Thermal Activation

The macroscopic observations made for the ALILE process motivated the formulation of an empirical model for the layer exchange by Nast and Wenham [Nas00a], however, the basic ideas of the model had already been pointed out by, *e.g.*, Ottaviani *et al.* three decades earlier [Ott74]. Recent calculations by Sarikov and coworkers [Sar06] were qualitatively able to prove the main consequences of this model taking into account the individual physical processes involved. Supposing a continuous diffusion of silicon atoms through the separating oxide, the formation of a supersaturation of silicon atoms in the aluminum matrix and the relaxation by adhesion to growing crystalline silicon grains is confirmed. Furthermore, the experimental finding of a suppressed nucleation in the presence of growing crystallites is reproduced in the calculations [Sar06].

The initial dissociation of silicon atoms from the amorphous network requires thermal activation. The bonding potential between covalently bonded silicon atoms is as high as 2 eV. However, a solid silicon phase in direct contact with solid aluminum is not stable in the pertinent temperature range of $500 - 550\,^{\circ}\mathrm{C}$, because then up to 1.5 at.% silicon atoms are soluble in the solid α-aluminum-silicon phase, and thus will be dissolved for entropic reasons [Mur90]. Still, this process is thermally activated with an activation energy as high as 1.83 eV, as calculated by Pabi for crystalline silicon dissolved in aluminum [Pab77]. Only the fact that the silicon initially is present in the amorphous phase enables the ALILE process within reasonable times below the eutectic temperature.

Indeed, the activation energies found in the literature are typically lower and amount to 0.8 eV [Qin82], 1.2 eV [Maj79], 1.2 eV [Kon92], 1.1 eV [Wid02], 1.3 eV [Nas00c], and 1.8 eV [Gju07]. Most of these values are very close to the thermal activation energy for the diffusion of silicon atoms in evaporated and wrought aluminum of 0.79 eV and 1.36 eV, respectively [McC71]. Thus, Qingheng *et al.*, Konno and Sinclair, and Widenborg and Aberle concluded that the silicon diffusion in the aluminum has become the rate-limiting step for the layer exchange process, which shows the effective reduction of the dissociation barrier for amorphous silicon [Qin82, Kon92, Wid02].

5.1.6 Interface Reactions

The question how the silicon and the aluminum layers can get in direct contact in spite of the separating oxide has been addressed by Kim and Lee [Kim96] and by Bierhals *et al.* [Bie98]. Both groups find that silicon oxide is not stable in contact with aluminum at elevated temperatures either. Instead, the aluminum is found to reduce silicon oxide to aluminum oxide while elemental

silicon can precipitate. Similar observations, namely that already at room temperature aluminum starts to reduce the silicon oxide, have been reported earlier, *e.g.*, by Bauer and coworkers and by Anandan [Bau80, Ana95]. Bierhals *et al.* observed that additional to reducing the silicon oxide, the aluminum forms spikes penetrating through the insulating barrier of an oxidized silicon wafer at temperatures as low as 300 °C [Bie98]. The resulting microscopic fracture sites in the separating oxide barrier have been directly observed by Kim and Lee [Kim96]. Via this microscopic process the silicon and aluminum phases can get into contact with each other despite the presence of the oxide barrier [Rad91, Ash95, Haq94].

These facts are very important prerequisites for ALILE in a layer configuration, where a thin aluminum film is deposited on top of an oxidized amorphous silicon layer. However, the reversed layer sequence of amorphous silicon on top of an aluminum film is even more commonly used for the ALILE process. While the native aluminum oxide is found to form a chemically stable barrier throughout the layer exchange, the presence of physical fracture sites in the oxide membrane due to the thermal stress is likely, which enables aluminum spiking. Thus, the very similar microscopic conditions lead to the similar observations for the overall layer exchange in both geometries [Nas00b, Nas00c].

Consequently, the oxide barrier does not need to be completely transmissible for the diffusion of silicon atoms, but can be pinged by local aluminum spike formation. Of course, this process also exhibits a thermally activated kinetic behavior and shows characteristic properties, which make it difficult to be distinguished from, *e.g.*, a diffusion process [Bie98].

For example, the spike formation can be assumed to occur randomly distributed over the oxide interface. If the oxide thickness is increased, successful spiking takes place at fewer sites, leading to an overall reduced number of silicon diffusion channels. The experimentally observed strongly reduced nucleation rate and hillock formation in this case agree with this model [Gju07]. If in contrast the layer exchange is performed at elevated temperatures, a large area concentration of oxide fracture sites can form, which induces a large nucleation density, and the high silicon flux into the aluminum film enables the rapid layer exchange, as found experimentally.

However, the consequences of the heterogeneous distribution of transport channels through the oxide barrier are evident from the ALILE polycrystalline silicon films. Since the silicon diffusion paths are localized at the oxide pinholes created by the aluminum spikes, the crystalline silicon grains are found to nucleate close to these regions and also the aluminum is repelled around these fracture sites. Consequently, also hillocks in the top layer grow predominantly around these areas where the repelled aluminum comes first into contact with the amorphous silicon [Wid02].

In the model by Sarikov *et al.* which neglects the existence of such aluminum spikes and considers only conventional diffusion through a homogeneous oxide barrier, large quantitative discrepancies result with respect to known material properties, namely a factor of 180 in the Al-Si interface energy. However, because the change in the silicon flux with time due to the generation of diffusion channels and the heterogenous nucleation are not respected for, this deviation is not astonishing [Sar06].

Seemingly, especially the early phases during ALILE until the diffusion channels have formed, should be separated in the simulations from the mere growth phase of existing silicon grains. Then, if further nucleation is suppressed, only the diffusion through the aluminum matrix is the limiting process. This explains why the dominant part of the activation energies presented in

the previous section come close to the activation energy for the diffusion of silicon atoms in aluminum [Qin82, Kon92, Wid02].

5.1.7 Diffusion Processes

The microscopic processes that are responsible for the macroscopic layer exchange are diffusional processes such as the diffusion of silicon atoms within the aluminum film or along aluminum grain boundaries. Also the spike formation introduced above is initiated by diffusion of aluminum, silicon and oxygen atoms in the vicinity of the oxide barrier. Since the involved atoms are bound in a solid state environment, all of these diffusion mechanisms depend strongly on the temperature, and can thus contribute to the overall thermal activation of the ALILE process.

Hereby, the overall layer exchange will mainly exhibit the highest thermal activation energy among the various diffusion processes that are involved in ALILE. While this overall activation energy can be determined from the time required for the ALILE process, it is difficult to separate the influence of the individual microscopic processes, which may exhibit quite different thermal activation energies.

5.1.8 Oxide barrier-free structures

If the aluminum is prevented from forming the oxide barrier, the precipitation of the silicon nuclei can in principle occur anywhere in the layered sample, resulting in a structure where the aluminum remnants are completely intermixed with the polycrystalline silicon after the annealing [Nas00c]. However, already a very thin oxide interface seems to be sufficient for defining the geometry of the final polycrystalline film. While Konno and Sinclair observe the partial destruction of an aluminum-amorphous silicon multilayer structure without oxide interlayers after annealing below the eutectic temperature [Kon92], Qingheng and Tsaur *et al.*, in contrast, observe a layer exchange leading to well-defined crystalline silicon layers on crystalline and polycrystalline silicon substrates even without the presence of an intentional oxide interface [Qin82, Tsa81].

This apparent discrepancy might originate from the rapid formation of the native aluminum oxide even under vacuum conditions. For example, a 1 nm native aluminum oxide is observed to form within minutes at an oxygen pressure as low as 10^{-5} mbar [Lin00]. Accordingly thinner oxide films forming at the reported background pressures of 10^{-6} mbar might already suffice to act as the interpenetration barrier. Using common deposition methods, the formation of an oxide interface layer is thus difficult to be completely suppressed. By reversing the layer structure and depositing aluminum onto an amorphous silicon layer, which oxidizes more slowly than the aluminum, however, the layer exchange speed can be vastly increased while the layered structure is preserved [Gju07].

5.1.9 Structure of the Silicon Precursor

As explained above, a difference in Gibbs free energy is required to induce the ALILE process of amorphous silicon. If the silicon is crystalline already before the crystallization, a sufficient dissolution of silicon atoms in contact with the aluminum phase will not occur. Pabi calculated the thermal activation energy for the dissolution of silicon in the unsaturated α-phase [Pab77].

He obtained a value of 177 kJ mol^{-1}, corresponding to 1.83 eV per atom, which is significantly larger than what most groups report for ALILE (see Subsection 5.1.5). However, if the silicon does not form a bulk crystal but instead only a crystalline cluster of reduced size, the relative contribution of the then large surface can dominate the free energy of the crystal.

For instance, the chemical potential of a surface silicon adatom is smaller than that of a full-valently bonded silicon atom inside of the crystal. Thus, the mean Gibbs free energy of the silicon surface atoms will be significantly higher than that of a large silicon crystal due to the large relative surface energy contributions, similar to the size-dependent melting effects (compare Subsection 3.2.2 and Equations 3.6 and 3.7). In this sense, also a nanocrystalline silicon film could be used as the metastable precursor layer for a aluminum-induced recrystallization.

The influence of the silicon crystalline structure on the recrystallization behavior as mediated by aluminum was first examined by Pihan *et al.* [Pih04]. In their study, silicon films with different degrees of disorder were applied ranging from amorphous to nano- and microcrystalline silicon layers deposited by sputtering and radio frequency plasma enhanced chemical vapor deposition (RF-PECVD). As a result, they find the nucleation density weakly increased by the choice of either a nano- or microcrystalline precursor layer. While the overall layer exchange is slightly retarded for an initially microcrystalline silicon, a compromise between the final crystallite size and the total process time can be found using a mixture of amorphous and nanocrystalline material [Pih04].

However, the process kinetics were not analyzed as a function of the annealing temperature in this study, which would have allowed conclusions on a different thermal activation of the layer exchange. Also, the aluminum films employed in their samples were exposed to ambient air for relatively long periods of time leading to thick aluminum oxide films. Instead, conditions with thin oxide barriers should be chosen to elucidate the impact of the structural quality of the precursor layer on the kinetics of the layer exchange process.

5.2 ALILE with Silicon Nanocrystals

5.2.1 Structural Properties

To apply ALILE to silicon nanocrystal layers, microwave reactor silicon nanocrystals and hot wall reactor silicon nanoparticles were suspended in ethanol and ball milled according to the procedure in Chapter 2. The obtained dispersions were spin-coated onto glass substrates that had been coated with a thermally evaporated aluminum thin film before. While the typical film thickness of the aluminum film was around 200 nm, the thickness of the silicon films was typically in the range of 500 nm $-$ 1.2 μm to compensate for the large porosity of the spin-coated silicon particle network. These layers were annealed under protective nitrogen atmosphere at temperatures ranging from 400 $-$ 550 °C, and the progress of the layer exchange was monitored *in situ* with a microscope through the glass substrate. After the annealing, the residual aluminum and remnants of the silicon layer were removed by wet chemical etching for some of the analytical methods described in the following.

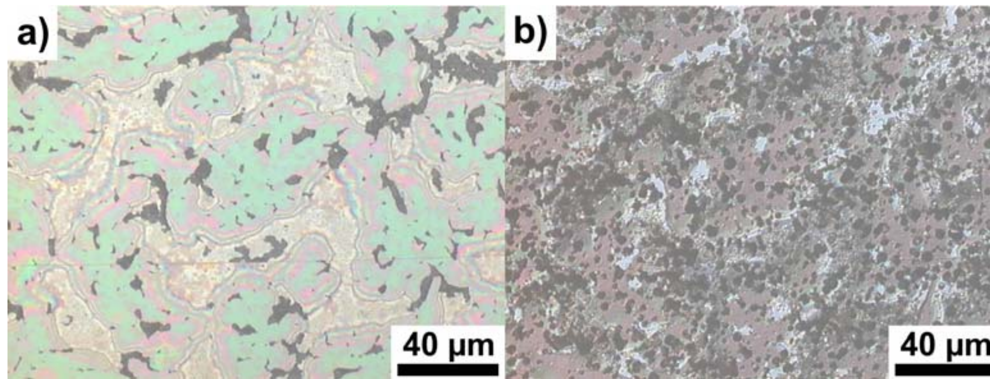

Figure 5.3: Reflected light, (a), and (b), transmitted light optical micrographs of a polycrystalline silicon film on glass from ALILE with microwave reactor silicon nanocrystals. Remnants of aluminum and silicon nanocrystals have been removed by wet chemical etching.

Morphology

The appearance of layers that were recrystallized with the help of the ALILE process is very similar for both microwave reactor silicon nanocrystals and hot wall reactor silicon nanoparticles. However, significant differences compared to layers from amorphous silicon precursor layers are evident. Apart from a prolonged process time for the overall layer exchange, the resulting films are not perfectly closed, giving the first impression that the layer exchange has not yet come to an end. It turns out, however, that this is a general consequence of using the spin-coated silicon particle films as the precursor layer for the ALILE process. Moreover, even prolonged annealing does not lead to a perfectly closed layer as can routinely be obtained from an amorphous silicon precursor.

Crystalline grains Figure 5.3 shows the result of the ALILE process with microwave silicon nanocrystals after the removal of the aluminum and silicon nanocrystal remnants. The initial aluminum film had a thickness of 250 nm, whereas a 1.2 μm thick silicon layer was spin-coated on top. The annealing was performed at a temperature of 550 °C for 30 h. The reflected light micrograph in Figure 5.3 a) displays relatively large polycrystalline silicon grains on the order of 50 μm. These grains exhibit a dendritic or branched morphology and appear in a bright greenish color.

This color effect is due to thin-film interferences of the reflected white light, which indicates the presence of a flat surface of homogenous thickness in these areas. From Equation 4.4, a value of 240 nm is obtained for the thickness of the crystalline grains in these areas from the reflectance spectrum if the refractive index of crystalline silicon is used (which is a valid assumption as Section 5.2.4 will show).

Similarly, the colored stripe patterns which are encountered in the regions between neighboring silicon grains indicate a rapid decrease of the layer thickness within a lateral width of 10 μm. The multiple color change can be correlated with a decrease of the thickness down to about 50 nm (at silicon thicknesses of 66, 100, 133, 166, 200, and 233 nm reflection maxima or minima are present for green light at 550 nm wavelength). Thin crystalline silicon regions of this thickness are found to cover a significant area fraction and connect the thicker neighboring silicon grains.

Pinholes The silicon grains in Figure 5.3 a) are interrupted by dark areas, which appear bright in the transmission micrograph (b). Thus, they can be identified as pinholes in the silicon film after the layer exchange process. The typical dimensions of these pinholes are $10 - 50\,\mu$m. These pinholes already form within the aluminum matrix during the ALILE process with spin-coated silicon particles and they are present in the polycrystalline film on the substrate even before the wet-chemical removal of the residual aluminum. Moreover, prolonged annealing does not produce completely coalesced layers of polycrystalline silicon, contrary to the situation with amorphous silicon precursor layers.

This general observation for ALILE with silicon particles cannot be circumvented by merely increasing the relative thickness of the silicon particle layer. If the silicon layer is chosen thinner than the aluminum film, the layer exchange comes to a halt at an earlier stage, before neighboring silicon grains can coalesce. It is thus concluded that the pinholes in the layer are a consequence of partial dewetting of the substrate by the aluminum film during the annealing. Moreover, also the formation of the thin interconnecting polycrystalline regions can be explained by this effect. Such dewetting phenomena are commonly observed at the elevated temperatures of around $500\,^{\circ}$C, which were present during these experiments. This interpretation will be included in a phenomenological model for the microscopic mechanisms occurring during ALILE with nanoparticle precursors in Section 5.2.3.

Inclusions As evident from the transmitted light optical micrograph in Figure 5.3 b), the silicon films after the ALILE process with silicon particles exhibit a large amount of inclusions in the polycrystalline layer. While the polycrystalline silicon phase is still partly transparent at the pertaining thickness, these inclusions are opaque and appear as dark spots in the image. The typical lateral size of these inclusions is about $5\,\mu$m in diameter, which corresponds to the typical width of the silicon branches in the crystalline dendrites. In the reflected light micrograph, the inclusions are found to be covered with a thin silicon film, which due to an additional phase shift has a pink appearance in the regions of thick silicon and a brown color in the thin silicon areas.

Furthermore, the inclusions are situated at the glass-silicon interface, which is evident from optical micrographs taken through the transparent glass substrate. They can consequently be identified with small volumes of aluminum that was trapped between the growth fronts of polycrystalline silicon and the substrate. Isolated from continued diffusional silicon supply, the further silicon grain growth in these regions was prevented. The formation of these inclusions can be observed already during initial stages of the layer exchange, suggesting that the silicon nucleates mainly close to the interface between the aluminum and the silicon layer, similar as for ALILE with amorphous silicon [Nas00c]. An illustration of these processes will be given in Figure 5.9.

Hillocks and island formation For the polycrystalline silicon films grown by the ALILE process with silicon nanocrystals and nanoparticles, no so-called hillocks or island-like silicon structures are found on top of the polycrystalline layer, which has formed on the substrate. In contrast, Pihan *et al*. observed a strong formation of crystalline hillocks and islands on top of the polycrystalline silicon if microcrystalline precursor layers from RF-PECVD were applied. They found that a polycrystalline silicon film grown on the substrate is not completely closed after annealing for two hours at a temperature of $500\,^{\circ}$C, while a large number of silicon islands has formed on top covering a significant fraction of the total area. Apparently, the large amount of material consumed by the recrystallization at the position of the precursor layer inhibits further

growth of the silicon film in the lower aluminum matrix [Pih04]. Almost the opposite result is obtained if an initially amorphous silicon precursor layer with nanocrystalline inclusions is applied. Then, no islands or hillocks form, and a relatively smooth polycrystalline film is received [Pih04].

As follows from a comparison of the respective Raman signatures, the crystalline quality of our silicon nanoparticles and nanocrystals comes quite close to that of the microcrystalline film examined by Pihan and coworkers. Thus, it can be concluded that the absence of hillocks and silicon islands in our case is a specific property of the particulate nature of the precursor layer and does not originate from its microcrystalline structure alone. The illustrative model for the ALILE process with silicon particles introduced in Section 5.2.3 will explain how this circumstance can be understood.

Crystallinity of ALILE crystallized silicon nanocrystals

Raman analysis The considerable changes in the structural properties during the ALILE process with spin-coated silicon precursor layers can be illustrated by Raman spectroscopy. In Figure 5.4 a), the Raman spectrum of an as-deposited layer of hot wall reactor grown silicon nanoparticles is shown in comparison with the same sample after annealing in contact with a 200 nm thick aluminum layer. Also, a crystalline silicon sample is given as a reference. The latter exhibits a peak position of 521.2 cm^{-1} and a full width at half maximum of 4.4 cm^{-1}, respectively. The Raman spectrum of the as-deposited hot wall nanoparticles can be fitted with the phonon confinement model following a log-normal size distribution. As was shown in Subsection 4.1.3, good agreement is found if a mean size of 5 nm, a standard deviation of $\sigma = 1.5$ and a small amorphous silicon background contribution are accounted for (full line). The effective peak position and peak width are 518.5 cm^{-1} and 9 cm^{-1}, respectively.

After the ALILE process, the spectrum can be described well by a single Lorentzian distribution at a peak position of 520.6 cm^{-1} with a width of 4.9 cm^{-1}. The asymmetric shape of the Raman spectrum has disappeared after the recrystallization. A very similar result is obtained for the recrystallized microwave reactor silicon nanocrystals in Figure 5.4 b). This spectrum exhibits a symmetric peak centered around 520.0 cm^{-1} with a peak width of 4.2 cm^{-1}. It has to be noted that the nanocrystals in this case were significantly larger, with an average diameter of 20 nm, leading to an effective peak position at 520.1 cm^{-1} and an asymmetric peak width of 6 cm^{-1}.

In both cases, after the ALILE process, the peak position and the peak width have approached the value of the crystalline silicon reference sample. This demonstrates that the silicon films formed during ALILE with spin-coated silicon layers show the characteristic Raman spectra of crystalline silicon without significant finite-size effects. As can be concluded from the phonon confinement model, the crystalline grains in these films exceed a crystallite size of 30 nm. This result is in agreement with the optical micrographs and the etching experiments presented in the following subsection, which indicate a macroscopic grain size on the order of several micrometers.

The small peak shifts on the order of $0.6 - 1\,cm^{-1}$ still present after ALILE with respect to the Raman signal of the crystalline silicon reference can be attributed to thermal strain. Due to the different thermal expansion coefficients of silicon and the fused silica substrates, thermal strain will develop within the layer upon cooling down from the process temperature to room temperature. For a temperature difference of about $\Delta T = 500\,K$, the thermal stress, σ_{th}, can be

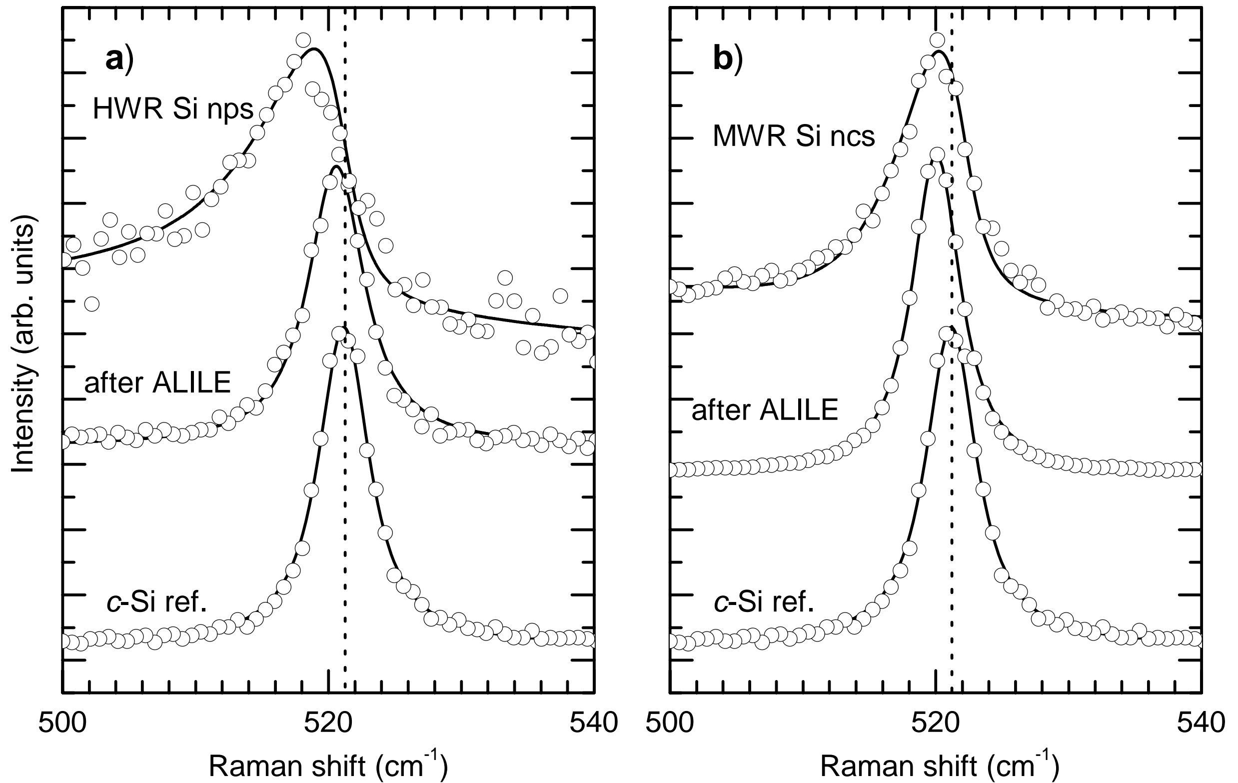

Figure 5.4: Room temperature Raman spectra of hot wall reactor silicon nanoparticle and microwave reactor silicon nanocrystal layers as-deposited and after the ALILE process. For comparison, also crystalline silicon reference spectra are displayed.

calculated according to [Len02]:

$$\sigma_{\mathrm{th}} = \Delta\alpha \cdot \Delta T \cdot \frac{E_\gamma}{1 - \gamma_{\mathrm{P}}} \tag{5.5}$$

where $\Delta\alpha$ is the difference between the thermal expansion coefficients of the film and the substrate, E_γ and γ_{P} are Young´s modulus and the Poisson ratio for the crystalline silicon film, respectively. While the latter is given by $\gamma_{\mathrm{P}} = 0.45$, E_γ generally depends on the crystallographic orientation and varies between the values of 187 GPa and 170 GPa for forces along the [100]-axis in (111)-silicon and along the [111]-axis in (100)-oriented silicon crystals, respectively [Eis02, Len02].

A rough estimation for our situation leads to tensile thermal strain of $\sigma_{\mathrm{th}} = 0.65\,\mathrm{GPa}$, which translates into a Raman redshift of $\Delta\omega = -2.7\,\mathrm{cm}^{-1}$ if the relation for biaxial stress is applied ($\Delta\omega = -3.7\,\mathrm{cm}^{-1} \cdot \sigma_{\mathrm{bs}}/\,\mathrm{GPa}$ [Ana91]). This exceeds the experimentally observed value by far, which only corresponds to a temperature difference of only 200 K. This result is an indication that mechanisms for partial stress relaxation occur in the polycrystalline silicon films grown by the ALILE method. Indeed, also other authors report on the absence of significant strain contributions in the Raman spectra of ALILE crystallized amorphous silicon on glass and fused silica substrates [Nas98, Nas00c, Len02].

Grain boundaries The dendritic shape of the polycrystalline silicon grains visible in the optical micrographs in Figure 5.3 hints on a dendritic growth regime of these crystals. Under

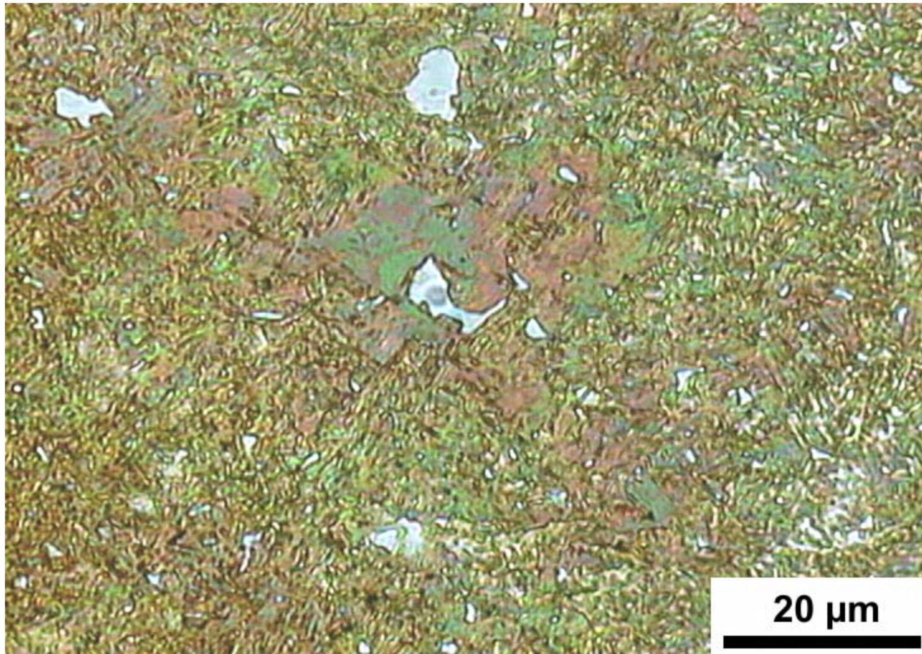

Figure 5.5: Transmission optical micrograph of a polycrystalline silicon film crystallized by ALILE with silicon nanocrystals after defect etching. The etch has attacked and removed defect-rich grain boundary areas revealing the crystallite substructure.

such conditions, the formation of intragrain defects such as twin formation and dislocations is probable inducing an effective smaller crystallite size in the polycrystalline layer. To visualize internal grain boundaries, the samples were exposed to a defect etch consisting of $K_2Cr_2O_7$ and dilute hydrofluoric acid (0.15 mol of $K_2Cr_2O_7$ in water with an equal amount of 10% HF [Eis02]). Due to the rapid etching of the layers, only short etching times were applied ($5-10$ s at room temperature), before the samples were rinsed with deionized water and blown dry with nitrogen.

Figure 5.5 shows the result of such an etching procedure with an ALILE recrystallized layer of silicon nanocrystals. While the thin interconnecting regions between the large grains similar to those in Figure 5.3 are already removed by the etch, this micrograph accentuates around one of the large crystalline grain regions after etching. As a consequence of a large concentration of intragrain boundaries and defects also in these regions, clearly a fine structure inside the crystalline areas becomes visible by this defect etching.

Instead of smooth polycrystalline regions, now a large density of pinholes is present in the sample and needle-like crystalline grain structures become evident from the micrograph. The effective grain size of these structures can be estimated to about $1-2\ \mu$m in width at a length of $2-4\ \mu$m. Only in the upper center of the micrograph, a larger crystalline region with dimensions of $10 \times 10\ \mu m^2$ remains unaffected, which can be identified with the center region of one of the formerly large grains that formed the thick flat polycrystalline areas during the early stages of the ALILE process.

The relatively small crystallite sizes observed here are in agreement with the observations for ALILE from amorphous silicon at similar temperatures. Also, internal twinning within the apparent single-crystalline grains is a well-known phenomenon observed here. The grain size for

such samples is found to decrease with increasing process temperature as a consequence of increased nucleation densities for higher temperatures. Accordingly, at temperatures of 550 °C a typical grain size smaller than 2 μm is expected [Nas00c]. The homogeneous nucleation of silicon grains in the case of amorphous precursor layers induces rather circular polycrystalline grains, whereas in the situation of the silicon particle precursors, the low nucleation density and the slow grain growth leads to the observed needle-like structures.

5.2.2 Process Dynamics

Due to the use of transparent glass substrates, the progress of the layer exchange can be monitored *in situ* during the annealing via a microscope and a digital camera. The crystalline silicon grains exhibit a significantly reduced reflectivity in the visible part of the optical spectrum compared to the surrounding aluminum matrix. Thus, once crystalline grains have reached the glass substrate and their lateral size exceeds about 1 μm, they can be distinguished from the aluminum, and their growth can be directly observed. The kinetics of the overall layer exchange is then evaluated from the change in the overall image brightness. In the following, the area coverage by crystalline silicon grains normalized to the final silicon crystallite area will be used to describe the progress of the layer exchange.

Silicon precursor

Figure 5.6 a) displays the results of aluminum-induced layer exchange with hot wall silicon nanoparticles and microwave reactor silicon nanocrystals. For this experiment, three glass substrates were coated with 300 nm aluminum by thermal evaporation simultaneously. Directly after the aluminum deposition, one of the samples was spin-coated with 20 nm diameter microwave reactor silicon nanocrystals, the second was spin-coated with a layer of hot wall silicon nanoparticles (BET size $150 - 200$ nm diameter), and the third was transferred to a high vacuum deposition system, where a layer of amorphous silicon was deposited by electron beam deposition. The thickness of the silicon particle films was about 1 μm each, whereas the thickness of the amorphous silicon layer was 400 nm. The total time elapsed during transferring the samples between the different deposition chambers and before spin-coating of the silicon films was always kept below 10 min, to achieve a relatively short aluminum oxidation time.

As Figure 5.6 a) shows, the layer exchange kinetics with hot wall reactor or microwave reactor grown silicon is nearly identical. For the annealing process at a temperature of 550 °C, a surface coverage of 25% occurs at about 9.5 h, while the process has proceeded to 50% and 75% after 12 h and 14 h, respectively. In the figure, the times needed for a silicon coverage of 25%, 50% and 75% are denoted as t_{25}, t_{50}, and t_{75}, respectively. While the early stages of the process show a parabolic increase of the coverage with time, saturation sets in for area coverage larger than 90%, and it takes about $18 - 20$ h until the layer exchange has come to an end. In contrast, the layer exchange performed with the amorphous silicon sample at the same temperature has already finished within an overall time of 20 min (not shown). Here, the time needed to cover 25%, 50%, and 75% of the sample area are to only 3.6 min, 4 min, and 4.8 min, respectively.

The results with the amorphous silicon samples obtained here agree well with the kinetics of ALILE with amorphous silicon reported in the literature [Gal02, Nas00c, Wid02, Gju07]. In di-

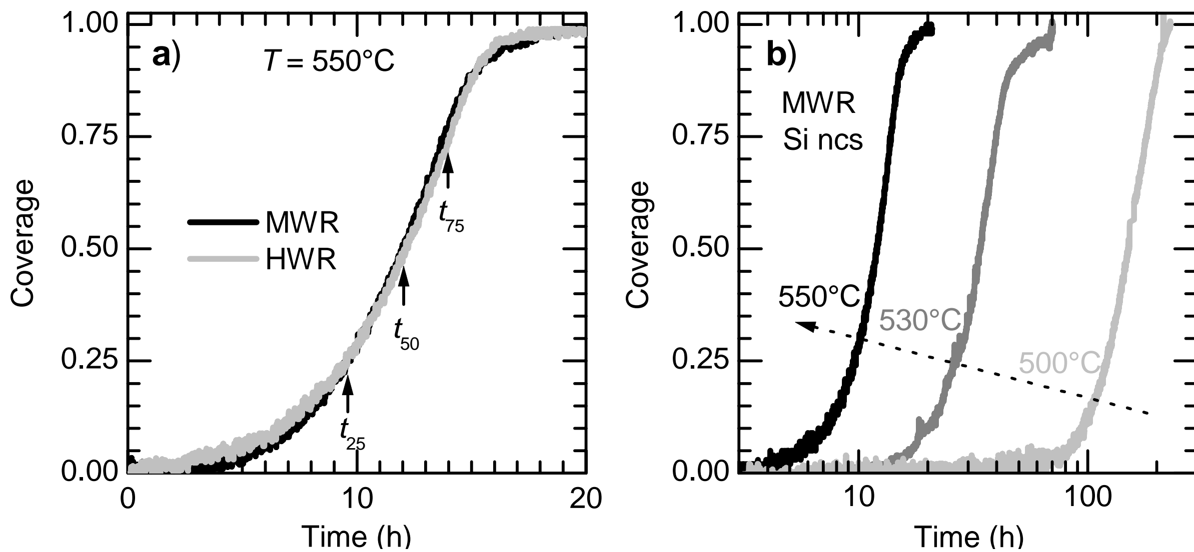

Figure 5.6: a) Area coverage by crystalline silicon grains in the aluminum matrix during ALILE at a temperature of 550 °C for hot wall reactor and microwave reactor material (gray and black lines, respectively). b) Area coverage as a function of time for ALILE with microwave reactor silicon nanocrystals performed at temperatures of 500 °C, 530 °C, and 550 °C.

rect comparison with the amorphous precursor layer, the layer exchange with silicon nanocrystals or nanoparticles is extremely retarded by two orders of magnitude.

The observation that the process kinetics are very similar for silicon nanoparticles from the hot wall reactor and for microwave reactor nanocrystals indicates that the overall particle size is not the limiting factor during the layer exchange. As outlined in Section 4.1, indeed the relevant internal structure size of hot wall material is quite comparable to that of microwave reactor nanocrystals. However, the particular situation for the layer exchange with silicon particle layers leads to specific process retardation as will be shown in the following subsections.

Influence of temperature

Since the microscopic diffusion processes, which enable the aluminum-induced layer exchange are all thermally activated, the process can be strongly accelerated by raising the annealing temperature. This effect is depicted in Figure 5.6 b) for the ALILE process with microwave silicon nanocrystal precursor layers. The data correspond to three individual pieces cut of the same sample produced as described above, which were annealed at temperatures of 500 °C, 530 °C, and 550 °C. As can be seen in the graph, the time needed for half coverage is prolonged to 34 h and 150 h by reducing the annealing temperature down to 530 °C and 500 °C, respectively. The overall process time for the ALILE with silicon nanocrystals, in turn, is extended to about 70 h and 230 h. Evidently, as a consequence of the thermal activation, a reduction of the annealing temperature by 50 K gives rise to a deceleration of the layer exchange process by one order of magnitude.

Unfortunately, due to the relatively slow reaction kinetics for the layer exchange with spin-coated silicon layers, no process temperatures below 500 °C could reasonably be applied for the *in situ* observation by digital recording and image analysis. On the other hand, the eutectic tempera-

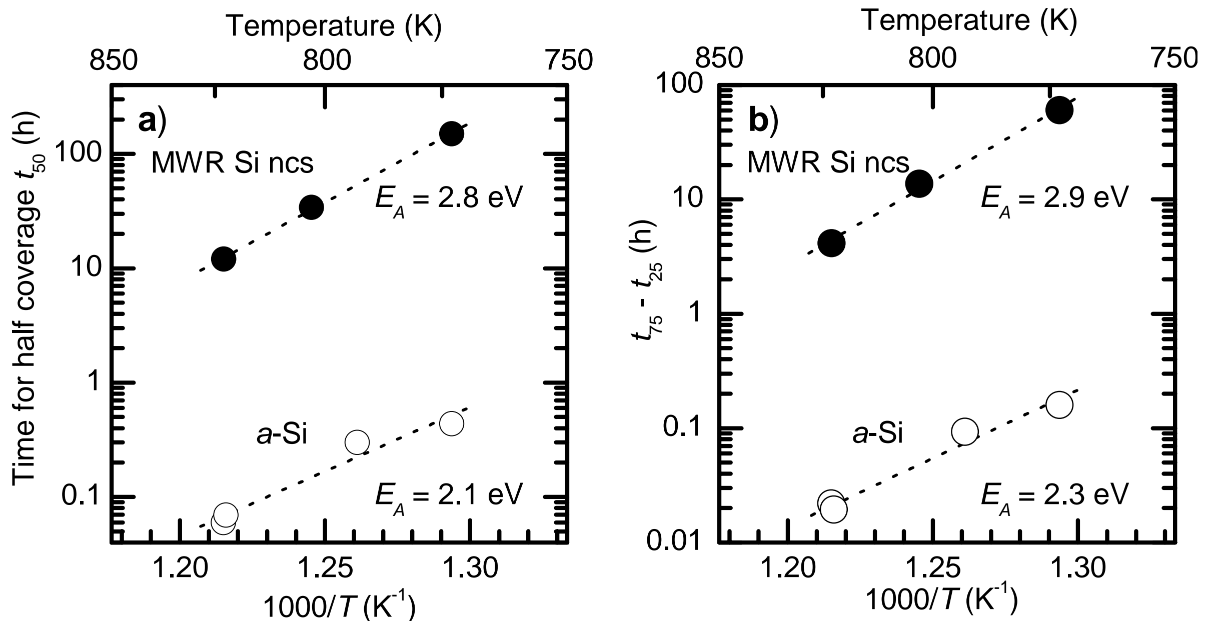

Figure 5.7: a) Arrhenius plot of the time for half coverage, t_{50}, versus the reciprocal temperature for ALILE with silicon nanocrystals and with an amorphous silicon precursor. b) Time difference $t_{75} - t_{25}$ between 25% and 75% coverage for the same data as in (a).

ture at 577 °C sets the upper bound for the ALILE process temperature. So, the temperature window applicable for the ALILE process with silicon nanocrystals and particles is inherently narrow. This fact also explains why the influence of the temperature on the grain size was not systematically studied here. However, the results with silicon nanocrystals qualitatively confirm the trends of decreasing crystallite size with higher annealing temperature as observed by Nast and Wenham [Nas00a] and Gall and coworkers [Gal02].

Thermal Activation Energy

To evaluate the process kinetics of the layer exchange, different approaches have been presented in the literature. While the thermal activation of the overall layer exchange process is most readily assessed by taking into account the time needed for half coverage of the sample area by silicon crystallites [Wid02, Gju07], also a differently defined period of time required for a fixed coverage of, *e.g.*, 20% or 90% can be used for this purpose [Nas00c]. Gall *et al.* have characterized the nucleation behavior during ALILE, separately from the overall layer exchange. By measuring the moment when the first crystalline grains appear at the glass/aluminum interface, they extracted an activation energy for the nucleation of 1.8 eV [Gal02]. However, especially the nucleation period is extremely sensitive to the interface conditions and the sample history.

Alternatively, the mere growth phase of the crystallites after the nucleation is completed can be analyzed for if the slope of the coverage versus time is evaluated as a function of the process temperature. This can be done, for instance by evaluating the difference in time between 25% and 75% coverage, $t_{75} - t_{25}$. At this stage of the layer exchange, the nucleation of crystalline grains has already seized and the number of crystalline grains stays almost constant. Indeed, the nucleation saturates at a time when an even smaller area fraction is covered by the silicon crystallites, typically below 15%, [Sch05].

Figure 5.7 shows the result of the analysis of the layer exchange kinetics with amorphous silicon and silicon nanocrystals. While in (a) the time for half coverage, t_{50}, was plotted logarithmically versus the inverse process temperature, (b) shows the corresponding Arrhenius plot for the time difference characteristic of the growth phase, $t_{75} - t_{25}$. As the figure shows, the absolute reaction times differ by two to three orders of magnitude for the different precursor materials.

In the case of the amorphous silicon precursor layer, the time for half coverage yields a thermal activation of 2.1 ± 0.3 eV, while the evaluation of the growth phase results in a value of 2.3 ± 0.3 eV. These numbers appear relatively high if compared to the results found in the literature. The values reported for the aluminum-induced crystallization of amorphous silicon are 0.8 eV [Qin82] and 1.2 eV [Maj79, Kon92], while for ALILE values of 1.1 eV [Wid02] and 1.3 eV [Nas00c] were stated. However, with the deposition systems used in our institute, the typical thermal activation energy for the ALILE process amounts to 1.8 ± 0.1 eV [Gju07]. Moreover, if the overall activation energy is evaluated from the 50% coverage data shown in their nucleation study, a value of 2.6 ± 0.3 eV can be deduced from the experiments performed by Gall *et al.* [Gal02]. Taking into account the large scatter of experimental values of different groups, it appears that the individual sample processing has a large influence on the observed activation energy, and extreme care should be taken when interpreting these results.

The samples recrystallized from the spin-coated silicon layers, in contrast, show an even higher thermal activation energy. If the time required for half coverage is respected for (a), a value of 2.8 ± 0.1 eV is obtained, while the result of the growth evaluation (b) yields 2.9 ± 0.1 eV. Here, samples produced from hot wall reactor silicon nanoparticle layers, which are not shown in the figure exhibit the same activation energy of 2.9 ± 0.2 eV. Similar to the findings of Nast [Nas00c], the same energy values are obtained if, *e.g.*, t_{25} or t_{75} are evaluated for these samples.

The high values for the thermal activation energy observed here are almost close to the thermal activation energy of solid phase crystallization of amorphous silicon. However, the latter is usually performed at higher temperatures because reasonable process times are only obtained at temperatures far above 600 °C [Spi98].

Anyhow, the above considerations show that the reaction kinetics of ALILE both with amorphous silicon and with the silicon nanoparticle layers each can be described by a thermal activation energy, which does not depend on the details of the evaluation method. Both the overall layer exchange as well as the growth phase of the silicon crystallites thus appear to be limited by the same physical process with a characteristic energy barrier. Since this value is above the range typically observed for amorphous silicon precursor layers, the specific microscopic mechanisms enabling continuous material supply from the porous silicon network for the crystallite growth might be the limiting factors for the process in this case.

Influence of the oxidation time

According to the observations reported for the aluminum-induced layer exchange, the interface between the aluminum film and the amorphous silicon decisively influences the process results. Nast, Widenborg, Gjukic, and Schneider with their coworkers find that thick oxide barriers on the one hand largely increase the time required for the overall layer exchange, while on the other hand also the average crystallite size is found to depend on the barrier thickness. This is mainly due to the reduced nucleation density and retarded silicon diffusion in the case of thick oxide barriers [Nas00b, Wid02, Gju07, Sch05].

Sample	Aluminum thickness	Air exposure period	Time for half coverage
A	200 nm	5 min	6.8 h
B	200 nm	2 weeks	9.9 h
C	45 nm	0	4.4 h
D	44 nm	5 min	2.8 h

Table 5.1: Effect of the exposure time to ambient air on the time for half coverage in ALILE with spin-coated silicon nanocrystals

To study the influence of the oxide thickness on ALILE with spin-coated silicon nanocrystal layers, different samples were produced using various oxidation conditions. To this end, two substrates were coated with aluminum by thermal evaporation with a thickness of 300 nm. While one sample (A) was spin-coated with a 1 μm thick film of silicon nanocrystals directly after the evaporation, *i.e.* after an exposure period of about 5 min, the other one (B) was aged in air for two weeks before a silicon nanocrystal layer of the same silicon thickness was deposited from the same silicon dispersion.

To test the effect of the very short exposure on the aluminum oxide thickness, an additional pair of samples was produced. Here, the aluminum was evaporated by our cooperation partners at Creavis Degussa in a deposition system connected to a protective atmosphere glove-box. After the deposition of 45 nm aluminum, the sample (C) was spin-coated with silicon nanocrystals inside the protective atmosphere avoiding any contact to air. For comparison with the standard exposure conditions with our samples, a reference sample (D) was produced in our institute. Here, a 44 nm thick aluminum layer was evaporated with our metal deposition system and exposed to air for 5 min before a similar silicon layer was deposited by spin-coating.

Subsequently, these samples were annealed in protective nitrogen atmosphere at a temperature of 550 °C, and the layer exchange kinetics were recorded. The results of the evaluation are given in Table 5.1. As expected, the sample (A) which was exposed to air for only 5 min exhibits a faster layer exchange behavior than the long-term exposed sample (B). This trend is a general observation with the ALILE experiments performed with spin-coated silicon layers. However, the difference between the periods of time required for half coverage of the samples is only a factor of 1.5, and the full layer exchange process still takes about ten hours for completion.

In the case of the samples (C) and (D), the situation is different. Here, the sample processed under protective atmosphere shows a reaction retarded by a factor of 1.6 compared to the sample (D) exposed to ambient air for a period of time of 5 min. However, these samples both show more rapid layer exchange kinetics compared to (A) and (B) due to the reduced aluminum thickness (see Section 5.2.2). As the oxidation time is not the only relevant parameter for the ALILE process speed, here the influence of the different deposition setups outweighs that of the ambient air exposure time. For instance, the aluminum grain size which strongly depends on the deposition conditions is known to determine the nucleation density of silicon grains, leading to a more rapid area coverage [Nas00a].

From this experiment, it can be concluded that even by processing the samples exclusively under inert gas conditions, the process time for the layer exchange with silicon nanocrystals cannot be accelerated significantly. As a consequence of the fast but self-limiting aluminum oxide growth [Lin00], it is already sufficient to keep the exposure time to ambient atmosphere as short as about

5 min to achieve reasonable process times. However, due to high porosity of the spin-coated silicon network, oxidation of the underlying aluminum film can in principle also occur after the deposition of the silicon layer by diffusion of oxygen through the porous network. Such aging effects, however, had only minor effects on the ALILE kinetics even after prolonged storage periods of up to two months, most probably because the decisive points of contact between the silicon layer and the aluminum film are not strongly affected.

Also, it needs to be considered that the surface of the individual silicon nanocrystals is covered with a native oxide after the ball milling dispersion procedure with ethanol (cf. Subsection 4.2.2). Thus, in the case of spin-coated silicon precursor layers, a large number of oxide diffusion barriers are present between the aluminum and the silicon cores of the particles. These barriers might have a comparable impact on the reaction kinetics as the native aluminum oxide thickness, which is an additional explanation for the relatively weak trends in the data from Table 5.1.

Influence of the aluminum film thickness

To study the influence of the aluminum layer thickness on the process kinetics, three glass substrates were coated with aluminum by thermal evaporation with different values of the thickness of 300 nm, 200 nm, 44 nm, and 16 nm. Immediately after the aluminum evaporation, each of the samples was spin-coated with an about 1 μm thick layer of microwave reactor silicon nanocrystals, which implies an exposure of the aluminum film to ambient air for about $5 - 10$ min. Figure 5.8 a) shows the result of decreasing the aluminum thickness on the aluminum-induced layer exchange. The samples consisting of an aluminum film with a thickness of 200 nm and 44 nm are observed to react faster by factors of 1.6 and 4.2 compared to the sample with a 300 nm aluminum layer. Moreover, the 16 nm thick aluminum film leads to an even more accelerated layer exchange by a factor of about 50 compared to the sample with the thickest aluminum layer.

However, the resulting samples exhibit important differences. While the 200 nm and 44 nm aluminum films lead to coherent polycrystalline silicon layers on the substrate after ALILE, in the case of the 16 nm aluminum layer only disjunct silicon islands were present after removal of the silicon and aluminum remnants. Thus, in this case, a complete layer exchange has not occured. Instead, here the aluminum induces crystallization of silicon grains on the substrate, but the aluminum film is too thin to mediate the formation of a coherent polycrystalline film. Thus, the 16 nm data in the Figure 5.8 can not really be compared with those of the thicker aluminum layer samples.

In Figure 5.8 b), the coverage data shown in (a) have been evaluated for the time needed for half coverage during the ALILE process and for the characteristic crystal growth time $t_{75} - t_{25}$ between 25% and 75% coverage and are displayed versus the aluminum thickness. In the double logarithmic plot, the data for the thicker aluminum films follow more or less a linear slope of the process time with the aluminum thickness (dotted lines), independent of the fact, whether the half coverage or the growth time is evaluated. Due to the only partial layer exchange with the 16 nm thick aluminum film, the corresponding data points are well below this line.

A linear increase of the process time with the aluminum thickness allows the interesting conclusion to distinguish whether the limiting mechanism during ALILE with spin-coated silicon layers is the diffusional silicon material supply or, *e.g.*, the silicon adhesion process to the growing silicon grains. As the thickness of the polycrystalline silicon grains growing on the substrate

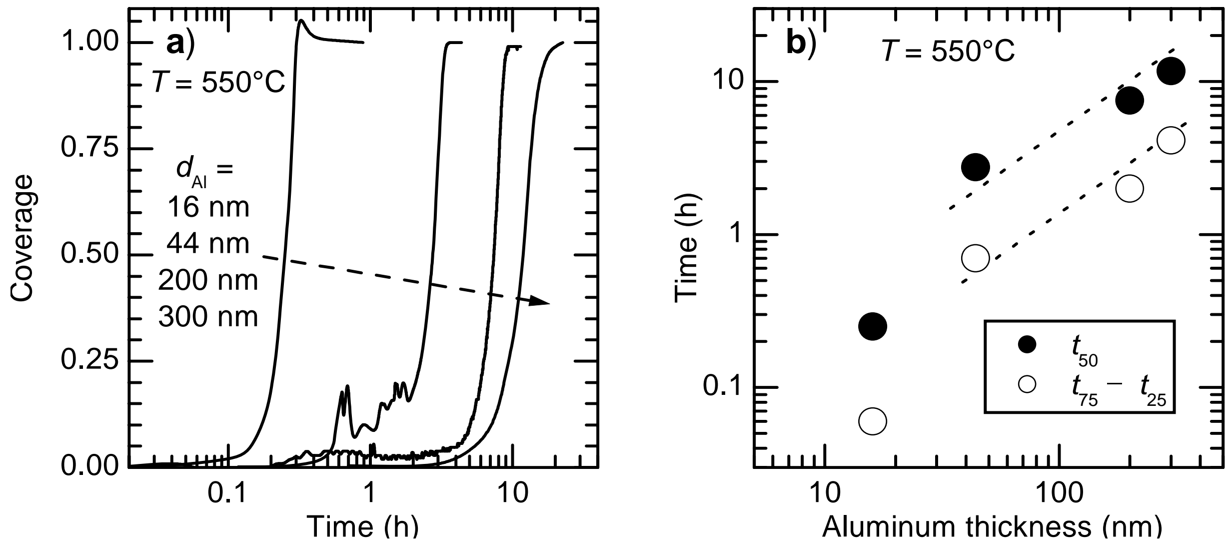

Figure 5.8: Layer exchange kinetics of ALILE with microwave reactor silicon nanocrystal layers at 550 °C with the aluminum thickness varied from 16 nm to 44 nm, 200 nm and 300 nm.

is given by the former aluminum film thickness, simple geometrical considerations can allow to answer this question.

If we consider first the diffusional silicon supply through the interface to be a constant, which is much slower than the typical adhesion process to the growing grains, all silicon atoms will be incorporated into the volume of the growing silicon grains. As a result, we obtain the process speed of the layer exchange, υ, to depend inversely proportional on the layer thickness, d:

$$\upsilon = \frac{\mathrm{d}A}{\mathrm{d}t} = \frac{\mathrm{d}N_{\mathrm{Si}}}{\mathrm{d}t}\frac{1}{d\rho_{\mathrm{at}}} \propto \frac{1}{d}, \tag{5.6}$$

where $\mathrm{d}A/\mathrm{d}t$ is the change of the covered substrate area, A, with time, and ρ_{at} is the atomic density of crystalline silicon. The constant $\mathrm{d}N_{\mathrm{Si}}/\mathrm{d}t$ is the total silicon amount diffusing into the aluminum matrix per unit time.

If instead the adhesion of the silicon atoms to the growing silicon grains (approximated by a cylindrical shape) is the limiting process step, with a constant adhesion rate, R_{Ad}, the process speed does not depend on the aluminum layer thickness:

$$\upsilon = \frac{\mathrm{d}A}{\mathrm{d}t} = \frac{R_{\mathrm{Ad}} 2\pi r d N_{\mathrm{cryst}}}{d\rho_{\mathrm{at}}} = \mathrm{const}(d). \tag{5.7}$$

Here, R_{Ad} is defined as the number of silicon atoms that can adhere to the crystalline grains per unit area and unit time, N_{cryst} is the total number of crystalline grains formed in the sample, and r is the mean radius of the silicon grains. While of course the mean radius of the silicon grains varies during the layer exchange, still the process speed is independent of the aluminum thickness. The here assumed cylindrical growth mode of the crystallites comes close to the sample geometry with the crystallites´ lateral extensions exceeding the vertical dimensions by far.

From these - however simplifying - considerations we can conclude that the material supply is the limiting process step in ALILE with silicon particles. Together with the other findings of the

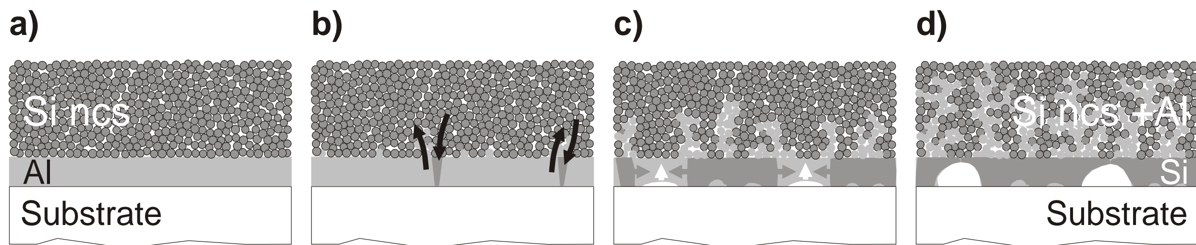

Figure 5.9: Schematic drawing of the ALILE process with spin-coated silicon nanocrystals. a) Displays the initial sample configuration. b) During annealing, the aluminum-silicon interface reaction is enabled, leading to solute silicon in the aluminum matrix, while aluminum, in turn, diffuses into the porous silicon layer. Crystalline silicon grains precipitate in the aluminum matrix. c) Crystalline silicon grains grow laterally in the aluminum film. Diffusional silicon supply is yielded by aluminum branching through the silicon particle network. d) Partial dewetting of the substrate interface by the aluminum occurs and thinner contact regions are formed between adjacent polycrystalline silicon grains. The layer exchange stops.

above subsections, this result enables the formulation of an empirical model for the overall layer exchange in the case of particle precursors in the following subsection.

5.2.3 Phenomenological model for ALILE with silicon particle layers

A schematic model for the aluminum-induced layer exchange with the silicon nanoparticle layers is depicted in Figure 5.9. Here, the respective processes known from ALILE with amorphous silicon precursors have been adapted to the different situation with spin-coated silicon particles with respect to the pertinent experimental observations.

The initial sample system consisting of the substrate/aluminum/silicon particles before the layer exchange is shown in (a). In the sketch, the particulate nature of the spin-coated silicon film is schematically indicated by small silicon spheres. The high porosity of the silicon particle film implies a relatively small direct contact area between the silicon and the aluminum layers. During annealing, the aluminum-silicon interface reaction sets in (b), leading to solute silicon in the aluminum layer and to the precipitation of silicon grains in the aluminum matrix. In turn, aluminum is repelled to the upper layer into the silicon porous particle network. Here, it can diffuse into the pores or into the silicon particle volumes forming an aluminum network with a high concentration of solute silicon. This forming aluminum network then acts as a diffusion bridge connecting the silicon particle layer with the bottom aluminum film on the substrate.

Once the crystalline silicon grains have reached the substrate interface by isotropic growth, they continue to grow laterally, until neighboring grains coalesce with each other (b-d). During these processes, it can occur that closed aluminum regions are trapped in the form of aluminum inclusions at the silicon-substrate interface.

In Figure 5.9 c) and d) the additional substrate dewetting by the aluminum film is included, which is suggested to cause the resulting nonuniform silicon regions of reduced thickness in between neighboring silicon grains. This dewetting can start in regions where no good contact of the aluminum film with the substrate had been present. Since a large amount of aluminum is absorbed by the in-diffusion into the porous silicon network, the remaining aluminum film decreases in thickness while maintaining the wetting of the formed polycrystalline silicon grains

and of the oxidized aluminum surface layer below the silicon nanoparticle film. If additionally also partial dewetting of this upper interface occurs, areas that are completely free of aluminum can form between the nanocrystal layer and the substrate. Consequently, no silicon grains can form in such regions, which persist as pinholes in the resulting samples. For reasons of clarity, the illustration of this effect has been omitted in the figure.

The mechanism of the aluminum diffusion into the silicon network is not known, however. While bulk in-diffusion is possible, also surface diffusion might be a possible explanation. Moreover, the presence of the native surface oxide on the spin-coated silicon nanoparticles has to be taken into account. Consequently, a small fraction of the aluminum is spent also during the chemical reduction of the silicon oxide layers to aluminum oxide and is lost for the metallic aluminum diffusional network. And the thermal activation barrier of this interface reduction reaction most probably contributes significantly to the overall increase of the thermal activation energy with respect to amorphous precursors.

Apart from several details that still remain to be clarified, the above given picture of the ALILE process with silicon particles is able to explain the trends and findings of the previous subsections:

- The ALILE process is rather independent of the size of the particles in the precursor layer such that both hot wall reactor nanoparticles and microwave reactor nanocrystals show similar reaction kinetics.
- The thermal activation energy considerably exceeds the values for amorphous precursor layers, indicating additional energy barriers for the overall reaction.
- The impact of the aluminum oxidation conditions is less pronounced than is typical for amorphous precursors.
- A typical supply-limited thickness dependence of the growth rate has been observed.

All of these results can be regarded as consequences of the particulate structure of the precursor in the phenomenological model outlined above. Thus, from the fact itself that a porous layer of silicon particles is used as the precursor, the severe differences in the morphology and the reaction kinetics with respect to the conventional ALILE process can be understood.

5.2.4 Optical Properties

After the layer exchange and even before remnants of the aluminum have been removed, the macroscopic optical appearance of the samples has changed completely: the metallic reflectivity of the aluminum layer has disappeared, the samples have gained partial transparency during the process, and a thin film interference colored layer can be distinguished from the substrate side. These observations are supported by optical measurements, which indicate substantial changes in the material properties from those of the porous silicon particle films towards that of polycrystalline silicon.

Reflectivity and index of refraction

Figure 5.10 a) shows the reflectivity spectra of a layer of microwave reactor silicon nanocrystals before and after the ALILE process. The sample consisted of a glass substrate coated with a 250 nm thick aluminum film and 1.2 μm thick silicon nanocrystal layer was spin-coated on top. A part of the sample was annealed for 50 h at a temperature of 550 °C, and the aluminum and silicon nanocrystal remnants were removed. For comparison, also the reflectance spectrum of a crystalline silicon wafer is displayed in the figure.

As the graph shows, the characteristic Van-Hove-peaks in the ultraviolet spectral region are even more pronounced after ALILE and mirror the reflectivity of the crystalline silicon reference. Also in the visible and near infrared region, significant changes occur in the spectra. Here, the thin-film interference fringes change their spacing and position with respect to the situation in the spin-coated layers. After ALILE, the number of the oscillations has decreased by a factor of two, indicating a much thinner film or a reduced optical density. By evaluating the refractive index from the energy positions of the reflectivity extrema, it turns out, however, that the optical dispersion has strongly increased and is similar to the refractive index of bulk crystalline silicon. If the thickness of the initial aluminum film is used as the thickness of the ALILE silicon film, the refractive index matches perfectly with the literature data as demonstrated in Figure 5.10 b). Here, the results of measurements with ALILE crystallized microwave reactor silicon nanocrystals and hot wall reactor silicon nanoparticles are shown (full and open symbols, respectively). While all spin-coated layers exhibit the refractive index of a porous silicon particle network with a porosity of about 60% in the Bruggemann model, after ALILE thin layers of crystalline silicon are formed on the substrate with a thickness of the former aluminum film. The good agreement of the thickness of the ALILE recrystallized films with the thickness of the initial aluminum film has also been corroborated by atomic force microscopy measurements.

The observation of the thin-film interference fringes does not necessarily imply the presence of a closed layer of silicon on the substrate. Only a layer with a homogeneous thickness is required to cover a significant surface fraction of the samples [Swa84]. Hence, the existence of pinhole areas and thinner silicon regions as shown in the morphology section is not in contradiction with the occurrence of the oscillation pattern. However, from the absence of a second superimposed oscillation with different energy spacing, it can be concluded that no ordered hillock or island formation is present in the case of ALILE with silicon nanocrystal and nanoparticle layers [Lec03, Gju07]. For ALILE with spin-coated silicon layers, we can conclude that flat silicon grains grow only within the former aluminum layer and do not form island-like structures on top as known for ALILE with amorphous silicon [Wid02].

Absorption

Along with the index of refraction, also the absorption behavior of ALILE crystallized layers changes in comparison with the spin-coated silicon layers. This effect is evident best for the hot wall reactor silicon nanoparticles, which are represented by the open symbols in Figure 5.10 b): while spin-coated layers of this material showed significant absorption and complete suppression of the thin-film interferences already around a photon energy of 1.8 eV, the ALILE crystallized layers from this precursor show interference fringes up to 3.2 eV, which do not differ significantly from polycrystalline silicon films obtained from the layer exchange with microwave reactor silicon nanocrystals.

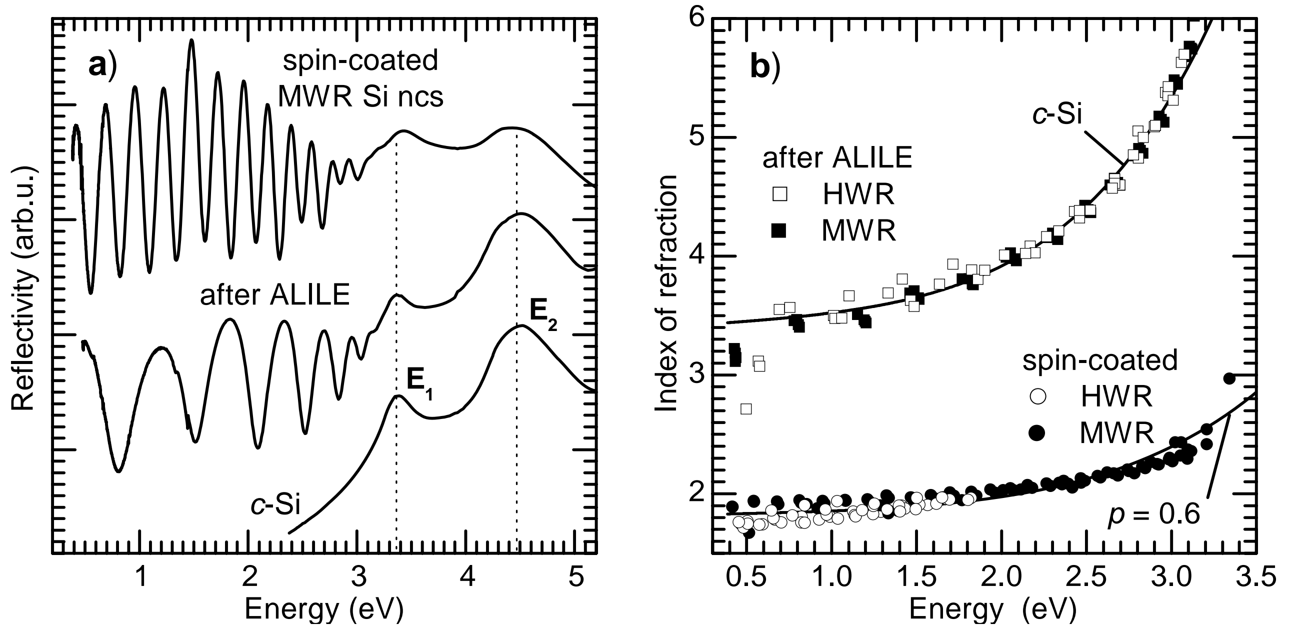

Figure 5.10: a) Reflectivity spectra of a layer of silicon nanocrystals grown in a microwave pasma reactor, before and after the ALILE process. The reference spectrum of crystalline silicon is given for comparison. b) Refractive index of spin-coated silicon layers before and after ALILE as derived from the thin-film interferences in the reflectivity spectra. Literature values for crystalline silicon [Asp99] and the calculated curve for a 60% porous silicon particle network are shown by the solid lines.

From transmission measurements the strong interband absorption typical for crystalline silicon in the near ultraviolet region can be observed with the ALILE crystallized spin-coated silicon layers. Yet, due to the presence of pinholes or void area fractions in the obtained layers, this procedure also requires a correction for the overall pinhole area fraction. In the visible and near infrared spectral region however, the extraction of the absorption coefficient becomes inaccurate due to the thin-film interference fringes.

On the other hand, the large concentration of inclusions in the polycrystalline films after ALILE does not allow the characterization via photothermal deflection spectroscopy. A saturated PDS signal over the full spectral range prevents reasonable interpretation of the obtained spectra. In the case of polycrystalline silicon from ALILE with amorphous silicon, the absorption coefficient in the visible and ultraviolet region of the spectrum coincides well with that of bulk crystalline silicon, whereas in the infrared spectral region around the fundamental bandgap constant absorption levels are found. Inclusions and defects are most likely responsible for this observation, while a small contribution can be assigned to free carrier absorption as a consequence of the implicit aluminum doping during ALILE [Gju07, Lec03].

5.2.5 Electrical Properties

After ALILE, the recrystallized spin-coated silicon layers show a high electrical conductivity. Not only was the structure changed from nanoparticles to macroscopic polycrystalline grains, but also the percolation has been improved largely. After the layer exchange, no oxide barriers are present between neighboring crystalline grains, which now exceed sizes of several microns, and

noticeable electrical conductivity is observed without any precedent etching step in hydrofluoric acid.

Conductivity

The electrical conductivity of the polycrystalline silicon films obtained via ALILE from silicon particle layers is typically in the range of $3 - 5\,\Omega^{-1}\,\mathrm{cm}^{-1}$. These high values correspond to an increase of the electrical conductivity by more than ten orders of magnitude compared to the as-deposited situation of the silicon particles after spin-coating and removal of the native oxide. However, this finding is closely related to several major changes that have occurred during the layer exchange:

- The crystalline structure was completely rebuilt, with an increase in the grain size from about 20 nm to several micrometers. The corresponding number of interfaces for the electrical transport through the layer has thus decreased by a factor of $10^2 - 10^3$, if a one-dimensional model is considered.
- The silicon nanocrystal surfaces were covered with native oxide before, whereas the polycrystalline film consists of interconnected silicon crystalline grains The native oxide present around the silicon particles has been reduced and gettered by the aluminum matrix. Without these interfacial oxide barriers, electrical transport is not strongly thermally activated and carriers do not need to tunnel through barriers.
- Due to the intimate contact with the aluminum, the polycrystalline ALILE silicon film is inherently doped with the aluminum shallow acceptors. If amorphous silicon is crystallized via ALILE, the concentration of free carriers in the resulting polycrystalline films corresponds to the solubility of aluminum in crystalline silicon at the process temperature [Maj79, Gju05]. The pertinent values are relatively large and range around $6 \times 10^{18}\,\mathrm{cm}^{-3}$ for aluminum in silicon (compare Figure 3.5).

Mobility and carrier concentration

To determine the physical origin of the largely increased electrical conductivity, Hall effect measurements were performed with the ALILE recrystallized nanocrystal samples. The samples were found to be *p*-type, and the typical hole concentration at room temperature was $2 \times 10^{18}\,\mathrm{cm}^{-3}$. This value is in good agreement with the results of ALILE polycrystalline silicon from amorphous silicon precursor layers [Maj79, Nas98, Gju05]. The carrier mobility that we observe for samples crystallized at a temperature of $550\,^{\circ}\mathrm{C}$ ranges from $20\,\mathrm{cm}^2\,\mathrm{V}^{-1}\,\mathrm{s}^{-1}$ to $40\,\mathrm{cm}^2\,\mathrm{V}^{-1}\,\mathrm{s}^{-1}$.

Interestingly, the hole Hall mobility observed with the recrystallized spin-coated silicon nanocrystal layers is somewhat smaller than for ALILE layers from amorphous silicon. There, the carrier mobility approached values as high as $100\,\mathrm{cm}^2\,\mathrm{V}^{-1}\,\mathrm{s}^{-1}$. However, several factors deteriorate the carrier mobility in the polycrystalline silicon films:

- The layers were grown at relatively high temperatures leading to an increased solubility of aluminum in silicon and to a relatively small effective silicon grain size. While the first

effect results in increased Coulomb scattering at the charged aluminum acceptors at room temperature, the second fact invokes enhanced grain boundary scattering as a consequence of the reduced crystallite size [Gju07].

- The thickness of the films is significantly smaller in the interconnecting regions. Indeed, thinner films have been observed to lead to increased surface scattering, reducing the carrier mobility [Gju07].
- The pinhole fraction in the ALILE layers with spin-coated silicon is a known factor to decrease the apparent Hall mobility of the carriers [Gju05].

So, from the relatively high temperature necessary to achieve the layer exchange within reasonable periods of time and from the particular morphology of the obtained polycrystalline silicon films, it can be understood why a reduced carrier mobility results in the case of spin-coated silicon precursor layers. However, the achieved mobility values are still respectable if compared to state-of-the-art techniques such as amorphous or microcrystalline silicon. There, hole mobilities on the order of 0.1 are attainable [Saz04, Sun07].

5.3 Acceptor Passivation of ALILE crystallized Silicon nanocrystals

The electrical properties of ALILE recrystallized spin-coated silicon layers have been shown above to be slightly inferior to those known from the layer exchange with amorphous silicon precursor layers. Apart from the structural peculiarities of these layers, also a detrimental influence of the high aluminum concentration on the carrier mobility was considered possible. To test whether the mobility could be increased by decreasing the concentration of active acceptors, deuterium passivation experiments were performed. Here, the hydrogen isotope deuterium (^{2}H or D) was chosen to achieve a better detectability in thermal effusion measurements.

5.3.1 Effusion experiments

Deuterium passivation was found to be an applicable method to decrease the free hole concentration in polycrystalline silicon layers from ALILE with silicon nanocrystal layers. After a long-term exposure to a remote deuterium plasma, the resistivity of the samples had increased by two orders of magnitude.

To prove that this is due to the passivation of aluminum acceptors by incorporated deuterium and to exclude possible damage by the plasma treatment, thermal effusion experiments were performed. Since the deuterium is only weakly bound inside the silicon lattice, out-diffusion and desorption takes place at moderate temperatures, which leads to a recovery of the pre-passivated situation [Pan84]. This reversibility was tested by heating the samples in high vacuum at a well-defined heating rate, and recording the partial pressure of deuterium as a function of the temperature.

The resulting data of two samples that had been deuterated for a period of 144 h are shown in Figure 5.11 b) for two different heating rates of 5 K min^{-1} and 20 K min^{-1}. The sample size was 3×3 mm^2 and the thickness of the polycrystalline silicon film was 300 nm. For comparison, the

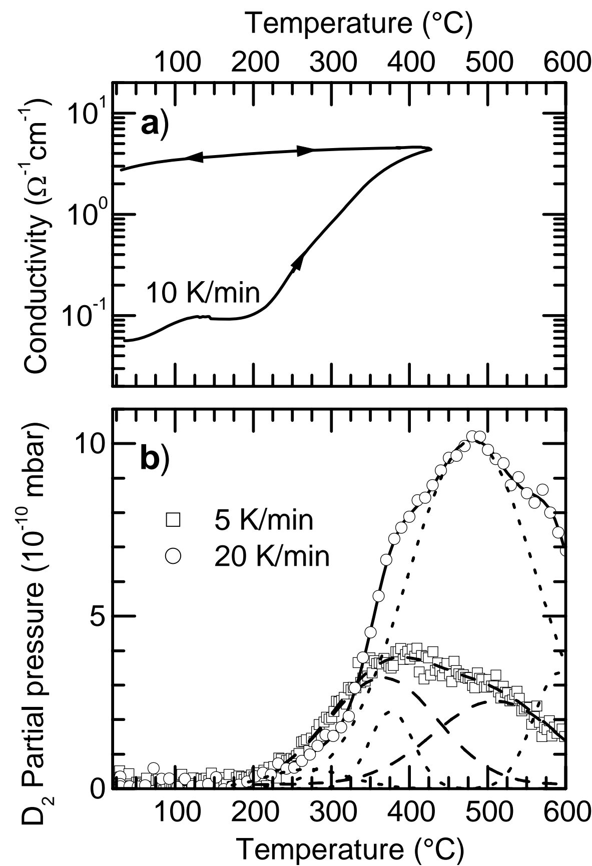

Figure 5.11: a) Electrical conductivity and (b) deuterium partial pressure of ALILE crystallized spin-coated silicon nanocrystal layers during temperature programmed desorption experiments.

electrical conductivity of a similar sample measured *in situ* during annealing is given in (a) for an intermediate heating rate of $10\,\mathrm{K\,min^{-1}}$.

At temperatures in the range of $300 - 600\,^{\circ}\mathrm{C}$, for both heating rates a significant increase in the deuterium partial pressure is evident in (b), which is not observed for unpassivated samples or during a repeated heating cycle. While these effusion data clearly show the presence of deuterium in the passivated samples, the conductivity data show that the deuterium desorbed from the samples was indeed responsible for the reduced conductivity of the samples. As evident from Figure 5.11 a), the electrical conductivity changes upon annealing from room temperature to $430\,^{\circ}\mathrm{C}$ by two orders of magnitude from $0.05\,\Omega^{-1}\,\mathrm{cm}^{-1}$ to $5\,\Omega^{-1}\,\mathrm{cm}^{-1}$. After this first annealing, the effusion of hydrogen is already complete and the conductivity change in the same temperature range due to thermal carrier activation is limited to a factor of 1.7 in all subsequent heating cycles (indicated by the arrows in the figure). The corresponding activation energy of the conductivity in this regime amounts to about $23\,\mathrm{meV}$. This is a typical value observed for unpassivated ALILE-recrystallized silicon particle layers, which proves the recovery of the nearly degenerate aluminum doping after the effusion.

This reversible deuterium effusion experiment demonstrates that the substantial changes in the electrical properties that will be in the focus of the following subsection are not a consequence of, *e.g.*, structural damage introduced into the samples during the deuterium plasma passivation procedure. Instead, reversible aluminum-deuterium bonds are formed in the passivated mate-

rial that passivate the electrical activity of the aluminum acceptors. Stavola *et al.* could correlate the reduced activity of the aluminum acceptors in crystalline silicon with the occurrence of aluminum-hydrogen and aluminum-deuterium vibrational modes in infrared spectroscopy. They also observed the thermal reactivation of the aluminum acceptors during annealing in the temperature range of $200-300\,^{\circ}\mathrm{C}$ [Sta88].

The shape of the deuterium effusion peaks shown in (b) is a consequence of the specific desorption channels of deuterium and hydrogen in crystalline silicon [Stu91, Kim01]. While the deuterium atoms become highly mobile in crystalline silicon by diffusion at temperatures above 150 °C, the desorption is limited by surface-bound deuterium atoms, forming silicon-deuterium complexes. At characteristic temperatures related to the specific binding energy of the respective compound, deuterium atoms recombine pairwise to form deuterium molecules, which are then easily desorbed from the crystalline silicon surface.

For a heating rate of $20\,\mathrm{K\,min^{-1}}$, the desorption processes observed during the effusion of deuterium from crystalline silicon around 350 °C and 500 °C correspond to the thermal disruption of silicon dideuteride ($Si{=}D_2$) and silicon monodeuteride ($Si{-}D$) surface bonds, respectively [Stu91, Kim01]. Our results for this heating rate are given by the open circles in Figure 5.11 b). The line fit to the experimental data was performed by a superposition of three Gaussian peaks and the individual fit contributions are indicated by the dotted lines in the figure. While the temperature values of the small effusion peak at 375 °C and the large contribution around 480 °C are very close to the literature values and can thus be assigned to the above-mentioned deuterium desorption channels, a third small contribution is visible centered around a peak temperature of about 600 °C.

If a heating rate of $5\,\mathrm{K\,min^{-1}}$ is applied (open squares in the figure), two peaks occur at slightly different temperatures of 350 °C and 520 °C, and no third high temperature contribution is evident from the data. It is a well-known effect in desorption experiments that desorption peak temperatures can shift significantly if the heating rate is varied [Bey82]. While no such shift can be stated for our data, we observe an intensity increase of the silicon dideuteride peak with respect to the monodeuteride peak for the lower heating rate. The peak positions are again close to the values observed, *e.g.*, by Kim *et al.* who reported the mono- and the dideuteride desorption peaks at temperatures of 400 °C and 520 °C, respectively if a heating rate of $2\,\mathrm{K\,min^{-1}}$ was chosen [Kim01].

To be more accurate, instead of fitting with Gaussian contributions, the deuterium effusion peaks should be analyzed by the help of a physical model respecting for the desorption kinetics of the deuterium atoms. This can be adequately accomplished, *e.g.*, in a Polanyi-Wigner analysis as performed by Kim and coworkers [Kim01]. However, the surface of our polycrystalline samples is rather undefined and the resulting spectra exhibit broad peak structures. Still, the qualitative results obtained from the simple peak analysis performed here shows the presence of deuterium in the passivated samples and proves the passivation of the aluminum acceptors in the ALILE crystallized spin-coated silicon layers by the in-diffused deuterium atoms. To quantify the consequences of the passivation on the conductivity, on the carrier concentration, and on the mobility, a time-resolved passivation study was undertaken.

5.3.2 Electrical properties of passivated layers

For an experimental series studying the effect of the passivation time, a fused silica substrate coated with 230 nm aluminum was spin-coated with a 1 μm thick layer of microwave reactor silicon nanocrystals (20 nm diameter). The sample was annealed at 550 °C for 1.5 d and remnants of silicon and aluminum were removed. Six similar rectangular pieces were cut from the same sample, each about $3 \times 3\,\mathrm{mm}^2$ in size. For the electrical characterization, aluminum contacts were deposited by thermal evaporation in van-der-Pauw geometry. The characterization of the electrical properties was then performed via Hall and conductivity measurements at room temperature. Subsequently, three of the samples were passivated in a remote plasma deuterium passivation setup. The passivation procedure was executed in several steps with the passivation time being increased stepwise, starting from 10 min to 30 min, 1 h, 3 h, 23 h, and 43 h. After each passivation step, the electrical characterization was repeated.

Figure 5.12 a) shows the result of the passivation procedure on the hole concentration in the polycrystalline silicon films. Here, the hole concentration at room temperature is plotted as a function of the integral passivation time. As the figure shows, the hole concentration is observed to decrease by a factor of 20 from the initial value of $2 \times 10^{18}\,\mathrm{cm}^{-3}$ before the passivation down to $10^{17}\,\mathrm{cm}^{-3}$ after a passivation time of 165 h. After this process, it can be concluded that 95% of the aluminum acceptors are passivated by in-diffused deuterium atoms. Since the passivated acceptors exhibit a neutral charge state, this reduction should directly translate into a decreased Coulomb scattering of remaining carriers, thus increasing the carrier mobility if Coulomb scattering is the dominant scattering mechanism. In the case of crystalline silicon, the same decrease in the hole concentration would correspond to an increase in the hole mobility by a factor of 2.7 from $120\,\mathrm{cm}^2\,\mathrm{V}^{-1}\,\mathrm{s}^{-1}$ to $320\,\mathrm{cm}^2\,\mathrm{V}^{-1}\,\mathrm{s}^{-1}$ [Sze07].

However, the situation with the ALILE crystallized silicon nanocrystals is different. Figure 5.12 b) depicts the change in the Hall mobility versus the integral passivation time. After four hours of passivation the mobility collapses down to values of $2 - 3\,\mathrm{cm}^2\,\mathrm{V}^{-1}\,\mathrm{s}^{-1}$. Continued passivation leads to a further decrease of the mobility to $1\,\mathrm{cm}^2\,\mathrm{V}^{-1}\,\mathrm{s}^{-1}$. For passivation times exceeding 50 h, however, a clear recovery of the mobility is visible, approaching values of $5 - 6\,\mathrm{cm}^2\,\mathrm{V}^{-1}\,\mathrm{s}^{-1}$ again. As this behavior contradicts the expectations stated above regarding the Coulomb scattering of carriers, it follows that the latter is not the limiting scattering process for the hole mobility within these samples. In contrast, the occurrence of a mobility minimum during the passivation process is a consequence of the polycrystalline nature of the ALILE crystallized spin-coated silicon layers. This will be demonstrated in the following in the framework of the grain boundary barrier theory introduced in Section 3.6.5.

5.3.3 Grain boundary barriers in ALILE recrystallized films

While the hole mobility exhibits a minimum as a function of the passivation duration, the hole concentration decreases continuously during the passivation process as Figure 5.12 a) shows. Thus, if the mobility data is plotted as a function of the hole concentration, also a minimum of the mobility should be evident. The result shown in Figure 5.13. While early stages of the passivation procedure change little in both hole concentration and mobility, a sudden decrease is evident at a hole concentration of $1.0 - 1.5 \times 10^{18}\,\mathrm{cm}^{-3}$. Further decreasing the carrier concentration below $5 \times 10^{17}\,\mathrm{cm}^{-3}$ leads to minimum mobility values around $1\,\mathrm{cm}^2\,\mathrm{V}^{-1}\,\mathrm{s}^{-1}$, whereas the mobility recovers to values of around $5\,\mathrm{cm}^2\,\mathrm{V}^{-1}\,\mathrm{s}^{-1}$ at a hole concentration of $10^{17}\,\mathrm{cm}^{-3}$.

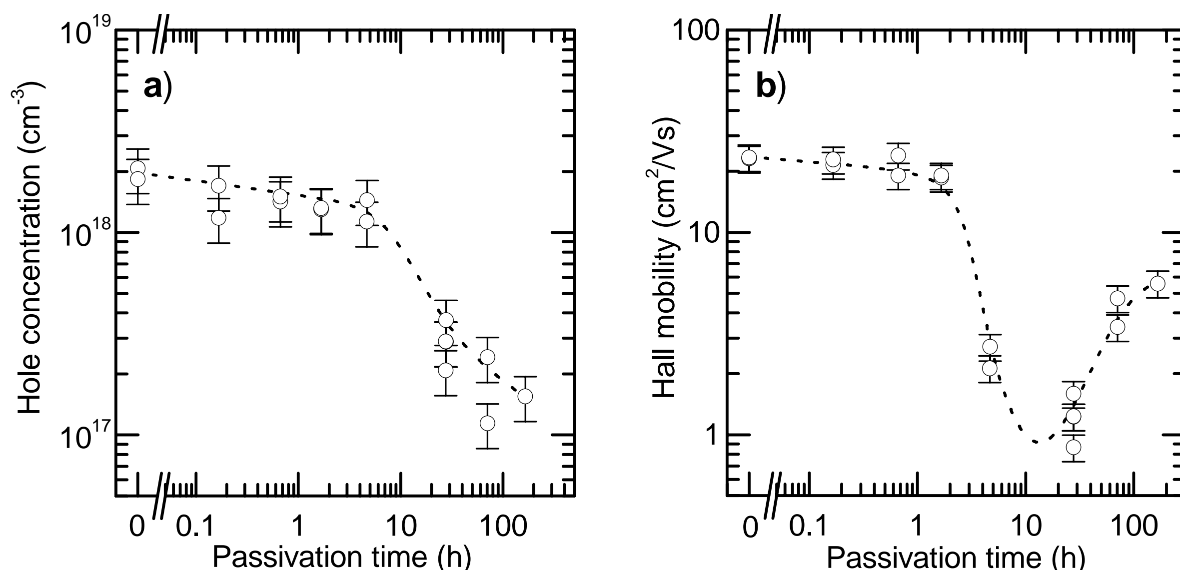

Figure 5.12: a) Room temperature hole concentration and (b) Hall mobility of ALILE crystallized polycrystalline silicon films from spin-coated layers as a function of the integral passivation time. The dotted lines are guides to the eye.

The observed behavior is exemplary for grain boundary limited transport as described, *e.g.*, by the theory by Seto [Set75]. As presented in Section 3.6.5, a critical doping concentration exists in the polycrystalline films, at which the energy barriers for electrical transport between neighboring crystalline grains becomes maximal. This is a consequence of a maximum amount of charge trapped at the interface defect states under full depletion of the grains. This critical carrier concentration amounts to $N = Q_t/L$, with the defect density, Q_t, and the crystal size, L.

As the position of the critical doping concentration is quite well defined by the experimental data in Figure 5.13, a numerical fit to Equation 3.28 can be performed. The result is given by the dotted line in the figure, which corresponds to a critical doping concentration of $5 \times 10^{17}\,\mathrm{cm}^{-3}$. Accordingly, the interface defect concentration is obtained as $Q_t = 5 \times 10^{13}\,\mathrm{cm}^{-2}$, if the crystal size is assumed to be on the order of $L = 1\,\mu$m.

This result is an extraordinary high number of defect states, which is one to two orders of magnitude higher than what is typically present at interfacial areas in crystalline and polycrystalline silicon [Joh83, Set75, Bac78]. In general, quantitative deviations can be expected for the grain boundary barrier model, because it is based on a simplifying one-dimensional approach to the physical situation. However, the discrepancy in this case appears too far from reality.

Instead, because the crystallite size exceeds the film thickness, not only the crystallite lateral dimensions but also the film thickness has to be considered. Especially in the situation of the ALILE recrystallized particle films, the properties of the very thin interconnecting silicon regions can determine the overall electrical behavior of the films.

Due to the effective thickness of these areas of only 50 nm, the critical doping concentration is shifted to relatively large doping concentrations. If the defect concentration is evaluated using the mobility data in combination with this vertical dimension, a trap density of $Q_t = 3 \times 10^{12}\,\mathrm{cm}^{-2}$ is obtained, which is in reasonable agreement with the typical values [Joh83, Set75, Bac78]. Unfortunately, the direct determination of the defect density is not possible by electron param-

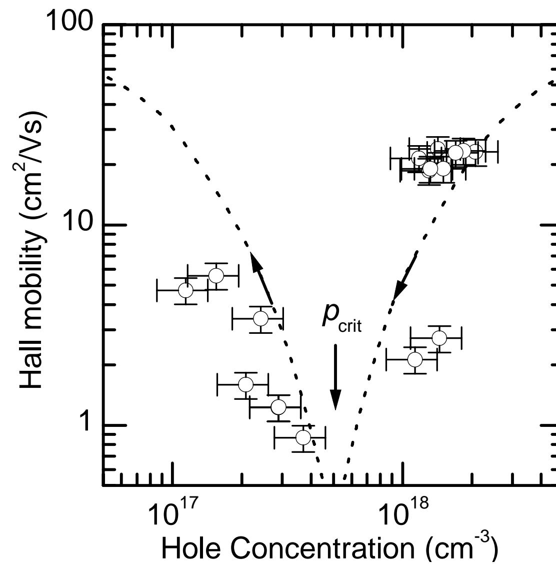

Figure 5.13: Room temperature hole Hall mobility of the hydrogen passivated spin-coated silicon films crystallized via the ALILE process plotted versus the free hole concentration.

agnetic resonance measurements. In the highly aluminum-doped films, the majority of dangling bonds is positively charged and thus invisible in EPR. Only if nearly full passivation is achieved, the true concentration of dangling bonds in the layers can be determined by this technique. As Figure 5.12 shows, large concentrations of holes are still present after long exposure times to the remote deuterium plasma.

The situation in the ALILE recrystallized films upon passivation can be interpreted in that way that the thin interconnecting crystalline silicon areas are completely depleted for hole densities around the critical hole concentration. At the surfaces and around grain boundaries, energy barriers inhibit current transport. Both, for higher and for lower hole concentrations, an increase of the mobility is present. For lower hole densities this is due to a smaller amount of localized charges at the interface defects, whereas for higher hole concentrations the barrier potential is shielded by additional free charges and non-depleted regions exist in the polycrystalline films. An illustrative interpretation of this situation has been given in [Gju07].

As the dotted line in Figure 5.13 suggests, the mobility could be further enhanced by reducing the carrier concentration even more, by passivating a higher fraction of the present aluminum acceptors. However, even after prolonged passivation periods, a passivation efficiency exceeding 95% was not achieved in these experiments. However, in the literature, passivation efficiencies for aluminum acceptors in silicon of up to 99% have been reported [Pan84], which would translate into a hole concentration of only $2 \times 10^{16}\,\mathrm{cm}^{-3}$ in our situation. From this point of view, the possibility to improve the hole mobility with respect to the initial value before the passivation procedure cannot be excluded.

6 Laser Annealing of Silicon Nanocrystal Layers

Laser crystallization nowadays has become one of the most relevant techniques used in the semiconductor industry. It is mainly used to transform amorphous silicon into polycrystalline silicon layers on glass substrates for applications in active matrix thin film transistor arrays for liquid crystal displays [Bro99]. Still at a stage of research, the method is also applied to improve the structural and electrical properties of low-temperature deposited silicon for high efficiency transistors and for thin film solar cells [Das00, And03].

As the laser crystallization of amorphous and hydrogenated amorphous silicon (*a*-Si, *a*-Si:H) has emerged to be an extremely successful approach, we will test in the following the applicability of this method to the spin-coated silicon nanocrystal layers. A short overview over the common experimental practice will be given first, to motivate the method of laser pulse series annealing implemented here.

6.1 Laser Crystallization of Silicon

6.1.1 Laser systems

A great advantage of laser crystallization techniques is the possibility to crystallize only a very thin film of silicon on almost arbitrary substrates. The minimum silicon material demand here is not only of economic benefit, but also helps to keep the substrate´s thermal budget low, *i.e.* the time integral over the temperature, due to the small thermal capacity of the thin film. Of course, the laser wavelength has to meet the requirement of very efficient absorption in such a thin film. For a 100 nm thick layer of amorphous silicon, this brings about the need for a wavelength shorter than 600 nm to limit the transmission losses (the absorption coefficients at 2 eV of amorphous and of hydrogenated amorphous silicon amount to $10^5\,\mathrm{cm}^{-1}$ and $3 \times 10^4\,\mathrm{cm}^{-1}$, respectively [Iof08, Buc98]).

While, *e.g.*, continuous wave (cw) Ar^+ lasers with a wavelength of 514.5 nm can be applied [And98], it has been found that the high thermal load during this procedure can even lead to out-diffusing of boron contaminants from the glass substrates. Pulsed laser systems, in contrast, due to the extremely short pulse duration operate far from quasi-static heat flow conditions to the substrate. Instead, the power is introduced within tens of nanoseconds, heating efficiently only the absorbing layer. Thus, it has become possible to use a wide variety of substrates including metal coated glass or plastic foil [Bre03a, Len02].

As the pulsed laser systems, for example neodymium-doped synthetic crystals such as yttrium orthovanadate (YVO_4) or yttrium aluminum garnet (YAG, $Y_3Al_5O_{12}$) can be used as the laser-active medium [Das00, Aic99]. Since both solid state lasers exploit the neodymium laser transitions, their main emission line occurs at a wavelength of 1064 nm. By frequency-doubling with a second harmonic generator, a wavelength of 532 nm is achieved suitable for the crystallization of silicon thin films. By ultrafast switching of the quality factor of the laser cavity (Q-switch),

the pulsed emission of a 1 J light pulse can be stimulated within $8 - 10$ ns in a small laboratory system, resulting in laser pulses in the 100 MW power regime.

Moreover, excimer lasers can be employed, which usually exploit the excited state of a noble gas-halogenide complex for lasing. This class of pulsed laser systems with typical pulse durations of $25 - 30$ ns currently dominates the market of industrial laser crystallization of silicon. The most used lasing media in this case are krypton fluoride (KrF) and xenon chloride (XeCl) with emission wavelengths of 248 nm and 308 nm, respectively [Bro99, And03, ImK93]. The ultraviolet emission of excimer lasers leads to very short absorption lengths of the irradiated light of about 10 nm, which, together with the short pulse time, induce melt durations of the silicon layer of $50 - 100$ ns [ImK93].

The maximum possible repetition rate of the laser pulses depends on the lasing medium and the pumping mechanism. While the excimer lasers can be run with pulse frequencies of up to $300 - 1000$ Hz, the solid state Nd:YAG and Nd:YVO_4 lasers allow higher repetition rates and can be operated at frequencies of up to 100 kHz [Das00]. Thus, the latter enable a significantly higher throughput for industrial large-area applications.

6.1.2 Pulsed laser crystallization of amorphous silicon

Im, Kim, and Thompson have found that several energy density regimes can be distinguished during the pulsed laser crystallization of amorphous silicon [ImK93]. In the low energy density region, an energy density threshold exists around 100 mJ cm^{-2}, which is found necessary for the melting of a surface layer. Above this value, a small grain size around 20 nm results after the rapid re-solidification starting from the still solid underground layer. At higher energy density, a second threshold occurs marking the energy density necessary for melting of the full silicon layer. If this value is exceeded, the silicon melt undergoes supercooling and solidifies from statistically formed nucleation spots. Since the resulting nucleation density is quite high, also in this case nanocrystalline silicon films exhibiting relatively small crystallite grain sizes in the range of 20 nm are obtained [ImK93]. In between these two energy density regimes, a narrow parameter interval is found, referred to as "super lateral growth" (SLG) regime. Here, grain sizes as large as $300 - 400$ nm result from a low density of remaining silicon grains within the almost completely liquefied film.

To further increase the grain size obtained by laser annealing, several successful approaches have been reported. By scanning the substrate or the laser during the crystallization, lateral dimensions of the silicon crystallites of larger than 10 μm can be achieved [Das00]. Also, interference crystallization has been applied to produce silicon grains exceeding several micrometers [Aic99, Eis02].

It should be noticed that often an amorphous silicon oxide capping layer is deposited on top of the amorphous precursor layer [Bro99]. This is to reduce the amount of silicon lost during the laser treatment by evaporation and to provide a planar sample surface for device fabrication. Especially in the case of laser crystallization under vacuum, this additional layer is an important prerequisite for the good quality of crystallized layers [ImK93].

6.1.3 Stepwise laser crystallization

The usual precursor layer for the laser crystallization of silicon is amorphous silicon. Although sputtered or thermally evaporated amorphous silicon can be used for this purpose, chemical vapor deposition (CVD) processes will be preferred for the reason of better defect passivation by hydrogen, higher stability against oxidation and high deposition rates. However, the large hydrogen concentration of about 10% in the films deposited, *e.g.*, via plasma enhanced chemical vapor deposition (PECVD), causes problems. To avoid destruction of the layer by explosive hydrogen effusion during the laser crystallization, the hydrogen content within the silicon layer needs to be kept below 1% [Aic99]. This can be achieved either by low pressure CVD implying low deposition rates [ImK93, Das00], or by pre-annealing of the hydrogenated amorphous silicon at a temperature of about 450 °C prior to the laser crystallization step [Mei94].

An interesting alternative has been developed by Mei and coworkers and Lengsfeld *et al.*. By performing three subsequent laser crystallization procedures with increasing energy density, Mei *et al.* managed to effuse the hydrogen from within the silicon film, reducing the hydrogen content below 1% [Mei94]. In contrast, Lengsfeld and coworkers performed laser crystallization using a continuously increasing energy density during subsequent laser pulses. The idea behind this gradual energy density increase is to crystallize the silicon layer under the presence of a largest possible concentration of hydrogen to passivate grain boundary defects *in situ*. Indeed, a hydrogen content of 5% has been detected to remain in completely laser-crystallized layers [Len00].

A stepwise increase of the laser energy density has also been applied in this study of the laser crystallization of the spin-coated silicon nanocrystal layers as described in Section 2.1.7. If the laser energy was increased to the final value in one shot, instead, the layers were severely damaged for higher pulse energies. This fact can be attributed to the relatively large internal surface of the spin-coated network. During the fast laser heating, a large amount of water and gases adsorbed to this surface is evaporated immediately, leading to explosive desorption similar to the situation of the hydrogen in hydrogenated amorphous silicon.

6.1.4 Laser crystallization of silicon nanocrystals

Although laser crystallization lends itself as a high potential method for the annealing of silicon nanoparticle layers, little research has been performed regarding this subject as yet. Bet and Kar published a combined theoretical and experimental study on the laser annealing properties of silicon nanocrystals [Bet04]. However, while they present a geometrical theory describing the sintering of spherical nanocrystals as a function of particle size and laser energy, the experimental section, apart from melting point depression analysis, deals with the laser assisted nickel-induced crystallization of silicon nanoparticles on nickel substrates. While the authors are aware that silicon crystallization is strongly influenced by the presence of nickel, they completely neglect this fact in their analysis.

In the experimental part of that study, silicon nanocrystals were brought into aqueous dispersions to form films on nickel foil substrates. The fundamental laser emission line of a Nd:YAG laser at 1064 nm was used in cw operation to locally heat the sample with a power density of $500 - 900\,\mathrm{W\,cm^{-2}}$ for several minutes. The presented experimental data show a strong intermixing of the metal with the silicon phase as already reported by, *e.g.*, Brendel *et al.* for the

laser crystallization of amorphous silicon deposited on nickel-coated substrates [Bre03a]. The presented fragmentary experimental results leave many open questions and are subject to partial misinterpretation. Extremely doubtful are the results of laser-assisted doping experiments using nitrogen gas and boron from a "powder source" as dopants [Bet04].

In contrast to the publication by Bet *et al.*, in the present work, care has been taken not to intermix the laser annealing with different crystallization techniques such as metal-induced crystallization. Thus, we are able here to assess the influence of the laser crystallization on the structural and electrical properties of the silicon nanocrystals. Also, a better defined doping process has been applied here in combination with the presented analytical methods to verify the actual doping concentrations.

6.2 Structural Properties

Before the laser treatment, the spin-coated porous silicon nanocrystal layers were etched to remove the native silicon surface oxide. This procedure was identified as a crucial technological step to achieve conductive films after laser annealing. Otherwise, badly reproducible material with high resistivity was obtained. The laser annealing procedure itself consisted of ten shots of increasing pulse energy as described in Section 2.1.7. Only the highest laser energy density value of each pulse series will be used in the following, whenever energy density values are referred to. The structural properties of the resulting layers after the laser treatment will be highlighted in the following.

6.2.1 Morphology

Increase of structure size

The sample morphology as a function of the laser annealing energy density is shown in Figure 6.1 a) – h). The initial microwave reactor silicon nanocrystals had an average size of 20 nm. The as-deposited sample situation in (a) corresponds to the spin-coated films depicted in Figure 4.4. After a laser treatment with a laser energy density of 40 mJ cm^{-2}, almost no changes can be distinguished within the resolution of the scanning electron micrograph (b). After annealing with a laser energy density of 60 mJ cm^{-2}, the typical structure sizes have increased significantly to about 100 nm, while agglomerates of unaffected nanocrystals are present at the same time (c). The trend of further increasing structure sizes with increasing laser energy density continues for values of 80 mJ cm^{-2} and 100 mJ cm^{-2} (d) – (e). At 80 mJ cm^{-2}, lateral silicon connections have formed throughout the film, which seem to form a percolating silicon network. Only few silicon nanocrystals are present after this laser annealing step. In (e), the energy density amounted to 100 mJ cm^{-2}, which leads to the formation of additional relatively large spherical structures on top of the sintered silicon network. The observed size of these drop-like features saturates around a typical value of 400 nm, and even further enhancement of the energy density does not induce further growth in size of these structures any more (f). Beyond energy densities of 120 mJ cm^{-2}, the overall morphology deteriorates and ablation from the substrate becomes probable. As a conclusion, an intermediate energy density of $100 - 120$ mJ cm^{-2} is expected to give the best material quality.

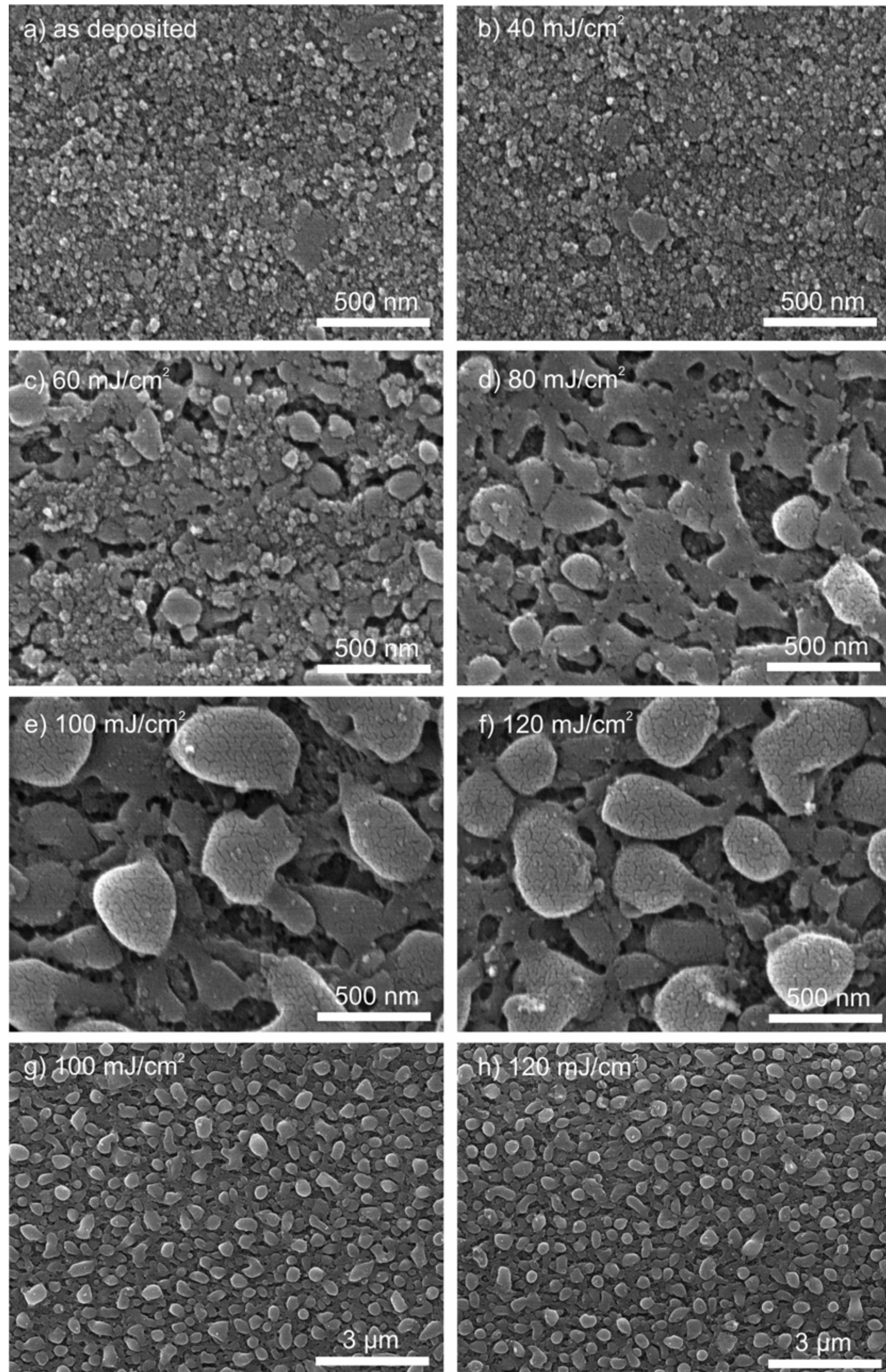

Figure 6.1: a) Scanning electron micrograph of an as-deposited silicon nanocrystal film. Pulsed laser annealing at the indicated energy densities leads to the morphologies shown in (b) – (h).

Silicon nanocrystal melting

The structural changes observed in the scanning electron micrographs can either be ascribed to sintering or melting of the primary nanocrystals. As defined in Section 3.2, here sintering refers to solid state processes that lead to substantial change in the morphology, whereas during melting the transition to the liquid phase is crossed.

The outer appearance of the silicon structures in Figure 6.1 e) – h) is drop-like with a rather spherical shape. This suggests the melting of neighboring silicon nanocrystals to form great silicon clusters. Indeed, the volume of a 400 nm diameter silicon sphere corresponds to a total of 8000 primary silicon nanocrystals in a simple geometrical consideration. Also solid state diffusion processes could in principle be responsible for such transformations as, *e.g.*, observed during the annealing of thin silicon-on-insulator films. There, after a period of $2-30$ min at elevated temperatures of $900-950\,^{\circ}$C, the silicon agglomerates to large drop-like structures with a diameter of $200-500$ nm over distances of $0.5-2\,\mu$m [Dor06]. Due to the fact that the heat exposure time is rather short during the pulsed laser annealing, it can be concluded that melting of the silicon nanocrystals is involved in the restructuring processes of the spin-coated silicon layers, at least for the high energy density values. The absence of facetted surfaces, *e.g.*, in Figure 6.1 g) and h) is another indication that a melting transition has occurred [Dor06].

An assessment of the energy absorbed in the silicon layer might help in this discussion. The absorbed fraction, w_{abs}, of the incoming laser energy density, w_{laser}, in a silicon nanocrystal film (thickness $d = 500$ nm) follows from the typical reflectivity, $R(\lambda) \approx 0.2$, and the absorption coefficient, $\alpha(\lambda) \approx 10^4\,\mathrm{cm}^{-1}$, at the laser wavelength $\lambda = 532$ nm:

$$w_{\mathrm{abs}} = (1-R)(1-\mathrm{e}^{-\alpha d})w_{\mathrm{laser}} \approx 0.3 \cdot w_{\mathrm{laser}} \tag{6.1}$$

If heat conduction to the substrate and to the surrounding gas atmosphere and radiational losses are neglected, the absorbed laser energy density can be expressed as an integral of the specific heat of silicon, c_{p}, over the temperature:

$$w_{\mathrm{abs}}(T) = \rho_{\mathrm{Si}} \cdot (1-p)d \cdot \int_{300\,\mathrm{K}}^{T} c_{\mathrm{p}}(T)\mathrm{d}T \equiv \rho_{\mathrm{Si}} \cdot (1-p)d \cdot \mathrm{Int}(T), \tag{6.2}$$

where ρ_{Si} is the specific mass density of silicon, and p is the porosity of the silicon layer. The integral can be solved numerically using literature data for c_{p} [Iof08] (in the considered size range, no significant change of c_{p} is present for silicon nanocrystals [HuW04]), so that the laser energy density required for the complete melting of a porous silicon layer can be calculated:

$$w_{\mathrm{laser}} = \frac{\rho_{\mathrm{Si}} \cdot (1-p)d}{0.3}\left[\mathrm{Int}(T_{\mathrm{m}}) + c_{\mathrm{lat}}^{\mathrm{Si}}\right]. \tag{6.3}$$

Here, the integration was performed up to the melting point, $T_{\mathrm{m}} = 1414\,^{\circ}$C, and the latent heat of bulk crystalline silicon ($c_{\mathrm{lat}}^{\mathrm{Si}} = 1805\,\mathrm{J\,g^{-1}}$, [Mad84]), was also taken into account. Interestingly, this term even exceeds the specific heat contribution: $\mathrm{Int}(T_{\mathrm{m}}) = 1254\,\mathrm{J\,g^{-1}}$. The resulting value for the laser energy density then amounts to

$$w_{\mathrm{laser}} = \frac{2.33\,\mathrm{g\,cm^{-3}} \cdot 5 \times 10^{-5}\,\mathrm{cm} \cdot 0.4}{0.3} \cdot 3059\,\mathrm{J\,g^{-1}} = 475\,\mathrm{mJ\,cm^{-2}}. \tag{6.4}$$

This value is much larger than the threshold energy density usually observed in the experiments. Here, values around $50\,\mathrm{mJ\,cm^{-2}}$ are sufficient to achieve a significant change in the structural properties of the layer, while we saw that an energy density of $120\,\mathrm{mJ\,cm^{-2}}$ leads to the formation of 400 nm large spherical structures.

The discrepancy between the values seems to indicate the presence of sintering effects or non-complete melting of the silicon layer. However, here the specific heat, the melting point, and the latent heat of bulk crystalline silicon were used, which are expected to differ from the values of silicon nanocrystals. While the specific heat is primarily given by the vibrational properties and is not strongly influenced by the particle size [HuW04], the melting point and the latent heat can be significantly depressed due to the metastability of the nanocrystalline phase. In Section 3.2.2, the melting point depression was discussed comparing theory with experimental data from the literature. While Goldstein reported a strong size dependence of the melting temperature [Gol96], in a recent study on silicon nanocrystals from MWR1, Schierning and coworkers observed the melting transition to occur already around 730 °C both for $5-20$ nm nanocrystals [Sch08]. As another useful physical quantity, Bet and Kar determined the latent heat of crystallization, to $177\,\mathrm{J\,g^{-1}}$ and $835\,\mathrm{J\,g^{-1}}$ for silicon nanocrystals with mean sizes of 5 nm and 30 nm, respectively [Bet04].

If we combine the reduced melting point and the latent heat results from Schierning, and Bet *et al.* with Equation 6.3, the energy required to heat layers of 30 nm diameter nanocrystals to their melting point is only about $90\,\mathrm{mJ\,cm^{-2}}$. The energy densities necessary for full melting are $120\,\mathrm{mJ\,cm^{-2}}$ and $220\,\mathrm{mJ\,cm^{-2}}$, respectively, in the case of 5 nm and 30 nm silicon nanocrystals.

These results are in better agreement with the typical energy densities of $50-120\,\mathrm{mJ\,cm^{-2}}$ from our experiments performed with silicon nanocrystals in the size range of $5-50$ nm. Among additional potential sources of error are the incomplete melting of the nanocrystal layer and the residual heat from previous laser pulses during the laser treatment. The repetition rate of the series pulses was $1\,\mathrm{s^{-1}}$, leaving ample time for the thermalization of the samples to temperatures below 500 °C. However, if a mean temperature of 300 °C is maintained between the pulses, the melting transition can occur for the larger particles at a pulse energy density of only $55\,\mathrm{mJ\,cm^{-2}}$, and full melting can be achieved at $180\,\mathrm{mJ\,cm^{-2}}$. Apparently, the low energy density threshold observed in the laser annealing experiments is a consequence of the reduced crystallite size in combination with a high degree of thermal isolation.

Porosity of laser-crystallized layers

From Figures 6.1 e) – h) it is evident that the silicon layers still exhibit a significant porosity after the laser annealing at energy densities around $100\,\mathrm{mJ\,cm^{-2}}$. Only the pore size and distribution has strongly changed. From an initial nanocrystal network with a porosity of about 60%, the structure has been transformed into an ensemble of dense solidified silicon droplets. Since we can assume these droplets to consist of bulk silicon, a macroscopic porosity is present due to the pores and voids between the spherical silicon structures. This macroscopic porosity after the laser annealing will be estimated in the following.

The first important information is the height of the resulting films after the laser treatment. However, the large surface roughness on the order of optical wavelengths prevents the occurrence of thin film interferences in optical measurements and their evaluation. Thus, only profilometer measurements could be applied. Here, no significant change in the average film thickness of the

silicon films before and after the laser annealing could be found within relatively large error bars of ± 100 nm.

To estimate the porosity, the laser-annealed silicon layer can be compared with an ensemble of spheres, adjacently positioned on a two-dimensional lattice. The resulting porosity then amounts to 48% for a square lattice model, whereas 40% results if a triangular lattice arrangement is supposed. These considerations show that the porosity of laser-annealed silicon layers can amount to similar high values as the primary particle layers. However, a more realistic estimation would need to take into account the real structure size and pore size distributions present in the laser-annealed layers. Additionally, a bottom layer of primary nanocrystals which is unaffected by the annealing step might be necessary to be included in such a model.

Dewetting behavior

The reason for the drop-like feature formation on top of the laser-crystallized silicon nanocrystal layers can be found in the high surface energy of the molten silicon during the annealing. Already at temperatures around 900 °C where only silicon diffusion processes are enabled, this high surface energy contribution can induce dewetting of silicon-on-insulator structures [Dan06, Dor06].

Thus, the molten silicon nanocrystals agglomerate during the laser annealing to effectively reduce their free surface. If the process parameters like the laser energy density and the film thickness are chosen appropriately, this enables the formation of a contiguous network of fused silicon. Probably, the presence of small silicon nanocrystals in between and below the large drop-like silicon features in the annealed films prevents the latter from merging completely to form detached islands on the substrate. If instead a layer thickness is chosen that is much smaller than the final lateral size of the evolving clusters, exactly this situation can occur.

As an example, Figure 6.2 a) shows a transmission micrograph of a 200 nm thick layer of spin-coated silicon nanocrystals after laser annealing at 100 mJ cm^{-2}. Dark areas in the micrograph correspond to molten silicon structures, whereas the bright areas represent void regions. As the micrograph illustrates, in this case the areal density of the spherical silicon structures is too low, and they are separated from each other by the extended void areas. The resulting film is not contiguous and thus cannot be used for applications where lateral transport through the silicon is required. Apparently the interface energy to the substrate is too high, which prevents the formation of a thin molten film on the substrate and induces dewetting instead.

A similar droplike dewetting behavior has been observed for the flash-lamp annealing of silicon nanocrystals on fused silica substrates [Pet05]. Here, 1 μm thick layers of spin-coated silicon nanocrystals were transformed into disperse $2 - 4$ μm large spherical droplets on the substrate. These silicon islands were completely disjoint and isolated from each other, with a small areal density of about 0.012 μm^{-2}, and no lateral electrical conductivity could be obtained with the resulting samples. In this method, the substrate is preheated and the films remain at high temperatures for relatively long durations after each flash lamp pulse. The corresponding long persistence time of the silicon in the liquid phase allows the disintegration of the liquid films to large droplets. In contrast, the laser annealing procedure applied here might represent an optimum compromise by applying a high thermal energy density for only short heat exposure times. In combination with a sufficient layer thickness, contiguous recrystallized silicon films can be achieved.

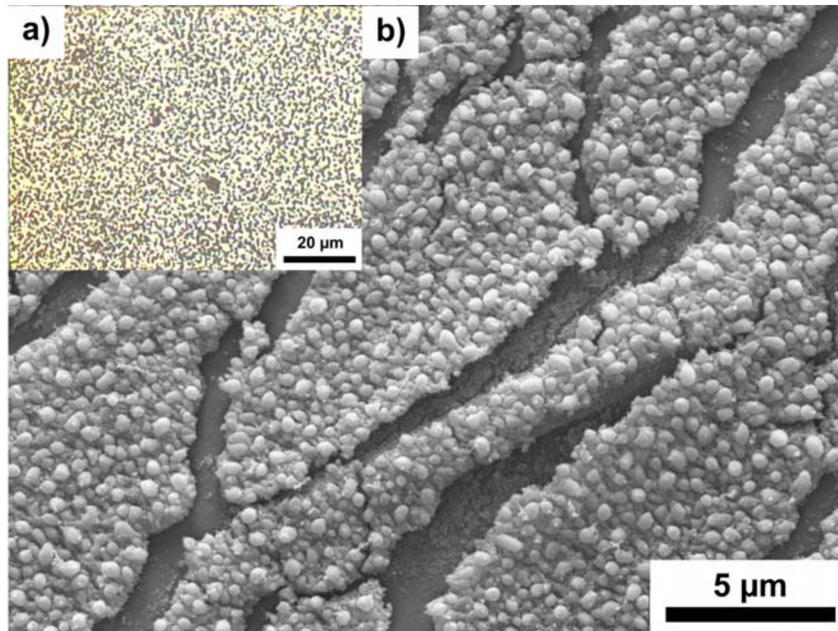

Figure 6.2: a) Optical transmission micrograph of a 200 nm thick silicon nanocrystal layer after laser anealing at 100 mJ cm^{-2}. b) Scanning electron micrograph of a 700 nm thick silicon nanocrystal film, laser-annealed at 120 mJ cm^{-2}, under severe bending.

Substrate interface

In the experiments performed on Kapton polyimide polymer foils it is found that the silicon layers adhere well to this substrate surface after the laser crystallization. This fact is illustrated in Figure 6.2 b), showing a scanning electron micrograph of the silicon layer microstructure during severe bending ($<$ 0.5 mm bending radius). The silicon film had a thickness of 700 nm and was laser-annealed at an energy density of 120 mJ cm^{-2}. Upon bending and substantial straining of the substrate, cracks form in the silicon layer, but the strong connection with the substrate remains. The crystallized silicon film does not flake off the substrate, which indicates that a partial fusion with the polymer substrate has occurred.

Indeed, the polyimide substrate material exhibits a glass transition temperature of about 380 °C above which softening of the material sets in [Dup08]. This softening enables the fusing of the bottom part of the silicon layer with the substrate mediating the strong interconnection. This effect can be of advantage during the fabrication of devices from laser-crystallized spin-coated silicon nanocrystal layers. No strong connection with the substrate can form if the thickness of the silicon nanocrystal layer is chosen too large. The limited penetration depth of the laser and the small thermal conductivity of the nanocrystal films cannot induce sufficient substrate surface heating in this case. Consequently, only weak mechanical bonding to the polymer substrate has been observed for laser-annealed 2 μm thick silicon nanocrystal films.

A cross-sectional scanning electron micrograph of a 500 nm thick layer of silicon nanocrystals on a crystalline silicon substrate after laser annealing at an energy density of 100 mJ cm^{-2} is depicted in Figure 6.3. Apart from the large recrystallized silicon structures known already from Figure 6.1, here also the presence of a fraction of non-molten silicon nanocrystals becomes evident. These nanocrystals appear rather unaffected by the laser treatment and still have sizes

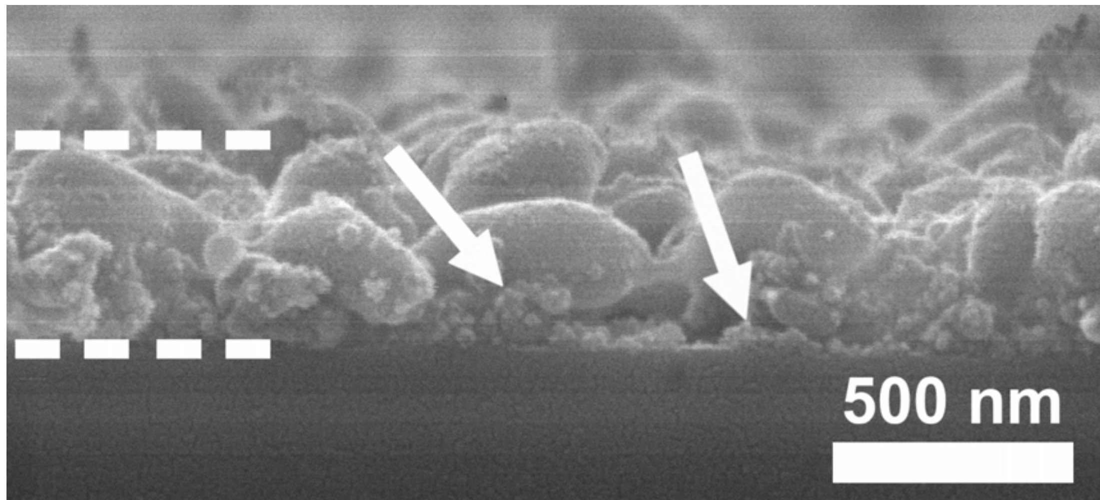

Figure 6.3: Cross-sectional scanning electron micrograph of a silicon nanocrystal film after laser annealing at 100 mJ cm^{-2} on a crystalline silicon substrate. The dashed lines mark the layer boundaries. Nanocrystals that were unaffected by the laser annealing and still are about 20 nm in diameter are highlighted by the arrows. They can be found in between and below the large molten surface structures.

on the order of the initial nanocrystal diameter (20 nm). They are found below and in between the large droplet-like silicon structures.

The existence of this fraction of non-molten nanocrystals might explain why the laser-annealed films do not disintegrate into droplets as discussed in the previous subsection. The reasons for the non-perfect melting may lie in the intensity profile of the laser light in the nanocrystal film and in the heat flow to the substrate. While the first ideally follows an $\exp(-\alpha d)$-decay, in reality, scattering effects may evoke inhomogeneous heating of deeper regions of the nanocrystal layer. The light intensity, and in first approximation also the temperature profile inside the layer, has typically decreased by one half at the substrate interface for a layer thickness of 500 nm in the homogeneous situation. Due to scattering effects, only the surface layer is homogeneously heated, while especially in between and below the large spherical structures lower heating is achieved. The latter leads to an effective increase of the thermal gradient in the vicinity of the substrate.

This effect is sufficient to prevent the full layer thickness from melting, while thermal sintering of these regions can still play a role. Similarly, it is a well-known phenomenon that an amorphous or fine-grained crystalline material is present in a bottom layer on the substrate in laser-crystallized amorphous silicon [Len00, Bro93].

6.2.2 Raman analysis of laser-crystallized films

The changes visible in the scanning electron micrographs should also be apparent from Raman spectroscopy, which is highly sensitive to the crystal size for diameters in the range of $3-20$ nm. To resolve structural changes on a scale which is hard to resolve with electron microscopy, we performed this Raman analysis with silicon nanocrystals having a size of 4.3 nm. A laser annealing series was performed with laser energy densities in the range of $0-100$ mJ cm^{-2} and the obtained spectra are displayed in Figure 6.4 a) together with that of a crystalline silicon

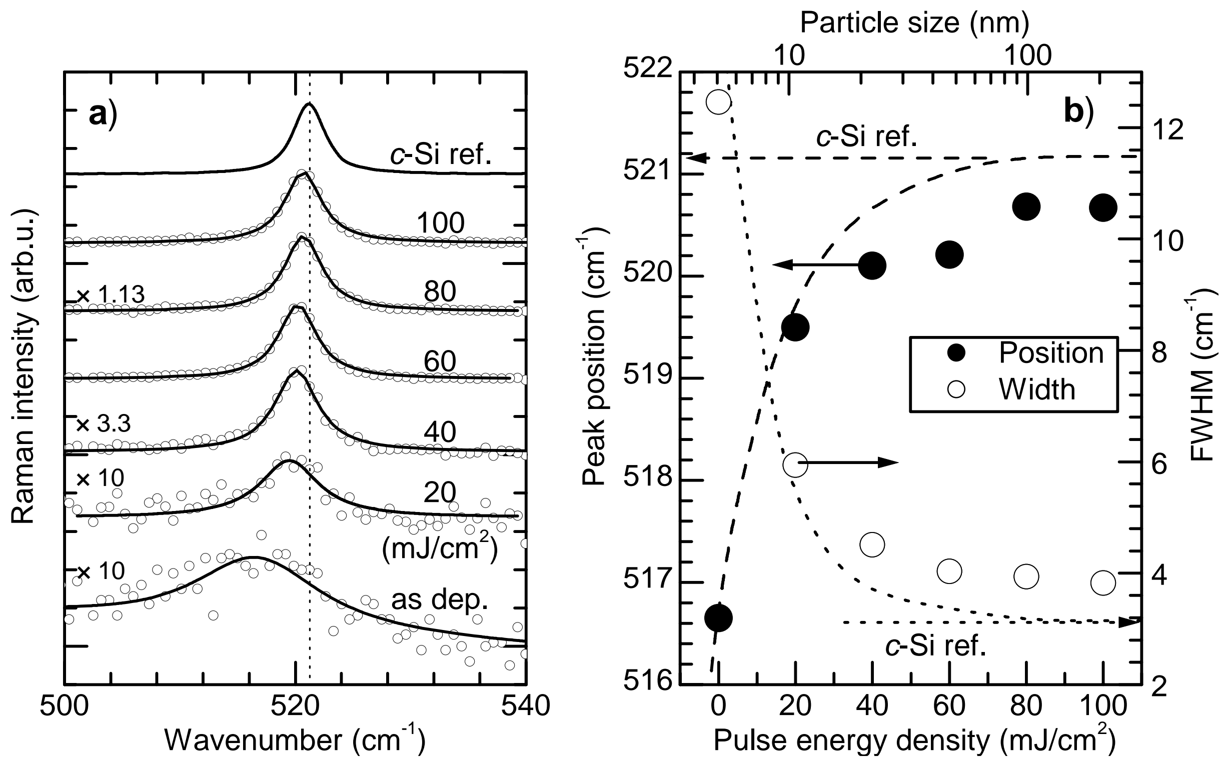

Figure 6.4: a) Raman spectra of laser-crystallized silicon nanocrystal layers for different laser energy densities. b) Peak position and width of the Raman spectra in (a) as a function of the laser pulse energy density (full and open symbols, respectively). The dashed and dotted lines give the position and width as a function of the particle size (top axis) according to the phonon confinement model for monodisperse particles.

reference sample. The spectra were shifted vertically and were scaled to comparable peak heights with the scaling factors given in the figure.

As the figure shows, the broad and slightly asymmetric Raman signal obtained for the as-deposited layer shifts to higher energies and decreases in width with increasing laser pulse energy density. Here, the strongest changes occur in the energy density range below $40\,\mathrm{mJ\,cm^{-2}}$, whereas for higher laser pulse energies, further shifts are hard to recognize by the eye. Thus, the peak positions and the full width at half maximum (FWHM) for each of the spectra in (a) have been evaluated from fitting single Lorentzian peaks and are displayed in (b) (full and open symbols, respectively).

Figure 6.4 b) demonstrates that the Raman peak position of the laser-annealed spin-coated silicon layers increases continuously with the pulse energy density, while the peak width constantly decreases at the same time. Both quantities approach the values of the crystalline silicon reference with increasing laser energy density ($521.2\,\mathrm{cm^{-1}}$ $vs.$ $3.1\,\mathrm{cm^{-1}}$, as marked by the dashed and dotted arrows, respectively).

As the observed behavior indicates an increase in the crystallite size, calculated values of the peak position and width are also included in (b) by the dashed and dotted lines, respectively. These theoretical values originate from the phonon confinement model for monodisperse silicon nanocrystals (*cf.* Subsection 3.3.2) and are plotted as a function of the crystallite size (top axis). Here, no direct functional connection between the top axis and the bottom axis exists. Instead,

the axes were aligned in such a way that the values of the initial size of the silicon nanocrystals and of the final size on the order of 200 nm after laser annealing coincide with the laser energy density values of 0 mJ cm^{-2} and 100 mJ cm^{-2}, respectively.

In the graph, the experimental values and the calculated curves are in relatively good agreement with each other, if a logarithmic size scale is chosen for the top axis. This is not an unrealistic constraint because an exponential increase of the structure size with the laser energy density can be imagined for all kinds of thermally activated growth mechanisms. Anyway, the good correlation between the peak position and the peak width indicates that indeed phonon confinement is the main reason for the peak shift and the broadening of the Raman spectra. Still, the correlation between the laser energy density and the particle size obtained from Figure 6.4 b) has to be regarded as qualitative.

In the case of high laser energy densities, systematic deviations from the calculated values are visible from the figure. Two possible interpretations can be thought of as the origin of this effect. Either, the laser-crystallized films still exhibit a small-grained crystalline structure, confining the phonons to volumes on the order of $20-50$ nm. This would mean that the large silicon structures visible in Figure 6.1 e) and f) consist of several such small crystallites and grain boundaries. However, this assumption seems unrealistic because the typical crystallite sizes obtained via the laser crystallization of silicon amount to $200-2000$ nm [ImK93, Len03], which is in good agreement with the feature sizes visible in our scanning electron micrographs. As an alternative and more convincing explanation, additional effects can come into play such as thermal stress. Due to the different thermal expansion coefficients of silicon and the polyimide substrate, redshifts of the Raman peak position by 2 cm^{-1} corresponding to biaxial strain as high as 570 MPa were observed during the laser crystallization of amorphous silicon on Kapton foil substrates [Len02]. A distribution of inhomogeneous strain over the probed sample area could also explain the slightly increased width by about 1 cm^{-1}.

In our case, the deviation in the peak shift is even smaller and amounts to only about 0.5 cm^{-1}. If we translate this peak shift into a biaxial or bisotropic strain, we end up with a value of only 135 MPa. This value is smaller than what Lengsfeld *et al.* observed for the crystallized amorphous silicon films, which can be a consequence of incomplete melting of the silicon nanocrystal layer during the laser annealing or be due to a partial strain relief in the layer or of the substrate during softening above the glass transition.

The phonon confinement model applied here used a monodisperse size distribution of nanocrystals. This is a good agreement with the initially very small silicon nanocrystals. These obey a $\sigma = 1.2$ log-normal size distribution, which is very similar to the case of monodisperse silicon particles (*cf.* Section 4.1.3). Upon laser annealing, the sintering and melting leads to an increase of the average structure size and to a broadening of the size dispersion function ($\sigma > 1.5$). However, if this effect would be accounted for in Figure 6.4 b), an even more rapid increase of the structure size for small pulse energy densities would be obtained. In the high pulse energy density region, the same physical implications remain present as discussed above. For reasons of simplicity and transparency, thus the monodisperse phonon confinement model was preferred.

6.2.3 Defect density

As a consequence of the large increase in the structure size during the laser annealing, a concomitant reduction of internal surfaces would be expected. If the typical interface dangling bond

concentration is assumed to stay constant, this should lead to a significant decrease in the total dangling bond defect concentration of the samples. Here, the typical increase in the structure size by one order of magnitude from about 20 nm to 200 nm is connected with a decrease of surface and internal interface areas by one order of magnitude. Consequently, the dangling bond volume concentration should decrease by a factor of 10 after laser annealing at energy densities around $100\,\mathrm{mJ\,cm^{-2}}$.

However, this is not observed. Instead, the concentration of paramagnetic defects amounts to about $2 \times 10^{19}\,\mathrm{cm^{-3}}$ and does not significantly change with the laser annealing for energy densities ranging from $0 - 200\,\mathrm{mJ\,cm^{-2}}$. A possible reason, why the expected decrease in the defect concentration is not observed may be the presence of non-molten silicon nanocrystals as found in Figure 6.3. Since a significant volume fraction of the initial particles is preserved, a spin signal background on the order of the initial value can exist. These paramagnetic defects then conceal the decrease in the defect density of the recrystallized fraction of the silicon nanocrystal layers.

As an additional explanation, the possibility exists that the large spherical structures contain a relatively small inner grain structure. To explain the rather constant defect level, the typical grain size after the annealing should be on the order of 50 nm. However, this assumption can be mainly ruled out by the experience of pulsed laser crystallization of amorphous silicon. Here, the grain size is limited by competing nucleation, and grain sizes on the order of $200\,\mathrm{nm} - 2\,\mu\mathrm{m}$ are readily obtained [Len00].

A weak decrease of the dangling bond density with the laser annealing energy density is present in the case of the samples doped with a boron concentration of $10^{19}\,\mathrm{cm^{-3}}$ atoms. This interesting fact will be addressed in more detail in Section 6.4.5, where the influence of the carrier concentration on the dangling bond density will be analyzed and a correlation with the electrical properties is established.

6.2.4 Dopant Segregation

In Subsection 4.2.3 it was shown that phosphorus specifically tends to segregate towards the silicon surface during growth at high temperatures. Also the laser induced melting and sintering might induce the partial outdiffusion of phosphorus dopants and a "pile-up" of phosphorus at the surface or at the internal silicon-oxide interface [Mar72].

As a test of the segregational behavior of phosphorus and boron dopants during laser annealing, SIMS measurements were performed before and after the laser treatment and after a subsequent etching step. If significant surface segregation of phosphorus occurs, this should lead to a reduction of the overall phosphorus concentration after the removal of the native oxide formed immediately after the laser recrystallization.

However, no significant difference in the phosphorus concentration of laser-annealed layers is observed, independent whether wet-chemical etching in dilute hydrofluoric acid was applied or not. Under this procedure, also boron-doped silicon nanocrystal layers maintain the same overall boron concentration as before the laser annealing. Consequently, both boron and phosphorus do not segregate during the laser annealing step. Part of this different behavior compared to the growth period may be ascribed to the rapid resolidification and cooling down of the layers after the short laser pulse irradiation.

6.3 Optical Properties

After the laser annealing, the spin-coated silicon nanocrystal layers exhibit a significant surface roughness, which prevents the determination of the refractive index by the evaluation of thin-film interference fringes as described in Section 4.3.2 [Swa84]. Also, the polyimide substrates applied for the laser annealing limit the spectral region accessible for transmission and PDS measurements. However, for strong absorption conditions in the presence of free carriers in the laser-annealed layers the direct determination of the absorption coefficient via PDS has turned out to be applicable as will be shown in the following subsection. A second subsection will focus on the optical interaction of free carriers in the films with phonons and local vibrational modes, which will be used to determine the carrier concentration.

6.3.1 Absorption coefficient

The absorption coefficients of as-deposited and laser-annealed films with and without doping are shown in Figure 6.5. The spectra of the as-deposited nanocrystal layers in the Figure were taken on fused silica substrates to resolve also small values of the absorption coefficient. In contrast, the laser annealing experiments had to be performed on polyimide substrates due to the incompatibility of fused silica with the necessary etching step. Unfortunately, for energies below 1.0 eV, the PDS absorption spectra of the latter samples are dominated by the absorption of the polyimide substrate. The absorption peaks at 0.65 eV, 0.75 eV, 0.87 eV, and 1.1 eV are characteristic for polyimide and are not influenced by the laser annealing. Apart from these features, the absorption coefficient of laser-annealed silicon nanocrystal layers is identical with that of the as-deposited samples.

As the spectrum of the laser-annealed silicon nanocrystals with large boron concentration shows, the free carrier plasma absorption in the infrared spectral region increases upon laser annealing. Thus, only faint signatures of the substrate absorption peaks are visible in this spectrum. While the simulation of the free carrier absorption with the Drude model gave a hole concentration of $10^{20}\,\mathrm{cm}^{-3}$ for the as-deposited sample, after laser annealing, a value of $8 \times 10^{20}\,\mathrm{cm}^{-3}$ is obtained (dotted line and dashed line, respectively). The latter value comes quite close to the nominal value of $10^{21}\,\mathrm{cm}^{-3}$ boron atoms in the sample. This finding adds further proof to the hypothesis of a partly interstitial boron incorporation during nanocrystal growth as argued in Subsection 4.3.4.

A comparable increase of the free carrier absorption after laser annealing is not present for the highly phosphorus-doped samples. In this case, the maximum doping concentration available amounted to $3 \times 10^{19}\,\mathrm{cm}^{-3}$. Consequently, the free carrier absorption is less pronounced and is partly disguised by the characteristic absorption bands of the Kapton substrates.

In the calculations of the absorption coefficient according to Equation 3.20, a damping constant of $\Gamma = 1.4 \times 10^{14}\,\mathrm{s}^{-1}$ was applied, which corresponds to a carrier mobility of $15\,\mathrm{cm}^2\,\mathrm{V}^{-1}\,\mathrm{s}^{-1}$ in the laser-annealed film. A similar value of $14\,\mathrm{cm}^2\,\mathrm{V}^{-1}\,\mathrm{s}^{-1}$ had been deduced for the as-deposited film (compare Subsection 4.3.4).

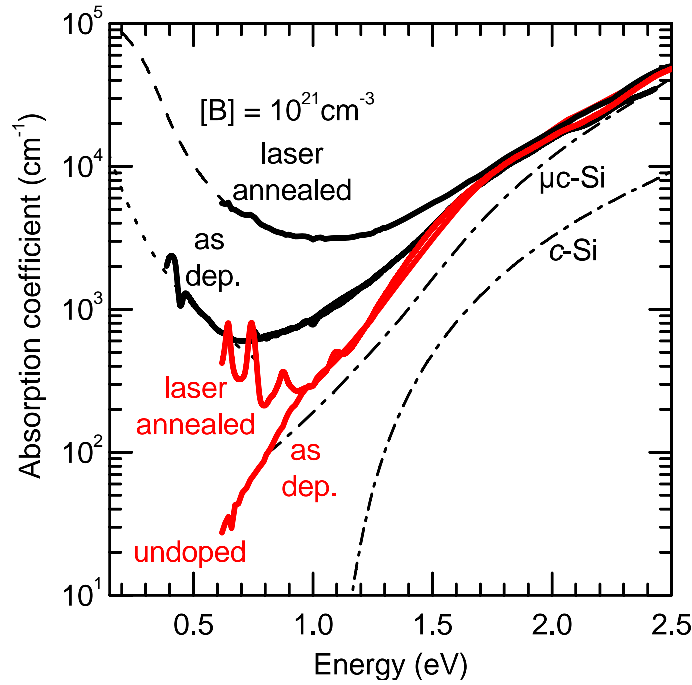

Figure 6.5: Absorption coefficient of doped and undoped silicon nanocrystal layers before and after laser annealing at 120 mJ cm^{-2}. The absorption coefficients of crystalline and microcrystalline silicon are also shown. The calculated absorption coefficients of a free carrier plasma are given by the dashed line and the dotted line for carrier concentrations of 8×10^{20} cm^{-3} and 10^{20} cm^{-3}, respectively.

6.3.2 Fano effect

Influence of free carriers on the phonon spectra

In addition to the absorption of low energy photons by plasmons, the free carrier concentration is visible in Raman scattering. At very high doping concentrations a continuum of states for the carriers is present around the Fermi level. This continuum of states can interact with discrete vibrational modes such as phonons or local vibrational modes. As a consequence of this interaction, the absorption or emission lines of these modes in optical spectroscopy can adopt an asymmetric or inverted shape, depending on the excitation wavelength and the carrier concentration.

These so-called Fano resonances have been observed for the case of infrared absorption bands in highly doped semiconductors [Sim95] and are also a common observation in Raman spectra of highly doped semiconductors [Cer73]. They represent a favorable non-contact method to characterize carrier concentrations in a variety of highly doped materials including crystalline silicon, laser-crystallized silicon layers, silicon nanowires and nanocrystals [Cer73, Nic00, Fuk06, Hay96].

Instead of a Lorentzian function, the zone center optical phonon Raman spectrum in the presence of a high carrier concentration adopts the form of a special Fano resonance lineshape [Cha78]:

$$I(\omega) \propto \frac{(q\gamma + \omega - \Omega_p - \Delta\Omega)^2}{\gamma^2 + (\omega - \Omega_p - \Delta\Omega)^2}, \tag{6.5}$$

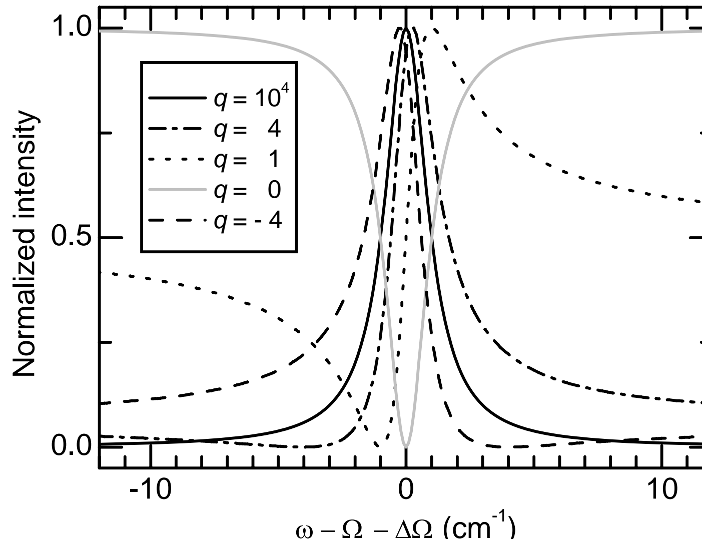

Figure 6.6: Influence of the asymmetry parameter, q, on the shape of a Fano interference according to Equation 6.5. The Fano linewidth has been kept constant at $\gamma = 1\,\text{cm}^{-1}$ for the calculations.

where I is the Raman scattering cross section as a function of the wavenumber, ω, q is the asymmetry parameter, γ is the Fano linewidth, Ω_p is the phonon wavenumber in the probed material, and $\Delta\Omega$ is the peak redshift. While $\Delta\Omega$ and γ merely influence the peak position and width, q has the strongest influence on the resulting shape of the spectrum. Here, large absolute values of $|q| > 10$ lead to a rather symmetric lineshape, whereas small positive and negative values provoke a large asymmetric tail towards the high and low energy side of the spectrum, respectively. For values around $|q| \approx 0$, the corresponding spectrum even exhibits a distinct minimum around the resonant energy. Figure 6.6 shows exemplary lineshapes calculated for different values of q. In the graph, the Fano linewidth has been kept constant at $\gamma = 1\,\text{cm}^{-1}$.

All of the parameters introduced above are found to depend strongly on the charge carrier concentration, and especially q also varies with the probing wavelength. For the same value of the carrier concentration, the observed Fano effect is much stronger for longer wavelength light, because at lower photon energies the ratio between the phononic and the electronic Raman scattering cross sections decreases significantly. This characteristic interplay between the carrier concentration and the laser wavelength can be exploited to measure the carrier concentration from Fano resonance spectra.

Several authors have reported typical values for the Fano resonance parameters, which are displayed in Figure 6.7 for different probing wavelengths as a function of the hole concentration [Cer73, Cer74, Cha80]. In (a) the asymmetry parameter, q, is given, while in (b) and (c) the Fano linewidth and the peak shift are shown, respectively. All data are room temperature values of boron-doped crystalline silicon samples.

As the figure illustrates, in boron-doped silicon the occurrence of the Fano effect becomes significant for hole concentrations above $5 \times 10^{19}\,\text{cm}^{-3}$. Only then, the absolute value of q decreases below ten for typical laser wavelengths in the range of $488.0 - 647.1\,\text{nm}$, and peakshifts larger than $1\,\text{cm}^{-1}$ and line broadening beyond $3\,\text{cm}^{-1}$ occur. While the peak shift and the peak width (as the real and the imaginary part of the self-energy in the interaction with the free holes) are practically independent of the excitation wavelength, it is evident from (a) that the asymmetry

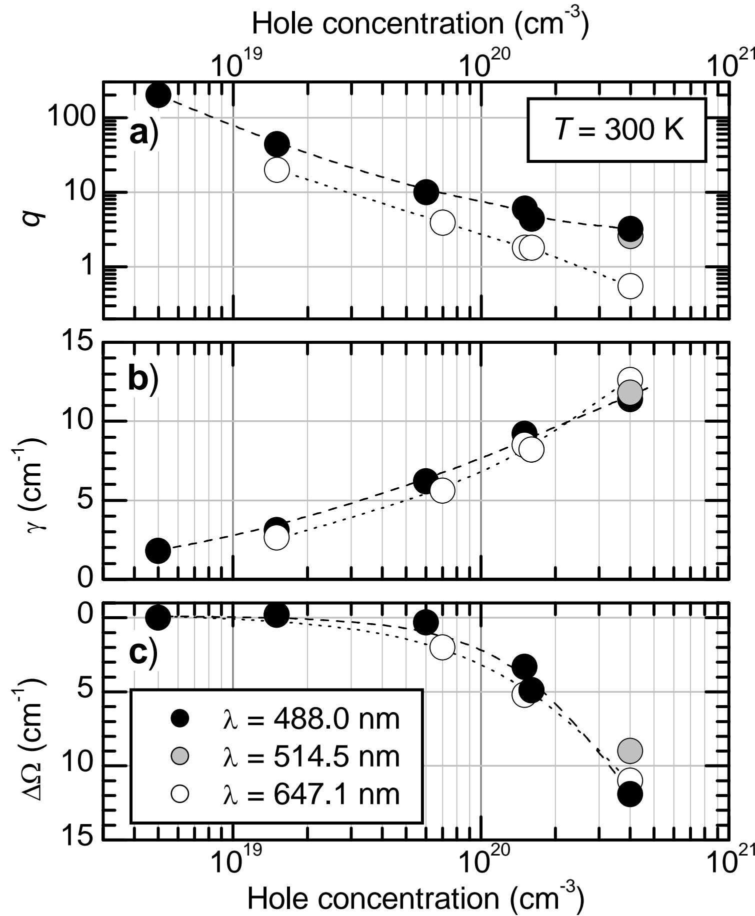

Figure 6.7: Typical values for the asymmetry parameter, q, the linewidth, γ, and the redshift, $\Delta\Omega$, for Raman spectra of boron-doped crystalline silicon as a function of the hole concentration for different probing wavelengths. Data are taken from [Cha80, Cer73, Cer74].

is much stronger in the case of a red probing laser at 647.1 nm than in the case of blue light at 488.0 nm. Intermediate values for q are found during probing excitation at 514.5 nm. This fact can be correlated with the ratio between the phonon and the hole Raman matrix elements [Cha78]. At low excitation energy, the Raman matrix element of the free holes dominates and $|q|$ is minimized. A quite similar behavior is also found for lowering the temperature, which decreases the absolute of q, while γ and $\Delta\Omega$ are rather unaffected [Cer73].

Local boron vibrational modes

In the case of boron-doped silicon, the significant mass difference between boron and silicon atoms can help to distinguish local boron-silicon vibrations from the silicon optical phonons. These local modes of substitutionally incorporated ^{10}B and ^{11}B isotopes have been observed in highly doped crystalline silicon at 644 cm^{-1} and 620 cm^{-1}, respectively. In good agreement with their relative natural abundance (19.9% *vs.* 80.1%), the intensity ratio of the modes amounts to 1 : 4 [Cer74, Stu87a]. They can only be distinguished easily from second order acoustical phonon signatures for boron concentrations exceeding 5×10^{18} cm^{-3} atoms. Thus, the concomitant large hole concentrations evoke a Fano shift and asymmetric broadening of these modes,

Hole concentration (cm^{-3})	Wavelength (nm)	$q^{^{11}B}$	$\gamma^{^{11}B}$ (cm^{-1})	$\Delta\Omega^{^{11}B}$ (cm^{-1})	Reference
4×10^{20}	457.9	1.82	8.0 ± 1.5	-5 ± 2	[Cer74]
	514.5	1.16	7.4 ± 1.5	-6 ± 2	
	647.1	0.15	10.0 ± 1.5	-7 ± 2	
1.5×10^{20}	488.0	2.7	7.3	-5.2	[Cha80]
	647.1	0.93	6.4	-5.8	
1.5×10^{19}	488.0	8.0	6.0	-2.9	[Cha80]
	647.1	5.8	5.9	-2.7	

Table 6.1: Fano parameters for the ^{11}B local vibrational modes in highly boron-doped crystalline silicon samples.

too. To describe the resulting peak structure, again Equation 6.5 can be used replacing q, γ, and $\Delta\Omega$ by the respective values for the local modes, $q^{^{11}B}$, $\gamma^{^{11}B}$, and $\Delta\Omega^{^{11}B}$.

For the local boron modes, the Fano interaction is even stronger than that observed with the phonon resonance due to different values of the respective Raman cross sections, however the relative changes upon changing the probing wavelength are identical. Cerdeira and Chandrasekhar with their coworkers reported typical boron mode Fano parameters for different boron concentrations and laser wavelengths at room temperature, which are listed in Table 6.1 [Cer74, Cha80].

The parameters for the less abundant ^{10}B isotope approximately resemble that of the heavy species, only the peak intensity is decreased by a relative factor of 0.25 and the peak position is kept at a constant relative distance of 24 cm^{-1}. Due to the small energy spacing between both modes with respect to, *e.g.*, the difference to the silicon phonon energy, these approximations only cause negligible errors [Cer74].

Fano effect and local boron modes in laser-annealed silicon nanocrystals

Figure 6.8 shows Raman spectra of highly doped silicon nanocrystal layers that have been laser-annealed at an energy density of 120 mJ cm^{-2}. In comparison with the spectra of undoped samples in Figure 6.4, the strong influence of the doping on the Raman spectra becomes evident. While (a) the spectrum of a sample with a boron concentration of 10^{21} cm^{-3} exhibits a rather asymmetric shape, that of a sample doped with 3×10^{19} cm^{-3} phosphorus atoms comes closer to the crystalline silicon reference at a position of 521.5 cm^{-1} and a width of 3.5 cm^{-1} (b). In the spectrum of the extremely boron-doped sample in Figure 6.8 a), additionally local vibrational modes are visible in the spectral region of 620−650 cm^{-1}. Akin to the zone center phonon signal, these peaks exhibit an asymmetric tail towards large wavenumbers in the Raman spectrum.

The strong asymmetric peak in the spectrum in Figure 6.8 a), was successfully fitted with a Fano lineshape (full line) according to Equation 6.5. The fit procedure returns parameter values of $q = 3.1$, $\gamma = 12.0\,cm^{-1}$, and the resulting peak shift amounts to $\Delta\Omega = 14.1\,cm^{-1}$. This set of parameters is fully compatible with a free hole concentration of about 4×10^{20} cm^{-3} according to the correlations given in Figure 6.7, which corresponds to 40% of the boron concentration present in the initial material as determined by mass spectroscopy analysis.

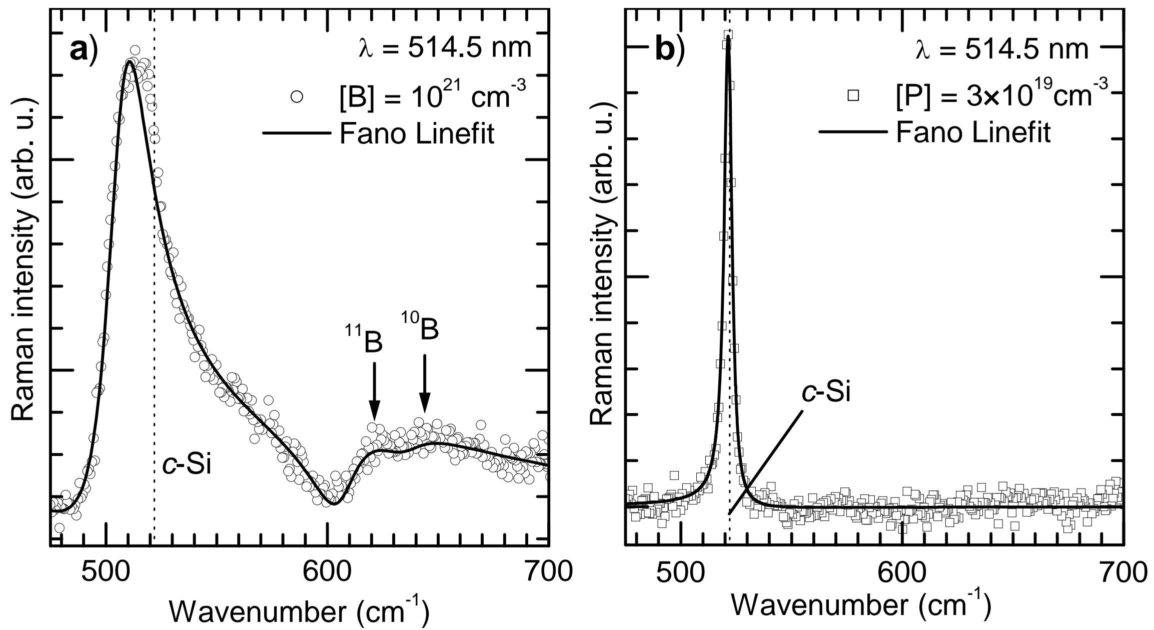

Figure 6.8: Fano interferences in the Raman spectra of laser crystallized silicon nanocrystal layers with high (a) boron and (b) phosphorus doping concentrations. Full lines are the results of Fano linefits with parameters given in the text, while the Raman peak position of the undoped crystalline silicon reference is marked by the dotted line.

Additional to the silicon optical phonons, also the resonant positions of the boron local vibrational modes were included in the fit. As expected from the situation in boron-doped crystalline silicon, the obtained peak parameters were different from those of the zone-center phonon line: $q^{^{11}\mathrm{B}} = 0.5$, $\gamma^{^{11}\mathrm{B}} = 10 \pm 1\,\mathrm{cm}^{-1}$, and $\Delta\Omega^{^{11}\mathrm{B}} = 11 \pm 1\,\mathrm{cm}^{-1}$. From a comparison with the values listed in Table 6.1, it turns out that the Fano fit parameters indicate a slightly higher hole concentration exceeding $5 \times 10^{20}\,\mathrm{cm}^{-3}$, which approaches the boron concentration in the sample as determined from mass spectroscopy.

This result corroborates the findings of the SIMS analyses.that no significant surface segregation of boron dopants occurs during the nanocrystal growth. The free hole concentration detected here after dispersing, spin-coating, removal of the native oxide, and laser annealing of the nanocrystal layers is of the same order as the boron concentration determined from mass spectroscopy with the primary particles.

The Raman spectrum of the phosphorus-doped sample in Figure 6.8 b) exhibits an almost symmetric peak shape. Two reasons are responsible for this observation. First, the respective sample has a much smaller phosphorus doping concentration of about $3 \times 10^{19}\,\mathrm{cm}^{-3}$, which represents the highest effective phosphorus concentration that was available. This reduced carrier concentration leads to a weaker appearance of the carrier-mediated Fano effect. Second, it has to be noticed that the strength of the Fano interferences in n-type silicon is small, so that pronounced Fano lineshapes can only be observed at doping concentrations exceeding $10^{20}\,\mathrm{cm}^{-3}$ [Cha78].

The spectrum depicted in Figure 6.8 b) was fitted with a single Fano line according to Equation 6.5. The extracted parameters were $q = -25$, $\gamma = 2.0\,\mathrm{cm}^{-1}$, and a peakshift of $\Delta\Omega = 0.1\,\mathrm{cm}^{-1}$. These values confirm that the phosphorus concentration is below the value of $10^{20}\,\mathrm{cm}^{-3}$ where the observed Raman peak asymmetry in n-type silicon becomes strong enough, is accompanied

with significant peak broadening and redshift, and can thus be unambiguously assigned to a Fano resonance [Cha78, Nic00]. In the case of the spectrum shown in Figure 6.8 b), the asymmetry can also partly be explained by the structural quality of the sample. Anyway, an upper limit for the free electron concentration in the laser-annealed layer of $4 \times 10^{19}\,\mathrm{cm}^{-3}$ can be extracted from this measurement by comparing with the results of Nickel and coworkers ($q = -20$, $\gamma = 2.7\,\mathrm{cm}^{-1}$, and $\Delta\Omega = 0.4\,\mathrm{cm}^{-1}$ for a phosphorus concentration of $4 \times 10^{19}\,\mathrm{cm}^{-3}$ at a probing wavelength of 633 nm [Nic00]), which is in good agreement with the phosphorus concentration as determined from mass spectroscopy measurements of this sample ($3 - 5 \times 10^{19}\,\mathrm{cm}^{-3}$).

In conclusion, the optical properties of the undoped laser-annealed silicon nanocrystal films are quite comparable to the as-deposited layers. However, the effects of the free carriers become more visible after the laser treatment. Free carrier concentrations on the order of the doping concentration are observed in infrared absorption measurements and in Raman spectroscopy.

While a large fraction of the phosphorus dopants has segregated to the surface already during the nanocrystal growth, the Raman signal suggests nearly full substitutional incorporation of the remaining phosphorus dopants in the laser-annealed silicon nanocrystal layers for high doping concentrations. It should be noticed that the laser annealing does not induce further segregation of phosphorus, as was verified by SIMS analysis before and after oxide removal of a highly phosphorus-doped laser-annealed film. In the case of boron, almost full dopant incorporation is achieved in the core of the nanocrystals, however this occurs to a large extent at interstitial lattice sites. After laser annealing, the boron is almost fully incorporated on electrically active substitutional lattice sites.

While in the measurements shown here the impact of the free electrons and holes on the optical properties of the thin films was exploited to quantify the carrier concentration, the subsequent section will focus in more detail on the resulting electrical transport properties of the material.

6.4 Electrical Properties of Laser-Annealed Silicon Particle Layers

To make use of the laser-annealed spin-coated silicon nanocrystal layers in semiconducting devices, the electrical conductivity is required to be controlled, *e.g.*, by exactly adjusting the carrier concentration in the material. In the following subsections, the electrical characteristics of the laser-annealed silicon nanocrystal layers will be analyzed and the underlying conduction mechanisms will be identified. If not explicitly mentioned otherwise, here the electrical conductivities of the laser-annealed films have been determined by in-plane measurements using a lateral contact geometry.

6.4.1 Electrical conductivity after laser annealing

The result of electrical conductivity measurements as a function of the applied laser energy density is displayed in Figure 6.9. For this experiment, an undoped silicon nanocrystal layer, a sample doped with $10^{19}\,\mathrm{cm}^{-3}$ boron atoms, and a doped sample with a phosphorus concentration of $3 \times 10^{19}\,\mathrm{cm}^{-3}$ were laser-annealed by laser pulse sequences as described in Section 2.1.7. The thickness of these samples amounted to $500 - 700\,\mathrm{nm}$, and the maximum pulse energy density was varied from $0 - 180\,\mathrm{mJ\,cm}^{-2}$.

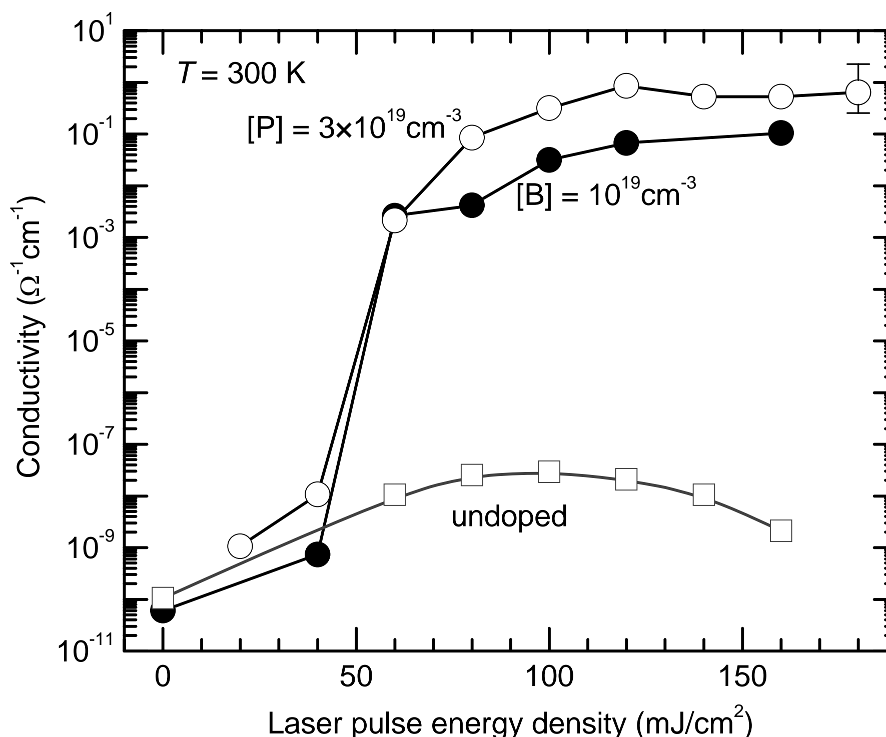

Figure 6.9: Room temperature dark conductivity of spin-coated silicon nanocrystal layers after laser annealing plotted versus the pulse energy density. The results of an undoped sample are compared with samples doped with 10^{19} cm^{-3} boron and 3×10^{19} cm^{-3} phosphorus atoms (open squares, full circles, and open circles, respectively).

As the laser energy is increased, for all samples an increase of the electrical conductivity is observed. For the undoped sample, the conductivity rises by two orders of magnitude from the as-deposited value of $10^{-10}\Omega^{-1}\,\mathrm{cm}^{-1}$ to $10^{-8}\Omega^{-1}\,\mathrm{cm}^{-1}$ after laser annealing at 60 mJ cm^{-2}, whereas it saturates at $3 \times 10^{-8}\Omega^{-1}\,\mathrm{cm}^{-1}$ for pulse energy densities in the range of $80 - 120$ mJ cm^{-2} and is found to decrease again for energy densities beyond 120 mJ cm^{-2}.

In the case of the highly boron- and phosphorus-doped samples, an even stronger increase of the conductivity is observed. While for laser energy densities below 50 mJ cm^{-2} the conductivity behaves similarly as for the undoped sample, above this value a sudden rise by more than five orders of magnitude is present. At even higher energy densities, the conductivity of these doped samples saturates at conductivity values exceeding that of the as-deposited situation by a factor of 10^9. Obviously, the electrical properties of the laser-annealed samples can be drastically improved by doping.

It should be noted that in the high energy density region above 140 mJ cm^{-2} the structural quality of the layers suffers. The high amount of deposited energy can induce the partial destruction of the samples and lead to a lift-off of the silicon film from the substrate. Thus, an effective process optimum is found in a laser pulse energy range of $100 - 120$ mJ cm^{-2}. If higher energy densities were applied, sometimes only fractions of the initial sample area could be evaluated to determine the conductivity values given in Figure 6.9.

The electrical conductivity values observed here are closely connected with the structural changes in the spin-coated silicon films during laser annealing. As was demonstrated by the electron

micrographs in Section 6.2.1, sintering and melting processes between neighboring particles enhance the connectivity and the percolation of the silicon nanocrystal network. Above a characteristic threshold energy density of $50\,\mathrm{mJ\,cm^{-2}}$, a significant increase of the structure sizes could be distinguished in the electron micrographs. The same threshold is found to be responsible for the abrupt rise in the conductivity and for the effective influence of the doping in the laser-annealed layers.

Thus, the sudden increase of the conductivity can be identified with a percolation threshold for the annealed nanocrystal layers. While for low energy densities only local agglomerates are sintered together, above $50\,\mathrm{mJ\,cm^{-2}}$ a macroscopic cluster of connected crystalline structures extends over the full layer, which results in a largely increased conductivity. Also, the areal density of interfaces is reduced by about a factor of $20 - 100$, and the interface regions are reconstructed completely.

Furthermore, a change in the conduction mechanism, *i.e.*, from tunneling and hopping to electronic band transport as a consequence of the sintering and melting can contribute to the large increase of the conductivity. However, as was shown in Section 4.4.3, the presence of such transport processes cannot unambiguously be identified in the spin-coated silicon layers.

6.4.2 Influence of the doping on the electrical conductivity

During measurements of the electrical conductivity of laser-annealed silicon films it turned out that many boron- and phosphorus-doped samples with low or intermediate doping concentrations exhibited conductivity values, which were identical to those of samples from undoped silicon nanocrystals. Within the experimental error bars and data scattering, for instance the same conductivity was found as a function of the laser energy density as for the undoped sample depicted in Figure 6.9 even for doping concentrations of $10^{18}\,\mathrm{cm^{-3}}$. To clarify the reasons for this observation, a systematic study of the conductivity as a function of the doping concentration was performed.

Critical onset of conduction

Figure 6.10 shows a plot of the resulting conductivities versus the doping concentration after laser annealing. The data shown here correspond to samples that have been laser-annealed with maximum pulse energy densities ranging from $100\,\mathrm{mJ\,cm^{-2}}$ to $120\,\mathrm{mJ\,cm^{-2}}$. These values correspond to the pulse energy density region where the laser treatment leads to the best conductivity results while maintaining the structural integrity of the samples at the same time. Here, the dark conductivity values at room temperature of samples doped with boron in concentrations ranging from $10^{15}\,\mathrm{cm^{-3}}$ to $10^{21}\,\mathrm{cm^{-3}}$ are depicted in (a), whereas those of samples containing $6 \times 10^{16} - 3 \times 10^{19}\,\mathrm{cm^{-3}}$ phosphorus atoms are plotted in (b).

As becomes evident by the figure, both p- and n-type doped silicon nanocrystal layers exhibit a similar electrical behavior after laser annealing. A guide to the eye is given by the dashed lines, which represent the same function of the doping concentration in both graphs, (a) and (b). This function consists of three adjacent sections defined as follows:

1. A constant conductivity value of $3 \times 10^{-8}\,\Omega^{-1}\,\mathrm{cm^{-1}}$ for doping concentrations below $10^{18}\,\mathrm{cm^{-3}}$,

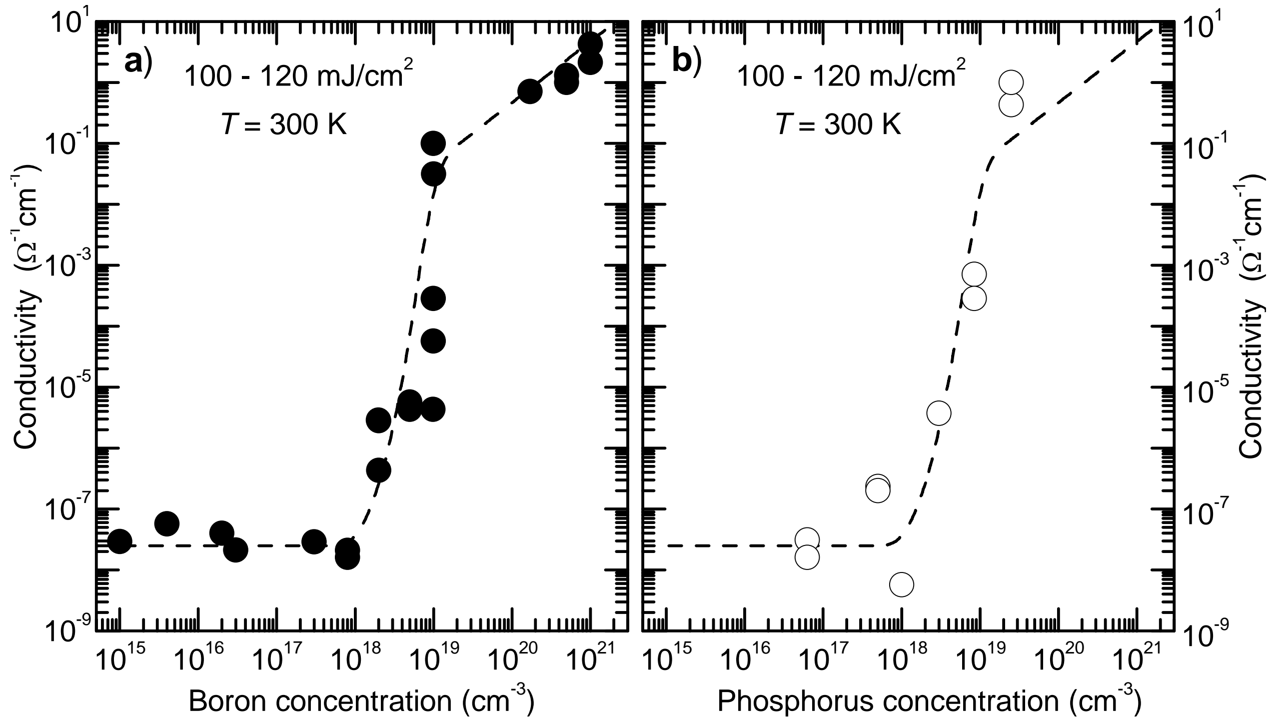

Figure 6.10: Dark electrical conductivity at room temperature of silicon nanocrystal layers laser-annealed at 100−120 mJ cm^{-2} versus the doping concentration for (a) boron and (b) phosphorus doping. The dashed line in both graphs is a guide to the eye.

2. an abrupt rise of the conductivity by seven orders of magnitude for doping densities around 5×10^{18} cm^{-3}, and
3. a region for doping concentrations exceeding 1×10^{19} cm^{-3} where the conductivity grows linearly with the doping concentration.

The experimental values for both phosphorus- and boron-doped silicon nanocrystal layers follow the function constructed as indicated above within the experimental scattering of about a factor of three to higher or lower conductivity values. Slight deviations for single samples occur, however, such as in the case of the sample doped with 3×10^{19} cm^{-3} phosphorus atoms, which exhibits a higher electrical conductivity than is typical for boron-doped samples in this doping concentration.

The implications that lead to the definition of the guide to the eye function can be understood as follows: For low and intermediate doping concentrations, the doping does not influence the electrical conductivity at all. Instead, independent of the actual doping concentration, the electrical conductivity is the same as usually observed in undoped layers after laser annealing, *i.e.* around $3 \times 10^{-8}\ \Omega^{-1}$ cm^{-1}. Since we know that, *e.g.*, the phosphorus dopants are substitutionally incorporated in the silicon nanocrystals, as is evident from quantitative EPR measurements at low temperatures, we have to think of a mechanism responsible for the loss of up to 10^{18} cm^{-3} electrons and holes.

Carrier compensation One possible scenario would be the compensation of the carriers either by other impurity species or by deep trap states caused by structural defects. We observe

the ineffectiveness of the doping both for boron acceptors as well as for phosphorus donors, and hence an amphoteric deep trap state, which can compensate both holes and electrons is probably the reason. While many transition metal impurities are responsible for such amphoteric states close to midgap in silicon, a concentration of such contaminants as high as $10^{19}\,\mathrm{cm}^{-3}$ would be required to explain the observed behavior. Yet, in our chemical analyses, no contaminants were found in nearly comparable quantities, which eliminates this possibility.

However, recalling the EPR measurements with silicon nanocrystal layers, a concentration of dangling bonds on the order of $10^{19}\,\mathrm{cm}^{-3}$ has been found in the as-deposited layers. These structural defects are present in a concentration that would be able to explain the compensation of the free carriers in the laser-annealed films. Indeed, in Subsection 6.2.3 a comparably high concentration of dangling bonds has been found present after laser annealing to be able to compensate $10^{19}\,\mathrm{cm}^{-3}$ carriers in the doped layers.

Moreover, the situation after laser annealing shows some parallels to the as-deposited situation presented in Section 4.4. The anti-correlation between the conductivity and the dangling bond signal from EPR clearly indicated the presence of defect compensation in the as-deposited silicon layers. A similar quantitative study of the dangling bond density for different doping concentrations in laser-annealed films will be given in Subsection 6.4.5.

Percolation of doped regions As an alternative interpretation, the abrupt rise of the electrical conductivity by seven orders of magnitude upon varying the doping concentration by only a factor of 10 around the critical doping density is also reminiscent of a phase transition. A similar situation is observed for the electrical conductivity of a porous material in the vicinity of the percolation threshold. Balberg and coworkers have determined a sudden increase by four orders of magnitude during the transgression of the percolation threshold in a system of oxide-embedded undoped silicon nanocrystals [Bal07]. When a network of semiconductor nanocrystals is lightly doped, the dopant atoms are distributed in a discrete manner over the individual particles, leading to highly doped and intrinsic particles at the same time. Thus, a percolation threshold can be imagined marking the position when electrical transport through doped nanocrystal channels is enabled.

In Section 3.6.2, a combined percolation model for a network of discrete doped and undoped silicon nanocrystals has been introduced, which correlates the doping concentration threshold with the nanocrystal size. After laser annealing, in contrast, the grain sizes of the silicon nanocrystal films by far exceed the dimensions at which such discrete doping effects can play a role. Only in combination with the above proposed compensation mechanism, the relevant crystal sizes can shift to effectively larger values. Still, no qualitative information can be extracted from the percolation model in this case, and the physical behavior will be dominated by the defect compensation.

Metal-insulator transition A third physical effect which leads to such abrupt changes in the conductivity is the Mott metal-insulator transition. If the doping density is so large that the effective Bohr radii of neighboring dopants overlap in real space, this leads to the formation of a half-filled impurity band of electronic states that are delocalized throughout the crystal. Above this critical concentration, a metal-like conductivity is found, which is independent of the temperature, whereas slightly below this value the conductivity exhibits strong thermal activation. Morin and Majta measured a difference of five orders of magnitude in the electrical conductiv-

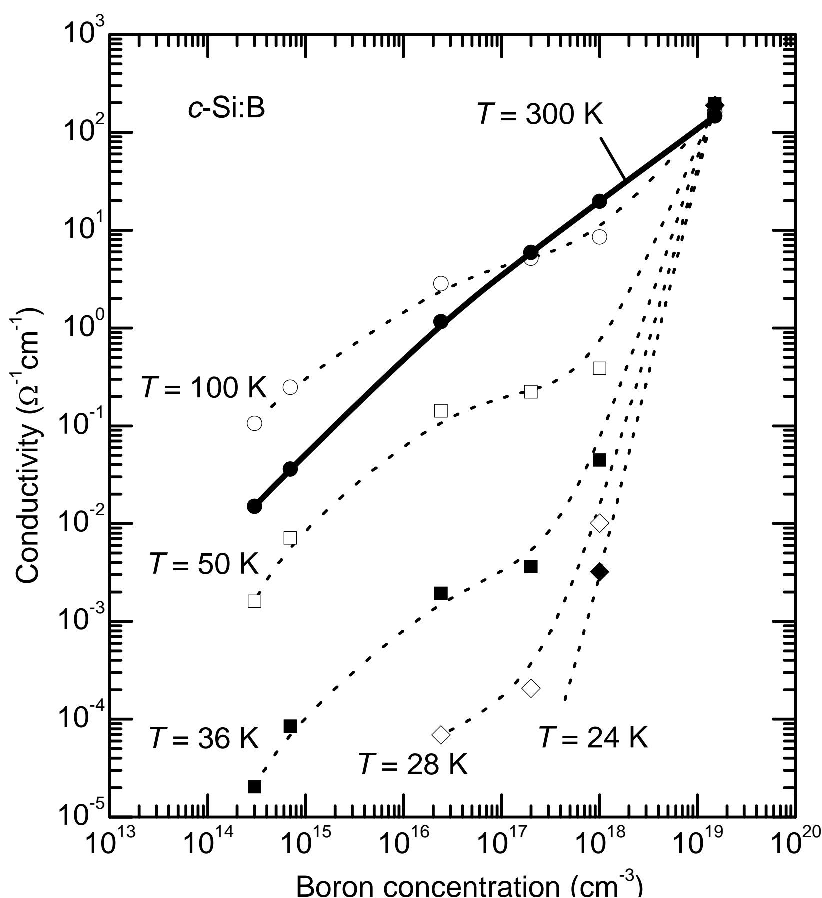

Figure 6.11: Conductivity of boron-doped crystalline silicon versus the boron concentration for different temperatures (data from [Mor54]). The metal-insulator transition occurring at a doping concentration of $10^{19}\,\mathrm{cm}^{-3}$ becomes evident at low temperatures.

ity at 24 K between two crystalline silicon samples with $10^{18}\,\mathrm{cm}^{-3}$ and $1.5 \times 10^{19}\,\mathrm{cm}^{-3}$ boron atoms [Mor54]. In this respect, the metal-insulator transition can be considered as a special case of a percolation threshold with a rather sharp onset of metallic behavior at the critical doping concentration.

However, this comparison does not hold at room temperature. Due to thermal activation of nearly all of the shallow boron acceptors, the difference in the electrical conductivity at room temperature is on the order of the difference in dopant concentrations and the electrical conductivity shows a continuous increase with the doping concentration, as Figure 6.11 illustrates. Thus, the large and sudden changes we observe with the laser-annealed silicon nanocrystal layers cannot be ascribed to a pure metal-insulator transition, either.

Still, the possibility exists that a percolation path through degenerately doped nanocrystals can form at the critical value of the doping concentration. This can, *e.g.*, be a consequence of the vastly reduced depletion lengths in extremely doped silicon. We will keep in mind such effects of degenerate doping during the discussion of grain boundary limited transport.

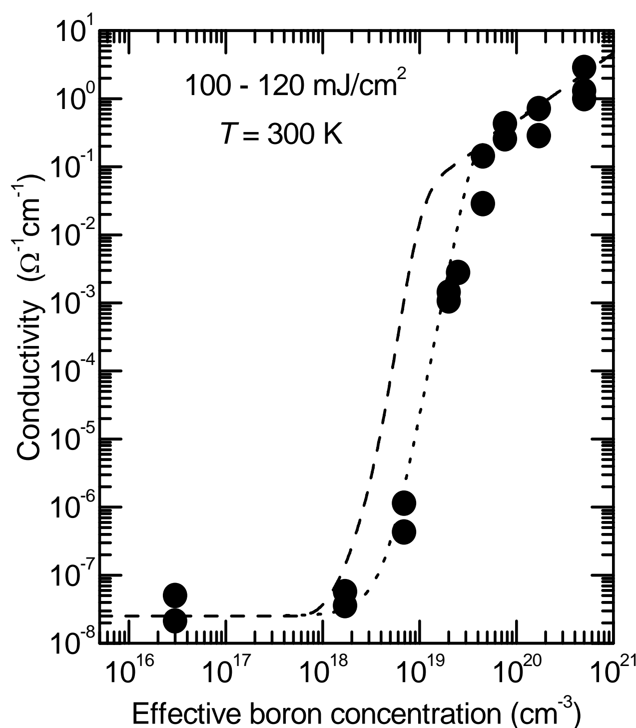

Figure 6.12: Room temperature conductivity of silicon nanocrystal layers after laser annealing at 100 − 120 mJ cm^{-2}. The effective boron concentration has been adjusted by intermixing of silicon nanocrystals with doping concentrations of 3×10^{16} cm^{-3} and 5×10^{20} cm^{-3}, respectively. The dashed line is the guide to the eye from Figure 6.10.

6.4.3 Conductivity of digitally doped layers

As explained in Subsection 2.1.4, the silicon nanocrystal ensembles with large boron concentrations ($> 10^{19}$ cm^{-3}) consisted of mixtures of heavily doped and lightly doped or undoped particles. In one such experiment, a dispersion of silicon nanocrystals doped with 5×10^{20} cm^{-3} boron atoms was mixed with a dispersion of particles with a doping concentration of 3×10^{16} cm^{-3} in varying ratios. Six composites with intermediate effective doping concentrations were obtained this way. The solid content in all of these dispersions amounted to 6 wt.%.

The mixed dispersions were magnet-stirred for 10 min and then spin-coated onto polyimide substrates. The native oxide was removed by etching, and the layers were laser-annealed at energy densities of 100 − 120 mJ cm^{-2}. The room temperature dark conductivity was measured and the results are displayed in Figure 6.12 versus the effective boron concentration, N_{eff}, as defined by Equation 2.1.

In this figure, the conductivity data form a smooth function of the effective doping concentration, which is illustrated by the dotted line as a guide to the eye. Once again, a steep increase of the conductivity is present at a critical doping concentration, very similar to the situation with the silicon nanocrystals that have been deliberately doped during growth in the microwave reactor. For better comparison of the two doping techniques, the guide to the eye from Figure 6.10 is also shown by the dashed line in the figure. A slight change can be seen around the critical onset of conduction. In the layers that stem from the mixed dispersions, the critical doping concentration appears to be shifted by a factor of 2.5 towards higher doping concentrations. This

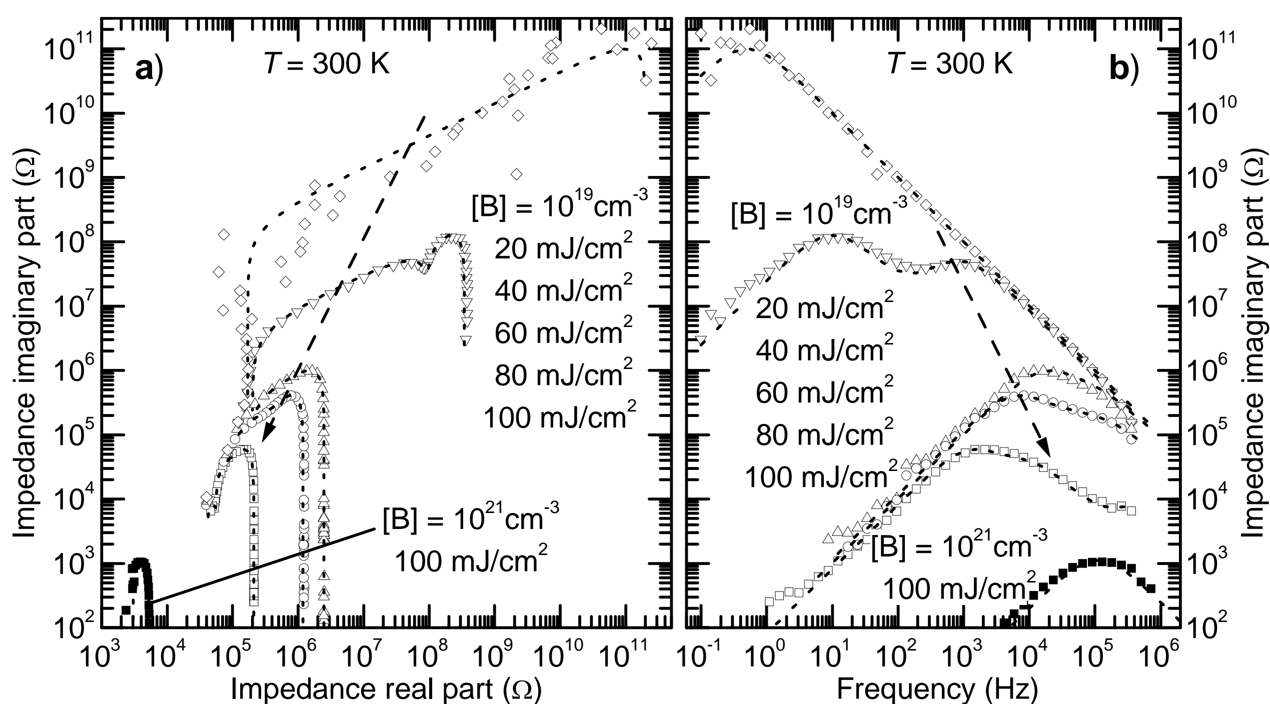

Figure 6.13: Imaginary part of the electrical impedance of laser-annealed boron-doped silicon nanocrystal layers (a) versus the real part of the impedance and (b) as a function of the angular frequency. Open symbols denote samples with a boron concentration of $10^{19}\,\mathrm{cm}^{-3}$ atoms laser-annealed at energy densities of $20 - 100\,\mathrm{mJ\,cm}^{-2}$. Full symbols stand for a sample doped with $10^{21}\,\mathrm{cm}^{-3}$ boron atoms after annealing at $100\,\mathrm{mJ\,cm}^{-2}$. The dotted lines are simulations of the impedance data.

may indicate a slightly higher concentration of dangling bond defects in the layers, due to the additional intermixing process, or can be a consequence of an inhomogeneous distribution of dopants in the highly boron-doped sample (see Subsection 2.1.4). However, also this critical value of about $10^{19}\,\mathrm{cm}^{-3}$ is still within the typical range of dangling bond concentrations and still slightly smaller than the spin densities usually detected in the spin-coated silicon layers.

An important conclusion can be drawn from the data in Figure 6.12. From only two available dispersions with different doping concentration, a variety of semiconducting films can be realized with a conductivity that extends over a range of more than eight orders of magnitude. The electrical properties of any two differently doped dispersions can thus be effectively interpolated in an arbitrary ratio. Owing to the specific physical behavior of the laser-annealed silicon films, this interpolation can follow a linear dependence on the effective doping concentration, as in the high doping concentration regime between $3 \times 10^{19}\,\mathrm{cm}^{-3}$ and $5 \times 10^{20}\,\mathrm{cm}^{-3}$, or an extremely superlinear correlation as in the vicinity of the critical doping concentration around $2 \times 10^{18}\,\mathrm{cm}^{-3} - 2 \times 10^{19}\,\mathrm{cm}^{-3}$. This digital doping method of mixing different silicon inks thus is indeed applicable to adjust the effective doping concentration in the laser-annealed films.

6.4.4 Impedance spectroscopy

The microscopic structural changes in the silicon nanocrystal network during laser annealing can be visualized in AC electrical characterization. Measurements of the complex impedance of laser-annealed silicon nanocrystal layers with lateral metallic contacts have thus been performed

Doping	Energy density (mJ cm^{-2})	ρ_p (Ω cm)	c (μF cm^{-2})	ρ_s (Ω cm)
[B] $= 10^{19}$ cm^{-3}	20	10^7	2	8.5
	40	1.3×10^4	80	10
	60	90	6	9
	80	37.5	40	4.5
	100	5.25	1400	2
[B] $= 10^{21}$ cm^{-3}	100	0.11	800	0.15

Table 6.2: Normalized parameters used for simulating the experimental impedance spectra of laser-annealed silicon nanocrystal layers.

in the frequency range of $0.1 - 10^6$ Hz using a Perkin Elmer Parstat 2263 setup (with reference and working electrodes put on the same electrical potential).

The resulting Bode plot of the imaginary part versus the real part of the complex impedance is given in Figure 6.13 a), while the imaginary part of the impedance is displayed in (b) versus the angular frequency, ω. In the figure, the results of boron-doped samples with a concentration of 10^{19} cm^{-3} boron atoms are shown for laser energy densities increasing from $20 - 100$ mJ cm^{-2} (open symbols). Unfortunately, as-deposited samples could not be investigated in this way due to their high electrical resistivity. For comparison, the impedance data of a highly boron-doped sample with a concentration of 10^{21} cm^{-3} atoms after laser annealing at 100 mJ cm^{-2} are also displayed in the figure (full symbols).

In Figure 6.13 a) the real and imaginary parts of the impedance basically show the typical phase correlation of parallel junctions of resistive and capacitive elements. Such an arrangement results in a half-circle in the Bode plot and in a single peak of the imaginary part of the impedance as a function of the angular frequency, ω. To simulate the data (dotted lines in the figure), a simple equivalent circuit consisting of a series resistance, R_s, and a resistor, R_p, plus a capacitance, C, in parallel was applied. Figure 6.14 a) shows how this observation can be interpreted microscopically with a granular particle network, while a simplified equivalent circuit is shown in the left hand side of Figure 6.14 b). Following from electric circuitry rules, the complex impedance, Z, of this basic circuit can be expressed as: $Z = R_\mathrm{s} + R_\mathrm{p}\frac{(1+i\omega R_\mathrm{p}C)}{1+\omega^2 R_\mathrm{p}^2 C^2}$.

In some cases, as for example the sample doped with 10^{19} cm^{-3} boron atoms annealed at 40 mJ cm^{-2}, also further contributions of similar elements (R_s2, C_2) in series with the first circuit had to be taken into account to fit the experimental data, as illustrated by the right hand side in Figure 6.14 b): $Z = R_\mathrm{s} + R_\mathrm{p}\frac{(1+i\omega R_\mathrm{p}C)}{1+\omega^2 R_\mathrm{p}^2 C^2} + R_\mathrm{p2}\frac{(1+i\omega R_\mathrm{p2}C_2)}{1+\omega^2 R_\mathrm{p2}^2 C_2^2}$. As evident from the dotted lines in Figure 6.13, a quantitative agreement with the experimental curves is achieved in this way.

After the fitting procedure, a proper normalization was performed to achieve physical information in the form of parameters that are independent of the sample geometry. Thus, the resistance values were transformed into specific parallel and series resistivity values, ρ_p and ρ_s, respectively, while the capacitance results were normalized to the sample cross-sectional area to obtain a specific capacitance, c. The resulting fit parameters for the dominant spectral contributions are listed in Table 6.2.

According to Table 6.2, the parallel resistivity, ρ_p, is found to decrease rapidly with increasing laser annealing energy density. A change by almost eight orders of magnitude is observed for this quantity, which is comparable with the corresponding change in the DC conductivity. Also, increasing the boron concentration by a factor of 100 induces a drop of the conductivity by a factor of 50, which is again a proof of efficient doping above the critical doping concentration. Regarding the influence of the laser annealing energy density and the doping concentration, the quantity can be used to characterize the DC properties of the material. This is however not surprising because ρ_p dominates the impedance at low frequencies, where the AC and DC measurements are equivalent.

In contrast, the series resistivity contribution, ρ_s, does not show a comparably strong reduction with increasing annealing energy density. For the sample with a boron concentration of $10^{19}\,\mathrm{cm}^{-3}$, the values range within the same order of magnitude of $2 - 10\,\Omega\,\mathrm{cm}$. If the doping concentration is increased to $10^{21}\,\mathrm{cm}^{-3}$ boron atoms, this resistivity decreases only by a factor of ten. This quantity dominates the impedance at high frequencies, when grain boundary barriers and percolation effects become negligible, and it can thus be considered a measure of the resistivity of the bulk grain material. The weak dependence of ρ_s on the annealing energy density shows that the inner-particle resistivity does not change strongly during the laser treatment.

After laser annealing at $100\,\mathrm{mJ\,cm}^{-2}$, ρ_p and ρ_s almost coincide, and their sum agrees well with the corresponding DC resistivity results. This shows that for these doping concentrations, the interface regions do not dominate the transport in the laser processed samples any longer. Instead, as a comparison of Figures 6.14 c) and d) shows, rather homogeneous current transport can take place in the laser-annealed samples in (d).

In addition to the resistivity values, the typical specific capacitance, c, contains valuable information about the microscopic structure. As the table shows, the values of c tend to increase with the annealing energy density, but are subject to considerable scatter. However, an overall increase by three orders of magnitude is evident upon increasing the energy density from $20\,\mathrm{mJ\,cm}^{-2}$ to $100\,\mathrm{mJ\,cm}^{-2}$.

This effect is directly connected to the growth of the structure size during the laser annealing. Not only has the number of capacitive elements joint in series decreased during these structural changes (compare Figures 6.14 c) and d)), but also the effective area increased significantly, which is directly mirrored in an increased effective capacitance. This result is a further qualitative confirmation of the microscopic picture of the laser annealing of silicon nanocrystal layers as it has emerged from the electron micrographs.

6.4.5 Carrier compensation in laser-annealed silicon nanocrystals

For the as-deposited silicon nanocrystal films, carrier compensation by dangling bond defects has been suggested as the origin of the onset of conductivity at the critical doping concentration of about $2 \times 10^{19}\,\mathrm{cm}^{-3}$. Since a similar situation is present after the laser treatment, also laser-annealed samples have been characterized in EPR measurements.

Figure 6.15 displays the dangling bond density versus the doping concentration for samples that were laser-annealed at an energy density of $100\,\mathrm{mJ\,cm}^{-2}$. Here, a weak but clear tendency of decreasing spin density with increasing doping concentration is present. The absolute concen-

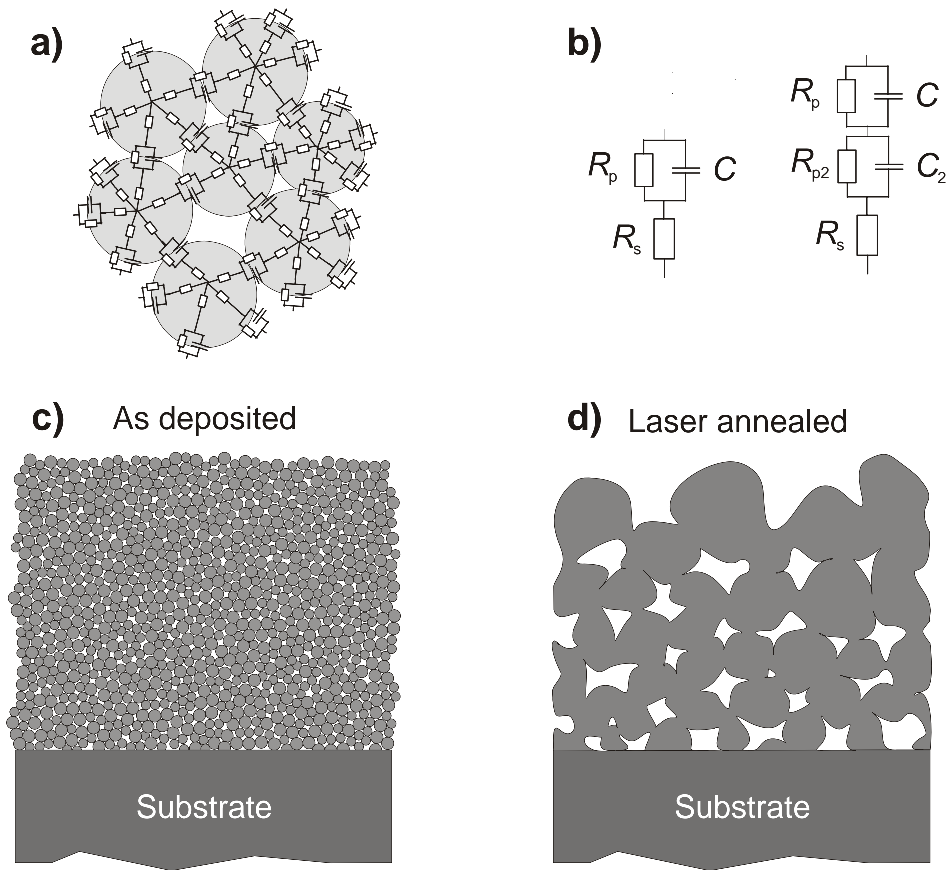

Figure 6.14: a) Schematic drawing of a model system for the electrical properties of a granular medium. The particle interfaces are modeled by capacitances and resistors in parallel, while the bulk resistivity contributes to an additional series resisitivity. b) Simplified equivalent circuits used to fit the AC impedance measurements with silicon nanocrystal layers. The layer microstructure is schematically depicted in (c) and (d) for the as-deposited and laser-annealed case, respectively.

tration of paramagnetic defects is found to decrease roughly by one third from $2.1 \times 10^{19}\,\mathrm{cm}^{-3}$ down to $1.4 \times 10^{19}\,\mathrm{cm}^{-3}$ upon adding a boron concentration of $5 \times 10^{20}\,\mathrm{cm}^{-3}$ atoms.

This decrease can be understood as a change in the charge state of $7 \times 10^{18}\,\mathrm{cm}^{-3}$ neutral paramagnetic defects towards the positively charged diamagnetic dangling bond state (db^+), which is invisible in EPR. The trapping of free holes from the valence band at deep dangling bond states is the microscopic reason for this change in the charge state and the disappearance of spins. Here, the absolute amount of trapped holes is in good agreement with the critical doping concentration of $5 \times 10^{18}\,\mathrm{cm}^{-3}$ observed in the conductivity data. Thus, we have quantitative evidence for the carrier compensation by dangling bonds also in the laser-annealed silicon nanocrystal films.

However, even after the laser treatment a rather large background of about $10^{19}\,\mathrm{cm}^{-3}$ paramagnetic defects is present in the films. A possible reason for this is the presence of defect-rich small-grained silicon material at the substrate interface and in between the molten structures as demonstrated in Subsection 6.2.1. The reason why no compensation is evident in the non-molten fraction is the coexistence of isolated doped and undoped nanocrystals in this ensemble.

It has to be recalled that the high boron concentrations required for this experiment were achieved by digital doping. The doping concentrations in the range of $10^{19} - 5 \times 10^{20}\,\mathrm{cm}^{-3}$ were realized

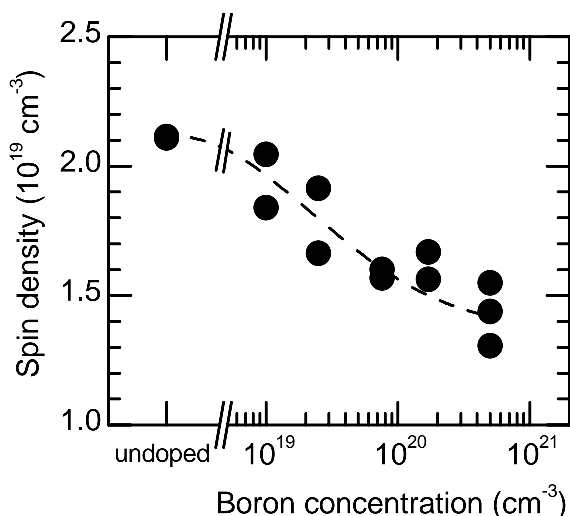

Figure 6.15: Volume density of silicon dangling bonds present in silicon nanocrystal films laser-annealed at 100 mJ cm^{-2} versus the doping concentration. The dashed line is a guide to the eye.

by mixing two differently doped silicon nanocrystal dispersions, one with a high boron concentration and the other virtually free of boron. The inhomogeneous dopant distribution in such an ensemble of nanocrystals can explain the presence of uncompensated dangling bonds in the non-molten fraction of the silicon films. While in the doped fraction of those nanocrystals, the majority of the dangling bonds will be charged by trapped carriers, the defects are isolated from free carriers in the undoped fraction. In this situation, the undoped fraction of non-molten silicon nanocrystals will contribute to a constant EPR background signal as observed here.

6.4.6 Temperature dependent conductivity

Further characteristic information on the conduction behavior can be obtained from temperature dependent measurements of the electrical conductivity. For the case of boron-doped silicon nanocrystal layers with doping concentrations ranging from 3×10^{16} cm^{-3} to 10^{21} cm^{-3} boron atoms, which have been laser-annealed at energy densities of $100 - 120$ mJ cm^{-2}, Figure 6.16 a) depicts the change in the electrical conductivity versus the inverse temperature in an Arrhenius plot. In the temperature range between 200 K and 300 K, the respective data of the laser-annealed layers can be approximated by a straight line over the full doping range under examination. Consequently, the conductivity in this temperature regime follows a thermally activated behavior according to the relation $\sigma(T) = \sigma_0 \exp(-E_A/k_B T)$, with a well-defined thermal activation energy, E_A.

The values of this activation energy vary strongly with the doping concentration. Here, weak and intermediate doping results in activation energies of several hundred meV, while for large doping concentrations, small values approaching zero are observed. To visualize the correlation with the dopant concentration, the values for E_A determined from the Arrhenius plot in Figure 6.16 a) have been plotted in (b) as a function of the doping concentration (full circles). Moreover, also the values of the similar experiments with phosphorus-doped silicon layers are shown in the graph. Both boron- and phosphorus-doped laser-annealed silicon layers follow the same general behavior.

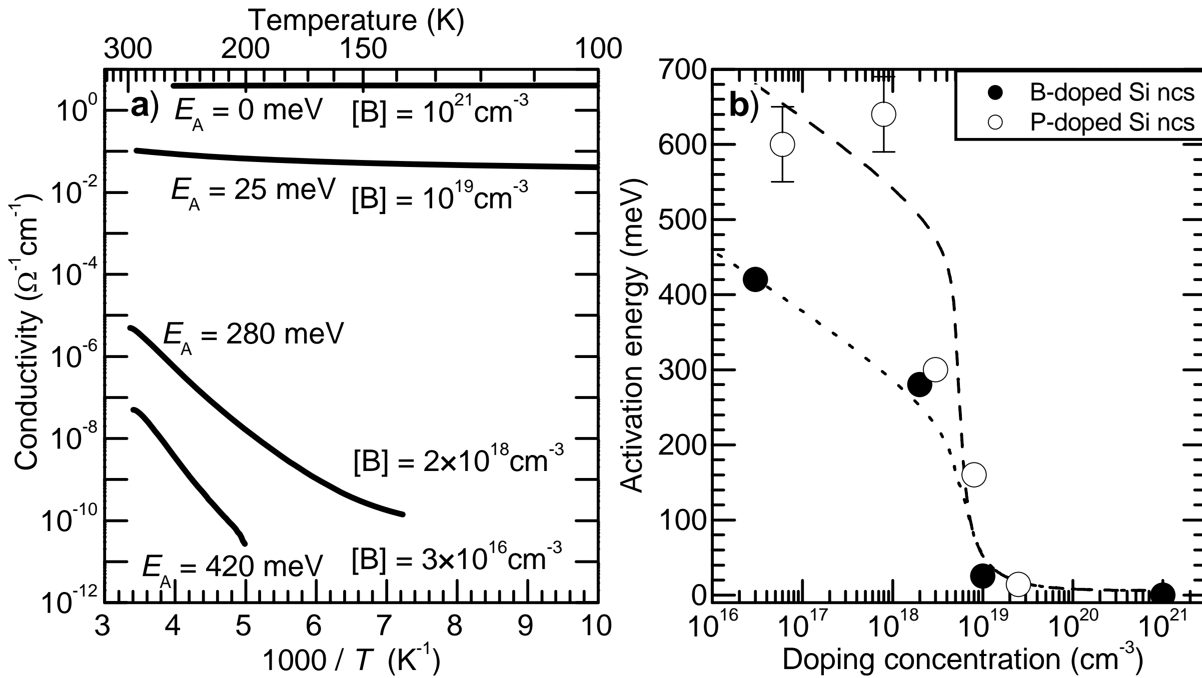

Figure 6.16: a) Temperature dependence of the electrical conductivity of boron-doped silicon nanocrystal layers after laser annealing at $100 - 120\,\mathrm{mJ\,cm^{-2}}$. b) Thermal activation energy of the conductivity of the boron-doped samples from (a) and of the corresponding phosphorus-doped layers determined in the temperature range $200 - 300\,\mathrm{K}$ versus the doping concentration. The dashed and dotted lines are guides to the eye.

At high doping levels, very small values of the activation energy of about $0-25\,\mathrm{meV}$ occur in the doping range of $10^{21} - 10^{19}\,\mathrm{cm^{-3}}$, but below $10^{19}\,\mathrm{cm^{-3}}$, the activation energy rises rapidly to values of 420 meV and 650 meV for weakly boron- and phosphorus-doped samples, respectively. Once again, a sudden change in the electrical characteristics is observed at the critical doping concentration.

Interpretation

A basically temperature-independent conductivity is also present in crystalline silicon at doping concentrations exceeding $10^{19}\,\mathrm{cm^{-3}}$ as a consequence of degenerate doping beyond the metal-insulator transition. However, for lower doping concentrations, the corresponding activation energies are typically smaller than 50 meV in this temperature range (compare Section 6.4.2). Instead, the values observed for the laser-annealed silicon layers approach midgap energies, as expected for the described compensation mechanism by the dangling bond deep trap states.

If the interpretation from the grain boundary barrier theory introduced in Section 3.6.5 is chosen, here the transition from grain boundary limited transport to a bulk-like conduction mechanism is witnessed. While thermal activation is necessary to overcome the energy barriers at the grain boundaries for low doping concentrations, above the critical doping level the barrier height rapidly decreases and the conductivity becomes independent of the temperature [Set75].

While the grain boundary barrier model assumes the trapped charges to be located at the grain boundary interfaces, in more disordered systems also potential fluctuations of the valence and

conduction band can result from the presence of charged defects in the laser-annealed layers. This alternative view, as introduced in Section 3.6.6, can be discerned from the grain boundary barrier situation by thermopower measurements, which will be described in Section 6.5.

Energy level of the trap states

For low doping concentrations, a difference in the activation energies is evident from Figure 6.16 b) depending on whether boron or phosphorus dopants were present. Following from Equation 3.29 i), this observation hints on an asymmetric energy level of the trap states within the forbidden energy gap of silicon. Using the values derived from (b), the energy distance from the valence band would amount to about 420 ± 50 meV, whereas that from the conduction band would be 625 ± 50 meV. In sum, these two values yield a value of 1.05 ± 0.10 eV, which comes close to the room temperature bandgap energy of crystalline silicon ($E_g = 1.12$ eV [Iof08]). However, the energy asymmetry is not typical for the situation in polycrystalline silicon.

In general the energy region of interest is limited by the +/0 and the 0/- charge transfer levels of the silicon dangling bonds, which are known to be situated at energies of 0.3 eV above the valence band edge and 0.32 eV below the conduction band edge, respectively [Stu87b, Joh83]. If the Fermi level is in between these two energy levels, the dangling bonds are present in a neutral charge state and can act as carrier traps for both holes and electrons. For the emission of electrons from grain boundary interface traps in *n*-type silicon, Seager and coworkers experimentally determined an energy difference of 0.57 eV between the conduction band edge and the highest occupied trap states [Sea79]. This result is equivalent to the grain boundary energy barrier height of 0.55 eV determined by Baccarani *et al.* in n-type silicon [Bac78]. The corresponding value for *p*-type silicon has been given by Seto with 0.52 eV [Set75], which again is very close to the midgap energy of silicon of 0.56 eV.

While these literature data suggest barrier heights and activation energies in polycrystalline silicon amounting to $E_g/2$ both for electron and hole conduction, the values found with the laser-annealed silicon nanocrystal layers seem to differ systematically from this behavior. However, whether this observation is a general property of the specific material or just a singular experimental observation has to be clarified in future experiments with independent experimental methods such as, *e.g.*, deep level transient spectroscopy or capacitance-voltage spectroscopy.

6.4.7 Carrier mobility

Beyond the critical doping concentrations exceeding $10^{19}\,\mathrm{cm}^{-3}$, the conductivity continues to rise linearly with increasing doping concentration. Such behavior characterizes a material with a constant carrier mobility, *i.e.* $\sigma = e\mu N \propto N$. Accordingly, the electrical properties of the laser-annealed silicon nanocrystal films become visible only if the doping concentration is sufficiently high. In crystalline silicon, the carrier mobility in this doping concentration is limited by the strong Coulomb scattering and amounts to $50\,\mathrm{cm}^2\,\mathrm{V}^{-1}\,\mathrm{s}^{-1}$ for holes and $100\,\mathrm{cm}^2\,\mathrm{V}^{-1}\,\mathrm{s}^{-1}$ for electrons, respectively [Mas83].

The local microscopic hole mobility derived in Subsection 4.3.4 from the free carrier absorption in infrared spectroscopy amounted to values of $15\,\mathrm{cm}^2\,\mathrm{V}^{-1}\,\mathrm{s}^{-1}$ for laser-annealed boron-doped silicon nanocrystal layers, which comes quite close to the literature values. However, the macro-

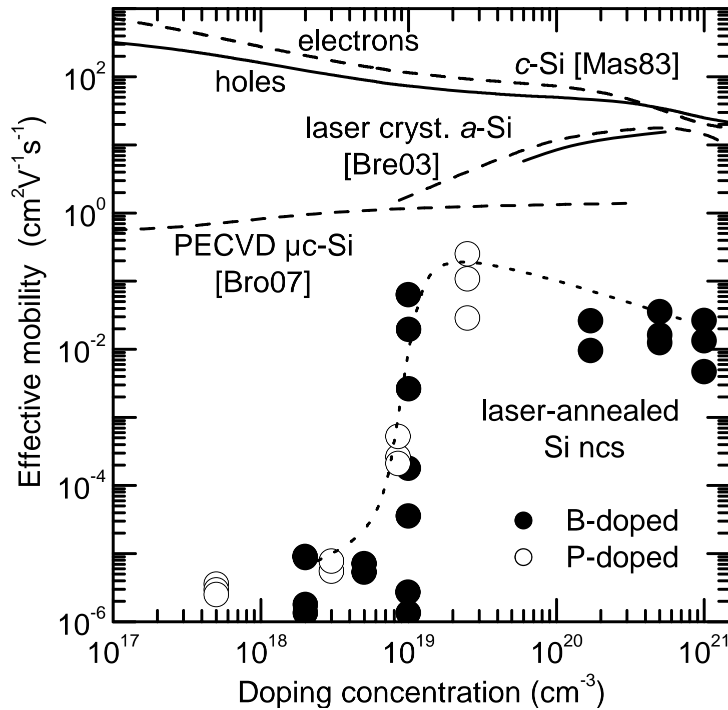

Figure 6.17: Effective carrier mobility of laser-annealed silicon nanocrystal layers versus the concentration of boron and phosphorus dopants. The full and dashed lines are literature data for holes and electrons in single crystalline silicon, laser crystallized amorphous silicon, and microcrystalline silicon, respectively [Mas83, Bre03, Bro07]. The dotted line is a guide to the eye.

scopic carrier mobility in the percolating silicon network of the laser-annealed samples was so small that no Hall characterization was possible. Thus, an effective mobility has been derived according to $\mu = \sigma / e N_{\mathrm{A,D}}$, where $N_{\mathrm{A,D}}$ is the concentration of acceptors or donors, respectively. In Figure 6.17, this effective mobility is displayed as a function of the doping concentration together with the literature values of monocrystalline silicon [Mas83], laser crystallized amorphous silicon [Bre03b], and microcrystalline silicon from plasma enhanced chemical vapor deposition (PECVD) [Bro07]. In contrast to the shown data for doped material, undoped samples in general exhibit larger mobility values [Sze07, Abr06, Das00].

As the figure illustrates, for overcritical doping concentrations the effective mobility values of the laser-annealed nanocrystal films are below the literature values for microcrystalline silicon by an order of magnitude. Below the critical doping concentration, however, the concept of the effective mobility is not applicable, because the actual carrier concentration in the layers is expected to be much smaller than the concentration of donors or acceptors. In contrast, if $N_{\mathrm{A,D}}$ exceeds the concentration of compensating dangling bond defects, N_{db}, by far, $N_{\mathrm{A,D}} > N_{\mathrm{db}}$, the approximation $N \approx N_{\mathrm{A,D}}$ is valid. According to the predictions of the grain boundary barrier theory, the mobility exhibits a pronounced minimum around the critical doping concentration, whereas it will increase again in the regime of full depletion at very small doping concentrations [Set75, Bac78].

Even for doping concentrations above $10^{20}\,\mathrm{cm}^{-3}$, the boron-doped samples exhibit values which are slightly smaller than that of the sample with the highest phosphorus concentration available. While the latter shows mobility values of $0.1 - 0.5\,\mathrm{cm}^2\,\mathrm{V}^{-1}\,\mathrm{s}^{-1}$, those of the former are in the

range of $10^{-2} - 10^{-1}\,\mathrm{cm^2\,V^{-1}\,s^{-1}}$. It should be noticed, however, that the effective mobility values derived here are the results of conservative estimations. During the calculation of the macroscopic layer conductivity, the full layer thickness of the laser-annealed films has been taken into account, whereas the current density within the films concentrates in much smaller contact areas between neighboring silicon grains (see Figure 6.14). If these reduced cross-sectional areas were taken into consideration, significantly higher conductivity and mobility values were obtained. On a microscopic scale, mobility values of the order of $10\,\mathrm{cm^2\,V^{-1}\,s^{-1}}$ are present after laser annealing, as has been derived from the infrared absorption data in Section 6.3.1. These numbers are in good agreement with the literature data of laser-annealed amorphous silicon also displayed in Figure 6.17.

6.4.8 Anisotropy of the electrical conductivity

As a consequence of the specific sample microstructure after laser annealing, it is conceivable that the samples would exhibit a higher effective conductivity normal to the substrate than parallel to the substrate plane. To determine whether such an anisotropy is present in the laser-annealed silicon nanocrystal layers, also the electrical conductivity in the vertical direction has been determined.

To this end, about 800 nm thick silicon nanocrystal layers with boron and phosphorus doping concentrations of $5 \times 10^{20}\,\mathrm{cm^{-3}}$ and $3 \times 10^{19}\,\mathrm{cm^{-3}}$ were spin-coated onto highly doped *p*- and *n*-type crystalline silicon wafers ($0.2 - 0.5\,\Omega\,\mathrm{cm}$ and $1 - 4\,\Omega\,\mathrm{cm}$, respectively) as well-defined conductive substrates, which are compatible with the pertinent process steps. The native oxide of the particles was removed and the silicon nanocrystals were laser-annealed at energy densities of $100 - 120\,\mathrm{mJ\,cm^{-2}}$. An array of aluminum back contacts was thermally evaporated onto the backside of the silicon substrates, whereas the top contact was formed by a mercury droplet, which does not wet the annealed layer or protrude into the silicon pores due to its high surface tension. The cross-sectional area covered by the droplet amounts to about $4 \times 10^{-3}\,\mathrm{cm^2}$. Ohmic characteristics of the back contacts were achieved by a short annealing at 500 °C.

The conductivity was determined from the current-voltage characteristics in a voltage range of -1 mV to 1 mV. As illustrated by the data in Table 6.3, the resulting values of the sample resistance increase significantly if laser-annealed silicon nanocrystal layers are involved. This increase by up to $10\,\Omega$ would correspond to a vertical conductivity of the layers of about $2 \times 10^{-3}\,\Omega\,\mathrm{cm}$. Instead, lateral conductivities of about $1\,\Omega^{-1}\,\mathrm{cm}^{-1}$ were found for these samples after laser annealing. However, the resistivity resolution in these vertical measurements with very thin sample layers is not very well-refined. Due to small contact resistances, already the measurements with the substrates give larger values than expected for the nominal bulk resistivity. Furthermore, the interface between the laser-annealed nanocrystals and the mercury can also contribute to an unknown contact resistance.

6.5 Thermoelectric Properties of Laser-Annealed Printed Silicon Layers

As mentioned before, also thermopower measurements can help to clarify transport processes in a material. Thus, the electrical characterization above will be supplemented in the present

Substrate	Si ncs doping	Typical substrate resistance (Ω)	Substrate with Si ncs (Ω)
p-type	$[B] = 5 \times 10^{20}\,cm^{-3}$	$5 - 20$	$10 - 30$
n-type	$[P] = 3 \times 10^{19}\,cm^{-3}$	$10 - 25$	$8 - 30$

Table 6.3: Resistivity data of vertical measurements through laser-annealed silicon nanocrystal layers on crystalline silicon substrates.

section by measurements of the Seebeck coefficient of the laser-annealed layers. By determining the thermal conductivity of the layers, it will furthermore be possible to assess the applicability of printed silicon layers for thermoelectric devices.

6.5.1 Seebeck coefficient

The buildup of a voltage, or thermopower, between the hot and cold ends of a material, which is known as the Seebeck effect, is especially pronounced in the case of semiconducting materials. This is a consequence of the typically large energy difference between the energy of thermally generated carriers and the Fermi-energy, provoking large values of the Seebeck coefficient, S, according to Equation 3.30. Moreover, the carrier concentration and mobility have a strong influence on the absolute values of S.

Dependence on the laser annealing

Using the different experimental setups described in Chapter 2, thermopower measurements were performed with the laser-annealed silicon nanocrystal layers. In Figure 6.18, exemplary thermopower results of various silicon nanocrystal samples are displayed as a function of the laser energy density applied. Here, the thermopower refers to the voltage difference, ΔU, between the cold and the hot contacts at a temperature difference of $\Delta T = 320\,K$ and an intermediate temperature level of 450 K.

As the figure shows, the thermopower of a sample doped with $10^{19}\,cm^{-3}$ boron atoms increases with the annealing energy density from about zero to $70 - 90\,mV$ around energy densities of $100 - 160\,mJ\,cm^{-2}$. For phosphorus-doped samples, a negative sign of the thermopower is observed and values of $-70\,mV$ occur in the same energy density interval for a phosphorus concentration of $3 \times 10^{19}\,cm^{-3}$. A slight decrease of the thermopower with annealing energy densities exceeding $160\,mJ\,cm^{-2}$ due to partial damage to the layers at these processing conditions can also be seen.

Similar to the situation for the electrical conductivity, a threshold energy density, which is necessary to observe a significant thermopower is present around $50\,mJ\,cm^{-2}$. Again, this effect can be correlated to the percolation threshold for the annealed silicon structures in the silicon layers after the laser treatment.

From the thermopower values depicted in Figure 6.18, the Seebeck coefficient can be calculated according to $S = \Delta U / \Delta T$. Thus, for the data shown in the figure, values of up to $|S| = 0.3\,mV\,K^{-1}$ are achieved. Yet, the doping concentration in the spin-coated silicon films is a deci-

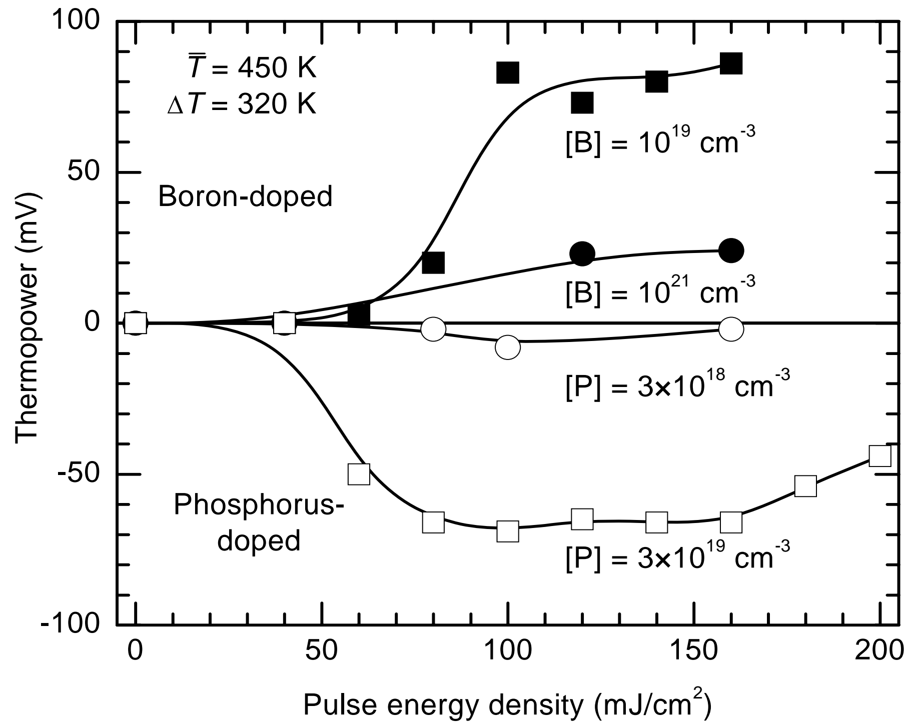

Figure 6.18: Thermopower of differently doped laser-annealed silicon nanocrystal layers as a function of the laser energy density. The values have been determined for a temperature difference of 320 K at a mean temperature of 450 K.

sive parameter for significant thermopower values after laser annealing. An order of magnitude above and below a doping concentration of $3 \times 10^{19}\,\mathrm{cm}^{-3}$, only a fraction of these maximum values are obtained. To elucidate this dependence on doping, systematic measurements of the thermopower as a function of the doping concentration will be presented in the following subsection.

Influence of the doping concentration

In Figure 6.19 a), the absolute thermopower values of a large variety of samples with doping concentrations ranging from $10^{18}\,\mathrm{cm}^{-3} - 10^{21}\,\mathrm{cm}^{-3}$ are shown. All samples have been laser-annealed at energy densities of $100 - 120\,\mathrm{mJ\,cm}^{-3}$, which corresponds to the process window giving the highest thermopower and conductivity results. The measurement conditions were as outlined before.

In agreement with Figure 6.18, a clear maximum of the thermopower is present at a doping concentration of $10^{19}\,\mathrm{cm}^{-3}$, independent of the dopant species. This maximum is accompanied by a continuous decay of the thermopower for higher doping concentrations as a consequence of the Fermi level shift towards the valence or conduction band, respectively.

At the low doping concentration side, the thermopower decreases rapidly to relatively low values below 10 mV, or $S < 30\,\mu\mathrm{V\,K}^{-1}$ for doping concentrations in the range $2 - 7 \times 10^{18}\,\mathrm{cm}^{-3}$. This is a consequence of the low conductivity in the laser-annealed films below the critical doping

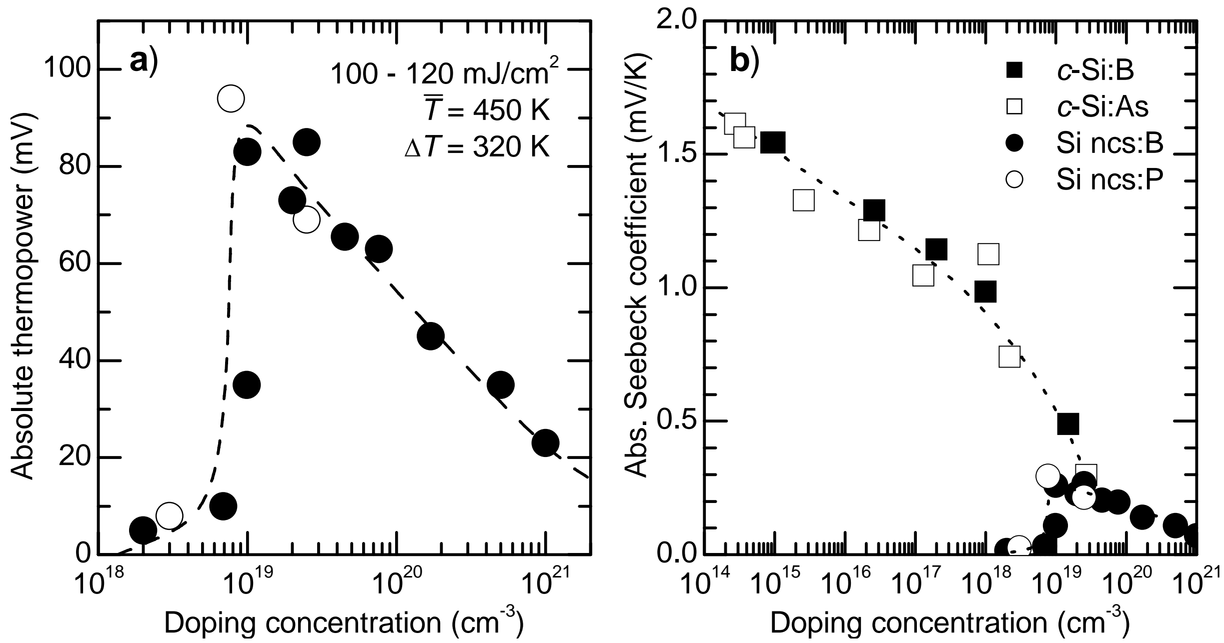

Figure 6.19: a) Absolute values of the thermopower of boron- and phosphorus-doped silicon nanocrystal layers laser-annealed at $100 - 120\,\mathrm{mJ\,cm^{-2}}$ as a function of the doping concentration. b) Absolute Seebeck coefficients of crystalline silicon samples [Geb55] in comparison with the laser-annealed silicon nanocrystal layers versus the doping concentration. Full and open symbols refer to p- and n-type samples, respectively.

concentration. In this regime, no reliable data could be achieved with the applied setup within reasonable acquisition times.

To compare the absolute values of the Seebeck coefficients with literature data of crystalline silicon as a function of the doping concentration, the latter are included in Figure 6.19 b) by the square symbols. Here, both for boron and arsenic dopants a continuous decrease of S occurs with increasing doping concentration. In direct comparison with these data, it turns out that the laser-annealed samples approach comparable values as do the crystalline silicon samples in the doping region above $10^{19}\,\mathrm{cm^{-3}}$. This fact opens up interesting perspectives regarding potential applications of the laser-annealed silicon layers as a material for thermoelectric devices.

Temperature dependence

As a function of temperature, the Seebeck coefficient of semiconductors typically varies due to the shift of the Fermi level, while the dimensionless scattering factor, A, usually does not show a strong temperature dependence. Figure 6.20 shows the results of temperature-dependent measurements of the Seebeck coefficient of several laser-annealed silicon nanocrystal layers with different boron and phosphorus doping concentrations.

The curves displayed in Figure 6.20 cannot be described by one single linear relation $|S(T)| = \frac{k_B}{e}A + \frac{\Delta E}{eT}$, but instead, at least two separate sections can be discerned, *e.g.*, for high temperatures $T > 300\,\mathrm{K}$, and for low temperatures $T < 300\,\mathrm{K}$. The following table lists the results of such piecewise linear approximations to the data:

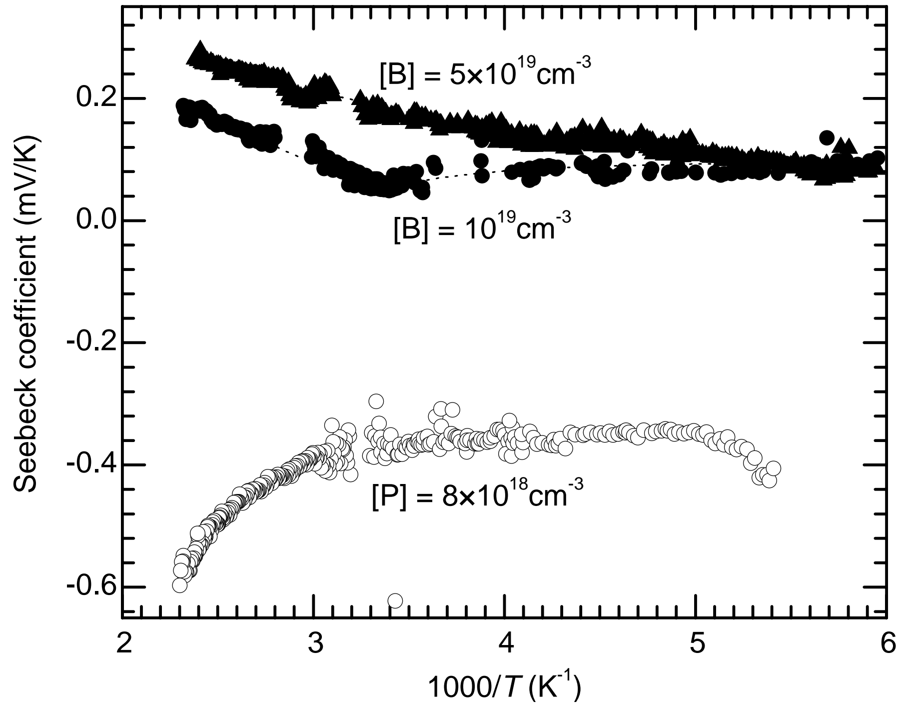

Figure 6.20: Seebeck coefficient of laser-annealed silicon nanocrystal layers as a function of the inverse temperature. The full circles, full triangles and open circles denote data of samples with doping concentrations of $10^{19}\,\text{cm}^{-3}$ and $5 \times 10^{19}\,\text{cm}^{-3}$ boron atoms and a phosphorus concentration of $8 \times 10^{18}\,\text{cm}^{-3}$, respectively.

Sample	$T > 300\,\text{K}$		$T < 300\,\text{K}$	
	ΔE (meV)	A	ΔE (meV)	A
$[\text{B}] = 10^{19}\,\text{cm}^{-3}$	116 ± 5	5.3 ± 0.2	3 ± 12	1.3 ± 0.6
$[\text{B}] = 5 \times 10^{19}\,\text{cm}^{-3}$	120 ± 7	6.4 ± 0.2	39 ± 1	3.5 ± 0.1
$[\text{P}] = 8 \times 10^{18}\,\text{cm}^{-3}$	$(-)217 \pm 3$	11.9 ± 0.1	$(-)16 \pm 5$	4.9 ± 0.3

The activation energies of the Seebeck coefficient are comparable to those of the electrical conductivity in this doping range slightly above the critical doping concentration. The fact that the activation energies and the scattering coefficient, A, vary strongly with the temperature indicates that it will be useful to determine the Q-function to eliminate the shift of the Fermi level from the temperature dependent data.

6.5.2 *Q*-function

From the results of the temperature-dependent conductivity and Seebeck measurements, the characteristic Q-function has been calculated according to Equation 3.31 for laser-annealed silicon nanocrystal layers. As Q itself is independent on the position of the Fermi level, this quantity can be used as a helpful means to evaluate the influence of potential fluctuations as depicted schematically in Figure 3.6.6.

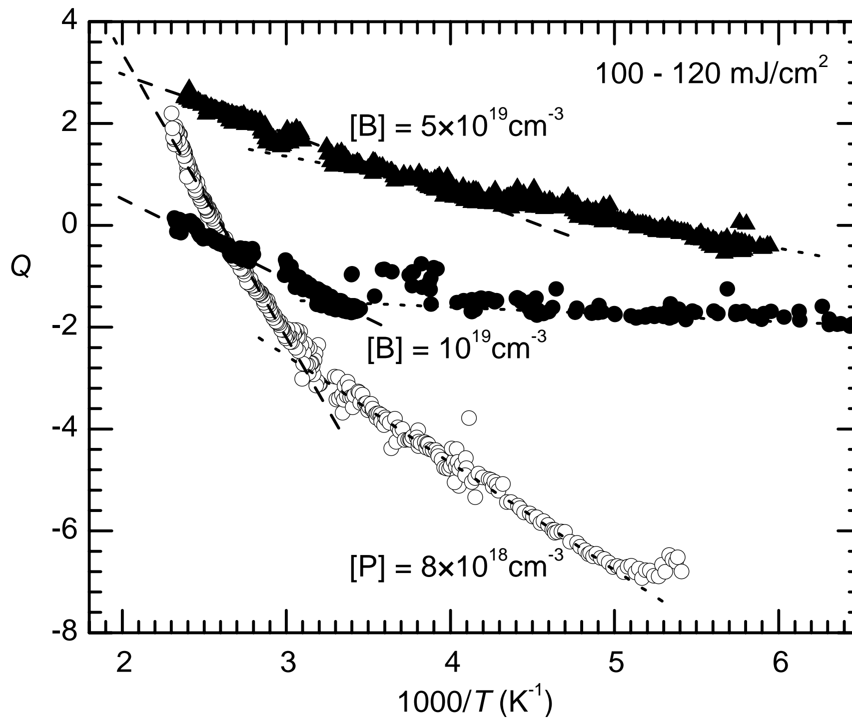

Figure 6.21: Plot of the Q-function of laser-annealed boron- and phosphorus-doped silicon nanocrystal layers versus the inverse temperature. The dopant species and concentrations are indicated in the graph.

Temperature dependence

For usual semiconductor materials, where both σ_0 and A are rather constant with temperature, also the value of Q is rather unaffected by temperature changes. In contrast, a significant temperature variation of Q can occur in disordered materials. Under the presence of potential fluctuations with an average height ΔE, and at temperatures where $\Delta E > 2k_\mathrm{B}T$, according to simulations the following relation is valid [Ove89]:

$$Q(T) = \ln(\sigma_0 \cdot \Omega\,\mathrm{cm}) + A + 1.8 - \frac{1.75}{k_\mathrm{B}T}\Delta E \equiv Q_0 - \frac{1.75}{k_\mathrm{B}T}\Delta E. \tag{6.6}$$

Thus, from an evaluation of the slope of $Q(T)$, the height of the potential fluctuations can be assessed. In Figure 6.21, the Q-functions for the three laser-annealed boron-and phosphorus-doped silicon layers of Figure 6.20 are displayed as a function of the inverse temperature. Indeed, in large temperature regions, $Q(T)$ can be described by linear curves in the graph. However, again two different slopes are present for the data corresponding to the temperature regions below and above 300 K, which are marked by the dotted and by the dashed lines in the graph, respectively.

The resulting values for Q_0 and ΔE obtained from fitting linear slopes to the data are summarized in the following table:

Sample	$T > 300\,\mathrm{K}$		$T < 300\,\mathrm{K}$	
	ΔE (meV)	Q_0	ΔE (meV)	Q_0
$[\mathrm{B}] = 10^{19}\,\mathrm{cm}^{-3}$	78 ± 7	3.7 ± 0.4	6 ± 2	1.0 ± 0.3
$[\mathrm{B}] = 5 \times 10^{19}\,\mathrm{cm}^{-3}$	54 ± 5	5.2 ± 0.4	32 ± 3	3.3 ± 0.4
$[\mathrm{P}] = 8 \times 10^{18}\,\mathrm{cm}^{-3}$	280 ± 30	14 ± 2	110 ± 10	3.7 ± 0.4

As evident from the table, most of the samples with dopant concentrations around $10^{19}\,\mathrm{cm}^{-3}$ typically show values of Q_0 that range around $3 - 5$. Furthermore, the energy fluctuation height, ΔE, is around $30 - 110\,\mathrm{meV}$ in the majority of the examined cases. Still, also quite exceptional values for ΔE and Q_0 can occur for the samples, which are very close to the critical doping concentration. Especially the sample doped with $8 \times 10^{18}\,\mathrm{cm}^{-3}$ phosphorus atoms exhibits rather high values for both at temperatures above 300 K. Contrarily, the boron-doped sample with a concentration of $10^{19}\,\mathrm{cm}^{-3}$ boron atoms has small values of Q_0 and ΔE, almost lacking thermal activation for temperatures below 300 K.

Discussion

In hydrogenated microcrystalline silicon with typical crystallite sizes of 10 nm, the quantity Q_0 amounts to $8.5 - 10.5$ and is rather independent of the sample growth conditions or of the doping concentration. Also, in amorphous silicon typical values of $Q_0 \approx 10$ are present [Ove81],.and the concept of potential fluctuations has proven to be a successful approach. There, typical values of $\Delta E = 130 - 180\,\mathrm{meV}$ are found from the temperature dependence of the Q-function, which is in good agreement with simulations [Ruf99].

In contrast, values of $Q_0 = 3 - 5$ are observed in the most cases for the laser-annealed silicon nanocrystal layers, which indicates a slightly different physical behavior. Also, the values of the potential fluctuations that can be derived from the data are rather small and range below 80 meV . At first sight, the transport paths in the material seem not to be determined by potential fluctuations. However, it should be noticed that the prefactor of ΔE in Equation 6.6 results from the assumption of statistically distributed charged centers throughout the material. A local concentration of charged centers can lead to higher potential fluctuations at smaller defect concentrations [Hau82]. Furthermore, the fact that Q is not independent of the temperature shows that the interpretation via potential fluctuations can contribute partly to the electrical properties.

The distribution of statistically distributed charged centers leads to relatively low potential fluctuations. Assuming a statistical distribution of charged dopants in the lattice and taking into account the Debye length for the screening of charges in the material, the energy height of the potential fluctuations can be derived [Bra98]:

$$\Delta E = \frac{e^2}{4\pi\varepsilon\varepsilon_0} \left(\frac{\varepsilon\varepsilon_0 k_\mathrm{B} T}{e^2 N}\right)^{1/4} \sqrt{N_\mathrm{d}}. \tag{6.7}$$

Here, N is the charge carrier concentration and N_d is the doping concentration. Under the assumption of full ionization of $10^{19}\,\mathrm{cm}^{-3}$ dopants, $N = N_\mathrm{d} = 10^{19}\,\mathrm{cm}^{-3}$, a value of $\Delta E =$

14 meV results for silicon at room temperature. This remarkably low value cannot account for the thermal activation energies observed in the experiments. Alternatively, the following relation can be applied, which has been derived from numerical simulations [Ove81]:

$$\Delta E = 2.1 \times 10^{-8}\,\mathrm{eV\,cm}\left(\frac{\varepsilon\varepsilon_0 k_\mathrm{B} T}{e^2 N}\right)^{1/4}\sqrt{N_\mathrm{d}}. \tag{6.8}$$

Again, the Debye length has been used in this equation as the relevant length scale for charge screening [Hau82]. Under the same conditions as chosen above, an energy height of $\Delta E = 25\,\mathrm{meV}$ is obtained in this case. Although significantly larger, also this value seems to disagree with the experimentally derived values.

However, under the presence of partial compensation, a different physical situation prevails in the laser-annealed layers than was assumed above. In addition to the ionized dopant atoms, trapped charges of opposite sign exist at dangling bond states. Since these are mainly localized at grain boundaries, the homogeneous statistical distribution of charged centers cannot be applied any longer. As a consequence, a quantitative underestimation of the potential fluctuations results from Equations 6.7 and 6.8. A similar effect is known for the situation in hydrogenated amorphous silicon [Hau82]. From the quantitative discrepancy between the dopant concentration and the potential fluctuation height, Hauschild and coworkers concluded that here a rather inhomogeneous distribution of charges is present. Also from the transport properties of chemical vapor deposited hydrogenated microcrystalline silicon, an inhomogeneous distribution of charges is evident [Ruf99]. Thus, potential fluctuation heights of $50 - 250\,\mathrm{meV}$ and $130 - 180\,\mathrm{meV}$ are observed in these two materials, respectively, even for doping concentrations of $5 \times 10^{18}\,\mathrm{cm}^{-3}$ and below.

Around the critical doping concentration, the thermal activation energies of the electrical conductivity of the laser-annealed silicon nanocrystal layers exhibited significant values of $100 - 300\,\mathrm{meV}$. These values are of the order that is predicted by the grain boundary barrier model as demonstrated in Section 3.6.5. The energy barriers at the grain boundaries reach their maximum value in the vicinity of the critical doping concentration, when the polycrystalline grains are fully depleted of carriers. According to Equation 3.27 ii), the maximum barrier height amounts to $E_\mathrm{B} = 400\,\mathrm{meV}$, if the critical doping concentration of $N = 5 \times 10^{18}\,\mathrm{cm}^{-3}$ evident from Figure 6.10 is applied. Here, a surface defect concentration of $10^{13}\,\mathrm{cm}^{-2}$ has been assumed, whereas a value of $3 \times 10^{13}\,\mathrm{cm}^{-3}$ would correspond to the experimentally found $10^{19}\,\mathrm{cm}^{-3}$ dangling bonds. On the other hand, relatively small effective crystallite sizes of the order of the initial nanocrystal size, $L = 20\,\mathrm{nm}$, need to be assumed, or otherwise extremely high values for E_B.are obtained. In contrast, the relevant crystallite dimensions after laser annealing amount to $100 - 400\,\mathrm{nm}$. These quantitative discrepancies might be a consequence of the one-dimensional treatment of the Poisson equation included in the grain boundary barrier model [Set75, Bac78].

In this light, the laser-annealed silicon nanocrystal layers discussed here adopt an intermediate position between grain boundary barrier limited transport and a material that is determined by potential fluctuations. As shown above from the temperature dependence of the Q-function, a significant amount of potential fluctuations is present in the layers due to ionized dopants and trapped charges at localized defects. However, the temperature-dependent conductivity data below the critical doping concentration can be qualitatively described within the framework of the grain boundary barrier theory. Thus, the latter will be preferred to explain the main electrical properties of the films. Especially around the critical doping concentration, the presence of relatively large values of ΔE has to be kept in mind, though.

6.5.3 Thermal conductivity

Nano-scale semiconductor structures are of high interest for applications where low thermal conductivity is desired. An interesting field in this respect are, *e.g.*, sensor applications. As an example, Scheel *et al*. report on the successful identification of the gas atmosphere surrounding silicon nanowires via the characteristic heat conductivity of the respective gases [Sch06]. Also, for thermoelectric devices the suppression of the heat conductivity in small-sized structures is expected to be beneficial.

To determine the thermal conductivity of laser-crystallized silicon nanocrystal layers, several different approaches were tested. This turned out to be a rather difficult task, due to the very small film thickness on the substrate. The direct measurement of steady-state electrical heating of the film by the help of an evaporated platinum filament failed, and thermal deflection spectroscopy measurements actually were limited by the thermal diffusivity of the substrate or that of the liquid detection medium if free-standing samples were employed. Thus, as a contactless approach, Raman scattering was applied to determine the thermal conductivity of the layers.

This technique is suitable also for highly porous films and was already employed to measure the thermal conductivity of wet chemically etched porous silicon with the porosity ranging from 38% to 74% [Per99, Lys99]. In this method, the sample layer is locally heated with a cw laser of variable power, and the resulting temperature is detected by analysis of the Raman signal. While Perichon and Lysenko with their coworkers evaluated the temperature dependent shift of the Raman peaks, alternatively and less ambiguously, the relative intensities of the Stokes and the Anti-Stokes Raman signatures can be exploited. As presented in Section 3.3.1, the intensity ratio of the red-shifted to the blue-shifted Raman scattering signals follows a Boltzmann distribution factor [Bal83]. Thus, from evaluating the integrated peak areas, the local temperature is obtained quite accurately.

To determine the effective thermal conductivity, also the heating power and the thermal gradient needs to be known. While the first is given by the absorbed fraction of the laser power, the second can be calculated from the thickness of the laser-crystallized film and the penetration depth of the laser light. As a thermal reservoir, in this case a crystalline silicon substrate was chosen, and a reference sample of the same material was also used.

A sketch of the method is shown in Figure 6.22. The beam of an Ar^+-ion laser at a wavelength of 514.5 nm was used to probe the sample. The laser was focussed by a microscope objective with a 50× magnification leading to a beam diameter of about 2 μm on the sample. A triple stage monochromator analyzes the Raman scattered fractions of the back-scattered light as described in Section 2.2.2.

The substrate was kept at room temperature without special experimental measures. Due to the high thermal conductivity of the silicon substrate and the weak absolute laser irradiation power, no significant heating of the substrate can occur during the measurements, which was tested with the silicon reference sample.

In the case of a thick uniform layer whose thickness exceeds the diameter of the heating laser, a, by far, the following relation can be used [Non92]:

$$\kappa = \frac{2P}{\pi a \Delta T}, \tag{6.9}$$

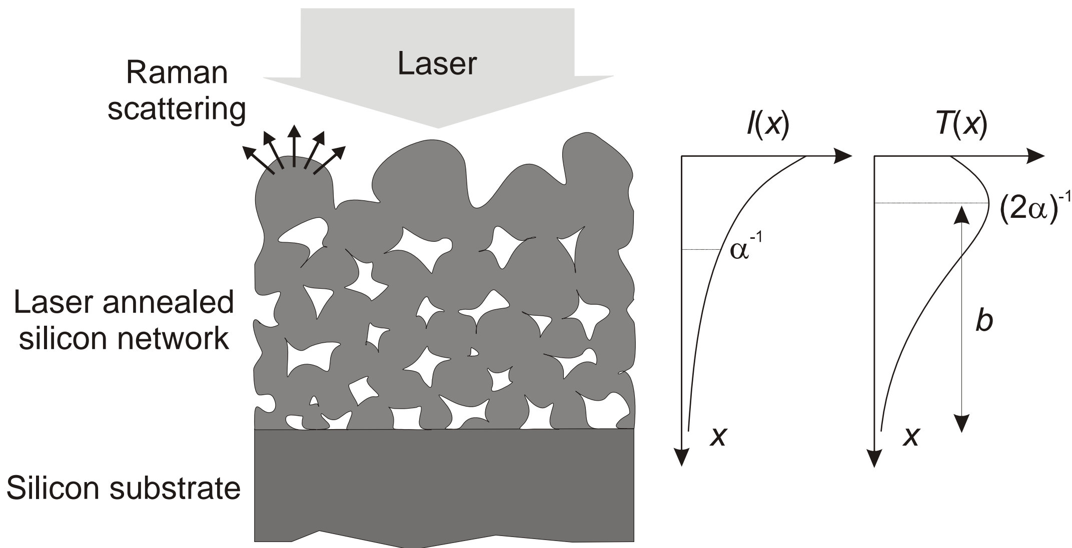

Figure 6.22: Schematic view of the thermal conductivity measurements via Raman scattering. The probing laser heats the sample and the temperature can be probed by the scattered Raman photons.

where P is the laser power and ΔT is the temperature difference between the probed spot and the surrounding. In this approximation, the thermal gradient is only estimated to spread over a distance, which resembles the width of the heating laser beam. However, the real situation can differ strongly from this assumption leaving ample room for erroneous values. Anyway, it would be favorable to have more detailed information on the thermal gradient forming in the sample.

As Figure 6.22 illustrates, this is the case for the situation of a relatively thin film of porous laser-annealed silicon nanocrystals. Here, the silicon substrate represents an almost perfect heat sink due to its inherently high thermal conductivity and the thermal length is limited by the film thickness. The film thickness is in the range of $0.5-1$ μm, which is smaller than the lateral width of the illuminated region. Thus, the situation can be approximated locally by a one-dimensional model. The heat flux per unit area is given by the absorbed part of the laser irradiation power density. In contrast to Equation 6.9, now the thermal conductivity is given by

$$\kappa = \frac{b \cdot w_{\text{abs}}}{\Delta T}. \tag{6.10}$$

Here, b is the length of the thermal gradient, w_{abs} is the absorbed fraction of the laser fluence per unit area, ΔT is the temperature difference between the laser heated region and room temperature. Due to Lambert-Beer´s law of absorption, the light intensity decreases exponentially along the penetration path. While the exact shape of the forming temperature profile is not of importance under steady-state conditions, the Raman probing depth where the local temperature is measured is given by the absorption coefficient, α. Thus, the length of the thermal gradient is $b = d - \frac{1}{2\alpha}$, where d is the film thickness, and κ can be calculated from Equation 6.10.

The results of Raman measurements of the thermal conductivity are displayed in Figure 6.23. In (a), the resulting spectra are shown for three different values of the nominal laser power of 13 mW, 33 mW, and 130 mW, while the respective temperature difference to room temperature evaluated from these data is plotted in (b) together with the results of a crystalline silicon reference sample (open and full symbols, respectively). Here, the Stokes-to-Anti-Stokes ratio has

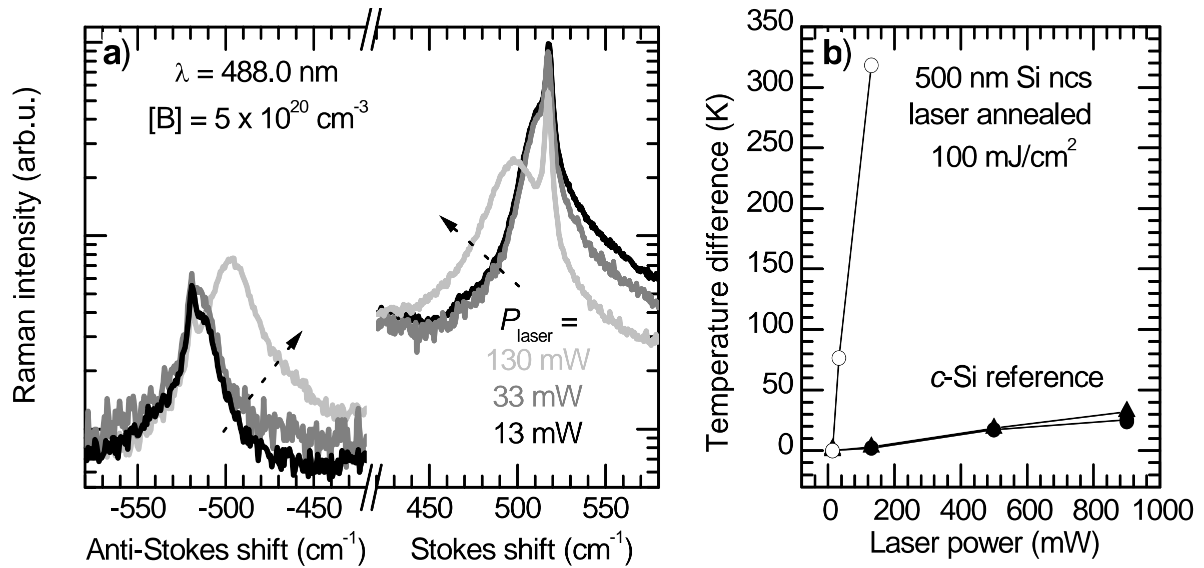

Figure 6.23: a) Measurement of the thermal conductivity of a laser-annealed boron doped silicon nanocrystal layer with a thickness of 500 nm by Raman scattering. b) Temperature difference as a function of the nominal laser power for the laser-annealed nanocrystals and for a silicon reference (open and full symbols, respectively). The data were extracted from the Stokes ratio for both materials (circles). For c-Si also the evaluation of the temperature-dependent peak shift was possible (triangles).

been used for determining the sample temperature, which gives temperature differences of about 320 K.

Note that the spectra in (a) show significant contributions of the silicon substrate at 520 cm^{-1} due to pinholes in the crystallized nanocrystal layer and due to the partial transmittance of the film. These contributions have been neglected for determining the thermal conductivity of the laser-annealed layers.

In the case of the silicon reference sample, the evaluation gives a temperature rise of about 30 K for a nominal laser output power of 900 mW. In this case, the laser power at the sample, which is much smaller due to losses at filters, mirrors, a beam splitter, and the microscope, amounts to about 23 mW, whereof 37% are reflected, and the thermal conductivity of the silicon reference can be calculated by Equation 6.9 to $\kappa = 150\,\mathrm{W\,m^{-1}\,K^{-1}}$. This value is quite close to the literature value of $130\,\mathrm{W\,m^{-1}\,K^{-1}}$ for crystalline silicon [Iof08], which is an astonishing agreement regarding the intrinsic uncertainty of the thermal gradient in Equation 6.9 as discussed above. Also if the temperature is evaluated from the known peak shift for crystalline silicon, a similar thermal conductivity value results.

In the case of the laser-crystallized silicon nanocrystal layers on silicon substrates, the temperature increase upon laser heating is by two orders of magnitude higher than in the case of the reference sample. This observation corroborates the above stated assumption in our one-dimensional model that the temperature gradient forms only across the layer thickness. If the typical absorption coefficient of laser-annealed silicon nanocrystals is accounted for, the probing depth can be assessed to be $200 - 300$ nm, and thus the thermal conductivity is calculated to

$$\kappa = \frac{300\,\mathrm{nm} \cdot 0.3 \cdot 3.3\,\mathrm{mW}}{3.14\,\mu\mathrm{m}^2 \cdot 320\,\mathrm{K}} = 0.3 - 1\,\mathrm{W\,m^{-1}\,K^{-1}}. \tag{6.11}$$

This result is in excellent agreement with literature values of the thermal conductivity obtained for wet chemically etched porous silicon samples. Here values of $0.8\,\mathrm{W\,K^{-1}\,m^{-1}}$ for a porosity of 64% [Ges97], $1\,\mathrm{W\,K^{-1}\,m^{-1}}$ for a porosity of about 50% [Per99], and values of $0.3\,\mathrm{W\,K^{-1}\,m^{-1}}$ and $0.9\,\mathrm{W\,K^{-1}\,m^{-1}}$ for porosities of 74% and 62%, respectively [Lys99], have been determined by different methods.

Two possible sources of experimental uncertainty have to be considered in this model, the high porosity and surface roughness of the laser-crystallized film and a possible thermal interface resistance between the film and the silicon substrate. While the first issue can alter the effective thickness of the film and thus cause an error of about $20 - 50\%$, the latter is more difficult to assess. However, the good agreement of our results with the literature data for a similar material system shows that the influence of a potential thermal interface resistance is only minor and that the above considerations are well applicable to the laser-annealed silicon nanocrystal films.

6.5.4 Figure of merit

The dimensionless variable which determines the efficiency of a material for thermoelectric power conversion is the figure of merit, ZT. As defined by $ZT = S^2\sigma T/\kappa$, this quantity represents a weighted compromise between the electrical conductivity, σ, the thermal conductivity, κ, and the Seebeck coefficient, S. This follows from the minimization of Ohmic losses in the material, while the thermopower should be at maximum to achieve a good thermoelectric effect. The thermal conductivity of the material, in contrast, should be as small as possible to maintain a large thermal gradient and to avoid direct heat losses by thermal conduction. Then, a fraction of the heat transported from the hot to the cold end will be converted into electrical power, similar as with a Carnot thermodynamic process.

Thermodynamic efficiency

The thermodynamic efficiency of a thermoelectric element is, like all power conversion devices, subject to the laws of thermodynamics and limited by the Carnot efficiency, η_c. Therefore, for two given hot and cold temperature levels, T_h and T_c, only efficiencies smaller than $\eta_c = 1 - T_c/T_h$ can be achieved. It can be demonstrated that the obtained efficiency, η, is given by [Iof57]:

$$\eta = \frac{\sqrt{1+ZT}-1}{\sqrt{1+ZT}+T_c/T_h}\eta_c. \tag{6.12}$$

It is easy to see that the prefactor in Equation 6.12 is smaller than 1. In fact, with values of $ZT \approx 1$, efficiencies in the range of $0.2 - 0.3\eta_c$ are achieved, depending on the temperature difference. Under the presence of an extreme temperature difference, the ratio T_c/T_h becomes negligible and an efficiency of $0.5\eta_c$ can be reached for a high value of $ZT = 3$. This is the main reason why so much effort has been made during recent decades to find materials with large values of ZT to achieve relevant efficiencies for thermoelectric power conversion.

Estimation of *ZT*

If the here observed values of the thermal and electrical conductivity, and the Seebeck coefficient are combined, a cautious estimation of the thermodynamic figure of merit can be given. Since the Seebeck coefficient of the laser-annealed silicon layers has been found to approach similar values as typically observed in crystalline silicon for a comparable doping concentration, the relevant quantity is the ratio σ/κ.

While the electrical conductivity is significantly smaller in the laser-annealed nanocrystal layers, a similar reduction is present for the thermal conductivity of the layers. Thus, the laser annealing of spin-coated silicon nanocrystal layers has the potential to achieve comparable values of ZT as can be realized with crystalline silicon. Since the values of ZT in silicon are rather low (0.01 at room temperature for an electron concentration of 2×10^{19} cm^{-3} [Web91]), further improvements are necessary to increase the thermoelectric performance of such systems. In the outlook section of the following chapter, a possible strategy towards this aim will be presented.

7 Summary and Outlook

In this final part, the most relevant of the findings presented in the previous chapters will be summarized. To demonstrate that spin-coated silicon nanocrystals can be used as the starting material for semiconductor applications, first implementations of the investigated techniques in basic device concepts will be presented. The concluding discussions focus on the feasibility of recrystallized silicon nanocrystal layers as possible candidates for the various applications which are anticipated to be realized some day by printable electronic devices.

7.1 Summary

Due to their high potential as a starting material for printable semiconductors, the properties of films of gas phase grown silicon nanocrystals and nanoparticles were examined. To this end, spherical crystalline microwave reactor silicon nanocrystals of $4-50$ nm diameter with a narrow size distribution and heterogeneous ensembles of hot wall reactor polycrystalline nanoparticles with a branched morphology and a size of $50-500$ nm were available. Liquid dispersions in ethanol can be used to produce relatively smooth particle layers by spin-coating, after a ball milling procedure has been applied. Optical reflectometry measurements allow the determination of a porosity of around 60% in these films. The absorption coefficient of spin-coated films of microwave reactor nanocrystals approaches the literature values of microcrystalline silicon if the porosity is corrected for. For hot wall material, a systematically higher absorption behavior is found due to the different microstructure. To remove the surface oxide shells of the nanocrystals a simple wet chemical etching step was applied. The absence of oxygen-related modes in the FTIR spectra demonstrates the efficiency of this method.

Successful doping of the silicon nanocrystals during growth in the microwave reactor could be shown for both, boron and phosphorus dopant atoms. For the latter, a surface segregation of $90-95\%$ during the particle growth was verified by dedicated SIMS analyses in combination with etching of the native surface oxide. In contrast, complete boron incorporation into the nanocrystals was demonstrated. Nevertheless, Raman analyses and the quantitative evaluation of infrared absorption measurements indicate that the majority of the boron atoms is situated most probably on interstitial lattice sites and is not electrically active in the as-grown silicon nanocrystals.

After removal of the native oxide shells, the electrical dark conductivity of the spin-coated nanocrystal films at room temperature is only $10^{-10}\Omega^{-1}\,\mathrm{cm}^{-1}$. No increase of the conductivity is present upon doping for low and intermediate doping densities, whereas a sudden increase of the conductivity by three orders of magnitude is present around a concentration of $10^{19}\,\mathrm{cm}^{-3}$ dopant atoms. A clear correlation of this critical doping concentration with the concentration of dangling bond defects present in the layers allows to identify defect compensation as the origin of this phenomenon. Also, the sudden decrease of the thermal activation energies of the conductivity at the critical doping concentration corroborates this interpretation. Here, the large number

of intrinsic dangling bond defects in the layers is a consequence of the ball milling procedure involved in the sample production.

The small conductivity and mobility values achievable with the spin-coated silicon nanocrystal layers motivate the implementation of a thermal post-processing step. Here, the aluminum-induced layer exchange (ALILE) process, which is a common method for the crystallization of amorphous silicon layers at low temperatures, has been found applicable also for the porous silicon particle films. In this technique, a layer of silicon nanocrystals is spin-coated on top of an about 200 nm thick aluminum film. During annealing under protective atmosphere, crystalline silicon nucleates and grows within the aluminum matrix, leading to a polycrystalline silicon film on the substrate after completion of the layer exchange. Several differences are observed with respect to the conventional ALILE with amorphous silicon precursor layers, whereas the fact whether the spin-coated films consist of microwave or hot wall reactor material has no effect on the result. The polycrystalline films from ALILE with spin-coated silicon layers exhibit a large number of pinholes and inclusions, whereas no strong formation of hillocks or island-like structures on top of the recrystallized films are present. In the films, large crystalline grains with a diameter of 50 μm and with the same thickness as the initial aluminum films are interconnected by thinner crystalline silicon regions, forming a coherent semiconducting film on the substrate. The most severe drawback of using the nanocrystal precursor layers is a retardation of the process speed by two orders of magnitude. Furthermore, an increased thermal activation energy for the overall process is observed, which necessitates relatively high temperatures of 550 °C to achieve reasonable process times. From the experimental observations, a phenomenological microscopic model was proposed to explain the specific morphological peculiarities of ALILE crystallized particle layers and the rather slow process kinetics.

Unlike the morphology and the process dynamics, the optical and the electrical properties of the recrystallized films are quite similar to those from amorphous precursors. As a consequence of the inherent aluminum incorporation during the layer exchange, free hole concentrations on the order of $2 \times 10^{18}\,\mathrm{cm}^{-3}$ are present in the polycrystalline films. Typically, the hole Hall mobility amounts to $20 - 40\,\mathrm{cm}^2\,\mathrm{V}^{-1}\,\mathrm{s}^{-1}$, which represents respectable values for semiconductor films from silicon nanocrystal precursor layers. Still, these mobilities are smaller than the corresponding values in conventional ALILE films due to the inferior layer morphology.

As a method to vary the carrier concentration in the polycrystalline films, deuterium passivation has been applied as a subsequent process step after ALILE. The characteristic correlation between the carrier concentration and the mobility upon passivation of the aluminum acceptors with deuterium could be quantitatively explained by trapping of majority charge carriers at interface and surface defects in the framework of the grain boundary barrier model. Around a critical hole concentration of $5 \times 10^{17}\,\mathrm{cm}^{-3}$ a pronounced minimum of the hole mobility occurs. This number enables the estimation of the areal density of trap states.at the polycrystalline silicon surface and interfaces to $Q_\mathrm{t} = 3 \times 10^{12}\,\mathrm{cm}^{-2}$. The depletion of carriers and grain boundary barrier formation in the thin interconnecting regions between the large silicon grains dominates the overall transport properties of the films.

As an alternative recrystallization method, laser annealing of spin-coated silicon nanocrystal layers was investigated. A frequency-doubled Nd:YAG laser was applied in pulsed operation at a wavelength of 532 nm. To avoid damage of the spin-coated layers, a process consisting of a series of ten pulses with increasing laser energy density was developed. Before this laser treatment, the native oxide is wet-chemically removed from the nanocrystal surfaces, which is decisive for the structural and electrical quality of the laser-annealed films. Flexible polyimide

foils were identified to be compatible both with the laser annealing and with the etching step and were thus mainly used for the experiments. Above a threshold value for the laser energy density, the pulsed laser annealing induces the formation of a network of sintered and molten neighboring nanocrystals. In agreement with quantitative estimations using literature data for size-dependent melting, this threshold energy density amounts to $50\,\mathrm{mJ\,cm^{-2}}$, while the best structural and electrical properties are achieved at $100-120\,\mathrm{mJ\,cm^{-2}}$ for 700 nm thick silicon nanocrystal films. Under optimized process conditions, polycrystalline silicon films exhibiting $200-400$ nm large spherical silicon structures at the sample surface are obtained. These spherical grains form a percolating porous network and are stably connected with the polymer substrate if suitable values for the laser energy density and for the layer thickness are chosen.

For the effective lateral electrical conductivity, the same threshold laser energy density value is present as observed for the microstructural properties. An increase of the conductivity by three orders of magnitude is present for undoped nanocrystal layers, whereas the conductivity of highly doped samples increases by up to nine orders of magnitude. The concomitant increase of the characteristic internal capacitances in impedance spectroscopy further indicates growing structure sizes and a decreasing number of internal interfaces with the annealing. Up to doping concentrations of $10^{18}\,\mathrm{cm^{-3}}$, the electrical conductivity of the laser-annealed silicon nanocrystal layers is unaffected by the doping concentration and amounts to $10^{-8}-10^{-7}\Omega^{-1}\,\mathrm{cm^{-1}}$ for both, phosphorus and boron doping. At a critical concentration of $5\times10^{18}-10^{19}\,\mathrm{cm^{-3}}$ dopant atoms, a sudden increase of the electrical conductivity by six orders of magnitude occurs, while for higher doping densities the conductivity is found to be linearly correlated with the doping concentration. Almost complete electrical activity of boron and phosphorus is found after laser annealing of highly doped silicon nanocrystal films concluding from optical and electrical measurements, and from mass spectroscopic analysis. An effect which is highly interesting for the application as a printable semiconductor material has also been demonstrated by the possibility to adjust a desired doping level in a film of laser-annealed nanocrystals by "digital doping". Here, two silicon nanocrystal dispersions with different doping concentration are mixed in the appropriate ratio before spin-coating and laser annealing, and material with the characteristic properties for the effective doping concentration is obtained.

Also in the laser-annealed silicon nanocrystal films, carrier compensation by deep dangling bond defect states can be made responsible for the sudden onset of electrical conductivity at a critical doping concentration. Quantitative electron paramagnetic resonance measurements show a decrease of the defect signal with increasing the doping concentration over the critical value, as it would be expected for a change of the charge state of a fraction of the dangling bonds. The thermal activation energies of the electrical conductivity strongly decrease at the critical doping density, indicating that grain boundary barriers vanish and full depletion of carriers has ceased to exist. To identify the role of potential fluctuations on the electrical transport in laser-annealed silicon nanocrystals, temperature-dependent thermopower measurements were performed, which reveal weak activation energies of the Q-function. This characteristic quantity is a means to quantify potential fluctuations in a material, such as the influence of charged dopants and trapped carriers. Around the critical doping concentration, potential fluctuation heights of up to 280 meV are detected, which shows that potential fluctuations represent a legitimate alternative approach for the interpretation of the transport properties in this doping regime.

Conservative estimates of the carrier mobilities in the laser-annealed nanocrystal layers give values of $0.1-0.5\,\mathrm{cm^2\,V^{-1}\,s^{-1}}$ for electrons and $0.02-0.1\,\mathrm{cm^2\,V^{-1}\,s^{-1}}$ for holes. In combination with the large doping concentrations necessary for significant electrical conductivity in the mate-

rial, the potential spectrum of applications for these laser-annealed layers appears limited at first sight. However, relatively large values of the Seebeck coefficient have been determined in the laser-annealed nanocrystal films. While the electrical conductivity is decreased significantly with respect to that of crystalline silicon, also the thermal conductivity is reduced to a comparable degree. In the relevant figure of merit, these both effects cancel out. Consequently, laser-annealed films of highly doped silicon nanocrystals lend themselves as a material system for thermoelectric applications, and a first estimation shows that efficiencies comparable to those of crystalline silicon devices are possible.

7.2 Outlook

The high structural and electrical quality of ALILE recrystallized polycrystalline silicon films from silicon particle layers are promising. Various semiconductor applications from solar cells to thin film transistors have been reported in the literature for ALILE films from amorphous silicon precursors on different substrates [Tsa81, Jae08]. However, the main drawback of the particle precursor layer approach can be found in the long process time, while also the compatibility of the preceding and the subsequent process steps with the annealing procedure has to be fulfilled. If this is accomplished, however, moderately doped polycrystalline films with relatively large carrier mobility can be exploited.

The laser annealing method, in contrast, has the benefit of being a very fast, high throughput technique, which avoids any excessive heating of the substrate. Especially on polymer foils, which have a rather limited thermal budget, this technique can unfold its strengths. However, the electrical properties of this material remain inferior to the ALILE recrystallized films due to the still small-grained structure with large defect concentrations after laser annealing.

To assess the applicability of this fast recrystallization method for semiconducting applications, first proof-of-concept experiments were performed. With these results in the following subsections, the experimental findings made in the course of this work will be concluded.

7.2.1 *pn*-Junctions

Structure

Two alternative sample geometries were tested to implement *pn*-diode test structures. The first (A) comprised a vertical stack of a highly *p*-type and a highly *n*-type silicon nanocrystal layers on a polyimide substrate that had been metallized with a 100 nm thick gold film. After the spin-coating of both layers subsequently and after oxide removal, the samples were laser-annealed at an energy density of $80\,\mathrm{mJ\,cm^{-2}}$, and the vertical current-voltage characteristics were analyzed. The film thickness of the *p*-type layer amounts to 700 nm, whereas the *n*-type top layer had a thickness of 400 nm.

Unfortunately, the laser treatment was found to represent a severe stress to the stacked layer system. If an energy density typical for the recrystallization of films on mere Kapton substrates was applied, large fractions of the film were lifted off the substrate. We associate this effect with the poor sticking conditions on the metallized substrate.

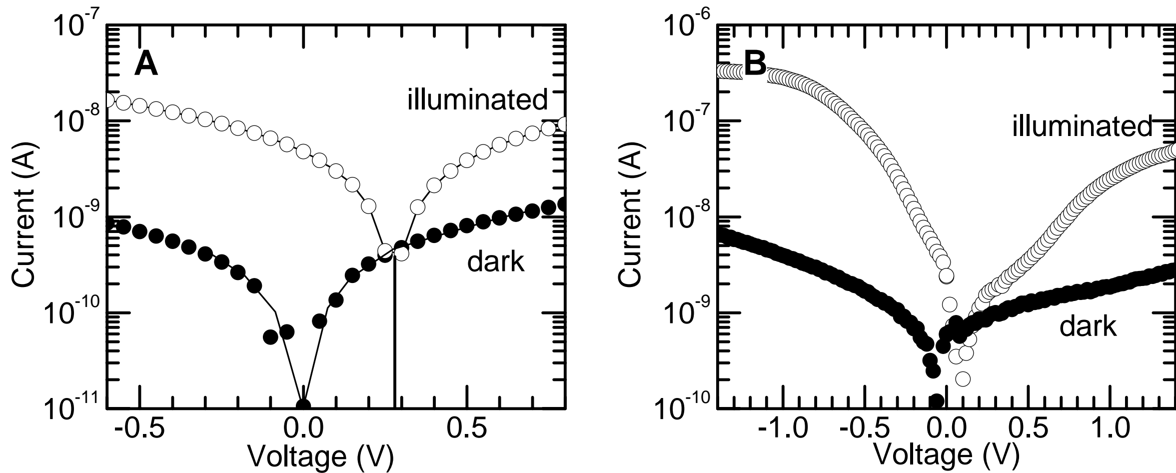

Figure 7.1: First *pn*-junctions of laser-annealed silicon nanocrystals in two different geometries. Significant photovoltage is observed in the layered structure A, whereas a clearer rectifying behavior is visible with the design B.

For an alternative diode design (B), a geometry with a transparent back contact was chosen. Here, an indium-tin oxide (ITO) coated glass was used as the supporting substrate. In contrast to the first method, here the silicon nanocrystals were oxide etched in a solution of dilute hydrofluoric acid (5%) in ethanol. After rinsing, the etched nanocrystals were dispersed in ethanol and then spin-coated on the substrate. The laser annealing was performed directly after spin-coating without applying an additional wet chemical etching step.

Then, a layer of nanocrystals of the complementary doping species was deposited on top, and the obtained multilayered structure of nanocrystals was again laser-annealed. With some samples, also double layers of each type of doped nanocrystals were used to achieve thicker layer geometries and to prevent short circuits. Metal front contact pads were evaporated through shadow masks and the characteristics were recorded versus the common transparent back contact.

Rectifying behavior and photovoltaic effect

As Figure 7.1 shows, the electrical characteristics of structure (A) indicate an almost ohmic behavior of the dark and illuminated current-voltage characteristics. Nevertheless, under illumination an open circuit voltage is observed. This voltage amounts to 270 mV. In state-of-the-art silicon solar cells, open circuit voltages of $0.5 - 0.6$ V are typical values under illumination. Nevertheless, the observed short-circuit current is quite small for the examined device. This, together with the almost linear current voltage characteristics suggests that a rather high resistivity region is present in series to the *pn*-junction. According to the cell design (A), this is not surprising. Better back contact designs will be necessary to extract a significant amount of the photogenerated carriers.

With the alternative cell design (B), indeed a larger photoconductivity is obtained. Still, the short circuit current of these devices is almost negligible. The more pronounced nonlinear current-voltage characteristics can be regarded as the consequence of more efficient carrier collection

by the planar contacts. Here, the diode-like current-voltage characteristics are less influenced by a series resistance. Stronger asymmetry versus applied current direction is the consequence. A rectifying ratio of about 30 can be observed under illumination. Interestingly, the dark characteristics show much weaker rectifying effects. Apparently, in the dark the transport paths are not dominated by the silicon *pn*-layers but are determined through leakage paths within the layer system.

7.2.2 Field Effect in Recrystallized Nanoparticle Layers

Gated structures

To test the influence of electrical field on the conductivity of a channel of laser-annealed silicon nanocrystals, two different gated design structures were implemented. Design (A) consisted of a 500 nm thick layer of silicon nanocrystals that was spin-coated on Kapton substrates, oxide etched, and laser-annealed at energy densities of $100-120\,\mathrm{mJ\,cm^{-2}}$. Then, an insulating polymer dielectric (PMMA) was deposited on top and dried in an oven at 120 °C for 10 min. A metallic gate contact was then printed on top with conductive silver paste.

As an alternative geometry (B), silicon nanocrystals were etched in dilute hydrofluoric acid as described above, re-dispersed in ethanol, and then spin-coated on oxidized silicon wafer substrates. The latter had a 200 nm thick thermal oxide, which was intended as the gate dielectric of these field effect structures. Source and drain contacts were structured lithographically and the electrical characteristics were recorded.

Characteristics

The electrical characteristics of a first field-effect structure is shown in Figure 7.2. Indeed, a correlation between the channel conductivity and the gate bias is present. The conductivity of the channel is found to decrease with increasing gate bias for hole conduction (a), whereas the opposite is found for *n*-type doped silicon layers (b). In this sense, the devices can be regarded as field effect structures, even though the amplitude of the effect is very small.

To exclude external effects, the leakage current through the gate dielectric was recorded with a high impedance electrometer. The corresponding values for the samples shown in Figure 7.2 a) and b) were smaller than 2 pA in both cases for the highest applied gate voltages. The only weak field effect of these first devices is predominantly due to the small effective electric fields in the gate dielectric. Here, the thickness of the dielectric polymer amounted to up to ten micrometers. Thinner layers were achieved by spin-coating, but then the problem of short circuits through the polymer marred the functionality.

From a simple consideration, the untypical characteristics of the device can be understood. The electric field within the channel region is of the order of $E = 10^5\,\mathrm{V\,cm^{-1}}$, whereas in usual MOSFET transistor devices fields of about $5 \times 10^6\,\mathrm{V\,cm^{-1}}$ are commonly present. The gate capacity follows from $C_\mathrm{g} = \varepsilon\varepsilon_\mathrm{r} A/d$, with the dielectric thickness, d, and the gate area, A,.and can be assessed for these gated structures to about 1 nF. For small electric fields, the transistor equation in the absence of saturation [Sze07] can be simplified to: $I_\mathrm{sd} \approx \mu C_\mathrm{g} V_\mathrm{gs} V_\mathrm{sd}$, where the width and length of the channel region have been assumed equal. With a carrier mobility of

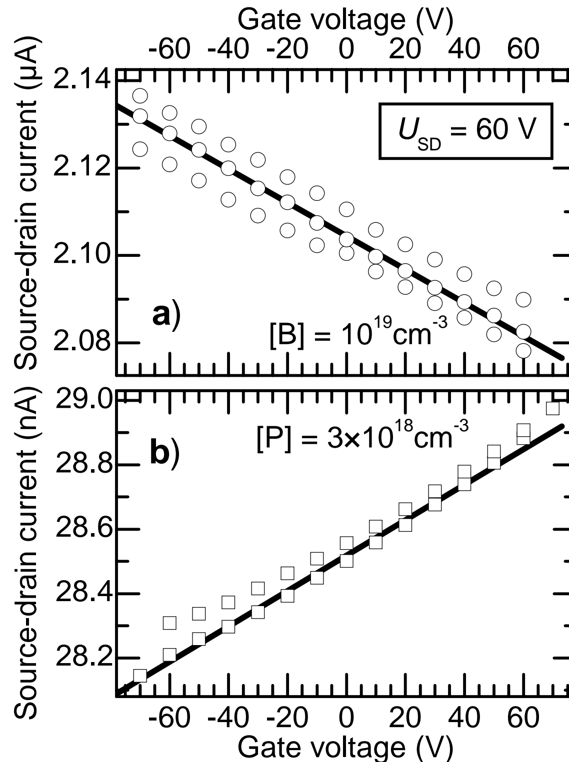

Figure 7.2: Modulation of the source-drain current by the gate potential in a printed structure of laser-annealed silicon nanocrystals with boron and phsophorus doping. The gate leakage current of both devices was smaller than 2 pA at a gate voltage of 60 V.

$10^{-2}\,\text{cm}^2\,\text{V}^{-1}\,\text{s}^{-1}$, this estimation gives a current amplitude of 40 nA, in good agreement with the data in Figure 7.2 a). This mobility is well in the range found for laser-annealed samples of this boron concentration, as Figure 6.17 illustrates. The smaller change of the channel current in the phosphorus-doped sample is a consequence of the low mobility due to carrier compensation at this low doping level.

Transistors with structure (B) showed no considerable lateral conductivity and no field-effect with the external bias. This was most probably a consequence of the etching procedure of the nanocrystals. Further optimization of the sample processing will be necessary. However, this better defined geometry should allow the assessment of a field effect mobility value in the future.

7.2.3 Thermoelectric Devices

Proof of concept

The thermopower values observed with the laser-annealed nanocrystal films ($cf.$ Section 6.5) can in principle be used to implement a thermoelectric power generator device. To this end, a prototype was built from p- and n-type laser-annealed silicon nanocrystal layers. The phosphorus concentration amounted to $3 \times 10^{19}\,\text{cm}^{-3}$, while a boron concentration of $1.6 \times 10^{20}\,\text{cm}^{-3}$ was chosen. The p- and n-type doped samples were connected pairwise with electrically conducting leads.and were suspended on one side by a glass carrier. A photograph of the realized device is

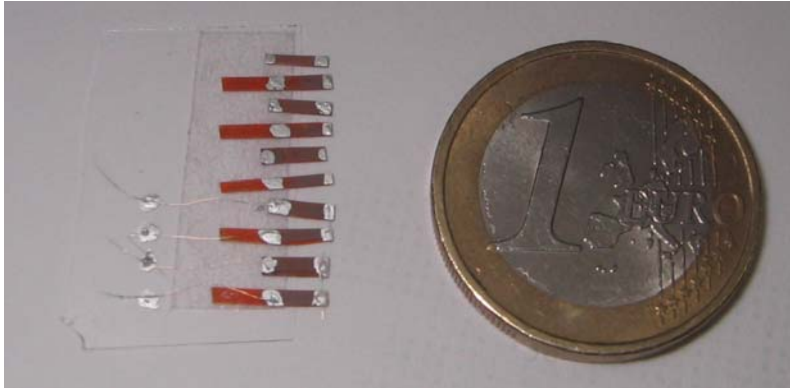

Figure 7.3: Proof of concept for a thermoelectric device made of spin-coated silicon nanocrystal layers on Kapton polymer foil after laser annealing. Five pairs of p- and n-type layers can be seen in the figure (long and short stripes, respectively).

shown in Figure 7.3. For characterization, a temperature gradient was applied along the stripe length by heating the protruding ends of the samples to a temperature of 350 °C. The other end was at room temperature without active cooling and the resulting thermopower at the terminal leads was measured with a high-impedance electrometer (Keithley 617).

If the thermoelements are to be used for power generation, both the thermopower and the achievable current determine the power output of the devices. While the thermopower values of the single individual elements add up in serial operation, the short circuit current is limited by the serial resistance of the highest resistivity element in the circuit. This circumstance is illustrated in Table 7.1, which summarizes the electrical data of single elements and series connected elements for a fixed temperature difference of $\Delta T \approx 300\,^{\circ}\mathrm{C}$. Indeed, the thermopower is found to sum up accordingly, whereas the current is determined by the highest resistance element.

Improvement of the figure of merit

Although the laser annealing of silicon nanocrystal layers is a potential approach to produce thermoelectric elements, still a lot of optimization will be required to improve the achievable efficiency. In Section 6.5.4, the figure of merit value of ZT for the laser-annealed films was estimated to come close to the value of crystalline silicon, which itself is quite low and amounts to around 0.01 at room temperature. Significantly higher values are required for efficient thermoelectric operation.

	Thermopower (mV)	Short circuit current (μA)
Single elements	$93 - 105$	$0.2 - 0.5$
Two elements in series	200	0.2

Table 7.1: Electrical current and thermopower values of thermoelectric demonstrators from laser-annealed silicon nanocrystal layers.

For the first thermoelectric devices shown above, the corresponding boron and phosphorus doping concentrations have not yet been optimized regarding the highest possible Seebeck coefficient, as a comparison with the thermopower data in Figure 6.19 shows. If the heat conductivity is assumed to be rather constant with the doping concentration, ZT is dominated by the product $S^2\sigma$. In the doping regime of interest, the electrical conductivity, σ, increases roughly proportional with the doping concentration, whereas S declines logarithmically. Consequently, a maximum is expected for the product for doping concentrations well above the critical concentration at around $5 \times 10^{19} - 10^{20}\,\mathrm{cm}^{-3}$. This agrees quite well with the typical doping level of $10^{20}\,\mathrm{cm}^{-3}$, which is required for a maximum value of the thermoelectric figure of merit in various thermoelectric materials [Sny08].

Apart from maximizing S and σ, also the thermal conductivity can be decreased further, *e.g.*, by alloying silicon with germanium. Then, alloy scattering of phonons can lead to a decrease of the thermal conductivity by a factor of up to ten. In bulk samples of the alloy $Si_{0.8}Ge_{0.2}$, thus ZT values of up to 0.9 are achieved at temperatures of 800 °C [Vin91, Ota04]. Additionally, also finite size effects can in principle be exploited to reduce the thermal conductivity. In the case of silicon nanowires with diameters of 20 nm, phonon drag effects of the thermopower and phonon scattering effects led to the observation of figure of merit values of 1 and 0.6 at temperatures of 200 K and at room temperature, respectively [Hoc08, Bou08]. Since this lateral size is close to that of the primary silicon nanocrystals discussed here, it will be difficult to make use of similar mechanisms with laser-annealed nanocrystal layers. However, if a suitable prestructuring has been applied before the laser annealing, in principle such effects can be exploited.

Acknowledgements

During the course of this work, I could benefit from many people who made these years at the Walter Schottky Institut a wonderful period of my life. Thus, I want to thank everybody who contributed directly and indirectly to the results of this work:

Prof. Dr. Martin Stutzmann for the opportunity to work as a PhD student at his chair under excellent conditions. Thank you for your support and your friendly way of encouraging a responsible working atmosphere!

Dr. André Ebbers, **Dr. Martin Trocha**, **Dr. Frank-Martin Petrat**, and **Dr. Jürgen Steiger** of Creavis, Evonik Degussa GmbH for large quantities of silicon nanocrystals and dispersions, and for financial support within the framework of the Science-to-Business Center Nanotronics in Marl. This project was also funded by the government of **North Rhine-Westphalia** and was co-financed by the **European Union**.

Dr. Hartmut Wiggers of the Universität Duisburg-Essen for the on-demand delivery of undoped and phosphorus-doped silicon nanocrystals of custom particle size.

The nanosilicon group at the WSI, namely **André Stegner**, **Roland Dietmüller**, and **Dr. Rui Pereira** for the exciting experience to discover the physics of new materials together. I wish to thank André and Roland also for their proof-reading of this manuscript. Good luck for your future and keep up the good work!

Dr. Mario Gjukic for his friendship, for his cheerful presence in times of trouble, and for entertaining discussions on physics and on so much else. Of course, I will never forget the good old SiGe days!

The rest of the ALILE task force, **Michael Scholz**, **Tobias Antesberger**, and **Christian Jäger** for the deposition of amorphous silicon layers and access to the vacuum annealing setup.

My master student **Nuryanti** for her patience with time-consuming passivation and thermal effusion measurements.

Georg Dürr on his mission to determine thermal conductivities, and **Konrad Schönleber** - good luck for your theses!

Florian Furtmayr for assistance with the SEM measurements.

All other highly engaged PhD students at E25, namely **Thomas Wassner** and **Bernhard Laumer**, who are strongly committed to maintain the analytic tools of E25 in a good condition.

Michi Fischer for help with all types of technical questions and for cheering up his roommates in S106 with his bavarian way of life and with life-sustaining automated goods.

Prof. Dr. Martin Brandt and the **EPR group** for tolerating the presence of the thermopower measurement setup in their busy lab.

All other members of E25, including, not least, **Veronika Enter** for taking care of all kinds of organizational questions.

Eva, for your love and support - and for so much else every day!

My **parents** for laying the foundations for this scientific work. Thank you also for your timely reminders to bring this thesis to an end!

List of publications

1. R. Lechner, M. Buschbeck, M. Gjukic, and M. Stutzmann, *Thin polycrystalline SiGe films by aluminum-induced layer exchange*, phys. stat. sol. (c) **5**, 1131 (2004).

2. M. Gjukic, M. Buschbeck, R. Lechner, and M. Stutzmann, *Aluminum-induced crystallization of amorphous silicon–germanium thin films*, Appl. Phys. Lett. **85**, 2134 (2004).

3. M. Gjukic, R. Lechner, M. Buschbeck, and M. Stutzmann, *Optical and electrical properties of polycrystalline silicon–germanium thin films prepared by aluminum-induced layer exchange*, Appl. Phys. Lett. **86**, 62115 (2005).

4. R. Lechner, H. Wiggers, A. Ebbers, J. Steiger, M. S. Brandt, and M. Stutzmann, *Thermoelectric effect in laser annealed printed nanocrystalline silicon layers*, phys. stat. sol. (RRL) **1**, 262 (2007).

5. R. N. Pereira, A. R. Stegner, K. Klein, R. Lechner, R. Dietmueller, H. Wiggers, M. S. Brandt, and M. Stutzmann, *Electronic transport through Si nanocrystal films: Spin-dependent conductivity studies*, Physica B **401–402**, 527 (2007).

6. A. R. Stegner, R. N. Pereira, K. Klein, R. Lechner, R. Dietmueller, M. S. Brandt, H. Wiggers, and M. Stutzmann, *Electronic transport in phosphorus-doped silicon nanocrystal networks*, Phys. Rev. Lett. **100**, 026803 (2008).

7. R. Lechner, A. R. Stegner, R. N. Pereira, R. Dietmueller, M. S. Brandt, A. Ebbers, M. Trocha, H. Wiggers, and M. Stutzmann, *Electronic properties of doped silicon nanocrystal films*, J. Appl. Phys. **104**, 053701 (2008).

8. A. R. Stegner, R.N. Pereira, R. Lechner, K. Klein, M. S. Brandt, H. Wiggers, and M. Stutzmann, *Interplay between Si dangling bond states and phosphorus doping in freestanding Si nanocrystals from the gas phase*, in preparation (2008).

9. R. Dietmüller, A. R. Stegner, R. Lechner, S. Niesar, R. N. Pereira, M. S. Brandt, A. Ebbers, M. Trocha, H. Wiggers, and M. Stutzmann, *Light-Induced Charge Transfer in Hybrid Composites of Organic Semiconductors and Silicon Nanocrystals,* in preparation (2008).

Patent Applications

1. R. Lechner, M. Gjukic, and M. Stutzmann (*inventors*), *Siliziumpulver enthaltende Dispersion und Verfahren zur Beschichtung*, German patent application DE 102005446A1, Degussa AG, disclosure date: 16.11.2006 (2005).

2. R. Lechner, M. S. Brandt, A. Ebbers, M. Trocha, H. Wiggers, and M. Stutzmann (*inventors*), *Poröser halbleitender Film sowie ein Verfahren zu dessen Herstellung*, German Patent Application DE 102007014608A1, Evonik Degussa GmbH, disclosure date 25.09.2007 (2007).

3. R. Lechner, M. S. Brandt, A. Ebbers, M. Trocha, C. Schulz, H. Wiggers, and M. Stutzmann (*inventors*), *Thermokraftelement oder Peltier-Elemente aus gesinterten Nanokristallen aus Silicium, Germanium oder Silicium-Germanium Legierungen*, German Patent Application, Degussa GmbH 200700594, non-disclosed (2007).

Bibliography

[Abr06] A. Abramov, Y. Djeridane, R. Vanderhaghen, and P. Roca i Cabarrocas, *Large grain μc-Si:H films deposited at low temperature: Growth process and electronic properties*, Journal of Non-Cryst. Solids **352**, 964 (2006).

[Aic99] G. Aichmayr, D. Toet, M. Mulato, P.V. Santos, A. Spangenberg, S. Christiansen, M. Albrecht, and H. P. Strunk, *Dynamics of lateral grain growth during the laser interference crystallization of a-Si*, J. Appl. Phys. **85**, 4010 (1999).

[Ana91] E. Anastassakis, *Strain characterization of semiconductor structures and superlattices*, in: *Light scattering in semiconductor structures and superlattices*, edited by D. J. Lockwood and J. F. Young, 173 (Plenum, New York, 1991).

[Ana95] C. Anandan, *X-ray photoelectron spectroscopic study of room-temperature evolution of oxide-covered hydrogenated amorphous silicon/aluminium interface*, Appl. Surf. Sci. **89**, 57 (1995).

[And98] G. Andrä, J. Bergmann, F. Falk, E. Ose, and H. Stafast, *Laser induced crystallization of amorphous silicon films on glass for thin film solar cells*, phys. stat. sol. (a) **166**, 629 (1998)

[And03] G. Andrä, J. Bergmann, F. Falk, and E. Ose, *Multicrystalline LLC-Si thin film solar cells on low temperature glass*, Proceedings of the 3rd World Conference on Photovoltaic Energy Conversion, Vol. **2**, 1174 (2003).

[Aqi02] A. K. S. Aqili and A. Maqsood, *Determination of thickness, refractive index, and thickness irregularity for semiconductor thin films from transmission spectra*, Appl. Optics **41**, 218 (2002).

[Ash95] M. S. Ashtikar and G. L. Sharma, *Silicide mediated low temperature crystallization of hydrogenated amorphous silicon in contact with aluminum*, J. Appl. Phys. **78**, 913 (1995).

[Asp83] D. E. Aspnes and A. A. Studna, *Dielectric functions and optical parameters of Si, Ge, GaAs, GaSb, InP, InAs, and InSb from 1.5 to 6.0 eV*, Phys. Rev. B **27**, 985 (1983).

[Asp84] D. E. Aspnes, A. A. Studna and E. Kinsbron, *Dielectric properties of heavily doped crystalline and amorphous silicon from 1.5 to 6.0 eV*, Phys. Rev. B **29**, 768 (1984).

[Asp99] D. E. Aspnes (Chapter Editor), *Optical properties of Si*, in: R. Hull (Editor), *Properties of crystalline silicon*, emis DataReviews Series **20** (INSPEC, London, 1999).

[Bac78] G. Baccarani, G. Spadini, and B. Ricco, *Transport properties of polycrystalline silicon films*, J. Appl. Phys. **49**, 5565 (1978).

[Bal83] M. Balkanski, R. F. Wallis, and E. Haro, *Anharmonic effects in light scattering due to optical phonons in silicon*, Phys. Rev. B. **28**, 1928 (1983).

[Bal06] R. K. Baldwin, J. Zou, K. A. Pettigrew, G. J. Yeagle, R. D. Britt, and S. M. Kauzlarich, *The preparation of a phosphorus doped silicon film from phosphorus containing silicon nanoparticles*, Chem. Commun. **2006**, 658 (2006).

[Bal07] I. Balberg, E. Savir, and J. Jedrzejewski, A. G. Nassiopoulou, and S. Gardelis, *Fundamental transport processes in ensembles of silicon quantum dots*, Phys. Rev. B **75**, 235329 (2007).

[Ban93] J. Bandet, J. Frandon, F. Fabre, and B. de Mauduit, *Selectively disorder activated Raman scattering in silicon films*, Jap. J. Appl. Phys. **32**, 1518 (1993).

[Bao97] Z. Bao, Y. Feng, A. Dodabalapur, V. R. Raju, and A. J. Lovinger, *High-performance plastic transistors fabricated by printing techniques*, Chem. Mater. **9**, 1299 (1997).

[Bau80] R. S. Bauer, R. Z. Bachrach, and L. J. Brillson, *Au and Al interface reactions with* SiO_2, Appl Phys. Lett. **37**, 1006 (1980).

[Bau05] A. Baumer, *Structural and electronic properties of hydrosilylated silicon surfaces*, PhD Thesis, Technische Universität München (2005).

[Bee07] P. Beecher, P. Servati, A. Rozhin, A. Colli, V. Scardaci, S. Pisana, T. Hasan, A. J. Flewitt, J. Robertson, G. W. Hsieh, F. M. Li, A. Nathan, A. C. Ferrari, and W. I. Milne, *Ink-jet printing of carbon nanotube thin film transistors*, J. Appl. Phys. **102**, 043710 (2007).

[Bel02] G. Belomoin, J. Therrien, A. Smith, S. Rao, R. Twesten, S. Chaieb, M. H. Nayfeh, L. Wagner, and L. Mitas, *Observation of a magic discrete family of ultrabright Si nanoparticles*, Appl. Phys. Lett. **80**, 841 (2002).

[Ber78] D. J. Bergmann, *The dielectric constant of a composite material - a problem in classical physics*, Phys. Rep. **43**, 377 (1978).

[Bet04] S. Bet and A. Kar, *Laser forming of silicon films using nanoparticle precursor*, J. Electron. Mater. **35**, 993 (2006).

[Bey79] W. Beyer, R. Fischer, and H. Overhof, *Transport in lithium-doped amorphous silicon*, Phil. Mag. B **39**, 205 (1979).

[Bey82] W. Beyer and H. Wagner, *Determination of the hydrogen diffusion coefficient in hydrogenated amorphous silicon from hydrogen effusion experiments*, J. Appl. Phys. **53**, 8745 (1982).

[Bie98] A. Bierhals, A. G. Aberle, and R. Hezel, *Improved understanding of thermally activated structural changes in Al/*SiO_x*/p-Si tunnel diodes by means of infrared spectroscopy*, J. Appl. Phys. **83**, 1371 (1998).

[Boc80] A. C. Boccara, D. Fournier, and J. Badoz, *Thermo-optical spectroscopy: Detection by the "mirage-effect"*, Appl. Phys. Lett. **36**, 130 (1980).

[Bou08] A. I. Boukai, Y. Bunimovich, J. Tahir-Kheli, J.-K. Yu, W. A. Goddard III, and J. R. Heath, *Silicon nanowires as efficient thermoelectric materials*, Nature **451**, 168 (2008).

[Bra98] M. S. Brandt, P. Herbst, H. Angerer, O. Ambacher, and M. Stutzmann, *Thermopower investigation of n- and p-type GaN*, Phys. Rev. B **58**, 7786 (1998).

[Bra06] R. Brayner, R. Ferrari-Iliou, N. Brivois, S. Djediat, M. F. Benedetti, and F. Fiévet, *Toxicological impact studies based on Escherichia coli bacteria in ultrafine ZnO nanoparticles colloidal medium*, Nano Lett. **6**, 866 (2006).

[Bre03a] K. Brendel, N. H. Nickel, P. Lengsfeld, A. Schöpke, I. Sieber, M. Nerding, H. P. Strunk, and W. Fuhs, *Excimer laser crystallization of amorphous silicon on metal coated glass substrates*, Thin Solid Films **427**, 86 (2003).

[Bre03b] K. Brendel, *Laserkristallisiertes polykristallines Silizium*, PhD Thesis, Philipps-Universität Marburg (2003).

[Bro59] R. Brout, *Sum rule for lattice vibrations in ionic crystals*, Phys. Rev. **113**, 43 (1959).

[Bro93] S. D. Brotherton, D. J. McCulloch, J. B. Clegg, and J. P. Gowers, *Excimer-laser-annealed poly-Si thin-film transistors*, IEEE Trans. Electron Devices **40**, 407 (1993).

[Bro99] S. D. Brotherton, J. R. Ayres, M. J. Edwards, C. A. Fisher, C. Glaister, J. P. Gowers, D. J. McCulloch, and M. Trainor, *Laser crystallised poly-Si TFTs for AMLCDs*, Thin Solid Films **37**, 188 (1999).

[Bro07] T. Bronger, R. Carius, *Carrier mobilities in microcrystalline silicon films*, Thin Solid Films **515**, 7486 (2007).

[Bru35] D. A. G. Bruggemann, *Berechnung verschiedener physikalischer Konstanten von heterogenen Substanzen - I. Dielektrizitätskonstanten und Leitfähigkeiten der Mischkörper aus isotropen Substanzen*, Ann. Phys. **416**, 636 (1935).

[Bru38] S. Brunauer, P. H. Emmett, and E. Teller, *Adsorption of gases in multimolecular layers*, J. Am. Chem. Soc. **60**, 309 (1938).

[Bru43] S. Brunauer, *The adsorption of gases and vapors, Vol. 1 Physical adsorption* (Princeton Univ. Press, Princeton, 1943).

[Bru94] L. Brus, *Luminescence of silicon materials: chains, sheets, nanocrystals, nanowires, microcrystals, and porous silicon*, J. Phys. Chem. **98**, 3575 (1994).

[Buc98] D. Búc, M. Zeman, and J. W. Metselaar, *Determination of optical properties of a-Si:H alloys*, Proceedings of the 43rd International Scientific Colloquium, Technische Universität Ilmenau, 494 (1998).

[Buf76] P. Buffat and J.-P. Borel, *Size effect on the melting temperature of gold particles*, Phys. Rev. A **13**, 2287 (1976).

[Bur97] T. A. Burr, A. A. Seraphin, E. Werwa, and K. D. Kolenbrander, *Carrier transport in thin films of silicon nanoparticles*, Phys. Rev. B **56**, 4818 (1997).

[Cam86] I. H. Campbell and P. M. Fauchet, *The effects of microcrystal size and shape on the one phonon Raman spectra of crystalline semiconductors*, Solid State Commun. **58**, 739 (1986).

[Can82] W. R. Cannon, S. C. Danforth, J. H. Flint, J. S. Haggerty, and R. A. Marra, *Sinterable ceramic powders from laser-driven reactions: I, Process description and modelling*, J. Am. Ceram. Soc. **65**, 324 (1982); W. R. Cannon, S. C. Danforth, J. H. Flint, J. S. Haggerty, and R. A. Marra, *Sinterable ceramic powders from laser-driven reactions: II, Powder characteristics and process variables*, J. Am. Ceram. Soc. **65**, 330 (1982).

[Can90] L. T. Canham, *Silicon quantum wire array fabrication by electrochemical and chemical dissolution of wafers*, Appl. Phys. Lett. **57**, 1045 (1990).

[Can05] G. Cantele, E. Degoli, E. Luppi, R. Magri, D. Ninno, G. Iadonisi, and S. Ossicini, *First-principles study of n- and p-doped silicon nanoclusters*, Phys. Rev. B **72**, 113303 (2005).

[Cer73] F. Cerdeira, T. A. Fjeldly, and M. Cardona, *Effect of free carriers on zone-center vibrational modes in heavily doped p-type Si. II. Optical modes,* Phys. Rev. B **8**, 4734 (1973).

[Cer74] F. Cerdeira, T. A. Fjeldly, and M. Cardona, *Raman study of the interaction between localized vibrations and electronic excitations in boron-doped silicon*, Phys. Rev. B **9**, 4344 (1974).

[Cha78] M. Chandrasekhar, J. B. Renucci, and M. Cardona, *Effects of interband transitions on Raman phonons in heavily doped n-Si*, Phys. Rev. B **17**, 1623 (1978).

[Cha80] M. Chandrasekhar, H. R. Chandrasekhar, M. Grimsditch, and M. Cardona, *Study of the localized vibrations of boron in heavily doped Si*, Phys. Rev. B **22**, 4825 (1980).

[Che06] Z. Chen, J. Appenzeller, Y.-M. Lin, J. Sippel-Oakley, A. G. Rinzler, J. Tang, S. J. Wind, P. M. Solomon, and P. Avouris, *An integrated logic circuit assembled on a single carbon nanotube*, Science **311**, 1735 (2006).

[Coa04] K. M. Coakley and M. D. McGehee, *Conjugated polymer photovoltaic cells*, Chem. Mater. **16**, 4533 (2004).

[Cof05] H. Coffin, C. Bonafos, S. Schamm, N. Cherkashin, M. Respaud, G. Ben-Assayag, P. Dimitrakis, P. Normand, M. Tencé, C. Colliex, and A. Claverie, *Oxidation of Si nanocrystals fabricated by ultra-low energy ion implantation in thin SiO_2 layers*, Mater. Res. Soc. Symp. Proc. **830**, D6.6.1 (2005).

[Cou77] P. R. Couchman and W. A. Jesser, *Thermodynamic theory of size dependence of melting temperature in metals*, Nature **269**, 481 (1977).

[Cul75] P. R. Cullis and J. R. Marko, *Electron paramagnetic resonance properties of n-type silicon in the intermediate impurity-concentration range*, Phys. Rev. B **11**, 4184 (1975).

[Dal06] G. M. Dalpian and J. R. Chelikowsky, *Self-purification in semiconductor nanocrystals*, Phys. Rev. Lett. **96**, 226802 (2006)

[Dan06] D. T. Danielson, D. K. Sparacin, J. Michel, and L. C. Kimerling, *Surface-energy-driven dewetting theory of silicon-on-insulator agglomeration*, J. Appl. Phys. **100**, 083507 (2006).

[Das55] W. C. Dash and R. Newman, *Intrinsic optical absorption in single-crystal germanium and silicon at 77°K and 300°K*, Phys. Rev. **99**, 1151 (1955).

[Das00] R. Dassow, J. R. Köhler, Y. Helen, K. Mourgues, O. Bonnaud, T. Mohammed-Brahim, and J. H. Werner, *Laser crystallization of silicon for high-performance thin-film transistors*, Semicond. Sci. Technol. **15**, L31 (2000).

[Del93] C. Delerue, G. Allan, and M. Lannoo, *Theoretical aspects of the luminescence of porous silicon*, Phys. Rev. B **48**, 11024 (1993).

[DeL96] D. M. de Leeuw, M. M. J. Simenon, A. R. Brown, and R. E. F. Einerhand, *Stability of n-type doped conducting polymers and consequences for polymeric microelectronic devices*, Synth. Met. **87**, 53 (1996).

[Dim02] C. D. Dimitrakopoulos and P. R. L. Malenfant, *Organic thin film transistors for large area electronics*, Adv. Mater. **14**, 99 (2002).

[Don83] E. P. Donovan, F. Spaepen, D. Turnbull, J. M. Poate, and D. C. Jacobson, *Heat of crystallization and melting point of amorphous silicon*, Appl. Phys. Lett. **42**, 698 (1983).

[Dor06] E. Dornel, J-C. Barbé, J. Eymery, and F. de Crécy, *Orientation-dependent dewetting of patterned thin Si film on SiO_2*, Mater. Res. Soc. Symp. Proc. **910**, A04-05 (2006).

[Dre07] M. S. Dresselhaus, G. Chen, M. Y. Tang, R. Yang, H. Lee, D. Wang, Z. Ren, J.-P. Fleurial, and P. Gogna, *New directions for low-dimensional thermoelectric materials*, Adv. Mater. **19**, 1 (2007).

[Dup08] Dupont™ Kapton® product information data sheet, available online at http://www2.dupont.com/Kapton/en_US/assets/downloads/pdf/summaryofprop.pdf (2008).

[Ebb07] A. Ebbers, private communication (2007).

[Ehb97] M. Ehbrecht, B. Kohn, F. Huisken, M. A. Laguna, and V. Paillard, *Photoluminescence and resonant Raman spectra of silicon films produced by size-selected cluster beam deposition*, Phys. Rev. B **56**, 6958 (1997).

[Eis02] C. Eisele, *Novel absorber structures for Si-based thin film solar cells*, PhD Thesis, Technische Universität München (2002).

[Erw05] S. C. Erwin, L. Zu, M. I. Haftel, A. L. Efros, T. A. Kennedy, and D. J. Norris, *Doping semiconductor nanocrystals*, Nature **436**, 91 (2005).

[ECB08] European Chemicals Bureau of the European Commission, *Council directive 67/548/EEC*, available online at http://ecb.jrc.it/classification-labelling/, zinc oxide substance classification listed at http://apps.kemi.se/nclass/SubstanceInfo.asp?id=31639 (2008).

[Fer06a] M. V. Fernández-Serra, C. Adessi, and X. Blase, *Surface segregation and backscattering in doped silicon nanowires*, Phys. Rev. Lett. **96**, 166805 (2006).

[Fer06b] M. V. Fernández-Serra, C. Adessi, and X. Blase, *Conductance, surface traps, and passivation in doped silicon nanowires*, Nano Lett. **6**, 2674 (2006).

[Fin06] K. Finkenzeller, *RFID Handbuch*, 4th Edition (Carl Hanser, München, 2006).

[Fon07] A. Fontcuberta i Morral, J. Arbiol, J. D. Prades, A. Cirera, and J. R. Morante, *Synthesis of silicon nanowires with wurtzite crystalline structure by using standard chemical vapor deposition*, Adv. Mater. **19**, 1347 (2007).

[Fri92] E. Friess, J. Nützel, and G. Abstreiter, *Phosphorus doping in low temperature silicon molecular beam epitaxy*, Appl. Phys. Lett. **60**, 2237 (1992).

[Fri94] S. K. Friedlander and M. K. Wu, *Linear rate law for the decay rate of the excess surface area of a coalescing solid particle*, Phys. Rev. B **49**, 3622 (1994).

[Fri04] S. E. Fritz, S. M. Martin, C. D. Frisbie, M. D. Ward, and M. F. Toney, *Structural characterization of a pentacene monolayer on an amorphous SiO_2 substrate with grazing incidence X-ray diffraction*, J. Am. Chem. Soc. **126**, 4084 (2004).

[Fri71] H. Fritzsche, *Optical and electrical energy gaps in amorphous semiconductors*, J. Non-Cryst. Solids **6**, 49 (1971).

[Fuj96] M. Fujii and Y. Kanzawa, S. Hayashi, and K. Yamamoto, *Raman scattering from acoustic phonons confined in Si nanocrystals*, Phys. Rev. B **54**, R8373 (1996).

[Fuj02] M. Fujii, A. Mimura, and S. Hayashi, Y. Yamamoto, and K. Murakami, *Hyperfine structure of the electron spin resonance of phosphorus-doped Si nanocrystals*, Phys. Rev. Lett. **89**, 206805-1 (2002).

[Fuj04] M. Fujii, Y. Yamaguchi, Y. Takase, K. Ninomiya, and S. Hayashi, *Control of photoluminescence properties of Si nanocrystals by simultaneously doping n- and p-type impurities*, Appl. Phys. Lett. **85**, 1158 (2004).

[Fuj05] M. Fujii, Y. Yamaguchi, Y. Takase, K. Ninomiya, and S. Hayashi, *Photoluminescence from impurity codoped and compensated Si nanocrystals*, Appl. Phys. Lett. **87**, 211919 (2005).

[Fuj06] H. Fujii, T. Matsumoto, S. Izutani, S. Kiguchi, and K. Nogi, *Surface tension of molten silicon measured by microgravity oscillating drop method and improved sessile drop method*, Acta Materialia **54**, 1221 (2006).

[Fuk06] N. Fukata, J. Chen, T. Sekiguchi, N. Okada, K. Murakami, T. Tsurui, and S. Ito, *Doping and hydrogen passivation of boron in silicon nanowires synthesized by laser ablation*, Appl. Phys. Lett. **89**, 203109 (2006).

[Fur88] S. Furukawa and T. Miyasato, *Quantum size effect on the optical band gap of microcrystalline Si:H*, Phys. Rev. B **38**, 5726 (1988).

[Gal02] S. Gall, M. Muske, I. Sieber, O. Nast, and W. Fuhs, *Aluminum-induced crystallization of amorphous silicon*, J. Non-Cryst. Solids **299–302**, 741 (2002).

[Geb55] T. H. Geballe and G. W. Hull, *Seebeck effect in silicon*, Phys. Rev. **98**, 940 (1955).

[Ges97] G. Gesele, J. Linsmeier, V. Drach, J. Fricke, and R. Arens-Fischer, *Temperature-dependent thermal conductivity of porous silicon*, J. Phys. D **30**, 2911 (1997).

[Gju04] M. Gjukic, M. Buschbeck, R. Lechner, and M. Stutzmann, *Aluminum-induced crystallization of amorphous silicon–germanium thin films*, Appl. Phys. Lett. **85**, 2134 (2004).

[Gju05] M. Gjukic, R. Lechner, M. Buschbeck, and M. Stutzmann, *Optical and electrical properties of polycrystalline silicon–germanium thin films prepared by aluminum-induced layer exchange*, Appl. Phys. Lett. **86**, 062115 (2005).

[Gju07] M. Gjukic, *Metal-induced crystallization of silicon–germanium alloys*, PhD thesis, Technische Universität München (2007).

[Gog99] Y. Gogotsi, C. Baek, and F. Kirscht, *Raman microspectroscopy study of processing-induced phase transformations and residual stress in silicon*, Semicond. Sci. Technol. **14,** 936 (1999).

[Gol96] A. N. Goldstein, *The melting of silicon nanocrystals: Submicron thin-film structures derived from nanocrystal precursors*, Appl. Phys. A **62**, 33 (1996).

[Gra76] C. G. Granqvist and R. A. Buhrman, *Ultrafine metal particles*, J. Appl. Phys. **47**, 2200 (1976).

[Hay90] S. Hayashi, S. Tanimoto, and K. Yamamoto, *Analysis of surface oxides of gas-evaporated Si small particles with infrared spectroscopy, high-resolution electron microscopy, and x-ray photoelectron spectroscopy*, J. Appl. Phys. **68**, 5300 (1990).

[Hay96] S. Hayashi and K. Yamamoto, *Optical properties of Si-rich SiO_2 films in relation with embedded mesoscopic particles*, J. Luminescence **70**, 352 (1996).

[Haq94] M. S. Haque, H. A. Naseem, and W. D. Brown, *Interaction of aluminum with hydrogenated amorphous silicon at low temperatures*, J. Appl. Phys. **75**, 3928 (1994).

[Hau82] D. Hauschildt, W. Fuhs, and H. Mell, *Optically induced potential fluctuations in a-Si:H films*, phys. stat. sol. (b) **111**, 171 (1982).

[Hea92] J. R. Heath, *A liquid-solution-phase synthesis of crystalline silicon*, Science **258**, 1131 (1992).

[Hei92] J. L. Heinrich, C. L. Curtis, G. M. Credo, K. L. Kavanagh, and M. J. Sailor, *Luminescent colloidal silicon suspensions from porous silicon*, Science **255**, 66 (1992).

[Her50] C. Herring, *Effect of change of scale on sintering phenomena*, J. Appl. Phys. **21**, 301 (1950).

[Her72] S. R. Herd, P. Chaudhari, and M. H. Brodsky, *Metal contact induced crystallization in films of amorphous silicon and germanium*, J. Non-Cryst. Solids **7**, 309 (1972).

[Hes07] C. M. Hessel, M. A. Summers, A. Meldrum, M. Malac, and J. G. C. Veinot, *Direct patterning, conformal coating, and erbium doping of luminescent nc-Si/SiO2 thin films from solution processable hydrogen silsesquioxane*, Adv. Mater. **19**, 3513 (2007).

[Hoc08] A. I. Hochbaum, R. Chen, R. Diaz Delgado, W. Liang, E. C. Garnett, M. Najarian, A. Majumdar, and & P. Yang, *Enhanced thermoelectric performance of rough silicon nanowires*, Nature **451**, 163 (2008).

[HuW04] X. Hu, G. Wang, W. Wu, P. Jiang, and J. Zi, *The vibrational density of states and specific heat of Si nanocrystals*, J. Phys.: Condens. Matter **13**, L835 (2001).

[ImK93] J. S. Im, H. J. Kim, and M. O. Thompson, *Phase transformation mechanisms involved in excimer laser crystallization of amorphous silicon films*, Appl. Phys. Lett. **63**, 1969 (1993).

[Iof57] A. F. Ioffe, *Semiconductor thermoelements and thermoelectric cooling* (Infosearch, London, 1957).

[Iof08] Ioffe Physico-Technical Institute Electronic Archive: *New semiconductor materials. Characteristics and properties*, available online at: http://www.ioffe.ru/SVA/NSM/ (2008).

[Ior07] F. Iori, E. Degoli, R. Magri, I. Marri, G. Cantele, D. Ninno, F. Trani, O. Pulci, and S. Ossicini, *Engineering silicon nanocrystals: Theoretical study of the effect of codoping with boron and phosphorus*, Phys. Rev. B **76**, 085302 (2007).

[Iqb79] Z. Iqbal, A. P. Webb, and S. Vepřek, *Polycrystalline silicon films deposited in a glow discharge at temperatures below* 250 °C, Appl. Phys. Lett. **36**, 163 (1980).

[Iqb82] Z. Iqbal and S. Vepřek, *Raman scattering from hydrogenated microcrystalline and amorphous silicon*, J. Phys. C: Solid State Phys. **15**, 377 (1982).

[Ish96] Y. Ishikawa, N. Shibata, and S. Fukatsu, *Fabrication of highly oriented Si:SiO_2 nanoparticles using low energy oxygen ion implantation during Si molecular beam epitaxy*, Appl. Phys. Lett. **68**, 2249 (1996).

[Isl05] M. N. Islam, A. Pradhan, and S. Kumar, *Effects of crystallite size distribution on the Raman scattering profiles of Si nanostructures*, J. Appl. Phys. **98**, 024309 (2005).

[Jac63] R. J. Jaccodine, *Surface energy of germanium and silicon*, J. Electrochem. Soc. **110**, 524 (1963)

[Jae08] C. Jaeger, T. Antesberger, and M. Stutzmann, *Hydrogen passivation of ultra-thin low-temperature polycrystalline silicon films for electronic applications*, J. Non-Cryst. Solids **354**, 2314 (2008).

[Joh69] D. L. Johnson, *New method of obtaining volume, grain-boundary, and surface diffusion coefficients from sintering data*, J. Appl. Phys. **40**, 192 (1969).

[Joh78] J. S. Johannessen, W. E. Spicer, J. F. Gibbons, N. J. Taylor, and J. D. Plummer, *Observation of phosphorus pile-up at the SiO_2-Si interface*, J. Appl. Phys. **49**, 4453 (1978).

[Joh83] N. M. Johnson, D. K. Biegelsen, M. D. Moyer, S. T. Chang, E. H. Poindexter, and P. J. Caplan, *Characteristic electronic defects at the Si-SiO_2 interface*, Appl. Phys. Lett. **43**, 563 (1983).

[Kam71] T. I. Kamins, *Hall mobility in chemically deposited polycrystalline silicon*, J. Appl. Phys. **42**, 4357 (1971).

[Kan93] Y. Kanemitsu, H. Uto, Y. Masumoto, T. Matsumoto, T. Futagi, and H. Mimura, *Microstructure and optical properties of free-standing porous silicon films: Size dependence of absorption spectra in Si nanometer-sized crystallites*, Phys. Rev. B **48**, 2827 (1993).

[Kel03] T. W. Kelley, D. V. Muyres, P. F. Baude, T. P. Smith, and T. D. Jones, *High performance organic thin film transistors*, Mater. Res. Soc. Symp. Proc. **771**, 169 L6.5 (2003).

[Kha04] M. A. H. Khalafalla, H. Mizuta, and Z. A. K. Durrani, *Coherent states in a coupled quantum dot nanocrystalline silicon transistor*, Appl. Phys. Lett. **85**, 2262 (2004).

[Kim96] J. H. Kim and J. Y. Lee, *Al-induced crystallization of an amorphous Si thin film in a polycrystalline Al/native SiO_2/amorphous Si structure*, Jpn. J. Appl. Phys., **35**, 2052 (1996).

[Kim01] H. Kim, T. Spila, and J. E. Greene, *Si (113) hydrogen desorption kinetics: a temperature programmed desorption study*, Surf. Sci. **490**, L602 (2001).

[Kir88] C. T. Kirk, *Quantitative analysis of the effect of disorder-induced mode coupling on infrared absorption in silica*, Phys. Rev. B **38**, 1255 (1988).

[Kni04] J. Knipping, H. Wiggers, B. Rellinghaus, P. Roth, D. Konjhodzic, and C. Meier, *Synthesis of high purity silicon nanoparticles in a low pressure microwave reactor*, J. Nanosci. Nanotech. **4**, 1039 (2004).

[Kob73] R. J. Kobliska and S. A. Solin, *Raman spectrum of wurtzite silicon*, Phys.Rev. B **8**, 3799 (1973).

[Kon92] T. J. Konno and R. Sinclair, *Crystallization of silicon in aluminium/amorphous-silicon multilayers*, Phil. Mag. B **66**, 749 (1992).

[Kon06] G. Konstantatos, I. Howard, A. Fischer, S. Hoogland, J. Clifford, E. Klem, L. Levina, and E. H. Sargent, *Ultrasensitive solution-cast quantum dot photodetectors*, Nature **442**, 180 (2006).

[Kor98] B. A. Korgel and D. Fitzmaurice, *Condensation of ordered nanocrystal thin films*, Phys. Rev. Lett. **80**, 3531 (1998).

[Kov96] D. Kovalev, G. Polisski, M. Ben-Chorin, J. Diener, and F. Koch, The temperature dependence of the absorption coefficient of porous silicon, J. Appl. Phys. **80**, 5978 (1996).

[Koy06] S. Koynov, M. S. Brandt, and M. Stutzmann, *Black nonreflecting silicon surfaces for solar cells*, Appl. Phys. Lett. **88**, 203107 (2006).

[Kri86] S. Krishnamurthy and A. Sher, *Band structures of* Si_xGe_{1-x} *alloys*, Phys. Rev. B **33**, 1026 (1986).

[Lau89] F. Lau, L. Mader, C. Mazure, Ch. Werner, and M. Orlowski, *A model for phosphorus segregation at the silicon-silicon dioxide interface*, Appl. Phys. A **49**, 671 (1989).

[Lec03] R. Lechner, *Optical and electronic properties of crystallized silicon-germanium thin-films for photovoltaic applications*, Diploma Thesis, Technische Universität München (2003).

[Lec05] R. Lechner, M. Gjukic, and M. Stutzmann (*inventors*), *Siliziumpulver enthaltende Dispersion und Verfahren zur Beschichtung*, German patent application DE 102005446A1, Degussa AG (*applicant*), disclosure date 16.11.2006 (2005).

[Led00] G. Ledoux, O. Guillois, D. Porterat, C. Reynaud, F. Huisken, B. Kohn, and V. Paillard, *Photoluminescence properties of silicon nanocrystals as a function of their size*, Phys. Rev. B **62**, 15942 (2000).

[Len00] P. Lengsfeld, N. H. Nickel, and W. Fuhs, *Step-by-step excimer laser induced crystallization of a-Si:H*, Appl. Phys. Lett. **76**, 1680 (2000).

[Len02] P. Lengsfeld, N. H. Nickel, Ch. Genzel, and W. Fuhs, *Stress in undoped and doped laser crystallized poly-Si*, J. Appl. Phys. **91**, 9128 (2002).

[Len03] P. Lengsfeld, S. Brehme, K. Brendel, Ch. Genzel, and N. H. Nickel, *Raman spectroscopy of heavily doped polycrystalline and microcrystalline silicon*, phys. stat. sol. (b) **235**, 170 (2003).

[Li99] B. Li, D. Yu, and S.-L. Zhang, *Raman spectral study of silicon nanowires*, Phys. Rev. B **59**, 1645 (1999).

[Lin00] E. K. Lindmark, J. J. Nowak, and M. T. Kief, *In situ ellipsometric measurements of thin-film aluminum oxidation*, Proceedings of SPIE **4099**, 218 (2000).

[Lor98] C. D. Lorenz, R. May, and R. M. Ziff, *Universality of the excess number of clusters and the crossing probability function in three-dimensional percolation*, J. Stat. Phys. **98**, 961 (2000).

[Luc83] G. Lucovsky, J. Yang, S. S. Chao, J. E. Tyler, and W. Czubatyj, *Oxygen-bonding environments in glow-discharge-deposited amorphous silicon-hydrogen alloy films*, Phys. Rev. B **28**, 3225 (1983).

[Lys99] V. Lysenko, S. Perichon, B. Remaki, B. Champagnon, and D. Barbier, *Thermal conductivity of thick meso-porous silicon layers by micro-Raman scattering*, J. Appl. Phys. **86**, 6841 (1999).

[Mad84] O. Madelung, M. Schulz, and H. Weiss, *Landolt-Börnstein: Zahlenwerte und Funktionen aus Naturwissenschaften und Technik, Neue Serie*, Gruppe III Band **17c** (Springer, Berlin, 1984).

[Maj79] G. Majni and G. Ottaviani, *Growth kinetics of ⟨111⟩ Si through an Al layer by solid phase epitaxy*, J. Cryst. Growth **46**, 119 (1979).

[Man05] L. Mangolini, E. Thimsen, and U. Kortshagen, *High-yield plasma synthesis of luminescent silicon nanocrystals*, Nano Lett.**5**, 655 (2005).

[Man07] L. Mangolini and U. Kortshagen, *Plasma-assisted synthesis of silicon nanocrystal inks*, Adv. Mater. **19**, 2513 (2007).

[Mar72] S. Margalit, A. Neugroschel, and A. Bar-Lev, *Redistribution of boron and phosphorus in silicon after two oxidation steps used in MOST fabrication*, IEEE Trans. Electron. Dev. **19**, 861 (1972).

[Mas83] G. Masetti, M. Severi, and S. Solmi, *Modeling of carrier mobility against carrier concentration in arsenic-, phosphorus-, and boron-doped silicon*, IEEE Trans. Electron. Dev. **30**, 764 (1983).

[McC71] J. O. McCaldin and H. Sankur, *Diffusivity and solubility of Si in the Al metallization of integrated circuits*, Appl. Phys. Lett. **19**, 524 (1971).

[McC06] I. McCulloch, M. Heeney, C. Bailey, K. Genevicius, I. Macdonald, M. Shkunov, D. Sparrowe, S. Tierney, R. Wagner, W. M. Zhang, M. L. Chabinyc, R. J. Kline, M. D. McGehee, and M. F. Toney, *Liquid-crystalline semiconducting polymers with high charge-carrier mobility*, Nat. Mater. **5**, 328 (2006).

[Mei94] P. Mei, J. B. Boyce, M. Hack, R. A. Lujan, R. I. Johnson, G. B. Anderson, D. K. Fork, and S. E. Ready, *Laser dehydrogenation/crystallization of plasma-enhanced chemical vapor deposited amorphous silicon for hybrid thin film transistors*, Appl. Phys. Lett. **64**, 1132 (1994).

[Mei07] C. Meier, A. Gondorf, S. Lüttjohann, H. Wiggers, and A. Lorke, *Silicon nanoparticles: Absorption, emission, and the nature of the electronic bandgap*, J. Appl. Phys. **101**, 103112 (2007).

[Mel04a] D. V. Melnikov and J. R. Chelikowsky, *Quantum confinement in phosphorus-doped silicon nanocrystals*, Phys. Rev. Lett. **92**, 046802 (2004).

[Mel04b] D. V. Melnikov and J. R. Chelikowsky, *Electron affinities and ionization energies in Si and Ge nanocrystals*, Phys. Rev. B **69**, 113305 (2004).

[Meu98] E. A. Meulenkamp, *Synthesis and Growth of ZnO Nanoparticles*, J. Phys. Chem. B **102**, 5566 (1998).

[Mey78] D. Meyerhofer *Characteristics of resist films produced by spinning*, J. Appl. Phys. **49**, 3993 (1978).

[Mim00] A. Mimura, M. Fujii, S. Hayashi, D. Kovalev, and F. Koch, *Photoluminescence and free-electron absorption in heavily phosphorus-doped Si nanocrystals*, Phys. Rev. B **62**, 12625 (2000).

[Mor54] F. J. Morin and J. P. Majta, *Electrical properties of silicon containing arsenic and boron*, Phys. Rev. **96**, 28 (1954).

[Mue04] D. C. Müller, *Deactivation and activation of donors in silicon*, PhD Thesis, Eidgenössische Technische Hochschule Zürich (2004).

[Mur90] J. L. Murray and A. J. McAlister, in: *Binary Alloy Phase Diagrams*, T. B. Massalski (ed.), p. 211 (ASM International, Materials Park, Ohio, 1990).

[Nas98] O. Nast, T. Puzzer, L. M. Koschier, A. B. Sproul, and S. R. Wenham, *Aluminum-induced crystallization of amorphous silicon on glass substrates above and below the eutectic temperature*, Appl. Phys. Lett. **73**, 3214 (1998).

[Nas00a] O. Nast and S. R. Wenham, *Elucidation of the layer exchange mechanism in the formation of polycrystalline silicon by aluminum-induced crystallization*, J. Appl. Phys. **88**, 124 (2000).

[Nas00b] O. Nast and A. J. Hartmann, *Influence of interface and Al structure on layer exchange during aluminum-induced crystallization of amorphous silicon*, J. Appl. Phys. **88**, 716 (2000).

[Nas00c] O. Nast, *The aluminum-induced layer exchange forming polycrystalline silicon on glass for thin-film solar cells*, PhD Thesis, Fachbereich Physik, Philipps-Universität Marburg (2000).

[Nic00] N. H. Nickel, P. Lengsfeld, and I. Sieber, *Raman spectroscopy of heavily doped polycrystalline silicon thin films*, Phys. Rev. B **61**, 15558 (2000).

[Nis02] K. Nishiguchi, X. Zhao, and S. Oda, *Nanocrystalline silicon electron emitter with a high efficiency enhanced by a planarization technique*, J. Appl. Phys. **92**, 2748 (2002).

[Non92] M. Nonnenmacher and H. K. Wickramasinghe, *Scanning probe microscopy of thermal conductivity and subsurface properties*, Appl. Phys. Lett. **61**, 168 (1992).

[Nüt96] J. F. Nützel and G. Abstreiter, *Segregation and diffusion on semiconductor surfaces*, Phys. Rev. B **53**, 13551 (1996).

[Ort80] J. W. Orton and M. J. Powell, *The Hall effect in polycrystalline and powdered semiconductors*, Rep. Prog. Phys. **43**, 1263 (1980).

[Ota04] M. Otake, K. Sato, O. Sugiyama, and S. Kaneko, *Pulse-current sintering and thermoelectric properties of gas-atomized silicon-germanium powders*, Solid State Ionics **172**, 523 (2004).

[Ott74] G. Ottaviani, D. Sigurd, V. Marello, J. W. Mayer, and J. O. McCaldin, *Crystallization of Ge and Si in metal films. I*, J. Appl. Phys. **45**, 1730 (1974).

[Ove81] H. Overhof and W. Beyer, *A model for the electronic transport in hydrogenated amorphous silicon*, Phil. Mag. B **43**, 433 (1981).

[Ove89] H. Overhof and P. Thomas, *Electronic transport in hydrogenated amorphous semiconductors* (Springer, Berlin, 1989).

[Pab77] S. K. Pabi, *On the variation of interface composition around a dissolving precipitate*, phys. stat. sol. (a) **80**, 305 (1983).

[Pai99] V. Paillard, P. Puech, M. A. Laguna, R. Carles, B. Kohn, and F. Huisken, *Improved one-phonon confinement model for an accurate size determination of silicon nanocrystals*, J. Appl. Phys. **86**, 1921 (1999).

[Pan75] J. I. Pankove, *Optical processes in semiconductors* (Dover, New York, 1975).

[Pan84] J. I. Pankove, R. O. Wance, and J. E. Berkeyheiser, *Neutralization of acceptors in silicon by atomic hydrogen*, Appl. Phys. Lett. **45**, 1100 (1984).

[Pav00] L. Pavesi, L. Dal Negro, C. Mazzoleni, G. Franzo, and F. Priolo, *Optical gain in silicon nanocrystal*s, Nature **408**, 440 (2000).

[Pea49] G. L. Pearson and J. Bardeen, *Electrical properties of pure silicon and silicon alloys containing boron and phosphorus*, Phys. Rev. **75**, 865 (1949).

[Pen96] C. Peng, K. D. Hirschman, and P. M. Fauchet, *Carrier transport in porous silicon light-emitting devices*, J. Appl. Phys. **80**, 295 (1996).

[Pet05] F.-M. Petrat, unpublished talk held at the 1st Degussa Summer School *"Science-to-Business Nanotronics"*, in Marl, Germany, August 29-30 (2005).

[Per99] S. Périchon, V. Lysenko, B. Remaki, B. Champagnon, and D. Barbier, *Measurement of porous silicon thermal conductivity by micro-Raman scattering*, J. Appl. Phys. **86**, 4700 (1999).

[Per08] R. N. Pereira, A. R. Stegner, K. Klein, H. Wiggers, M. S. Brandt, and M. Stutzmann, *Size dependence of the hyperfine splitting in phosphorus-doped silicon nanocrystals*, to be submitted (2008).

[Phi67] H. R. Philipp and H. Ehrenreich, *Ultraviolet optical properties - optical properties of III-V compounds*, Semiconductors and Semimetals **3**, 93 (Academic, New York, 1967).

[Pih04] E. Pihan, A. Slaoui, P. Roca i Cabarrocas, A. Focsa, *Polycrystalline silicon films by aluminium-induced crystallisation: growth process vs. silicon deposition method*, Thin Solid Films **451 – 452**, 328 (2004).

[Pik79] G. E. Pike and C. H. Seager, *The dc voltage dependence of semiconductor grain-boundary resistance*, J. Appl. Phys. **50**, 3414 (1979).

[Pod04] V. Podzorov, E. Menard, A. Borissov, V. Kiryukhin, J. A. Rogers, and M. E. Gershenson, *Intrinsic charge transport on the surface of organic semiconductors*, Phys. Rev. Lett. **93**, 086602 (2004).

[Pod05] V. Podzorov, E. Menard, J. A. Rogers, and M. E. Gershenson, *Hall effect in the accumulation layers on the surface of organic semiconductors*, Phys. Rev. Lett. **95**, 226601 (2005).

[Qin82] H. Qingheng, E. S. Yang, and H. Izmirliyan, *Diffusivity and growth rate of silicon in solid-phase epitaxy with an aluminium medium*, Solid-State Electronics **25**, 1187 (1982).

[Qin05] J. Qin, F. Xue, L. Huang, Y. L. Fan, X. J. Yang, Z. M. Jiang, Q. J. Jia, and X. M. Jiang, *Investigation of phosphorus surface segregation by X-ray scattering measurements*, Surf. Sci. **580**, 51 (2005).

[Rad91] G. Radnoczi, A. Robertsson, H. T. G. Hentzell, S. F. Gong, and M.-A. Hasan, *Al induced crystallization of a-Si*, J. Appl. Phys. **69**, 6394 (1991).

[Raf05] M. A. Rafiq, Y. Tsuchiya, H. Mizuta, S. Oda, S. Uno, Z. A. K. Durrani, and W. I. Milne, *Charge injection and trapping in silicon nanocrystals*, Appl. Phys. Lett. **87**, 182101 (2005).

[Raf06] M. A. Rafiq, Y. Tsuchiya, H. Mizuta, S. Oda, S. Uno, Z. A. K. Durrani, and W. I. Milne, *Hopping conduction in size-controlled Si nanocrystals*, J. Appl. Phys. **100**, 014303 (2006).

[Ram05] L. E. Ramos, H.-Ch. Weissker, J. Furthmüller, and F. Bechstedt, *Optical properties of Si and Ge nanocrystals: Parameter-free calculations*, phys. stat. sol. (b) **242**, 2977 (2005).

[Raz98] T. Raz, F. Edelman, and Y. Komem, M. Stölzer, and P. Zaumseil, *Transport properties of boron-doped crystallized amorphous $Si_{1-x}Ge_x$ films*, J. Appl. Phys. **84**, 4343 (1998).

[Rei07] A. Reindl, S. Aldabergenova, E. Altin, G. Frank, and W. Peukert, *Dispersing silicon nanoparticles in a stirred media mill – investigating the evolution of morphology, structure and oxide formation*, phys. stat. sol. (a) **204**, 2329 (2007).

[Ric81] H. Richter, Z. P. Wang, and L. Ley, *The one phonon Raman spectrum in microcrystalline silicon*, Solid State Commun. **39**, 625 (1981).

[Rid99] B. A. Ridley, B. Nivi, and J. M. Jacobson, *All-Inorganic Field Effect Transistors Fabricated by Printing*, Science **286**, 746 (1999).

[Rog01] J. A. Rogers, *Toward paperlike displays*, Science **291**, 1502 (2001).

[Ruf99] D. Ruff, *Elektrischer Transport in mikrokristallinem Silizium*, PhD Thesis, Philipps-Universität Marburg (1999).

[Sal07] A. Salleo, *Charge transport in polymeric transistors*, Materials Today **10**, 38 (2007).

[Sar85] A. K. Sarychev, A. P. Vinogradoff, and A. M. Karimov, *Calculation of percolation conductivity in 3D*, J. Phys. C: Solid State Phys. **18**, L105 (1985).

[Sar06] A. Sarikov, J. Schneider, M. Muske, S. Gall, W. Fuhs, *Theoretical study of the kinetics of grain nucleation in the aluminium-induced layer-exchange process*, J. Non-Cryst. Solids **352**, 980 (2006).

[Saz04] A. Sazonov and C. McArthur, *Sub-100°C a-Si:H thin-film transistors on plastic substrates with silicon nitride gate dielectrics*, J. Vac. Sci. Technol. A **22**, 2052 (2004).

[Sch70] H. Scher and R. Zallen, *Critical density in percolation processes*, J. Chem. Phys. **53**, 3759 (1970).

[Sch81] P. E. Schmid, *Optical absorption in heavily doped silicon*, Phys. Rev. B **23**, 5531 (1981).

[Sch00] F. Schwabl, *Statistische Mechanik* (Springer, Berlin, 2000).

[Sch05] J. Schneider, J. Klein, A. Sarikov, M. Muske, S. Gall, and W. Fuhs, *Suppression of nucleation during the aluminum-induced layer exchange process*, Mater. Res. Soc. Symp. Proc. **862**, A2.2.1 (2005).

[Sch06] H. Scheel, S. Reich, A. C. Ferrari, M. Cantoro, A. Colli, and C. Thomsen, *Raman scattering on silicon nanowires: The thermal conductivity determines the optical phonon frequency*, Appl. Phys. Lett. **88**, 233114 (2006).

[Sch08] G. Schierning, R. Theissmann, H. Wiggers, D. Sudfeld, A. Ebbers, D. Franke, V. T. Witusiewicz, and M. Apel, *Microcrystalline silicon formation by silicon nanoparticles*, J. Appl. Phys. **103**, 084305 (2008).

[Sea79] C. H. Seager, G. E. Pike, and D. S. Ginley, *Direct measurement of electron emission from defect states at silicon grain boundaries*, Phys. Rev. Lett. **43**, 532 (1979).

[Set75] J. Y. W. Seto, *The electrical properties of polycrystalline silicon films*, J. Appl. Phys. **46**, 5247 (1975).

[Sha05] I. D. Sharp, D. O. Yi, Q. Xu, C. Y. Liao, J. W. Beeman, Z. Liliental-Weber, K. M. Yu, D. N. Zakharov, J. W. Ager III, D. C. Chrzan, and E. E. Haller, *Mechanism of stress relaxation in Ge nanocrystals embedded in* SiO_2, Appl. Phys. Lett. **86**, 063107 (2005).

[She04] Z. Shen, T. Kim, U. Kortshagen, P. H. McMurry, and S. A. Campbell, *Formation of highly uniform silicon nanoparticles in high density silane plasmas*, J. Appl. Phys. **94**, 2277 (2004).

[Shi04] T. Shimizu-Iwayama, N. Kurumado, D. E. Hole, and P. D. Townsend, *Optical properties of silicon nanoclusters fabricated by ion implantation*, J. Appl. Phys. **83**, 6018 (1998).

[Sim81] E. Šimánek, *The temperature dependence of the electrical resistivity of granular metals*, Solid State Commun. **40**, 1021 (1981).

[Sim95] A. W. Simonian, A. B. Sproul, Z. Shi, and E. Gauja, *Observation of Fano resonance in heavily doped p-type silicon at room temperature*, Phys. Rev. B **52**, 5672 (1995).

[Sir99] H. Sirringhaus, P. J. Brown, R. H. Friend, M. M. Nielsen, K. Bechgaard, B. M. W. Langeveld-Voss, A. J. H. Spiering, R. A. J. Janssen, E. W. Meijer, P. Herwig, and D. M. de Leeuw, *Two-dimensional charge transport in self-organized, high-mobility conjugated polymers*, Nature **401**, 685 (1999).

[Sny08] G. J. Snyder and E. S. Toberer, *Complex thermoelectric materials*, Nat. Mater. **7**, 105 (2008).

[Spa74] F. Spaepen, *On the configurational entropy of amorphous Si and Ge*, Phil. Mag. **30**, 417 (1974).

[Spi98] C. Spinella, S. Lombardo, and F. Priolo, *Crystal grain nucleation in amorphous silicon*, J. Appl. Phys. **84**, 5383 (1998).

[Sta88] M. Stavola, S. J. Pearton, J. Lopata, and W. C. Dautremont-Smith, *Vibrational spectroscopy of acceptor-hydrogen complexes in silicon: Evidence for low-frequency excitations*, Phys. Rev. B **37**, 8313 (1988).

[Ste07] A. R. Stegner, R. N. Pereira, K. Klein, H. Wiggers, M. S. Brandt, and M. Stutzmann, *Phosphorus doping of silicon nanocrystals: Interface defects and charge compensation*, Physica B **401**, 541 (2007).

[Ste08a] A. R. Stegner, R. N. Pereira, K. Klein, R. Lechner, R. Dietmueller, M. S. Brandt, H. Wiggers, and M. Stutzmann, *Electronic transport in phosphorus-doped silicon nanocrystal networks*, Phys. Rev. Lett. **100**, 026803 (2008).

[Ste08b] A. R. Stegner, R.N. Pereira, K. Klein, M. S. Brandt, H. Wiggers, and M. Stutzmann, unpublished (2008).

[Stu87a] M. Stutzmann, *Hydrogen passivation of boron acceptors in silicon: Raman studies*, Phys. Rev. B **35**, 5921 (1987).

[Stu87b] M. Stutzmann, *On the structure of dangling bond defects in silicon*, Z. Phys. Chem. **151**, 211 (1987).

[Stu91] M. Stutzmann, J.-B. Chevrier, C. P. Herrero, and A. Breitschwerdt, *A comparison of hydrogen incorporation and effusion in doped crystalline silicon, germanium, and gallium arsenide*, Appl. Phys. A **53**, 47 (1991).

[Stu94] M. Stutzmann, *Amorphous semiconductors*, in: *Handbook on semiconductors*, edited by T. S. Moss, Vol. **3**, Elsevier (Amsterdam, Netherlands, 1994).

[Sun07] Y. Sun and J. A. Rogers, *Inorganic semiconductors for flexible electronics*, Adv. Mater. **19**, 1897 (2007).

[Swa84] R. Swanepoel, *Determination of surface roughness and optical constants of inhomogeneous amorphous silicon films*, J. Phys. E: Sci. Instrum. **17**, 896 (1984).

[Sze07] S. M. Sze and K. K. Ng, *Physics of semiconductor devices*, 3rd Edition (Wiley & Sons, Hoboken, New Jersey 2007).

[Tal05] D. Talapin and C. B. Murray, *PbSe nanocrystal solids for n- and p-channel thin film field-effect transistors*, Science **310**, 86 (2005).

[Tan80] M. Taniguchi, M. Hirose, Y. Osaka, S. Hasegawa, and T. Shimizu, *Current transport in doped polycrystalline silicon*, Jap. J. Appl. Phys. **19**, 665 (1980).

[Tan06] Y. W. Tang, J. Wang, and X. C. Zeng, *Molecular simulations of solid-liquid interfacial tension of silicon*, J. Chem. Phys. **124**, 236103 (2006).

[Tay52] W. E. Taylor, N. H. Odell, and H. Y. Fan, *Grain boundary barriers in germanium*, Phys. Rev. **88**, 867 (1952).

[The97] W. Theiß, *Optical properties of porous silicon*, Surf. Sci. Rep. **29**, 91 (1997).

[Tru60] F. A. Trumbore, *Solid solubilities of impurity elements in germanium and silicon*, Bell System Technical Journal **39**, 205 (1960).

[Tsa81] B. Y. Tsaur, G. W. Turner, and J. C. C. Fan, *Efficient Si solar cells by low-temperature solid-phase epitaxy,* Appl. Phys. Lett. **39**, 749 (1981).

[Tsu82] R. Tsu and J. G. Hernandez, Appl. Phys. Lett. **41**, 1016 (1982).

[Tub73] R. Tubino, L. Piseri, and G. Zerbi, *Lattice dynamics and spectroscopic properties by a valent force potential of diamondlike crystals: C, Si, Ge, and Sn*, J. Chem. Phys. **56**, 1022 (1972).

[Van58] L. J. van der Pauw, *A method of measuring specific resistivity and hall effect of discs of arbitrary shape*, Philips Res. Reports **13**, 1 (1958).

[Vin91] C. B. Vining, W. Laskow, J. O. Hanson, R. R. Van der Beck, and P. D. Gorsuch, *Thermoelectric properties of pressure-sintered $Si_{0.8}Ge_{0.2}$ thermoelectric alloys*, J. Appl. Phys. **69**, 4333 (1991).

[Wan07] W. Wang, J. Shi, W. Jiang, S. Guo, H. Zhang, B. Quan, and D. Ma, *High-mobility pentacene thin-film transistors with copolymer-gate dielectric,* Microelectronics Journal **38**, 27 (2007).

[Wau91] M. Wautelet, *Estimation of the variation of the melting temperature with the size of small particles, on the basis of a surface-phonon instability model*, J. Phys. D: Appl. Phys. **24**, 343 (1991).

[Web77] W. Weber, *Adiabatic bond charge model for the phonons in diamond, Si, Ge, and α-Sn*, Phys. Rev. B **15** (1977).

[Web91] L. Weber and E. Gmelin, *Transport properties of silicon*, Appl. Phys. A **53**, 136 (1991).

[Wei94] J. A. Weil, J. R. Bolton, and J. E. Wertz, *Electron paramagnetic resonance* (Wiley & Sons, New York, 1994).

[Wei63] R. Mc Neill, R. Siudak, J. H. Wardlaw, and D. E. Weiss, *Electronic conduction in polymers - I. The chemical structure of polypyrrole*, Australian J. Chem. **16**, 1056 (1963); B. A. Bolto and D. E. Weiss, *Electronic conduction in polymers - II. The electrochemical reduction of polypyrrole at controlled potential*, Australian J. Chem. **16**, 1076 (1963); B. A. Bolto, R. Mc Neill, and D. E. Weiss, *Electronic conduction in polymers - III. Electronic properties of polypyrrole*, Australian J. Chem. **16**, 1090 (1963).

[Wer94] E. Werwa, A. A. Seraphin, L. A. Chiu, C. Zhou, and K. D. Kolenbrander, *Synthesis and processing of silicon nanocrystallites using a pulsed laser ablation supersonic expansion method*, Appl. Phys. Lett. **64**, 1821 (1994).

[Wid02] P. I. Widenborg and A. G. Aberle, *Surface morphology of poly-Si films made by aluminium-induced crystallisation on glass substrates*, J. Cryst. Growth **242**, 270 (2002).

[Wig01] H. Wiggers, R. Starke, and P. Roth, *Silicon particle formation by pyrolysis of silane in a hot wall gasphase reactor*, Chem. Eng. Technol. **24**, 261 (2001).

[Xia95] H. Xia, Y. L. He, L. C. Wang, W. Zhang, X. N. Liu, X. K. Zhang, H. E. Jackson, and D. Feng, *Phonon mode study of Si nanocrystals using micro-Raman spectroscopy*, J. Appl. Phys. **78**, 6705 (1995).

[XuS07] Q. Xu, I. D. Sharp, C. W. Yuan, D. O. Yi, C. Y. Liao, A. M. Glaeser, A. M. Minor, J. W. Beeman, M. C. Ridgway, P. Kluth, J. W. Ager III, D. C. Chrzan, and E. E. Haller, *Superheating and supercooling of Ge nanocrystals embedded in SiO_2*, Journal of Physics: Conference Series **61**, 1042 (2007).

[Yan99] C.-S. Yang, R. A. Bley, S. M. Kauzlarich, H. W. H. Lee, and G. R. Delgado, *Synthesis of alkyl-terminated silicon nanoclusters by a solution route*, J. Am. Chem. Soc. **121**, 5191 (1999).

[Yan00] C.-S. Yang, S. M. Kauzlarich, Y. C. Wang, and H. W. H. Lee, *Photoluminescence as a function of aggregated size from n-butyl-terminated silicon nanoclusters*, J. Cluster Sci.**11**, 423 (2000).

[YuC99] P.Y. Yu and M. Cardona, *Fundamentals of semiconductors – physics and material properties*, 2nd Edition (Springer, Berlin, 1999).

[YuL07] D. Yu, S. Lee, and G. S. Hwang, *On the origin of Si nanocrystal formation in a Si suboxide matrix*, J. Appl. Phys. **102**, 084309 (2007).

[Zho07] Z. Zhou, M. L. Steigerwald, R. A. Friesner, L. Brus, and M. S. Hybertsen, *Structural and chemical trends in doped silicon nanocrystals: First-principles calculations*, Phys. Rev. B **71**, 245308 (2005).